

Copyright
by
Tuan Anh Ngo
2017

The Dissertation Committee for Tuan Anh Ngo
certifies that this is the approved version of the following dissertation:

Low Frequency AC Transmission for Power Systems

Committee:

Surya Santoso, Supervisor

Ari Arapostathis

Efstathios Bakolas

Ross Baldick

Gary Hallock

Low Frequency AC Transmission for Power Systems

by

Tuan Anh Ngo, Engineer; M.S.

DISSERTATION

Presented to the Faculty of the Graduate School of

The University of Texas at Austin

in Partial Fulfillment

of the Requirements

for the Degree of

DOCTOR OF PHILOSOPHY

THE UNIVERSITY OF TEXAS AT AUSTIN

May 2017

To my beloved mother, who dedicated her entire life to support me.
Even though you are not with me today, I believe that you are always looking forward
to seeing my complete work and graduation.

Acknowledgments

I would like to take this opportunity to express my deepest appreciation to all people who helped me to finish my work. I would like to express my sincere thanks to my advisor, Dr. Surya Santoso, for his mentorship and excellent guidance during this project. I was lucky to attend my advisor class on wind power plant modeling where I started initial steps on low frequency transmission studies. Dr. Santoso not only guides me through rigorous research but also shapes me in a positive attitude in life by his passion, patience, and diligence. I am also grateful to my committee members for dedicating their time and effort to provide valuable guidance. I want to thank Dr. Ari Arapostathis for his kindness and support. I am lucky to have him in my committee and being supervised by his former student in POSTECH, Dr. Kwanghee Nam. I am grateful to Dr. Efstathios Bakolas for his support and guide in control theory. Thank you for letting me in your wonderful classes and for your share. I want to thank Dr. Ross Baldick for his generous support. His explanations are always clear and easy to understand, and his emails cheer me up all the time. I want to thank Dr. Gary Hallock for all his support and kindness. Thank you for bringing me a great chance and experience to work with you on senior design classes.

I would like to thank Vietnam Education Foundation (VEF) for their generous financial support during my Ph.D. studies. Thanks to VEF board of directors, VEF staff and fellows for their dedication to make my dream to study in the United States become

true. I would like to appreciate the Electrical and Computer Engineering department at the University of Texas at Austin for many opportunities and experience not only in research but social events.

My Ph.D. life is memorable because I have friends who are not only willing to share their thoughts in research but also daily life. I want to thank my lab members for their technical support and cooperating in energy systems, and interesting discussions on culture. Thank you Min Lwin, Kyungwoo Min, Quan Nguyen, Hunter Estes, Naveen Ganta, Suma Jothibas, Harsha Padullaparti, Ranga Yadi Putra, Piyapath Siratarnsophon, Sundaravaradan Navalpakkam Ananthan, Sambuddha Chakrabarti, Wanki Cho, Jules Campbell, Pisitpol Chirapongsananurak, Swagata Das, Anamika Dubey, Yichuan Niu, Duhee Lee. I especially thank to David Orn Jonsson for his effort to help me understand musical and American culture. I would like to thank my Vietnamese friends at UT Austin, Cuong Nguyen, Kha Tran, Hieu Nguyen, Dung Phan, and Ha Bui for their support and encouragement. I also want to thank Dr. Samet Biricik and Dr. Tuyen Vu for their support and remote collaboration in research.

Last but not least, my Ph.D. work is done because of countless support and encouragement from my family and relatives. I want to thank my grandparents for always motivating me to pursue higher education. I sincerely appreciate my beloved aunties for their share and help at home while I study in the United States. I have motivation to finish my work because of these wonderful people.

Low Frequency AC Transmission for Power Systems

Publication No. _____

Tuan Anh Ngo, Ph.D.

The University of Texas at Austin, 2017

Supervisor: Surya Santoso

Conventional transmission systems utilize either high voltage ac (HVAC), operating at 50 or 60 Hz, or high voltage dc (HVDC) to transfer bulk power. The HVAC system is designed to operate at a high voltage level to reduce losses and increase bulk power transfer. This method is limited, however, by the constraints of installed transmission overhead lines, such as voltage level and power transfer capability. In contrast, the HVDC system can handle a large amount of power on the transmission line by utilizing dc current instead of ac. While the HVDC system has no limitation in transmission line length for power transfer, it does however, require a high initial cost for converter stations and specialized protection systems. Additionally, the HVDC system is a point-to-point connection, and thus not flexible for multi-terminal connection. The low frequency ac (LFAC) transmission system, first introduced in 2000, is another solution for bulk power transmission that inherits advantages from both high voltage ac and high voltage dc systems. The primary advantage of LFAC transmission is that by operating the system at a frequency lower than 50 or 60 Hz, the transmission line reactance can be significantly reduced, thus extending power capacity. Further advantages include multi-terminal connec-

tions, distance protection using alternating-current based circuit breakers, and improving power transfer capability close to that of an HVDC system. This dissertation investigates the benefits of an LFAC system in terms of power transfer capability and voltage stability. First, the steady-state performances of the transmission line under low frequency range are investigated, including the skin effect to see any possible changes in transmission line model. More importantly, the power transfer capability, and voltage profiles during no-load and full-load conditions are examined. Next, the system voltage stability under low frequency operations is studied in detail to analyze how the low frequency operation helps improve a power system stability. Furthermore, the system modeling, protection, and hardware platform to test the low frequency ac transmission are studied deeply. A new grid synchronization configuration to interface a low frequency system with a 60 Hz ac system is also proposed. Moreover, a fast and robust fault detection mechanism based on the second-order generalized-integrator (SOGI) grid synchronization technique is to develop and work properly in a low frequency system. Last but not least, a small-scaled transmission and distribution system is built to verify the basic performances of a power system at a low frequency operations.

Table of Contents

Acknowledgments	v
Abstract	vii
List of Tables	xiii
List of Figures	xiv
Chapter 1. Introduction	1
1.1 Background and Motivation	1
1.2 The State-of-Art of LFAC Transmission	2
1.3 Research Objective	4
Chapter 2. Steady-State Performance of LFAC Transmission	8
2.1 Steady-State Transmission Line Model	8
2.1.1 Transmission Line Parameters and Skin Effect	8
2.1.2 Transmission Line Model Under Low Frequency	10
2.2 Steady-State Analyses of LFAC Transmission	14
2.2.1 Power Transfer Capability of the LFAC System	15
2.2.2 Voltage Profile in LFAC Transmission	19
2.2.3 Power Losses in LFAC Transmission	22
Power losses calculations	23
Overhead line transmission systems	25
Power cable transmission systems	27
Simulation results	32

Chapter 3. Voltage Stability of LFAC Transmission	37
3.1 Power Flow Solution for Low Frequency AC Transmission	37
3.1.1 Equivalent Transmission Line Parameters between LFAC and HVAC Systems	38
3.1.2 Power Flow Simulation in HVAC and Multi-Frequency Systems . . .	41
Power flow in a conventional HVAC system	41
Validation of equivalent parameters of a transmission line at different frequencies	41
3.2 The $V - P$ and $Q - V$ Characteristic Curves	44
3.3 Modal Analysis Method for Stability Analysis	48
3.3.1 Modal Analysis Method for a Two-Bus System	48
3.3.2 The Proposed Modified Modal Analysis Method for an LFAC System	52
3.4 Voltage Stability of System: A Case Study	54
3.4.1 A five-bus system operating at a specific frequency	54
3.4.2 A six-bus system operating at a specific frequency	56
Chapter 4. System Modeling for LFAC Transmission	61
4.1 Grid Synchronization for Power Converter Systems	63
4.1.1 Review of SOGI Configuration	63
4.1.2 The Third-Order Grid Synchronization Configurations	65
Grid synchronization based on third-order system	67
The frequency controller and DHOIGI-FLL structure	70
4.1.3 Simulation Results	72
Single-phase grid with a HOGI	73
Three-phase grid with HOGIs	73
4.1.4 Experimental Results	78
4.2 Power Converter Configurations	80
4.2.1 Direct Frequency Conversion Systems	80
4.2.2 Indirect Frequency Conversion Systems	82
Mathematical model of power converter	83
4.3 Control Methods for a Power Converter	85
4.3.1 PI Controllers	85
Current controller	86

Voltage controller	87
4.3.2 <i>PR</i> Controllers	89
4.4 The Proposed <i>PR</i> Controller	90
4.4.1 The <i>PR</i> -based Controller Review	92
4.4.2 The proposed controller for frequency stability	96
4.4.3 Simulation Results	99
4.5 Simulation Results of a Multi-frequency Power Systems	102
Grid synchronization waveforms	102
Power converter waveforms	103
The transmission waveforms	105
Chapter 5. System Protection for LFAC Transmission	106
5.1 System Protection Analysis for LFAC Transmission	107
5.1.1 Critical Fault Clearing Time	107
5.1.2 Distance Protection	109
Impact on load encroachment	110
Impact on relay loadability	113
5.2 A Fast Fault Detection for LFAC Systems based on SOGI Technique	115
5.2.1 Fault Characteristics and Frequency-Lock Loop Method	118
The Fault Analysis	118
Frequency-Lock Loop Operating Principles and its Utilizations for Fault Detection	119
5.2.2 Simulation Results	123
Simulation Results in a Strong Power System	124
Single Line-to-Ground Faults	124
Capacitor Switching	125
Transformer Energizing	125
Timing Diagram	128
Simulation Results in a Weak Power System	130
The Proposed Method in LFAC Power Systems	134
Chapter 6. Hardware Testing for LFAC Transmission	145
6.1 Hardware Testing for Low Frequency AC Transmissions	145
The Hardware System for LFAC Operation Testing	147

Chapter 7. Conclusion	157
7.1 Conclusion	157
Bibliography	161
Vita	180

List of Tables

2.1	Reactive power Q_{Loss} in MVar (top) and real power losses P_{Loss} in MW (bottom) on the overhead line.	32
2.2	Reactive power Q_{Loss} in MVar (top) and real power losses P_{Loss} in MW (bottom) on the power cable.	33
3.1	Voltages and Powers in a Conventional HVAC System and a Multi-Frequency System in PSCAD/EMTDC.	44
3.2	Receiving-end bus eigenvalues.	53
3.3	Bus Data of Five-Bus System.	56
3.4	Bus Voltage Magnitude.	58
3.5	Eigenvalues (top) and self-sensitivities (bottom) at buses.	58
5.1	Critical clearing angle and clearing time.	109
5.2	Relay Loadability Limits at Different Frequencies (pu).	115
5.3	Event properties under SOGI-FLL analysis.	128
6.1	Current magnitude (A) at different load conditions.	149
6.2	RMS Voltage (V) along the line at different frequencies.	153

List of Figures

1.1	The general scope for LFAC research.	7
2.1	Skin effect on transmission line impedance.	9
2.2	Impedance in the of interest frequency range.	10
2.3	Transmission line section in distributed model.	11
2.4	Parameters $A(x)$ along transmission line.	13
2.5	Incident and reflected voltage magnitudes along the transmission line. . . .	14
2.6	A two-bus model for low frequency AC transmission.	15
2.7	Power circle diagram at different frequencies.	17
2.8	Power capability at different frequencies.	18
2.9	No-load voltages and currents at different frequencies.	21
2.10	Full-load voltages at different frequencies.	22
2.11	An equivalent two-bus transmission system.	23
2.12	(a) The receiving-end voltage in per unit in contour plot with power transfer and frequency, and (b) the receiving-end voltage in per unit versus frequency	26
2.13	Overhead line power losses in contour plot: (a) real power, (b) reactive power, and (c) at different load conditions.	28
2.14	(a) The receiving-end voltage in per unit in contour plot with power transfer and frequency, and (b) the receiving-end voltage in per unit versus frequency	30
2.15	Power cable power losses in contour plot: (a) real power, (b) reactive power, and (c) at different load conditions.	31
2.16	(a) Voltage profile along the line, and (b) voltage with load variations. . . .	35
2.17	Voltage profile along the line at different load conditions: a) 210MW, b) 270MW, and c) 300MW.	36
3.1	Equivalent transmission line models operated at different frequencies. . . .	40
3.2	Line power of a 5-bus test system operated at 60 Hz.	42
3.3	Multi-frequency system with line power equal to that of the conventional system.	43
3.4	V-P characteristics at (a) different frequencies and (b) different line lengths.	46

3.5	Stability reserved margin at different frequencies.	47
3.6	The eigenvalue trajectory with frequency variation.	50
3.7	The modified eigenvalue trajectory versus frequency.	54
3.8	A five-bus power system.	55
3.9	A six-bus LFAC system for wind applications.	57
3.10	Bus 5 profiles with different frequencies: (a) voltage magnitudes, (b) eigenvalues, and (c) self-sensitivities (\diamond 60Hz, \triangle 30Hz, \circ 10Hz, \square 5Hz).	60
4.1	Interface between an LFAC and a 60 Hz power system.	62
4.2	The overall power converter system.	62
4.3	A typical SOGI structure.	63
4.4	Voltage waveforms from a SOGI under distorted conditions.	65
4.5	Bode plots of third-order synchronization system.	67
4.6	A grid synchronization configuration based on CCF.	68
4.7	Configurations based on SOGI: a) general case, b) $k_r = 0$, and c) $k_i = 0$	69
4.8	Bode plots of ε_v and qv' in a third-order synchronization system.	70
4.9	The overall block diagram of DHOGI-FLL system.	72
4.10	a) Single-phase input and b) output waveforms.	74
4.11	The frequency controller response.	75
4.12	a) Three-phase input voltages and b) output waveforms.	76
4.13	a) Voltage magnitude and b) frequency detection.	77
4.14	a) Distorted grid voltage waveforms (188 V/div), and b) input voltages after Clarke's transformation.	79
4.15	a) Positive-sequence outputs, and b) frequency response in the third-order proposed DHOGI-FLL method.	79
4.16	A typical matrix converter.	81
4.17	A typical back-to-back converter.	82
4.18	A PWM converter configuration.	83
4.19	The overall control system.	85
4.20	The current loop using PI controllers.	87
4.21	The voltage loop using an IP controller.	88
4.22	The current loop using a PR controller.	90
4.23	The PR-based controllers: a) PR , b) $PRXF$, c) $PRXC$, and d) $PRX2$ configurations.	93

4.24	Bode plots of opened-loop (top-blue) and closed-loop (bottom-red): a) <i>PR</i> , b) <i>PRXF</i> , c) <i>PRXC</i> , and d) <i>PRX2</i>	94
4.25	Sensitivities versus frequency in the four controller configurations.	95
4.26	a) The concept controller with two <i>PRX2</i> , and b) its Bode plot.	97
4.27	a) The proposed controller configuration, and b) its closed-loop Bode plot.	98
4.28	The control reference currents in time-domain (top) and $\alpha\beta$ frame (bottom).	99
4.29	Current waveforms on the stationary frame in the: a) conventional <i>PR</i> controller, and b) proposed <i>PR</i> controller.	101
4.30	Phase angles from the synchronization system: 60 Hz (top) and 30 Hz (bottom).	102
4.31	The DC-link voltage waveform.	103
4.32	Converter output currents in: a) 60 Hz side, and b) 30 Hz side.	104
4.33	Voltages and currents on transmission level: a) 60 Hz system, and b) 30 Hz system.	105
5.1	Critical clearing time calculation.	109
5.2	Single-line diagram of three-bus system used in protection studies.	110
5.3	Shortest distance definition for protection at 60 Hz.	112
5.4	Shortest protection distance with different frequencies.	112
5.5	Maximum relay loadability with <i>mho</i> characteristics.	114
5.6	The current magnitude and phase angle at different operating frequencies.	119
5.7	A typical SOGI structure.	120
5.8	The block diagram of SOGI-FLL for positive-/negative-sequence calculation.	122
5.9	The overall block diagram of fast fault detection using SOGI-FLL.	123
5.10	The power system with three different events.	124
5.11	A single-phase to ground in a strong power system: (a) current magnitudes and (b) phase angle waveforms.	126
5.12	Capacitor switching in a strong power system: (a) current magnitudes and (b) phase angle waveforms (zoomed in).	127
5.13	Transformer energizing in a strong power system: (a) current magnitudes and (b) phase angle waveforms.	129
5.14	The proposed and cosine filter methods responses in a strong 60-Hz system.	130
5.15	A single-phase to ground in a weak power system: (a) current magnitudes and (b) phase angle waveforms.	132

5.16	Capacitor switching in a weak power system: (a) current magnitudes and (b) phase angle waveforms (zoomed in).	133
5.17	Transformer energizing in a weak power system: (a) current magnitudes and (b) phase angle waveforms.	135
5.18	The proposed and cosine filter methods responses in a weak 60-Hz system.	136
5.19	Relationship between the new method time response and the power system short-circuit capacity.	136
5.20	Timing diagrams in: (a) a strong and (b) a weak 10-Hz LFAC power systems.	139
5.21	Simulation results with transmission data: (a) currents and its sequences, and (b) tripping signal and angle.	140
5.22	Simulation results with distribution data: (a) currents and its sequences, and (b) tripping signal and angle.	141
5.23	(a) Fault current waveforms, and (b) fault detections in phase <i>a</i> .	142
5.24	(a) Fault detections in phase <i>b</i> , and (b) fault detections in phase <i>c</i> .	143
5.25	Sequence estimation: (a) the current waveforms, and (b) current magnitudes.	144
6.1	One-line diagram of the small-scaled testbed power system.	146
6.2	One-line diagram of the power system for LFAC operation testing.	147
6.3	(a) The test-bed power grid, and (b) transmission line model.	148
6.4	Current magnitude at different frequency at: (a) loaded condition, and (b) no-load condition.	150
6.5	The load current waveforms flowing into the system: a) 40 Hz, b) 60 Hz, and c) 80 Hz.	151
6.6	The no-load current waveforms flowing into the system: a) 40 Hz, b) 60 Hz, and c) 80 Hz.	152
6.7	Voltage magnitude along the transmission line: (a) Experiment and simulation data, and (b) experimental, simulation, and theoretical data.	154
6.8	Voltages at the sending-end terminal: a) 40 Hz, b) 60 Hz, and c) 80 Hz.	155
6.9	Voltages at the receiving-end terminal: a) 40 Hz, b) 60 Hz, and c) 80 Hz.	156

Chapter 1

Introduction

This chapter first presents the background and motivation for low frequency transmission research. Next, the state-of-art of this topic is briefly introduced, and the needs for low frequency operation studies are addressed. The research objective is then presented to provide the scope of the work on low frequency ac transmission for power systems.

1.1 Background and Motivation

Conventional transmission systems utilize either high voltage ac (HVAC), operating at 50 or 60 Hz, or high voltage dc (HVDC) to transfer bulk power efficiently and reliably. The HVAC system is designed to operate at a high voltage level to reduce losses and increase bulk power transfer. This method is limited, however, by the constraints of installed transmission overhead lines, such as voltage level and power transfer capability. In contrast, the HVDC system can handle a large amount of power on the transmission line by utilizing dc current instead of ac. The HVDC system has no limitation in transmission line length for power transfer; however, it requires a high initial cost for converter stations and specialized protection systems. This system is also a point-to-point connection, and is therefore not flexible for a multi-terminal connection. Another solution for bulk power transmission, first introduced in [1], that inherits advantages from both

HVAC and HVDC systems is to use a low frequency ac (LFAC) transmission system. The primary advantage of LFAC is that by operating the system at a frequency lower than 50 or 60 Hz, the transmission line reactance can be significantly reduced, thus extending power capacity [1, 2]. This allows the LFAC system to inherit advantages of both HVAC and HVDC systems, such as multi-terminal connections, distance protection using alternating-current based circuit breakers, and improving power transfer capability close to that of an HVDC system. An obvious application that can utilize an LFAC system instead of an HVDC or HVAC system is wind power transmission, where the wind farms are located less than 200 km from the collecting station. With existing technologies, the wind farm is able to generate low frequency output power [3] and then sends it to transmission lines. The system is then able to handle a large amount of electric power.

1.2 The State-of-Art of LFAC Transmission

The concept of using a low frequency ac (LFAC) transmission for power system transmission was proposed by Funaki in early 2000 [1]. The original idea was operating a power system with underground cables at a very low frequency, theoretically 0.1 Hz for XLPE cables, to transfer more electric power. The LFAC transmission method, however, did not draw interest until its superior benefits in wind power transmission were discovered. The increase of wind power penetration requires transmission lines to be capable of handling large amounts of power as more generation is injected into the grid. In an on-shore or off-shore wind farm where the transmission line length is less than 200 km, for example, the LFAC system offers benefits over the HVAC and HVDC systems. In practice, due to high capacitance in HVAC cables, both the real power transfer capability

and the transmission distance are limited [4]. The HVDC system, in contrast, has no limitation on transmission distance because dc currents are used to transfer power instead of ac currents. This technology, however, has faced challenges on the dc circuit breaker and space charge accumulation of power cables [5].

The advantages of an LFAC over a conventional 60 Hz system in terms of power transfer capability are deeply investigated in [3]. Since the power transfer is proportional to the reciprocal of transmission line reactance, as the operating frequency is reduced the power is increased. In [3], the availability for an LFAC system to use existing devices in the market - such as transformers, cables, switchgears, shunt reactors or protective ac circuit breakers - is discussed and compared with the conventional system. The possibility of generating electric power with a low frequency in the generator side has been studied as well. These studies, however, do not provide enough information about transmission line parameter variations or the voltages and reactive power characteristics at a low frequency.

The research on applications of LFAC transmission for wind power is more productive and prolific [4, 5]. A detailed report on the low frequency transmission for wind farms was released by PSERC in 2012 [2]. Many alternative configurations for low frequency transmission in wind farms are introduced with thorough considerations of optimal voltage level, cost, and power transfer capability. A dissertation accompanying this low frequency transmission project was also published in 2013 [6]. The time simulation converter modeling for an LFAC system is introduced. The current and voltage waveforms from a fractional frequency cyclo-converter are shown, but there is no transient study on faults or protection in the LFAC system. Given the fact that a cyclo-converter has limitations in dynamic control response, in voltage quality (due to high harmonic contents),

and in frequency conversion (typically one-third of source frequency), further transient studies in an LFAC system cannot be done with a power cycle-converter.

All previous studies on the LFAC transmission are based on assumptions that the power system is capable of operating at a low frequency without any stability issues. The LFAC system seems to be more stable, but no evidence has been shown. Furthermore, due to the limitation of a cyclo-converter in fractional frequency, the power system performances with a frequency under one-third of the grid frequency have not been examined. Moreover, a cyclo-converter outputs voltages and currents containing many harmonic components and thus it is not suitable for LFAC studies, especially fault or transient analysis. The lack of previous studies is what originally motivated examination of the steady-state performance, stability, transient analysis, and protections in LFAC transmission.

1.3 Research Objective

The goal of the work is to evaluate the superiority of a low frequency system and utilize it for bulk power transmission instead of using the HVAC and HVDC systems. We aim to investigate the transmission distance and operating frequency range that an LFAC system can be used for specific applications. The first objective is thus to examine the steady-state performance of the LFAC system under various operating frequencies. Specifically, the impacts of skin effect on the transmission line parameters are investigated to see if any line model corrections are needed. Additionally, power transfer capability and the relationship between voltage to real and reactive power are also inspected to evaluate the benefits of the LFAC system.

It is understandable that when the power system operates at a low frequency,

the transmission line reactance is significantly reduced and thus the voltage magnitude at each bus is higher in comparison to that in the conventional 60 Hz. To the best of our knowledge, however, no research has focused on the voltage stability when the operating frequency is lowered. There has been no investigations of the proximity to voltage instability or how close the system is to voltage instability mode. Is the power system weaker or more stable when it operates at a low frequency in comparison to the conventional 60 Hz system? How far can a low frequency drive a power system from instability mode? The second objective in this work is thus to find the answers to these questions. By utilizing the modal analysis method, the system voltage stability is deeply examined and later on evidences that supports the LFAC's better performance are shown.

As part of our work, we also plan to model low frequency power systems, and a switching model that includes a power converter for frequency conversion. In addition, we examine the protection system for low frequency operations. Since an LFAC is still an ac system, it can utilize the ac breakers, which are available in the market to clear the fault. However, due to the low frequency operation or the longer time in an electrical period, the response time of a protection system may last longer. The protection system for an LFAC system thus requires further investigation, and based on this research the operating frequency range can be determined. Our work also aims to build a hardware test-bed for a low frequency transmission. This system is to demonstrate a low operating frequency power system and to verify theoretical studies. A 100-mile transmission line and an inverter are installed on this small-scaled test-bed to examine the benefits of an LFAC system such as voltage profiles at no-load and full-load conditions. The research scope for this work is summarized in Fig. 1.1.

This dissertation is organized as follows:

- Chapter 2 presents the steady-state performance of transmission line under various frequencies with consideration of skin effect. We discover that in the operating frequency range of 1 Hz to 60 Hz, the skin effect is negligible. A two-bus system is then investigated to see the benefits of an LFAC system in terms of power transfer capability and voltage profiles along the transmission line. Furthermore, the real and reactive power losses on overhead line and power cable are investigated carefully.
- Chapter 3 investigates advantages of an LFAC system over the 60 Hz system in terms of voltage stability. The stability indexes, i.e. voltage magnitude and eigenvalue, obtained from load flow solution are calculated and compared. In this chapter, we present an equivalent circuit for an LFAC system referring to 60 Hz for power flow solution, and then the proposed modified stability indexes that work for low frequency systems.
- Chapter 4 discusses our work on system modeling for LFAC transmission. The grid synchronization that connects a low frequency system to a 60 Hz system is investigated carefully. In addition, we propose a new configuration for grid synchronization in this chapter. The multi-frequency system, which is a combination of a 60 Hz and a low frequency systems, is then modeled and simulated with power converters and proportional-resonant (*PR*) control algorithm. We also propose a new and simple *PR* control that is stable under the distorted frequency condition of the power grid.
- Chapter 5 examines the low frequency operation in terms of protection perspectives. The system distance protection and fault events are analyzed carefully. A fast and

robust fault detection mechanism, which is based on the second-order generalized-integrator grid synchronization technique, is developed to detect fault events in the power system. Our proposed mechanism shows that it can detect the faults faster than the cosine method, which is implemented in the conventional protection.

- Chapter 6 presents our implementation of LFAC transmission in a hardware platform to verify theories in LFAC transmission. A test-bed with transmission and distribution systems, which is a reflection of a real world power system, is built and tested with a variable frequency power source.
- Chapter 7 concludes our work on LFAC transmission for power systems.

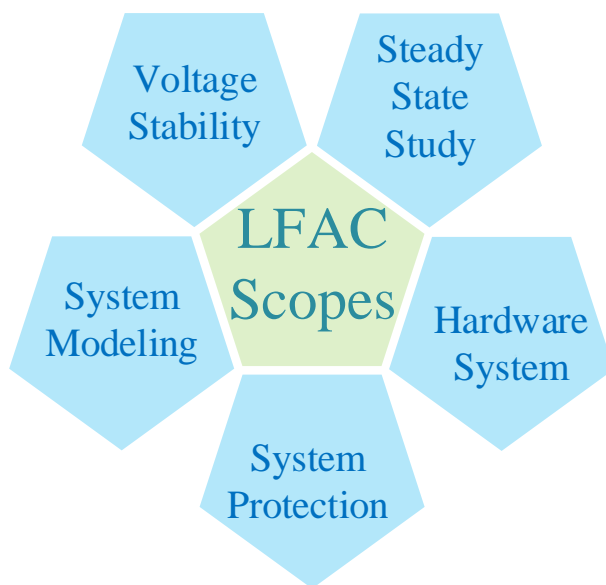


Figure 1.1: The general scope for LFAC research.

Chapter 2

Steady-State Performance of LFAC Transmission

This chapter aims to examine the steady-state performance of the LFAC system under various operating frequencies. Specifically, the impact of skin effect on the transmission line parameters is investigated to see if any line model corrections are needed. The relationship between voltage and real and reactive power is also studied and compared between LFAC, HVDC, and the conventional 60 Hz systems. Additionally, the power losses are investigated and then verified by simulation models in PSCAD/EMTDC.

2.1 Steady-State Transmission Line Model

This section analyzes how operation at lower frequencies impacts steady-state transmission line impedance parameters (resistance and reactance) and the skin effect of conductors. It also shows that the standard exact long transmission line model is applicable at lower frequencies.

2.1.1 Transmission Line Parameters and Skin Effect

Because the ac current density is not uniformly distributed and changes with frequency, the line resistance and reactance vary with frequencies. The frequency-dependent

impedance of a transmission line is given in (2.1) by [7]

$$\begin{aligned} r_{ac} &= r_{dc} \frac{ma}{2} \frac{M_0(ma)}{M_1(ma)} \cos(\theta_0(ma) - \theta_1(ma) + 3\pi/4) \\ x_{ac} &= r_{dc} \frac{ma}{2} \frac{M_0(ma)}{M_1(ma)} \sin(\theta_0(ma) - \theta_1(ma) + 3\pi/4) \end{aligned} \quad (2.1)$$

where r_{dc} is dc resistance, $ma = \sqrt{2\mu_0 f / r_{dc}}$, and $(M_0, \theta_0, M_1, \theta_1)$ are the magnitudes and phase angles of zero-order and first-order Bessel functions, respectively.

The variations in resistance and inductance per mile with frequency due to the skin effect on a conductor wire with a circular cross section of 5 mm diameter [8] are presented in Fig. 2.1. As the frequency is increased, the resistance increases while the inductance decreases. It is apparent, however, that the variations of resistance and reactance between 0 and 60 Hz are very small, i.e. 0.25% in resistance and 0.12% in inductance. This means the transmission line reactance and susceptance at a low frequency can be simply approximated from 60 Hz data using the frequency ratio.

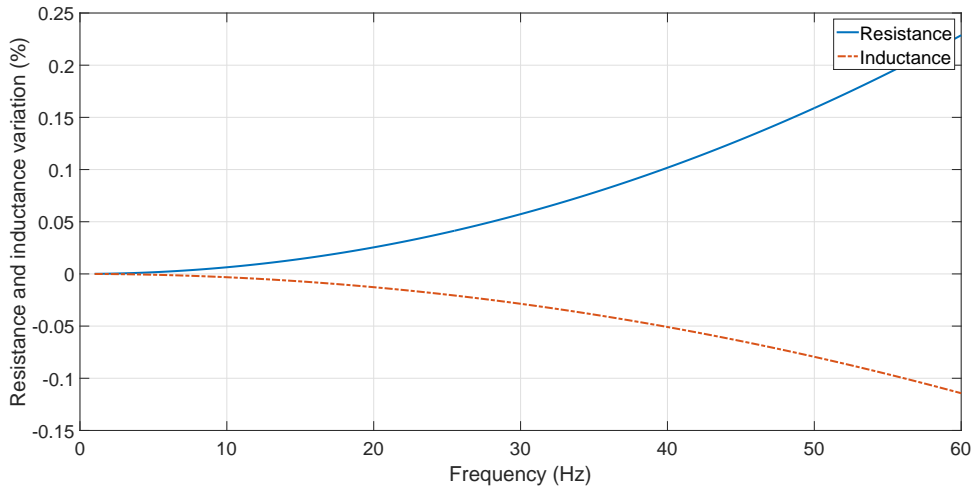


Figure 2.1: Skin effect on transmission line impedance.

Furthermore, as shown in Fig. 2.2, when the system operates between 1 and 10 Hz, the ac line impedance is close to the dc line resistance. At 1 Hz, the conductor ac impedance is 0.22736 m Ω , nearly identical to the resistance of the HVDC 5 mm thick conductor wire. The conductor ac impedance increases slightly to 0.22740 m Ω when the operating frequency is 10 Hz. In other words, the ac impedance of overhead conductors operating in low frequencies (between 1 and 10 Hz) is comparable to that of the HVDC.

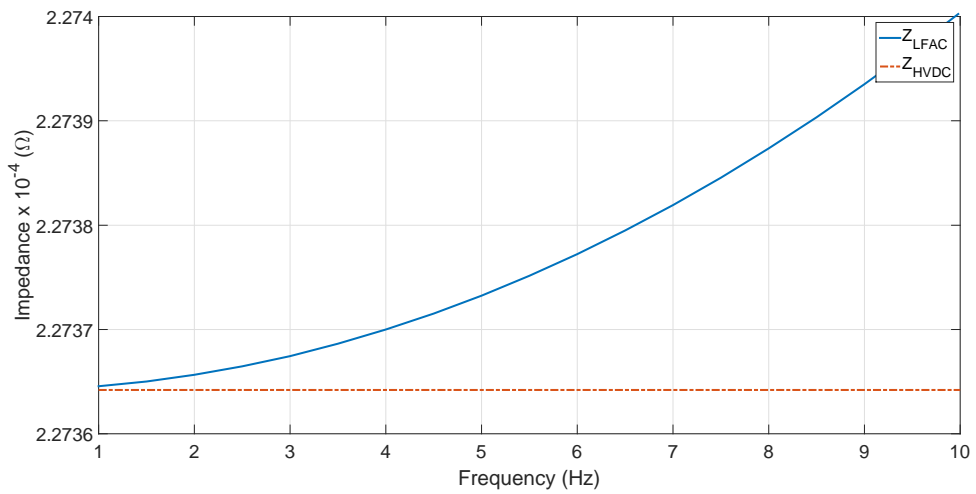


Figure 2.2: Impedance in the of interest frequency range.

2.1.2 Transmission Line Model Under Low Frequency

The transmission system under low frequency is investigated to see if any correction is needed. The exact model of a transmission line is uniformly distributed along the line length, as shown in Fig. 2.3 and can be described by differential equations.

The per-unit impedance and admittance are denoted as: $z = R + j\omega L$ and $y = G + j\omega C$. Assuming the transmission line operates with sinusoidal time-varying waveforms

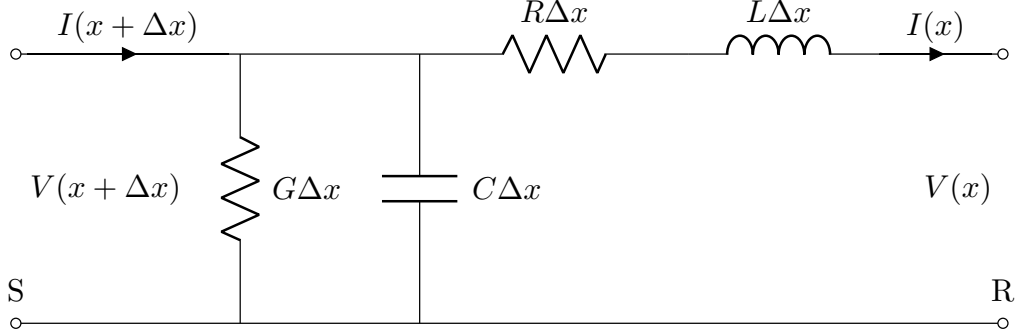


Figure 2.3: Transmission line section in distributed model.

at steady-state, the voltage and current in each transmission section can be derived as follows [9, 10]

$$\frac{\partial V}{\partial x} = (R + j\omega L)I, \quad \frac{\partial I}{\partial x} = (G + j\omega C)V \quad (2.2)$$

The wave equation for voltage is thus given by:

$$\frac{\partial^2 V}{\partial x^2} - [(RG - \omega^2 LC) - j\omega(RC + LG)]V = 0 \quad (2.3)$$

The general solution to (2.3) is the receiving-end voltage $V = V^+e^{\gamma x} + V^-e^{-\gamma x}$ with $\gamma = \sqrt{zy} = \sqrt{RG - \omega^2 LC + j\omega(RC + LG)}$. From the boundary conditions: $V(0) = V_R, I(0) = I_R$, the voltage and current are expressed [10]

$$V(x) = \left(\frac{e^{\gamma x} + e^{-\gamma x}}{2}\right)V_R + Z_c\left(\frac{e^{\gamma x} - e^{-\gamma x}}{2}\right)I_R \quad (2.4)$$

$$I(x) = \frac{1}{Z_c}\left(\frac{e^{\gamma x} - e^{-\gamma x}}{2}\right)V_R + \left(\frac{e^{\gamma x} + e^{-\gamma x}}{2}\right)I_R \quad (2.5)$$

where $Z_c = \sqrt{z/y} = \sqrt{(R + j\omega L)/(G + j\omega C)}$ is the characteristic impedance, which is the ratio of voltage and current along the line in one direction. This characteristic impedance is independent from line length but depends on the geometry and material of the transmission line [9].

The voltage and current in the distributed line that is x miles far from the receiving-end terminal can thus be given in matrix format in terms of the receiving-end voltage and current [10]

$$\begin{bmatrix} V(x) \\ I(x) \end{bmatrix} = \begin{bmatrix} A(x) & B(x) \\ C(x) & D(x) \end{bmatrix} \begin{bmatrix} V_R \\ I_R \end{bmatrix} \quad (2.6)$$

where $A(x) = D(x) = \cosh(\gamma x)$, $B(x) = Z_c \sinh(\gamma x)$, $C(x) = (1/Z_c) \sinh(\gamma x)$. The $ABCD$ parameters mathematically represent exact parameters of any transmission line.

The exact model in (2.6) with consideration of skin effect is complex due to the Bessel function. An estimated model is instead proposed. In this model, the transmission line parameters at a low frequency is obtained directly from the 60 Hz parameters. The resistance in low frequency is same as that in 60 Hz, and reactance is obtained by multiplying the 60 Hz reactance with the frequency ratio. Fig. 2.4 shows the transmission model parameter $A(x)$ for 200 miles, 345 kV line from receiving-end to sending-end in two different models. It can be observed that in the range of interested frequency, the parameters in exact and estimated models (dashed-line) are nearly identical. The differences are very small, i.e, on the order of 10^{-4} . This means that the estimated model can be used to represent the transmission line model at a low frequency operation. The parameters for the estimated model can be simply derived from the conventional 60 Hz transmission line model by scaling reactance with frequency and keeping the resistance constant.

Recall from (2.4) that the voltage along the transmission line is a combination of incident voltage $V_i = V^+ e^{\gamma x}$ and reflected voltage $V_r = V^- e^{-\gamma x}$. The incident voltage represents the forward propagating wave that transfers power to the load while the reflected voltage represents the backward wave that sends power back to the source. The

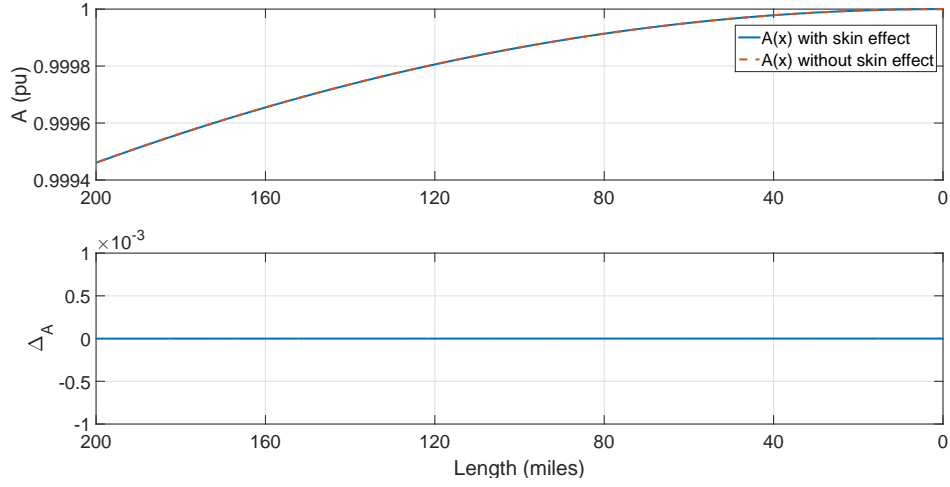


Figure 2.4: Parameters $A(x)$ along transmission line.

real power transfer depends on both of these voltages and is thus given by [9]

$$\begin{aligned}
 P &= \frac{1}{2} \text{Re}[(V_i + V_r)(I_i - I_r)^*] \\
 &= \frac{1}{2} \text{Re}\left[\frac{1}{Z_c} |V_i|^2 \left(1 + \frac{V_r}{V_i}\right) \left(1 - \frac{V_r}{V_i}\right)^*\right] \\
 &= \frac{1}{2Z_c} |V_i|^2 \left(1 + \left|\frac{V_r}{V_i}\right|^2\right)
 \end{aligned} \tag{2.7}$$

Fig. 2.5 shows incident and reflected voltage magnitudes along a 200-mile transmission line of a 345 kV system. It can be observed from the figure that a benefit of low frequency operation is a higher value of incident voltage magnitude. This means more power can be transferred at a low frequency, as dictated by (2.7). However, the reflected voltage magnitude, in terms of the corresponding incident magnitude, is also higher in the low frequency system. For example, to deliver the same 270 MW in the transmission line, the ratio between reflected and incident voltages is 14.6% at 5 Hz but 8.8% and 7.7%

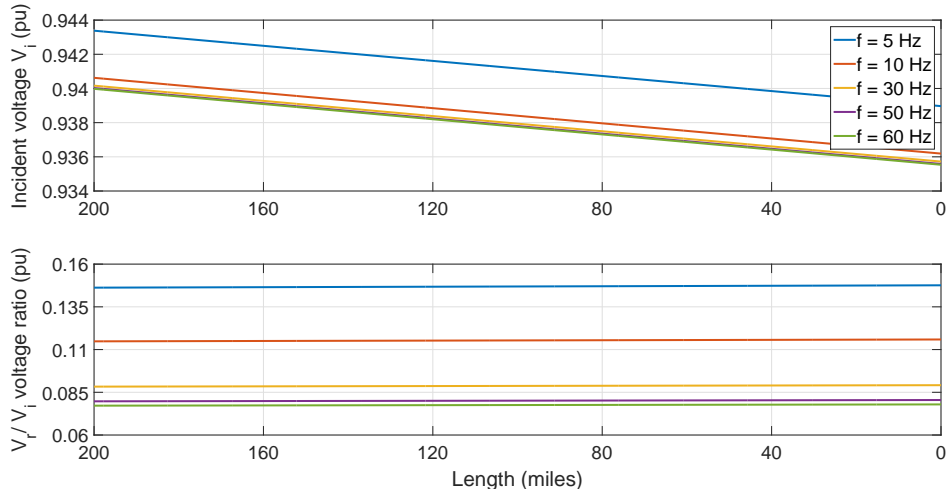


Figure 2.5: Incident and reflected voltage magnitudes along the transmission line.

if the system operates at 30 Hz and 60 Hz, respectively. This can be explained by the larger ratio R/X between resistance and reactance at a low frequency. By selecting a low resistance transmission overhead line, the reflected voltage can be reduced, and therefore less power is sent back to the source.

2.2 Steady-State Analyses of LFAC Transmission

The goal of this section is to demonstrate and quantify the steady-state performance of an LFAC transmission line in terms of power transfer capacity, voltage profiles, and $V-P$ and $Q-V$ characteristic curves. A two-bus model, shown in Fig. 2.6, consisting of two equivalent sources operating at 50 or 60 Hz equipped with an idealized and lossless power converter at each end of the LFAC line is used to aid the performance analysis.

2.2.1 Power Transfer Capability of the LFAC System

A two-bus system is used to demonstrate the power transfer capacity of an LFAC transmission line. The LFAC transmission line model is distributed as discussed in Section II and can be represented with an equivalent π -model [10] as presented in Fig. 2.6. The current flowing from the sending-end to the receiving-end is given by [11]

$$\bar{I}_R = \frac{\bar{V}_S - \bar{V}_R}{\bar{Z}} - \frac{\bar{Y}}{2}\bar{V}_R = \frac{V_S \angle \delta^\circ - V_R}{Z} - \frac{\bar{Y}}{2}V_R \quad (2.8)$$

where $\bar{Z} = R + j\omega L$ and $\bar{Y} = G + j\omega C$ are transmission line parameters, and power angle δ can be negative or positive depending on the power flow direction in the system.

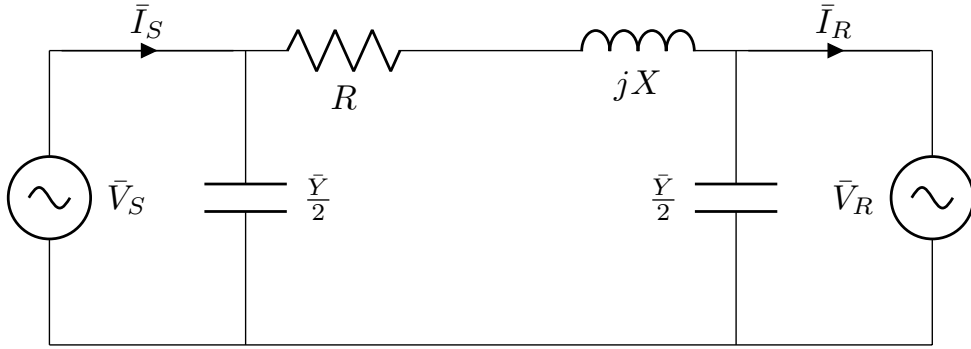


Figure 2.6: A two-bus model for low frequency AC transmission.

The apparent power at the sending-end and receiving-end in the network are given by:

$$\begin{aligned} \bar{S}_S = \bar{V}_S \cdot \bar{I}_S^* &= \frac{\bar{Y}^*}{2}V_S^2 + \frac{V_S^2}{\bar{Z}^*} - \frac{V_S V_R}{\bar{Z}^*}e^{j\delta} \\ \bar{S}_R = \bar{V}_R \cdot \bar{I}_R^* &= -\frac{\bar{Y}^*}{2}V_R^2 - \frac{V_R^2}{\bar{Z}^*} + \frac{V_S V_R}{\bar{Z}^*}e^{-j\delta} \end{aligned} \quad (2.9)$$

From (2.9), the apparent power can be expressed in the form

$$\begin{aligned}\bar{S}_S &= C_1 - R_a e^{j\delta} \\ \bar{S}_R &= C_2 + R_a e^{-j\delta}\end{aligned}\tag{2.10}$$

where $C_1 = \frac{\bar{Y}^*}{2} V_S^2 + \frac{V_S^2}{Z^*}$, $C_2 = -\frac{\bar{Y}^*}{2} V_R^2 - \frac{V_R^2}{Z^*}$, $R_a = \frac{V_S V_R}{|Z|}$.

It can be observed from (2.10) that the sending-end and receiving-end apparent power loci are circles in the complex coordinate. The center of the sending-end circle depends only on the sending-end voltage, and the center of the receiving-end circle depends only on the receiving-end voltage. Both circles, however, share the same radius: $R_a = V_S V_R / |Z|$ [12]. If the power angle δ increases from zero, the real power proportionally increases. From the geometry in Fig. 2.7, there is maximum value of real power transfer, which is limited by the power angle. This angle can be derived from (2.9) and is $\delta = 180^\circ - \angle Z$. It is obvious that the maximum real power transfer depends on sending-end voltage V_S , receiving-end voltage V_R , and transmission line impedance Z . Quantitatively, the transmission line maximum real power transfer capability can be increased by reducing impedance Z or increasing voltage level. If the system operates at a low frequency, the line impedance is small, and as a result the system can handle more real power. This is represented by a larger circle radius for the same plot at a lower frequency.

Fig. 2.7 shows the power circles for both ends of the transmission line for two different frequencies: 60 Hz and 10 Hz. The sending-end voltage is 345 kV or 1.0 pu, and the receiving-end voltage is 0.9 pu. The system base is 100 MVA with $|Z| = 125 \Omega$ at 60 Hz and $|Z| = 22 \Omega$ at 10 Hz for the equivalent π -model of 200 miles transmission line. The sending-end and receiving-end apparent power trace two circles and depend on the

power angle δ [12]. In the 60 Hz system (dashed-line), the radius is $R_a = 8.60$ pu, which is relatively small in comparison with that in the 10 Hz system, where $R_a = 48.83$ pu. This means that at the same power angle, the LFAC system can handle approximately six times more power transfer capacity compared to the 60 Hz system.

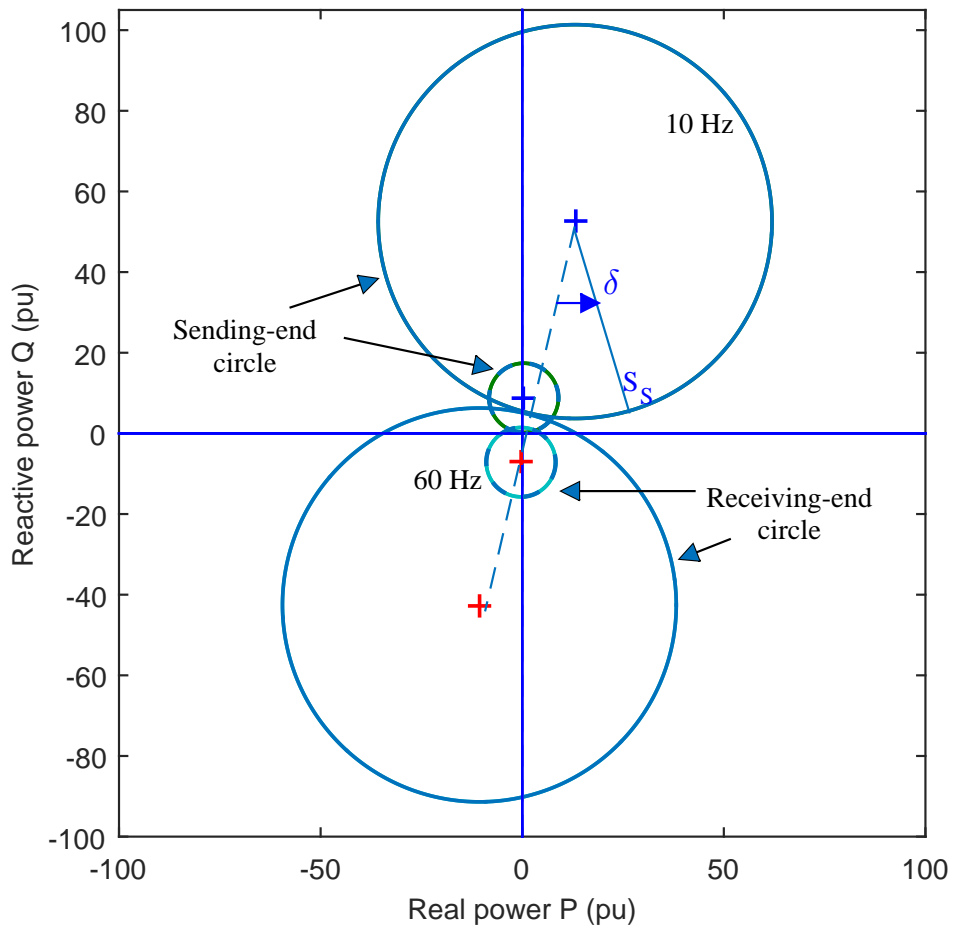


Figure 2.7: Power circle diagram at different frequencies.

The benefits of LFAC transmission become even clearer when further investigating the real and reactive power transfer capability. For example, from (2.9), the receiving-end

power can be expressed as:

$$\bar{S}_R = \bar{V}_R \cdot \bar{I}_R^* = V_R \left(\frac{V_S \angle -\delta - V_R}{\bar{Z}^*} - \frac{\bar{Y}^*}{2} V_R \right) \quad (2.11)$$

The real and reactive power at the receiving-end can be derived from the above equation as follows:

$$\begin{aligned} P_R &= -G \frac{V_R^2}{2} - R \frac{V_R^2}{|\bar{Z}|^2} + \frac{V_S V_R}{|\bar{Z}|^2} (X \sin \delta + R \cos \delta) \\ Q_R &= B \frac{V_R^2}{2} - X \frac{V_R^2}{|\bar{Z}|^2} + \frac{V_S V_R}{|\bar{Z}|^2} (X \cos \delta - R \sin \delta) \end{aligned} \quad (2.12)$$

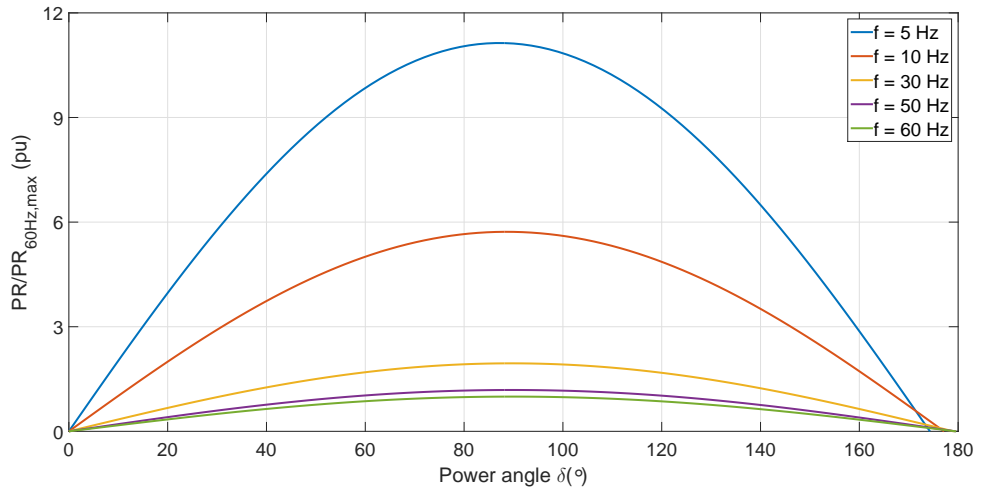


Figure 2.8: Power capability at different frequencies.

From (2.12), since the ac transmission line is dominated by the reactance, the real power transfer can be significantly improved by operating the system at a low frequency and thus reducing reactance. Fig. 2.8 shows the real power transfer capability at different frequencies. It is obvious that the maximum real power is significantly increased if the

frequency is reduced to 5 Hz. The maximum power at 5 Hz is approximately 11 times that of the 60 Hz system and is slightly less than the frequency ratio (60/5) due to the effect of resistance at low frequencies.

2.2.2 Voltage Profile in LFAC Transmission

The voltage profile along the transmission line is studied by comparing the system behavior under full-load and no-load conditions at different operating frequencies. From (2.8) and (2.11), assuming the sending-end voltage is $V_S = 1.0$ pu and denoting $a = (|1 + \bar{Y}\bar{Z}/2|)$, the receiving-end voltage $V_R \angle -\delta = V_{R,r} - jV_{R,i}$.

$$\begin{aligned} a(V_{R,r}^2 + V_{R,i}^2) &= V_{R,r} - (RP_R + XQ_R) \\ V_{R,i} &= XP_R - RQ_R \end{aligned} \quad (2.13)$$

then

$$\begin{aligned} aV_{R,r} &= \frac{1}{2} + \sqrt{\frac{1}{4} - a(RP_R + XQ_R) - a^2(XP_R - RQ_R)^2} \\ V_{R,i} &= XP_R - RQ_R \end{aligned} \quad (2.14)$$

The voltage magnitude at the receiving-end terminal is given by

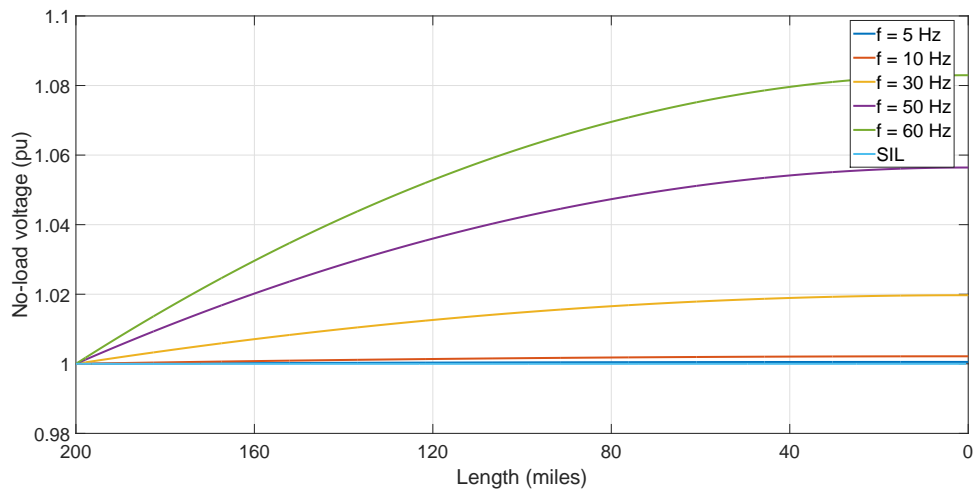
$$a^2V_R^2 = \frac{1}{2} + \sqrt{\frac{1}{4} - a(RP_R + XQ_R) - a^2(XP_R - RQ_R)^2 - a(RP_R + XQ_R)} \quad (2.15)$$

It is apparent from (2.15) that the receiving-end voltage is a function of transmission line reactance. If the line reactance X is high, the voltage at the receiving-end will be low. Therefore, if the reactance X is lowered, the voltage can be increased. In particular, the receiving-end voltage at a low frequency is higher than that at high frequency.

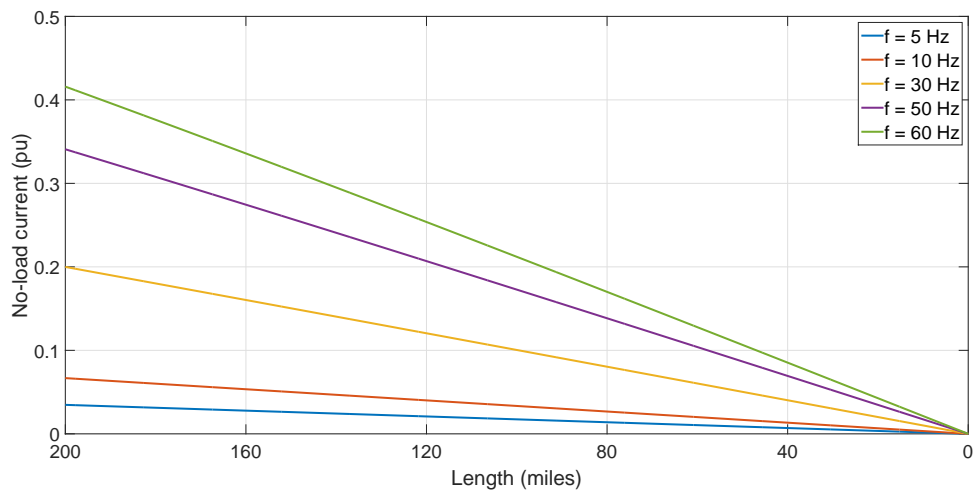
Using the distributed transmission line model with parameters in (2.6), the voltage and current profiles along the line in case of no-load condition are presented in Fig. 2.9. As expected, the 60 Hz system has the highest no-load voltage value of 1.083 pu (see Fig. 2.9(a)) which necessitates the use of reactive power compensation devices. The voltage in a 5 Hz system, on the other hand, is close to the surge impedance loading (SIL) voltage curve. In other words, the Ferranti effect in the LFAC system is less than that in the conventional 60 Hz system. It is of interest that, theoretically, no reactive power compensation devices are required. The no-load currents in the interested range of frequency are shown in Fig. 2.9(b). The no-load current at a low frequency is relatively small compared to that at a high frequency. At 60 Hz, the no-load current is 0.42 pu and decreases to 0.20 pu at 30 Hz. It further decreases to only 0.035 pu at 5 Hz. This means that in the no-load condition, losses on the transmission line are lower if the power system runs at a low frequency.

Fig. 2.10 shows the steady-state voltage at a full-load condition under different operating frequencies with the assumption that the systems transfer the same amount of electric power. It can be observed that the voltage drop in a 60 Hz system is large, and that the receiving-end voltage hits the lower limitation (i.e $V_R = 0.95$ pu). The voltage drop in the LFAC system is small compared to a traditional 60 Hz ac. The voltage at the receiving-end is 0.978 pu when the transmitted frequency is 10 Hz, and it reaches 0.982 pu when the frequency is reduced to 5 Hz. The voltage drop on an HVDC transmission line, which has same resistance as that of 60 Hz transmission line, is also plotted in Fig. 2.10 resulting in a receiving-end voltage of 0.9858 pu. If the AC system operates at very low frequency, such as 1 Hz, the receiving-end voltage is 0.9852 pu and the voltage profile

is similar to that of the HVDC system. The receiving-end voltage is further increased to 0.9856 pu if the frequency is lowered to 0.5 Hz, which is almost equal to that of the HVDC system.



(a)



(b)

Figure 2.9: No-load voltages and currents at different frequencies.

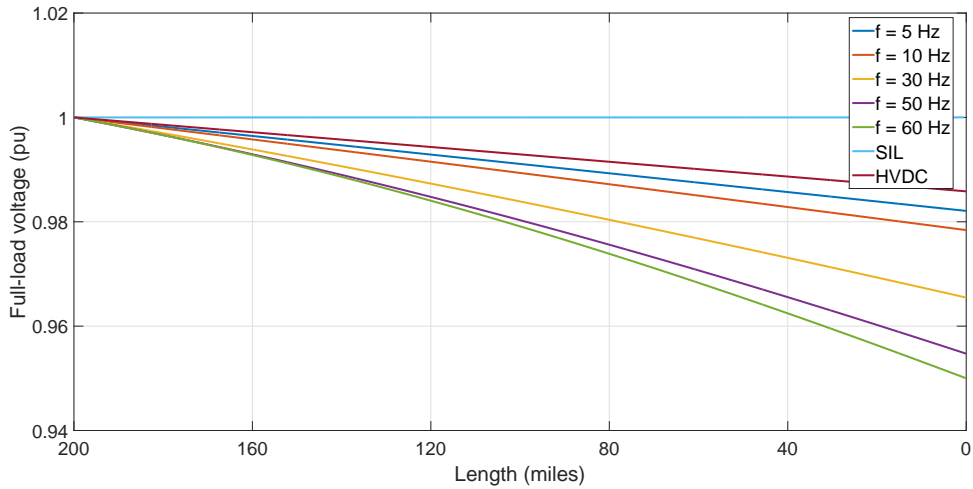


Figure 2.10: Full-load voltages at different frequencies.

In summary, analysis of the voltage profile for the LFAC transmission shows improvements when compared to the 60 Hz ac system. In the case of a no-load condition, the voltage at 5 Hz is almost constant and close to the surge impedance load (SIL) curve. In the case of the full-load condition, a voltage profile that is similar to an HVDC system can be obtained. In the following section, a transmission system is modeled in PSCAD/EMTDC to support the theoretical analysis.

2.2.3 Power Losses in LFAC Transmission

This section investigates the real and reactive power losses in both overhead line and power cable systems at different frequencies and at various amounts of power transfer. A two-bus system, as shown in Fig. 2.11, is used for the theoretical analysis. Note that this two-bus system is exactly same as that in Fig. 2.6, except that the receiving-end source is replaced by a real load. The transmission line models are the nominal equivalent

π -model for both overhead line and power cable. The analysis is then supported by the simulation results of a transmission model in PSCAD/EMTDC.

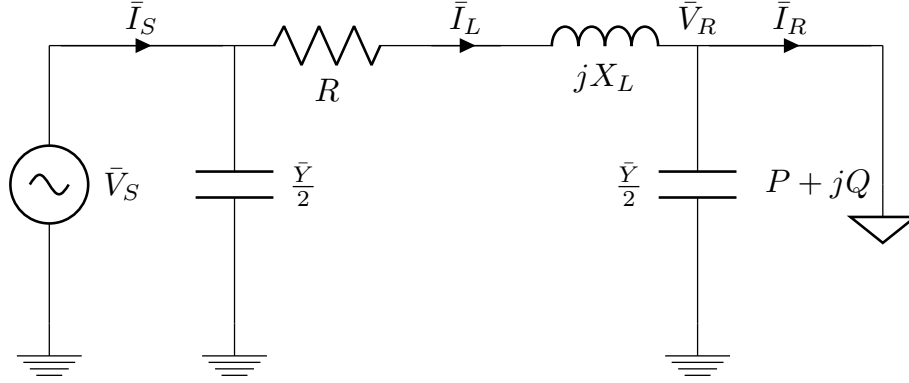


Figure 2.11: An equivalent two-bus transmission system.

Power losses calculations

It is intuitive to see that as the operating frequency is lowered, the transmission system reactance decreases significantly. In other words, the two-bus transmission system consumes less reactive power, and as a result the receiving-end voltage increases. The real power loss is more complicated because the resistance is constant but the current flowing through transmission line changes depending on the system operating conditions.

For the sake of clarity, some equations in section 2.2 are represented in this section. Assuming the impedance and admittance per unit are given by z and y , the π -model parameters for an l -length line are

$$Z' = Z_c \sinh(\gamma l) = \sqrt{\frac{z}{y}} \sinh(\gamma l) \quad (2.16)$$

$$Y/2 = (1/Z_c) \tanh(\gamma l/2) = (\sqrt{y/z}) \tanh(\gamma l/2) \quad (2.17)$$

where $Z_c = \sqrt{z/y}$ and $\gamma = \sqrt{zy}$ are characteristic impedance and propagation constant, respectively [10].

Assuming the sending-end terminal voltage is $\bar{V}_S = V_S \angle 0$, the receiving-end terminal voltage is $\bar{V}_R = V_R \angle \theta$ and supplies to load $S = P + jQ$. The load current is then given by $\bar{I}_R = (S/\bar{V}_R)^* = (P - jQ)/V_R \angle -\theta$. Denoting $jY_C = Y/2$, the sending-end voltage and current are

$$\bar{V}_S = \bar{V}_R + \bar{V}_{Z'} = \bar{V}_R + (\bar{I}_R + jY_C \bar{V}_R) \bar{Z}' \quad (2.18)$$

$$\bar{I}_S = jY_C \bar{V}_S + \bar{I}_L = \bar{I}_R + jY_C (\bar{V}_S + \bar{V}_R) \quad (2.19)$$

Substituting the load current \bar{I}_R and $Z' = R + jX_L$, the voltage at the sending-end is expressed as

$$\bar{V}_S = \bar{V}_R + \left(\frac{P - jQ}{V_R \angle -\theta} + jY_C \bar{V}_R \right) (R + jX_L) \quad (2.20)$$

$$V_S V_R \angle -\theta = V_R^2 + (P - jQ + jY_C V_R^2) (R + jX_L) \quad (2.21)$$

Decomposing to the real and complex parts of (2.21),

$$V_S V_R \cos \theta = (1 - Y_C X_L) V_R^2 + (PR + QX_L) \quad (2.22)$$

$$V_S V_R \sin \theta = (-Y_C R) V_R^2 + (QR - PX_L) \quad (2.23)$$

Both sides of (2.22) and (2.23) are squared and then added. After some manipulations, the receiving-end voltage is the solution of a quadratic polynomial equation

$$0 = [(Y_C R)^2 + (1 - Y_C X_L)^2] V_R^4 + [-2Y_C Q(R^2 + X_L^2) + 2(PR + QX_L)] V_R^2 + (R^2 + X_L^2)(P^2 + Q^2) \quad (2.24)$$

It is not difficult to find the analytical solution of (2.24). However, the solutions are not in nice forms and thus not presented here. Instead, these solutions are put in MATLAB

using symbolic function to further investigate the power losses which are the differences between the sending-end power and the receiving-end power

$$\bar{S}_{Loss} = P_{Loss} + jQ_{Loss} = \bar{V}_S \bar{I}_S^* - \bar{V}_R \bar{I}_R^* \quad (2.25)$$

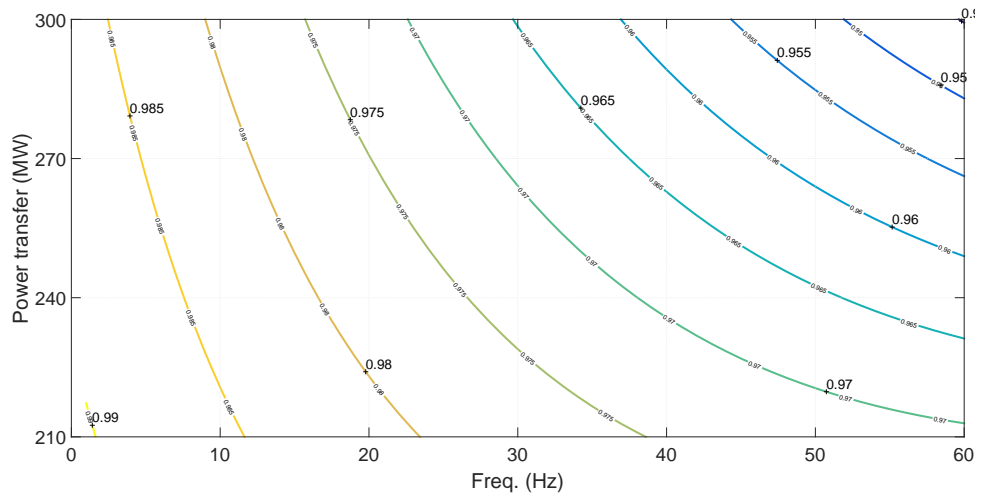
$$= \bar{V}_{Z'} \bar{I}_R^* - jY_C (\bar{V}_S + \bar{V}_R^*) (\bar{V}_R + \bar{V}_{Z'}) \quad (2.26)$$

It is expected that the power losses depend on the load condition $S = (P + jQ)$ and the operating frequency via $X_L = 2\pi fL$ by substituting V_R from (2.24). The following sections visualize this relationship.

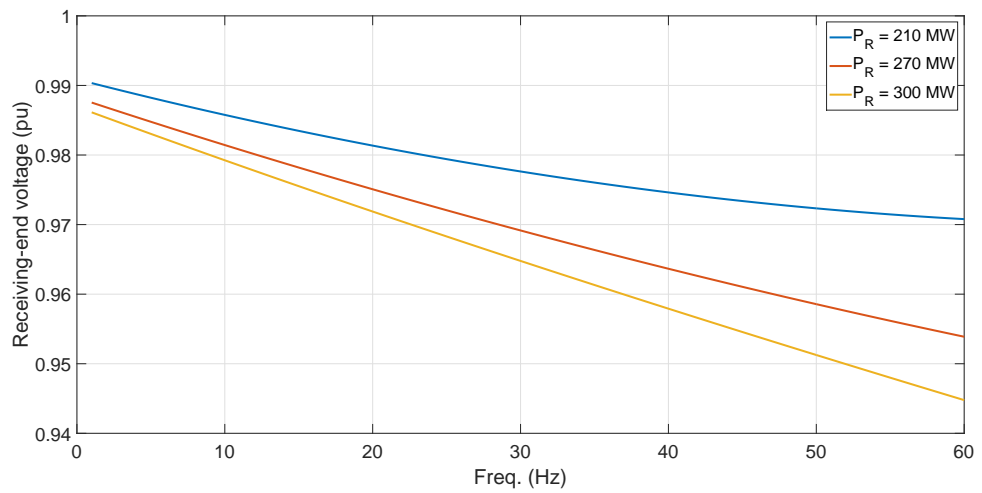
Overhead line transmission systems

In this section, a 345-kV overhead line is used to demonstrate the relationship between voltage and power losses, the operating frequency, and load conditions. The line parameters per mile are [10]: $R = 0.02 \Omega$, $L = 580.25238 \mu\text{H}$, $C = 0.006963 \mu\text{F}$, and the line length is 100 miles. These parameters are implemented into the above equations in MATLAB codes to examine power losses. It is worthwhile mentioning that the resistance is assumed constant, and the reactance is changed with frequency through the analysis.

The receiving-end voltage profile with load condition and frequency is shown in Fig. 2.12. The load power is in range of 200 - 300 MW with 0.95 lagging of power factor. The operating frequency range is from 1 Hz to 60 Hz. It is obvious that as the load demand increases, the voltage decreases, as shown in the contour plot of voltage in per unit in Fig. 2.12(a). Furthermore, the voltage as a function of frequency is plotted in Fig. 2.12(b) with three different load condition scenarios. The voltage is significantly reduced as the operating frequency increases. For example, if the load is 300 MW, the voltage at 1 Hz is close to 0.99 pu and is dropped to 0.945 pu at 60 Hz.



(a)



(b)

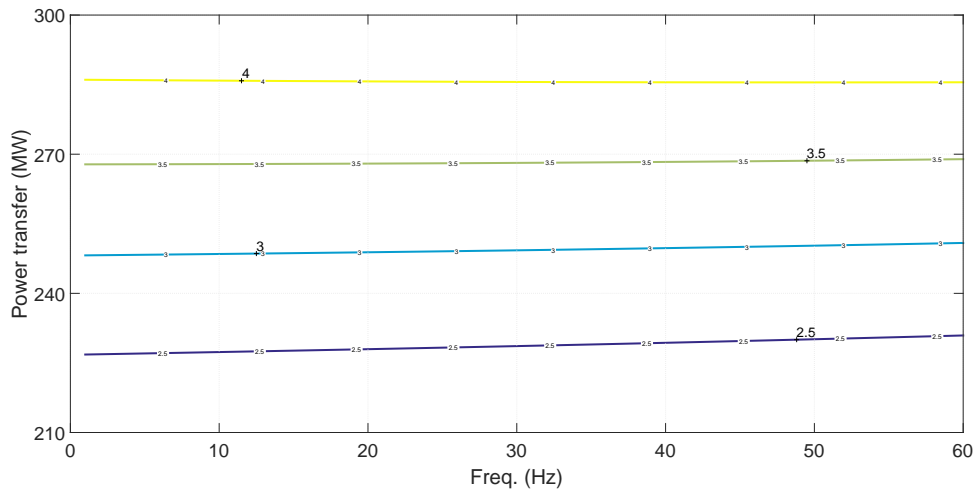
Figure 2.12: (a) The receiving-end voltage in per unit in contour plot with power transfer and frequency, and (b) the receiving-end voltage in per unit versus frequency

The power losses versus load condition and operating frequency on the transmission line are presented in Fig. 2.13. For a fixed frequency, the real power loss is increased when the load demand is high, Fig. 2.13(a). For example, the real power loss in a 10 Hz system, as seen from the top figure in Fig. 2.13(c), is doubled from 2.1 MW to 4.4 MW as the receiving-end load is extended from 210 MW to 300 MW, respectively. It is interesting to observe that this real power loss changes with load conditions. From the top of Fig. 2.13(c), if the load is 210 MW, the power loss actually decreases from 2.1 MW as the operating frequency is increased. The real power loss is almost constant at 3.55 MW within a wide range of frequency and 270 MW of load. If the receiving-end load is 300 MW, the real power loss is developed from 4.4 MW at 1 Hz to 4.5 MW at 60 Hz. It is worthwhile noting that the real power loss does not vary much with frequency changes. The reactive power loss, as expected, grows linearly with the frequency, as shown on the bottom of Fig. 2.13(c). Interestingly the reactive power loss decreases as load demand is increased at a specific operating frequency as shown in Fig. 2.13(b).

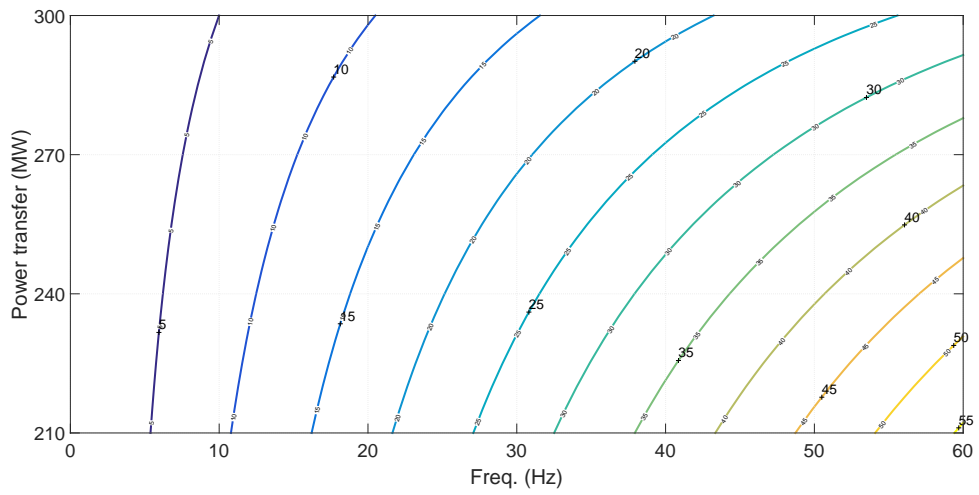
Power cable transmission systems

Similar to the overhead line transmission, a 345-kV power cable, which is designed for LFAC operations [13], is used to investigate the power losses profile. The power cable parameters per mile are: $R = 0.0193 \Omega$, $L = 72.946 \mu\text{H}$, $C = 0.1081 \mu\text{F}$, and the line length is 100 miles.

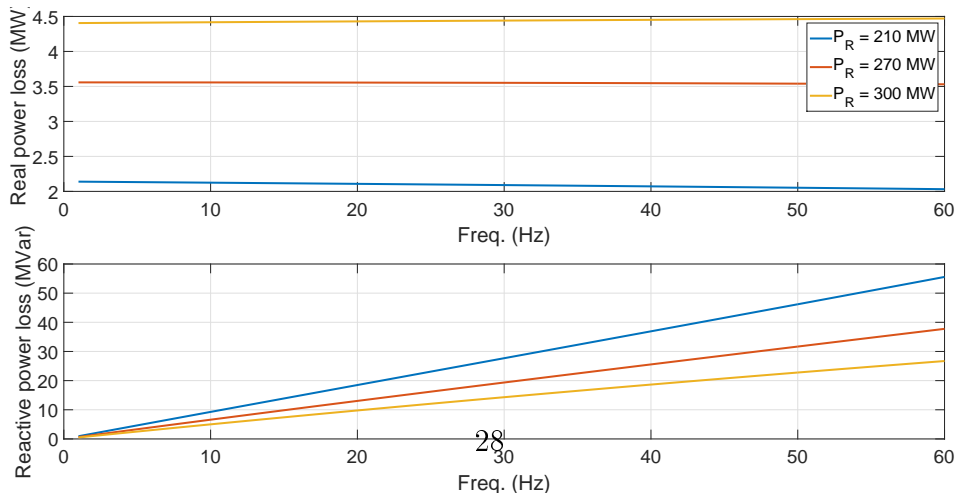
Because the power cable is capacitive, the receiving-end voltage can be higher than the sending-end voltage as shown in Fig. 2.14. At light load conditions, the voltage is expected to be higher compared to that at heavy load cases as in Fig. 2.14(a). The



(a)



(b)



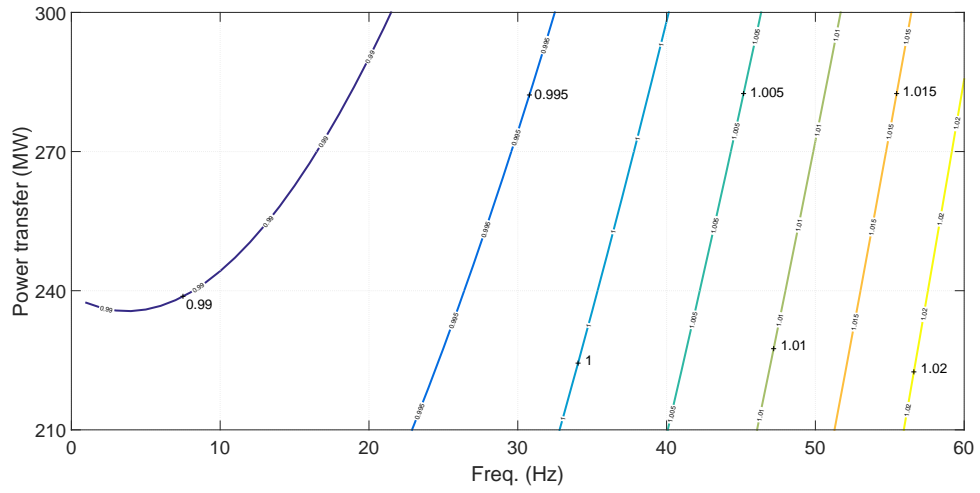
(c)

Figure 2.13: Overhead line power losses in contour plot: (a) real power, (b) reactive power, and (c) at different load conditions.

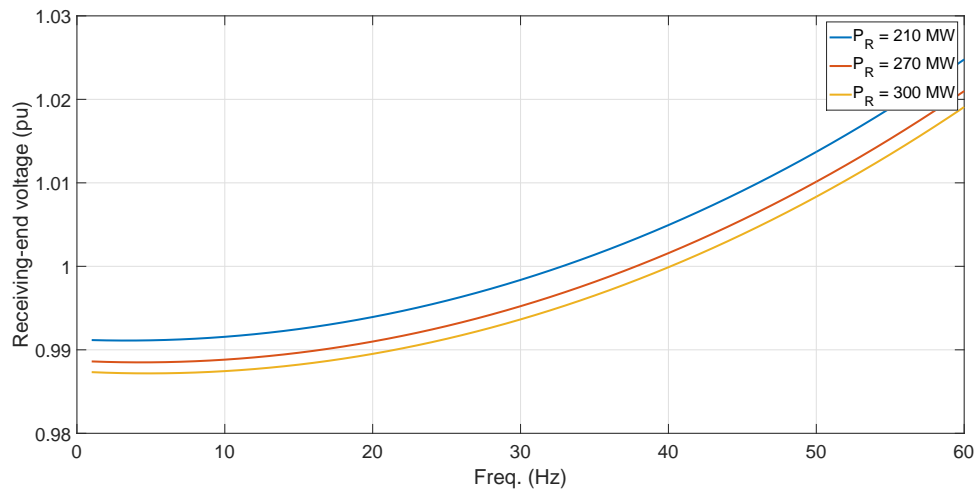
voltage is significantly increased when the operating frequency is from 1 Hz to 60 Hz. The benefits of low frequency operation, as seen in Fig. 2.14(b), are reduced voltage rising and less reactive power consuming as below.

The power losses in the power cable transmission system are presented in Fig. 2.15 for different scenarios of load cases and operating frequencies. Since the resistance is almost the same as in the overhead line system, the power losses are generally much higher. The real power loss variations range between 2 MW and 16 MW as frequency changes from 1 Hz to 60 Hz. The real power loss differences at various load conditions tend to be small as the operating frequency is increased. The real power loss is not a monotonic but a convex function of frequency. The minimum loss, in the case of 300 MW load, is obtained at the operating frequency $f = 7$ Hz, as in Fig. 2.15(c). The reactive power is extremely large in the power cable transmission system. This power is expected to increase linearly with the operating frequency growth, Fig. 2.15(b). Thus, operating a power cable transmission at a low frequency can significantly reduce the reactive power flow in the system.

In summary, the LFAC system offers benefits over the conventional 60 Hz system in terms of voltage and power losses on both overhead line and power cable transmission systems. Due to the significant impedance reduction, the voltage along the line is higher in a low frequency system. More importantly, the results show that the low frequency operating can greatly reduce the reactive power flow in the transmission system. In addition, a low frequency system can reduce the real power loss on the transmission line.

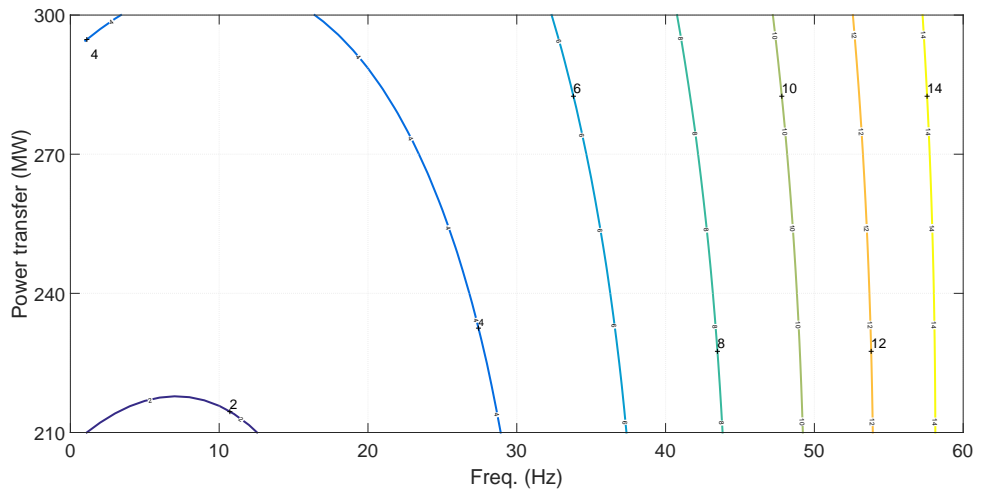


(a)

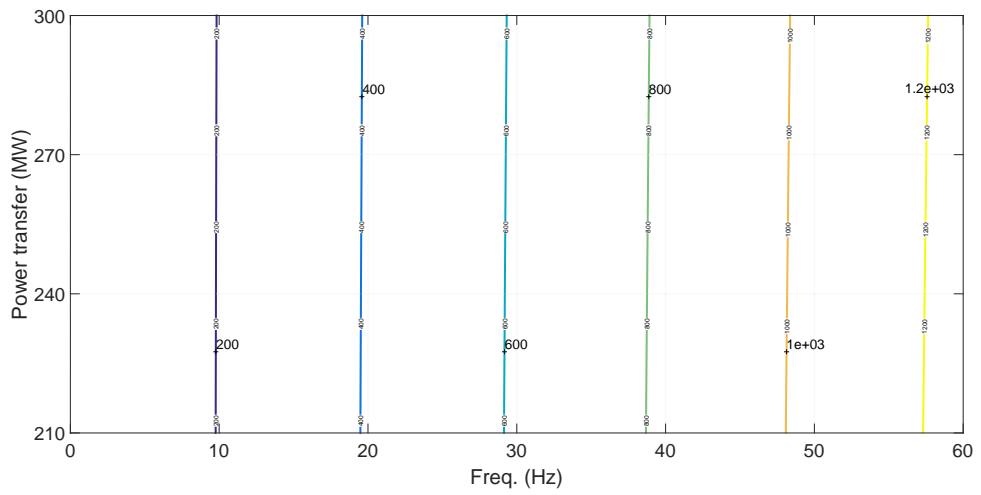


(b)

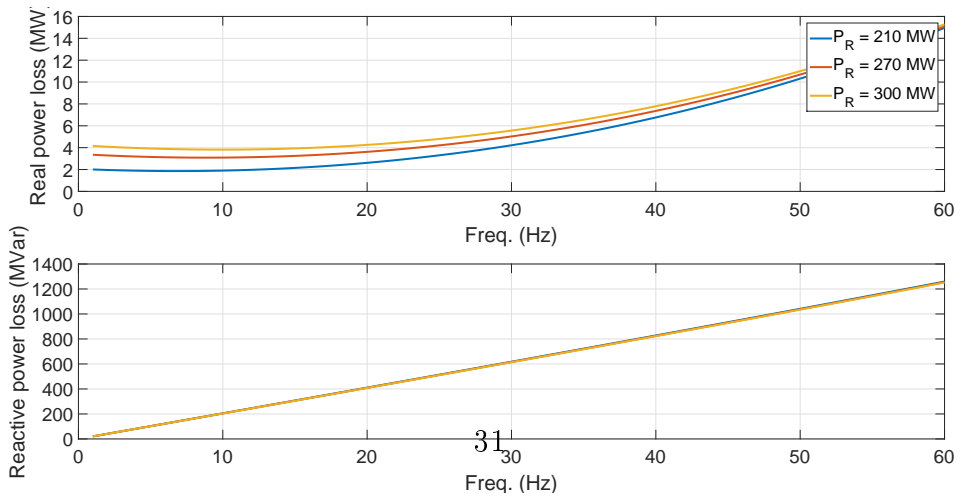
Figure 2.14: (a) The receiving-end voltage in per unit in contour plot with power transfer and frequency, and (b) the receiving-end voltage in per unit versus frequency



(a)



(b)



(c)

Figure 2.15: Power cable power losses in contour plot: (a) real power, (b) reactive power, and (c) at different load conditions.

Simulation results

In order to support theoretical analysis, the above two transmission systems are modeled in PSCAD/EMTDC to examine losses. The 100-mile transmission line is modeled with line parameters for the equivalent π -model as the previous section specifies. The transmission systems are simulated with three different scenarios of real power at the receiving-end, as shown in Fig. 2.13(c), with 0.95 lagging of power factor: $P_R = 210$ MW, $P_R = 270$ MW, and $P_R = 300$ MW.

Table 2.1: Reactive power Q_{Loss} in MVar (top) and real power losses P_{Loss} in MW (bottom) on the overhead line.

Frequency	60 Hz	30 Hz	10 Hz	5 Hz
$P_R = 210$ MW	55.1097	27.6333	9.2681	4.6461
$P_R = 270$ MW	37.1487	19.282	6.5988	3.3245
$P_R = 300$ MW	26.0062	14.2307	5.0015	2.5352
Frequency	60 Hz	30 Hz	10 Hz	5 Hz
$P_R = 210$ MW	2.113	2.111	2.127	2.132
$P_R = 270$ MW	3.644	3.58	3.56	3.556
$P_R = 300$ MW	4.605	4.474	4.421	4.408

The reactive and real power losses on the transmission system are presented in Table. 2.1. The simulation results are really close and matching with those results in Fig. 2.13(c). The reactive power losses are significantly reduced as the operating frequency is lowered because these losses are almost linearly proportional to the frequency. In addition, as the load demand is decreased, the reactive power loss is increased which is similar to the curves on the bottom of Fig. 2.13(c). The real power loss values also match the analytical results. The real power loss is increased when the load demand is grown. In the most cases, the real power loss at a low frequency is smaller than that in the 60 Hz operation.

However, the difference in real power loss between different frequencies is relatively small compared to that in reactive power loss. The results for the power cable transmission system are also matched with the theoretical analysis, and presented in Table. 2.2 for details.

Table 2.2: Reactive power Q_{Loss} in MVar (top) and real power losses P_{Loss} in MW (bottom) on the power cable.

Frequency	60 Hz	30 Hz	10 Hz	5 Hz
$P_R = 210\text{MW}$	1251.203	616.9235	204.8115	102.3681
$P_R = 270\text{MW}$	1246.084	614.3845	203.9675	101.9457
$P_R = 300\text{MW}$	1243.334	613.017	203.512	101.7184
Frequency	60 Hz	30 Hz	10 Hz	5 Hz
$P_R = 210\text{MW}$	15.806	4.394	1.92	1.878
$P_R = 270\text{MW}$	15.948	5.209	3.111	3.153
$P_R = 300\text{MW}$	16.147	5.749	3.839	3.924

Further investigations of the voltage profile along the transmission line and the system performance with load change are presented in Fig. 2.16. The voltage magnitude along the line at different frequencies is shown in Fig. 2.16(a). It is clear that in an overhead line, a low frequency system has less voltage drop and thus has a higher voltage profile, as seen in the top figure. In a power cable transmission, due to the capacitive charging effect, the voltage magnitude of a 60 Hz system increases, i.e. 1.02 pu. In a low frequency system, the capacitance is significantly reduced and thus the voltage still decreases. It is important to observe the low frequency system behavior with load variations. Fig. 2.16(b) presents the receiving-end voltages of a 60 Hz and a 10 Hz systems when the load demand is increased from $P_R = 240$ MW to $P_R = 300$ MW. Before the load change, the voltage magnitude is 0.9624 pu and 0.9827 pu for the 60 Hz and 10 Hz

systems, respectively. When the load demands 60 MW more, which makes total load in the system equal to 300 MW, the voltage magnitude in the 60 Hz system is dropped to 0.9450 pu below the lower limit (i.e. 0.95 pu). The 10 Hz system is less sensitive, or more stable, with load variation when the voltage magnitude is 0.9784 pu. In general, the low frequency system is more robust compared to the conventional 60 Hz system in terms of voltage stability, as analyzed in great detail in [14].

A further step to verify the conclusions of voltage profile in LFAC systems is to develop for a 345-kV transmission system with tower configurations in PSCAD/EMTDC. The tower type is 3-Conductor Flat with Chukar conductors. The operating conditions are similar to those in the above scenarios. Fig. 2.17 presents the voltage profile along the transmission line with three different load conditions. This figure once again confirms the benefits of low frequency transmission over the conventional 60 Hz system. The voltage drop on the transmission line is smaller in an LFAC system and thus results in better voltage profile along the line. In addition, when the load is increased, the conventional 60 Hz system cannot transfer much power without additional reactive compensation, because the receiving-end voltage is less than the lower limit, i.e. 0.95 pu. The LFAC system, on the other hand, is able to keep the voltage around 0.98 pu when the load increase to 270 MW and 300 MW.

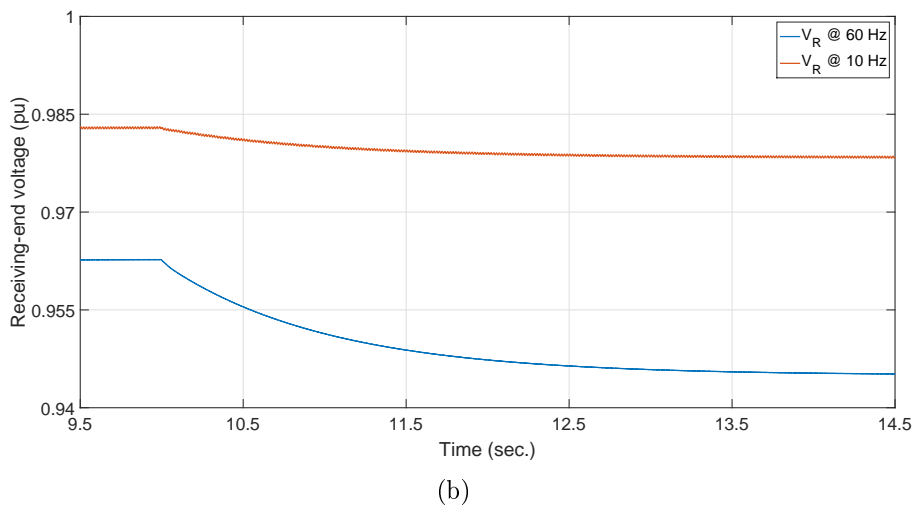
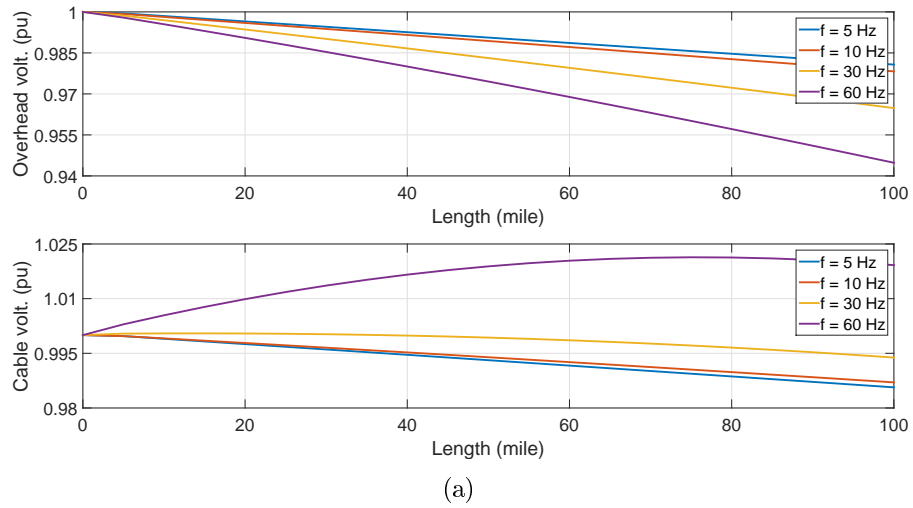
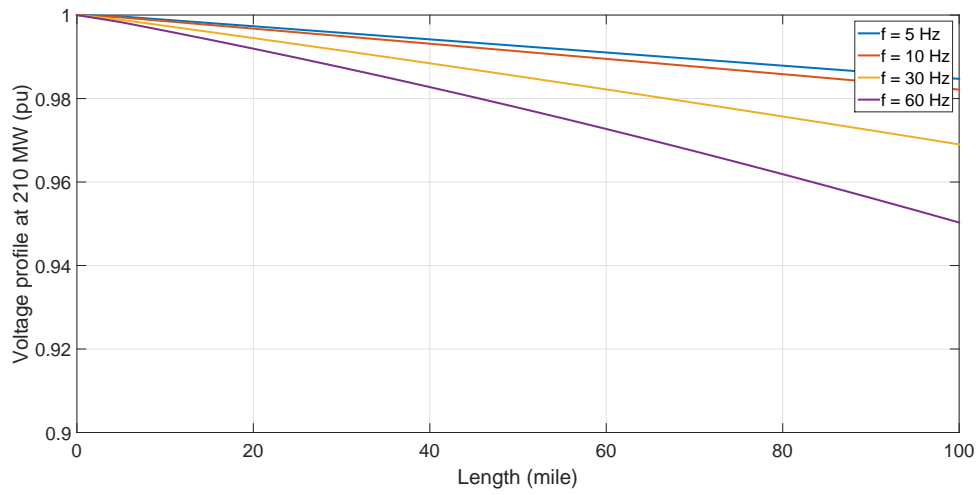
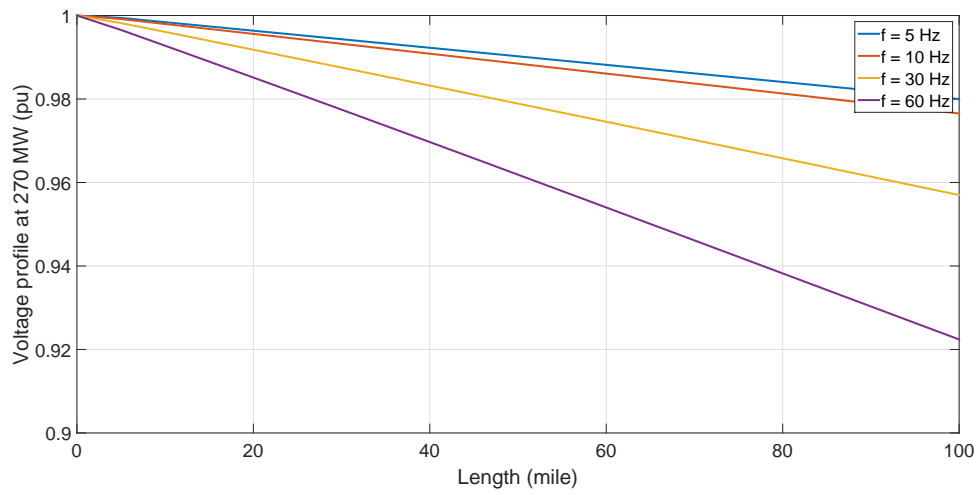


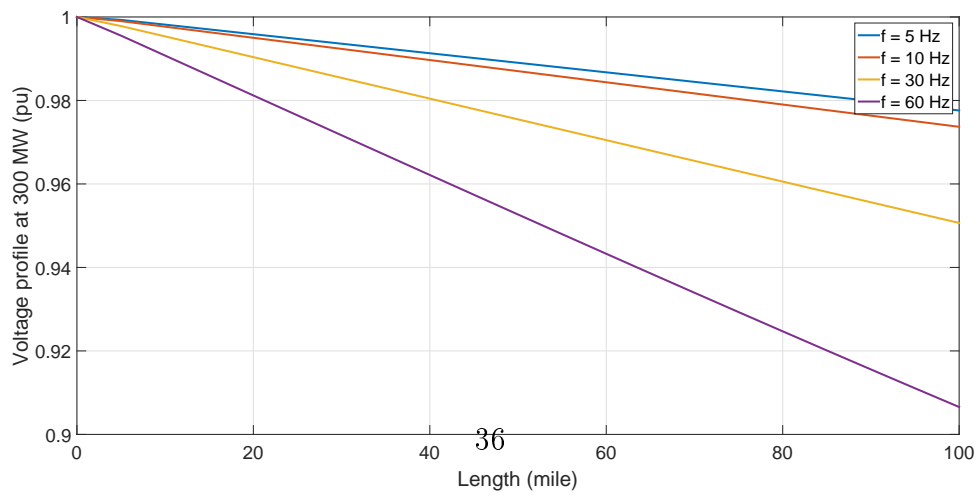
Figure 2.16: (a) Voltage profile along the line, and (b) voltage with load variations.



(a)



(b)



(c)

Figure 2.17: Voltage profile along the line at different load conditions: a) 210MW, b) 270MW, and c) 300MW.

Chapter 3

Voltage Stability of LFAC Transmission

This chapter presents the benefits of a low frequency ac system from the voltage stability perspective. Since the stability indexes - which are bus voltage magnitude, eigenvalue, and self-sensitivity - are obtained directly from load flow solution, an equivalent circuit of low frequency system referring to a 60 Hz system is derived in terms of real and reactive power. Conventional voltage stability curves, i.e. $V - P$ and $Q - V$, are then shown to demonstrate voltage improvements if operating at a low frequency. The theoretical analysis is based on a two-bus power system. Further examinations in voltage stability index are then presented by using the modal analysis method. In addition, a modified stability index is proposed to estimate system stability accurately at a low frequency operation. A five-bus and six-bus power system are then used to verify better performances of LFAC transmission in terms of static voltage stability.

3.1 Power Flow Solution for Low Frequency AC Transmission

The purpose of this section is to discover the relation between parameters of a transmission line that works at different frequencies but transfers the same amount of active and reactive power. Based on that relationship, the parameters of low frequency transmission lines in a multi-frequency system can be converted with precision into those

of the equivalent line operated at 60 Hz. Therefore, the power flow solution of the system after this conversion is unchanged, and the conventional load flow methods for ac systems are still applicable in multi-frequency power systems.

3.1.1 Equivalent Transmission Line Parameters between LFAC and HVAC Systems

For the sake of simplicity, the analysis in this section starts with the consideration of a short-length model of a transmission line [10]. The power system, shown in Fig. 3.1(a), is operating at a low frequency whereas the power system in Fig. 3.1(b) runs at a conventional 60 Hz. Assuming the two systems are equal in terms of real and reactive power transfer, the relation between transmission line parameters needs to be specified.

Denoting V_S, V_R, R_s, L_s as the sending-end voltage, receiving-end voltage, resistance, and inductance of the transmission line, respectively. The subscript “s” stands for parameters at a low frequency ω_s , while “e” stands for parameters at the conventional $\omega_e = 60$ Hz. Real and reactive power of the line operating at these frequencies are considered to be exactly analogous. The voltage magnitude ratios between the sending-end and receiving-end in two cases are assumed to be equal to each other, i.e. $(V_{Se}/V_{Ss})^2 = (V_{Re}/V_{Rs})^2 = a$, and the frequency ratio is defined as $s = (\omega_s/\omega_e)$. The power of the transmission line at the sending-end and receiving-end in these two cases are

For a low frequency system,

$$\begin{aligned}\bar{S}_{Ss} &= \bar{V}_{Ss}\bar{I}_s^* = V_{Ss}\angle 0 \frac{V_{Ss}\angle 0 - V_{Rs}\angle -\delta_s}{R_s - j\omega_s L_s} \\ \bar{S}_{Rs} &= \bar{V}_{Rs}\bar{I}_s^* = V_{Rs}\angle \delta_s \frac{V_{Ss}\angle 0 - V_{Rs}\angle -\delta_s}{R_s - j\omega_s L_s}\end{aligned}\quad (3.1)$$

For a 60 Hz system,

$$\begin{aligned}\bar{S}_{S_e} &= \bar{V}_{S_e} \bar{I}_e^* = V_{S_e} \angle 0 \frac{V_{S_e} \angle 0 - V_{R_e} \angle -\delta_e}{R_e - j\omega_e L_e} \\ \bar{S}_{R_e} &= \bar{V}_{R_e} \bar{I}_e^* = V_{R_e} \angle \delta_e \frac{V_{S_e} \angle 0 - V_{R_e} \angle -\delta_e}{R_e - j\omega_e L_e}\end{aligned}\quad (3.2)$$

where δ_s and δ_e are the power angles at the receiving ends, which can be negative or positive depending on the direction of power flow. Since the power is preserved, i.e. $S_{S_s} = S_{S_e}$ and $S_{R_s} = S_{R_e}$, then

$$V_{S_s} \frac{V_{S_s} - V_{R_s} \angle -\delta_s}{R_s - j\omega_s L_s} = V_{S_e} \frac{V_{S_e} - V_{R_e} \angle -\delta_e}{R_e - j\omega_e L_e} \quad (3.3)$$

$$V_{R_s} \angle \delta_s \frac{V_{S_s} - V_{R_s} \angle -\delta_s}{R_s - j\omega_s L_s} = V_{R_e} \angle \delta_e \frac{V_{S_e} - V_{R_e} \angle -\delta_e}{R_e - j\omega_e L_e} \quad (3.4)$$

By equating the real parts and imaginary parts of these two equations, the following result can be obtained: $R_e = aR_s$, $L_e = asL_s$, and $\delta_e = \delta_s$. The equivalent circuit for a low frequency transmission line referring to a 60 Hz is represented clearly in Fig. 3.1(c). The voltage source V_{S_s} and V_{R_s} are the same as those of the original low frequency line, and a transformer which has turn ratio $1/\sqrt{a}$ represents voltage conversion. The resistor and inductor are scaled by the voltage ratio and the product of voltage ratio and frequency ratio, respectively. The following cases are investigated according to two different values of the voltage ratio a :

1. Case 1: $a = 1$, then $R_e = R_s$ and $L_e = sL_s$. According to this equation the equivalent line can easily be obtained by keeping the resistance constant while scaling the inductance by the frequency ratio s .

2. Case 2: $a = 1/s$, then $R_e = R_s/s$ and $L_e = L_s$. This means that the inductance is constant while the resistance is scaled by the inverse of the frequency ratio. This result is similar to the well-known relationship seen in the development of the equivalent rotor circuit of an induction motor.

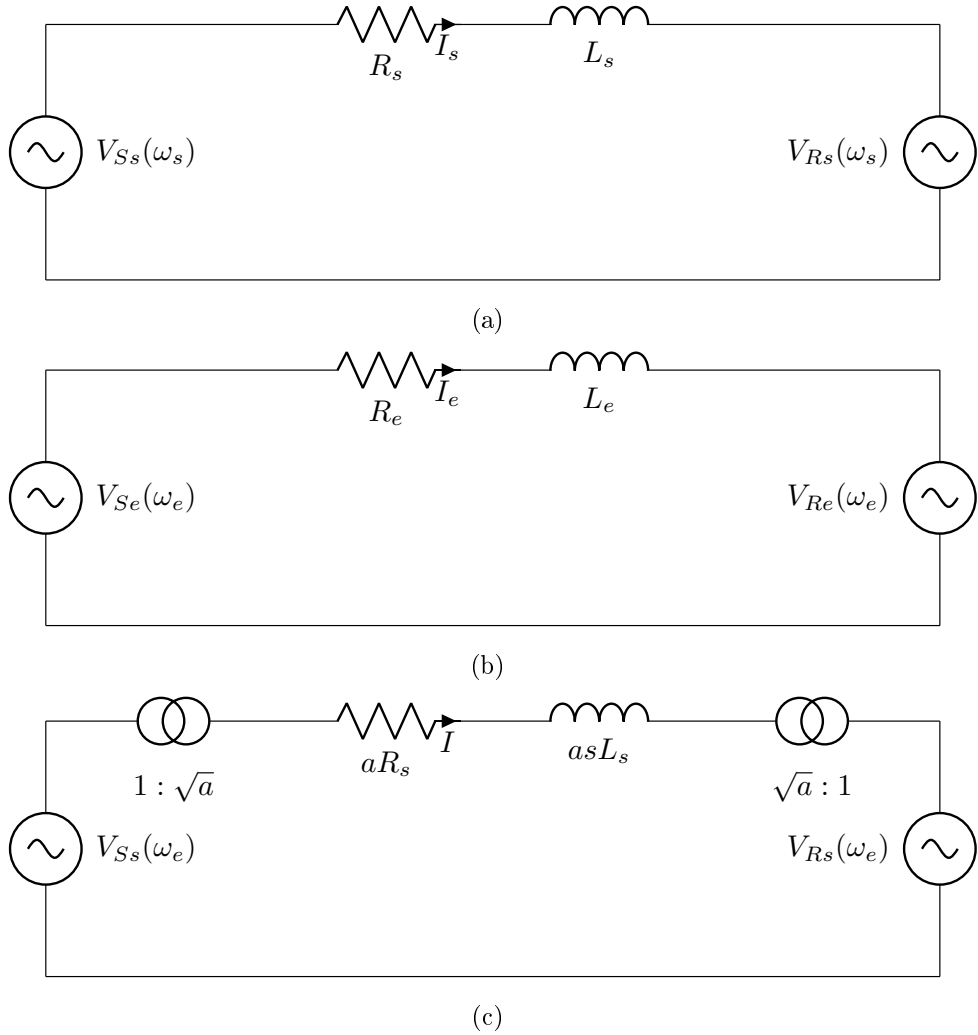


Figure 3.1: Equivalent transmission line models operated at different frequencies.

The same technique can be applied to other transmission line models to find the equivalent circuit in 60 Hz base of a low frequency power system. These are relationships between the parameters: 1) resistors and phase angles at the sending-/receiving-ends are equal and 2) capacitors and inductors are scaled by the frequency ratio [15, 16].

3.1.2 Power Flow Simulation in HVAC and Multi-Frequency Systems

This section focuses on the validation of the power flow solution proposed in section 3.1.1 using a power system that operates at the conventional 60 Hz and at multi-frequency conditions. The solutions are obtained by employing the Newton-Raphson numerical method and by simulation in PSCAD/EMTDC.

Power flow in a conventional HVAC system

Fig. 3.2 shows a 5-bus ac power system. The system structure as well as its input power and transmission line data can be found in [17]. Fig. 3.2 also includes the line power while the bus voltages and power solved by MATLAB and indicated from PSCAD/EMTDC model are summarized in the first section of Table 3.1. The results match with numerical data from load flow in MATLAB. This data will be used as a reference to evaluate the power flow in the multi-frequency power system where there is more than one operating frequency.

Validation of equivalent parameters of a transmission line at different frequencies

The system described above now includes a transmission line operated at a different frequency. Specifically, transmission line between bus 1 and bus 2 is operated at 10 Hz

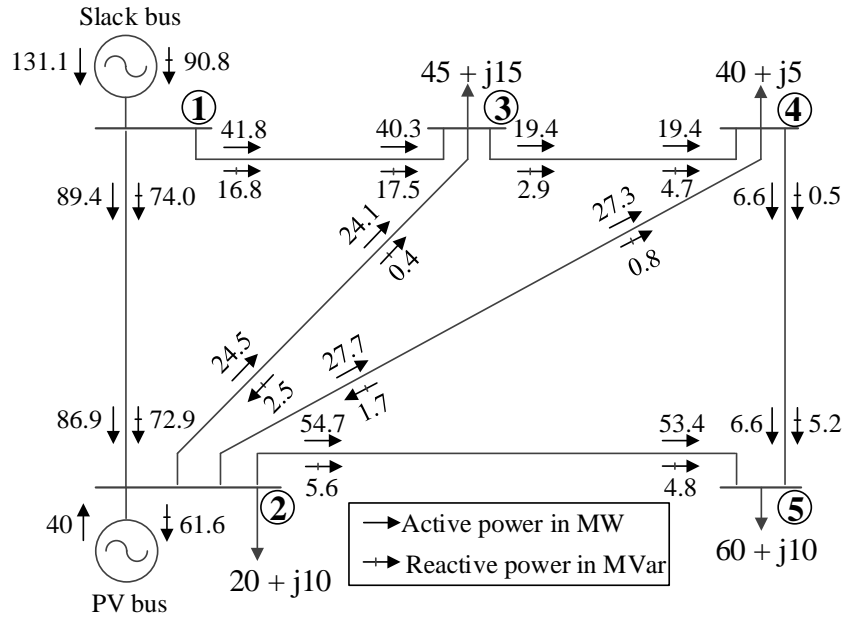


Figure 3.2: Line power of a 5-bus test system operated at 60 Hz.

instead of 60 Hz. This variation in frequency is achieved by employing two back-to-back converters located at the sending-end and receiving-end terminals of the line, as shown in Fig. 3.3.

The equivalent parameters in terms of power flow of the line 1-2 at 60 Hz and 10Hz, elaborated in section 3.1.1, are now verified. All the data about power at all buses and transmission lines when the system is operated at multi-frequency case is the same with those in the conventional case. The only difference is in the line between bus 1 and bus 2, where its shunt capacitance and series inductance are scaled by the inverse of the frequency ratio. Fig. 3.3 indicates the line power from PSCAD/EMTDC simulation while the bus voltages and powers are given in the third column of Table 3.1. By comparison, the values of the conventional and multi-frequency systems closely resemble. There is

only 0.08 MW (0.06 %) increase in active power generated at the slack bus in the multi-frequency case. This increase could be attributed to the losses of transformers, reactor, and switching and conducting losses of back-to-back converters. These analogous results confirm the conclusion about equivalent transmission line parameters in conventional 60 Hz and multi-frequency operating conditions.

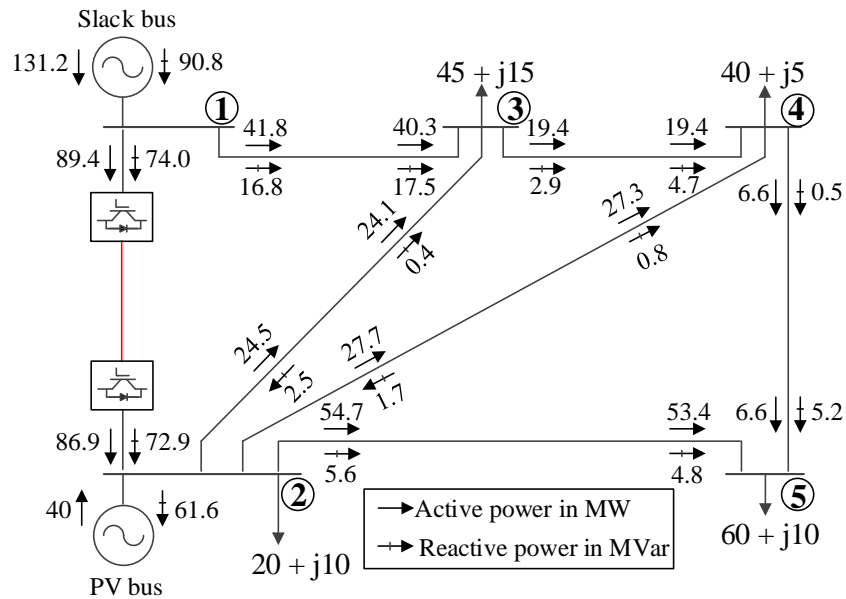


Figure 3.3: Multi-frequency system with line power equal to that of the conventional system.

In this section, the equivalent parameters in terms of power flow of a transmission line operated at different frequencies are proved, facilitating the process of solving power flow problem in multi-frequency systems. A station model mainly constructed by back-to-back converters as well as their control configuration are also described. The converter model and control blocks are built in PSCAD/EMTDC software, which can be effectively utilized for design and analysis of any multi-frequency power systems. A power system

Table 3.1: Voltages and Powers in a Conventional HVAC System and a Multi-Frequency System in PSCAD/EMTDC.

Bus	Type	Conventional HVAC				Multi-Frequency			
		U (<i>pu</i>)	θ (<i>deg</i>)	P_{gen} (<i>MW</i>)	Q_{gen} (<i>Mvar</i>)	U (<i>pu</i>)	θ (<i>deg</i>)	P_{gen} (<i>MW</i>)	Q_{gen} (<i>Mvar</i>)
1	slack	1.0600	0.00	131.12	90.83	1.0600	0.00	131.20	90.83
2	PV	1.0000	-2.06	20.02	-71.60	1.0000	-2.06	20.01	-71.61
3	PQ	0.9872	-4.64	-45.01	-15.00	0.9872	-4.64	-45.01	-15.00
4	PQ	0.9841	-4.96	-40.01	-5.00	0.9841	-4.96	-40.01	-5.00
5	PQ	0.9717	-5.76	-60.01	-9.99	0.9717	-5.77	-60.01	-9.99

is then modeled in PSCAD/EMTDC in both conventional 60 Hz and multi-frequency operating conditions. The simulation result verifies the proof of equivalent parameters of a transmission line at various operating frequencies and reveals the advantages of higher power carrying capacity when using the low frequency technology instead of the conventional method.

3.2 The $V - P$ and $Q - V$ Characteristic Curves

This section demonstrates the superiority of LFAC in terms of steady-state voltage stability. Power system voltage stability can be interpreted from the $V-P$ and $Q-V$ characteristic curves [11]. From (2.12), the real and reactive power is a function of voltage and reactance:

$$\begin{aligned}
 P_R &= -G \frac{V_R^2}{2} - R \frac{V_R^2}{X^2 + R^2} + \frac{V_S V_R}{X^2 + R^2} (X \sin \delta + R \cos \delta) \\
 Q_R &= B \frac{V_R^2}{2} - X \frac{V_R^2}{X^2 + R^2} + \frac{V_S V_R}{X^2 + R^2} (X \cos \delta - R \sin \delta)
 \end{aligned} \tag{3.5}$$

The voltage versus power (V - P) characteristic curves at different frequencies are plotted in Fig. 3.4 for a load power factor of 0.95 lagging. The real power is expressed in terms of the maximum power transfer in a 60 Hz system [10]

$$P_{max} = \frac{V_R V_S}{|B|} - \frac{|A| V_R^2}{|B|} \cos(\theta_B - \theta_A) \quad (3.6)$$

where (A, B) are parameters from $ABCD$ model in (2.6) and (θ_A, θ_B) are their angles, respectively.

From Fig. 3.4(a), it is observed that the operating frequency significantly impacts the V - P characteristics and that the voltage has better stability if the power system operates at a frequency lower than 60 Hz. This result makes sense considering that the voltage drop depends on the frequency, and active and reactive power as dictated by (3.5). With the same load demand, the ac system at 5 Hz has a much smaller voltage drop compared to that at 60 Hz, and thus the system can transfer power further or has more power transfer capability with the same transmission line. It is also worth noticing in Fig. 3.4(b) that as the system frequency is reduced by half, e.g. from 10 Hz to 5 Hz, while the transmission line length is doubled, the two V - P curves are close together. The maximum power transfer is 7.6 pu if the transmission line is 200 miles at 5 Hz and 9.2 pu if the transmission line is 100 miles long operating at 10 Hz. This means electric power can be carried further along the transmission line at a low operating frequency.

The system stability can also be estimated by observing the relationship between reactive power and voltage. This relationship is described by a Q - V curve, as shown in Fig. 3.5, and represents the reactive reserve margin, or Q -reserve margin, in the system. The Q -reserve margin of an ac system is defined as the distance from the minimum point

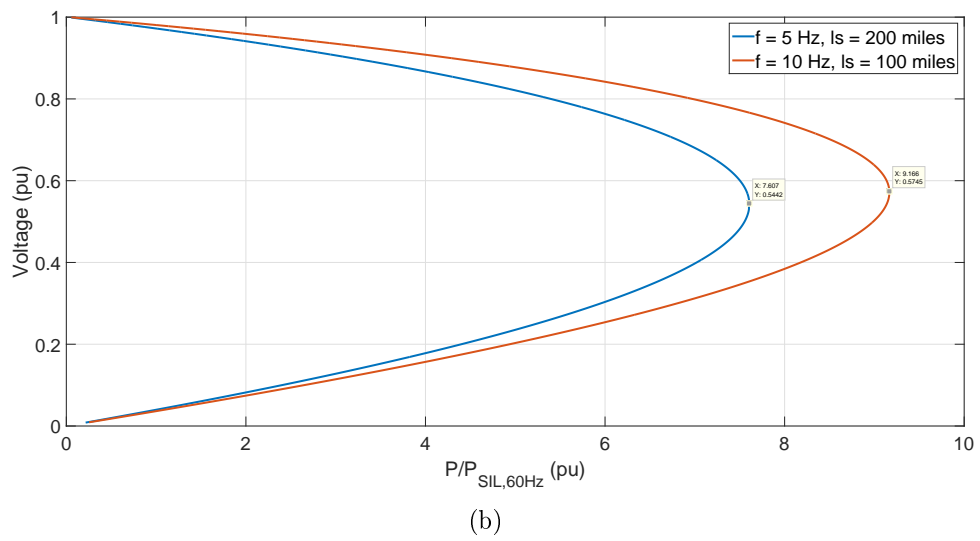
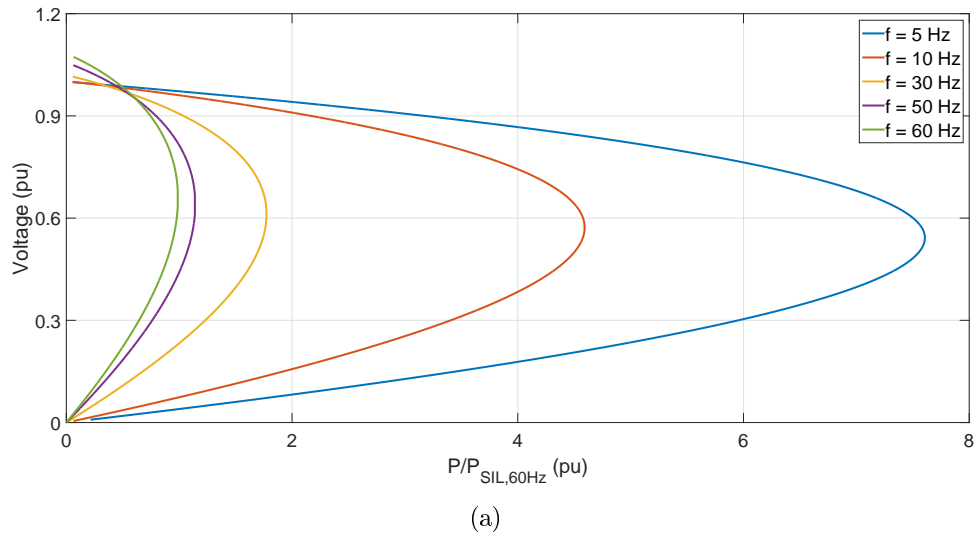


Figure 3.4: V-P characteristics at (a) different frequencies and (b) different line lengths.

(where $\partial V/\partial Q = 0$) to the zero-Q line. If a system has a large Q-reserve margin, then it is more stable [11, 18]. It can be seen clearly from Fig. 3.5 that at a lower frequency, the stability margin is higher and that the Q-reserve margin is inversely proportional to the frequency. For example, at 60 Hz the system has a stability margin of 0.3 pu, which increases to 2.5 pu when the frequency is lowered to 5 Hz, making the frequency more than 8 times that of the 60 Hz system. In other words, the system is more stable if it operates at a low frequency.

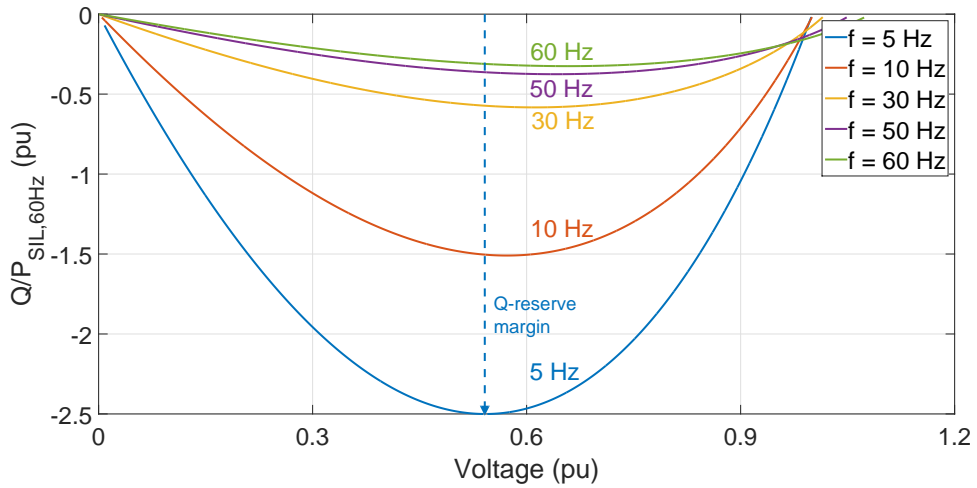


Figure 3.5: Stability reserved margin at different frequencies.

In summary, the LFAC transmission shows several benefits over the traditional 60 Hz system as illustrated in the analysis of power transfer capability, voltage drop, and voltage stability. The fundamental reason for these improvements is the reduction in transmission line reactance. A system operating at 5 Hz, for example, has a smaller voltage drop along the line, increased power transfer capability, and increased system stability margin.

3.3 Modal Analysis Method for Stability Analysis

In this section, the voltage stability of a low operating frequency power system is investigated with the modal analysis method. The traditional V - P and Q - V curve analysis methods do not provide knowledge about system stability, such as when the power system experiences, or comes close to experiencing, voltage instability, or where weak-voltage points exist. The modal analysis method, which is a numerical approach, can demonstrate power system voltage stability through the load flow results of a power system [19]. In addition, the modified stability index from the modal analysis method is proposed to estimate the system accurately under low frequency operations.

3.3.1 Modal Analysis Method for a Two-Bus System

For a two-bus system in Fig. 2.6, the sending-end voltage is assumed to stay constant at 1.0 pu since it is directly connected to the source, and the receiving-end voltage is changed with the load variations. By linearizing the system at its operating point, the relationship between power and voltage at the receiving-end terminal is given by

$$\begin{bmatrix} \Delta P_R \\ \Delta Q_R \end{bmatrix} = [J_{AC}] \begin{bmatrix} \Delta \delta_R \\ \Delta V_R \end{bmatrix} = \begin{bmatrix} \frac{\partial P_R}{\partial \delta_R} & \frac{\partial P_R}{\partial V_R} \\ \frac{\partial Q_R}{\partial \delta_R} & \frac{\partial Q_R}{\partial V_R} \end{bmatrix} \begin{bmatrix} \Delta \delta_R \\ \Delta V_R \end{bmatrix} \quad (3.7)$$

where the entries can be derived directly from (3.5)

$$\begin{aligned} \frac{\partial P_R}{\partial \delta_R} &= \frac{V_R}{X^2 + R^2} (X \cos \delta_R - R \sin \delta_R), & \frac{\partial P_R}{\partial V_R} &= \frac{(\cos \delta_R - 2V_R)R + X \sin \delta_R}{X^2 + R^2} - GV_R \\ \frac{\partial Q_R}{\partial \delta_R} &= \frac{-V_R}{X^2 + R^2} (X \sin \delta_R + R \cos \delta_R), & \frac{\partial Q_R}{\partial V_R} &= \frac{(\cos \delta_R - 2V_R)X - R \sin \delta_R}{X^2 + R^2} + BV_R \end{aligned} \quad (3.8)$$

From (3.7) since the reactive power variation mostly affects the voltage magnitude, their relationship is determined by setting $\Delta P_R = 0$ then:

$$\Delta Q_R = \left[\frac{\partial Q_R}{\partial V_R} - \frac{\partial Q_R}{\partial \delta_R} \left(\frac{\partial P_R}{\partial \delta_R} \right)^{-1} \frac{\partial P_R}{\partial V_R} \right] \Delta V = J_R \Delta V_R \quad (3.9)$$

Substitute all entries from (3.8) into (3.9) and after some manipulations

$$\Delta Q_R = \left[\frac{1 - 2V_R \cos \delta_R}{X \cos \delta_R - R \sin \delta_R} + BV_R + GV_R \frac{X \sin \delta_R + R \cos \delta_R}{X \cos \delta_R - R \sin \delta_R} \right] \Delta V_R = \lambda_R \Delta V_R \quad (3.10)$$

where λ_R is the eigenvalue of the reduced Jacobian matrix, J_R . In this example, it is easy to see λ_R is equal to the entry of J_R . For a power system transmission line, G is zero and BV_R is small and negligible in this case, then

$$\lambda_R \approx \frac{1 - 2V_R \cos \delta_R}{X \cos \delta_R - R \sin \delta_R} \quad (3.11)$$

Since $V_R \approx 1.0$ and $\cos \delta_R \approx 1.0$ then $\lambda_R < 0$, and the system is voltage stable with power variations. The magnitude of λ_R represents for how sensitive a bus to reactive power fluctuations or load changes. If λ_R is large, its corresponding bus voltage variation is small or this bus is robust. If λ_R is very small, any change in load will result in large fluctuation in the bus voltage or this bus is sensitive to load. In the worst case, if λ_R is equal to zero, the bus voltage collapses with any reactive power variation. The index λ_R is thus considered as a critical indicator for voltage stability in the power system. This λ_R can help to predict how far from an instability operating point a power system is.

From (3.11), it is obvious that λ_R is a function of bus voltage, phase angle, and impedance. Since our interests is in operating a power system at a low frequency, it is important to observe how this eigenvalue changes with the frequency. Fig. 3.6 shows

the relationship between λ_R and frequency f as a hyperbolic function. As frequency is increased, the eigenvalue is significantly reduced. For example, at 5 Hz the eigenvalue $\lambda_R = 100.2511$ and drops to 51.1960 at 10 Hz and 8.6873 at 60 Hz. This means the low frequency guarantees more voltage stable for power system in comparison with the conventional 60 Hz. Note that the effects of shunt admittance, B and G, on eigenvalue in (3.10) are small and also plotted as a dashed line in the figure. At low frequencies, the approximated value from (3.10) and the exact value from (3.11) are almost the same. At 60 Hz, there is a slight difference when the exact eigenvalue is reduced to $\lambda_R = 7.2851$.

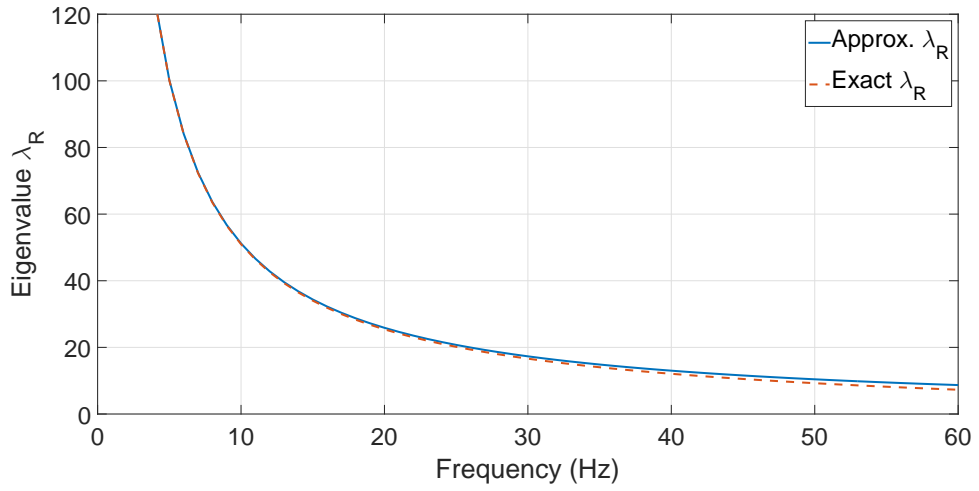


Figure 3.6: The eigenvalue trajectory with frequency variation.

For a large power system, the approach in the previous two-bus system can still be applied to each bus. The real and reactive power at bus i^{th} in a power system is given from bus voltage and Y -bus matrix

$$\begin{aligned}
 P_i &= \sum_{j=1}^n V_i V_j Y_{ij} \cos(\delta_i - \delta_j - \theta_{ij}) \\
 Q_i &= \sum_{j=1}^n V_i V_j Y_{ij} \sin(\delta_i - \delta_j - \theta_{ij})
 \end{aligned} \tag{3.12}$$

When there is a load change, the system behavior can be studied by using linearized equations at the steady-state operating point as follows

$$\begin{bmatrix} \Delta P \\ \Delta Q \end{bmatrix} = \begin{bmatrix} J_{P\delta} & J_{PV} \\ J_{Q\delta} & J_{QV} \end{bmatrix} \begin{bmatrix} \Delta\delta \\ \Delta V \end{bmatrix} \quad (3.13)$$

where $(\Delta P, \Delta Q)$ are increments in real and reactive power, and $(\Delta\delta, \Delta V)$ are increments in voltage angle and magnitude, respectively. The Jacobian matrix in the linearized equation is same as the Jacobian matrix from the load flow solved by Newton-Raphson method [19].

The same approach used in the two-bus system is applied to a large power system. Since the voltage magnitude depends mainly on reactive power, to investigate the system stability, let ΔP be 0 then

$$\begin{aligned} \Delta Q &= [J_{QV} - J_{Q\delta} J_{P\delta}^{-1} J_{PV}] \Delta V \\ &= J_R \Delta V \end{aligned} \quad (3.14)$$

or the voltage increment can be expressed in terms of reactive power increment

$$\Delta V = J_R^{-1} \Delta Q = \xi \Lambda^{-1} \eta \Delta Q = \sum_i^n \frac{\xi_i \eta_i}{\lambda_i} \Delta Q \quad (3.15)$$

where $J_R = \xi \Lambda \eta$ is decomposed into a diagonal eigenvalue matrix by right and left eigenvector matrices, and (ξ_i, η_i) are the i^{th} column right and row left eigenvectors of J_R . The matrix J_R is normally symmetrical and thus $\xi^{-1} = \eta$. The equation (3.15) can be rewritten as

$$\begin{aligned} \eta \Delta V &= \Lambda^{-1} \eta \Delta Q \\ v &= \Lambda^{-1} q \end{aligned} \quad (3.16)$$

where v and q is the vector of modal voltage and reactive power variations, respectively.

Because Λ^{-1} is a diagonal matrix, the voltage increment associated with i^{th} mode is given by

$$v_i = \frac{1}{\lambda_i} q_i \quad (3.17)$$

From (3.17), by investigating corresponding eigenvalues, the voltage stability between conventional 60 Hz and low frequency power systems can be estimated and compared. The details will be illustrated through the following case studies since the modal analysis method is a numerical one.

3.3.2 The Proposed Modified Modal Analysis Method for an LFAC System

In previous sections, the eigenvalue is used to estimate the system voltage stability. Recall from (3.9) and (3.14) that λ_i reflects the effects of reactive power variation ΔQ on each bus voltage. The eigenvalues are derived based on the assumption that real power has no effect on bus voltage. This assumption, however, is no longer correct if the operating frequency of a power system is low. From (3.13), the voltage variation is given by

$$\Delta V = J_R^{-1} \Delta Q - J_R^{-1} (J_{Q\delta} J_{P\delta}^{-1}) \Delta P \quad (3.18)$$

where $J_R = [J_{QV} - J_{Q\delta} J_{P\delta}^{-1} J_{PV}]$ as in the previous section.

In the case of the two-bus system, the above equation can be expressed in an explicit form

$$\Delta V = \frac{1}{\lambda_Q} \Delta Q + \frac{1}{\lambda_P} \Delta P \quad (3.19)$$

where $\lambda_Q = \lambda_2$, $\lambda_P = \lambda_Q \frac{(X \cos \delta_2 - R \sin \delta_2)}{(X \sin \delta_2 - R \cos \delta_2)}$.

In the conventional 60 Hz power system, the effects of real power on voltage variation is negligible because the ratio between two eigenvalues is large. However, as the frequency is lowered, two eigenvalues are close to each other. For example, with the same conditions of voltage and phase angle in the two-bus system, the ratio at 60 Hz is 7.7765 and at 10 Hz is 3.0328 and 5 Hz is 1.7799 as summarized in Table 3.2. This means real power variation effects on voltage should be considered in an LFAC system.

Table 3.2: Receiving-end bus eigenvalues.

Freq.	60 Hz	30 Hz	10 Hz	5 Hz
λ_Q	7.2851	16.6107	50.9623	100.1342
λ_P	56.6521	98.0558	154.5595	178.2276
λ_P/λ_Q	7.7765	5.9032	3.0328	1.7799
λ_S	7.2256	16.3774	48.3992	87.2994

Both eigenvalues λ_P and λ_Q should be taken into account in order to accurately estimate voltage stability in an LFAC system. The following proposed eigenvalue can be used as a single criteria for a low frequency system. From (3.19), it can be rewritten as

$$\Delta V = \frac{1}{\lambda_Q} \Delta Q + \frac{1}{\lambda_P} \Delta P = \frac{1}{\lambda_S} \Delta S \quad (3.20)$$

where $\lambda_S = 1/\sqrt{1/\lambda_P^2 + 1/\lambda_Q^2}$ and ΔS is power variation calculated from ΔP and ΔQ . The eigenvalue λ_S can be used to estimate the system voltage stability. This value is close to λ_Q in a high frequency system and distributed more evenly to λ_P and λ_Q when the operating frequency is low as shown in the last row of Table 3.2 and visualized in Fig. 3.7. For a large system, this calculation can still be applied to obtain eigenvalue λ_S at each bus.

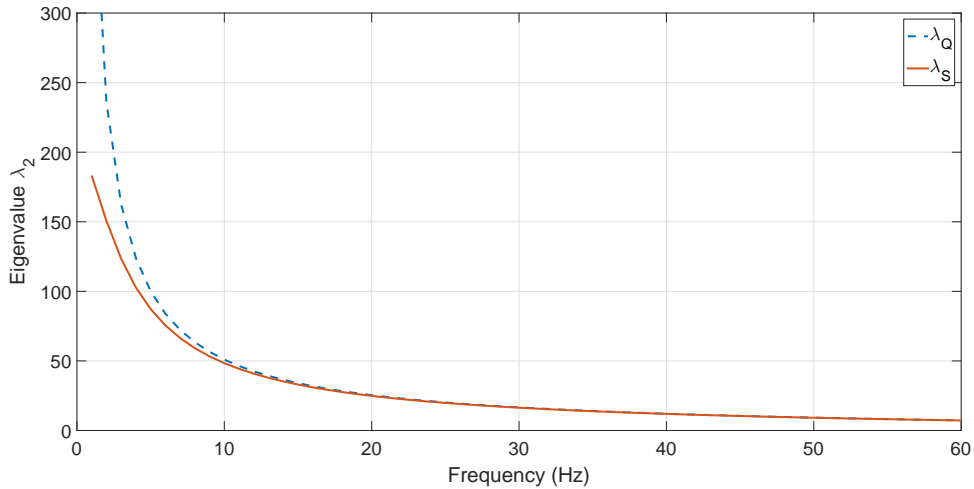


Figure 3.7: The modified eigenvalue trajectory versus frequency.

3.4 Voltage Stability of System: A Case Study

In this section, the voltage stability of LFAC transmission is investigated in terms of both the eigenvalues and the V - Q sensibility via modal analysis [11, 18]. A five-bus power system and a six-bus power system are used to calculate these quantities in different cases of low frequencies.

3.4.1 A five-bus system operating at a specific frequency

Fig. 3.8 presents a five-bus power system used to study voltage stability. Only voltages at Bus 3, Bus 4, and Bus 5 are investigated since Bus 1 and Bus 2 are connected to generators. The detailed specifications of this system can be found in [17].

The power flow for this system can be solved with the Newton-Raphson method. First, the entire system is tested at a specific operating frequency. Then at each frequency, the voltage magnitudes, eigenvalues from the Jacobian matrix, and self-sensitivity values

at each bus are collected in Table. 3.3.

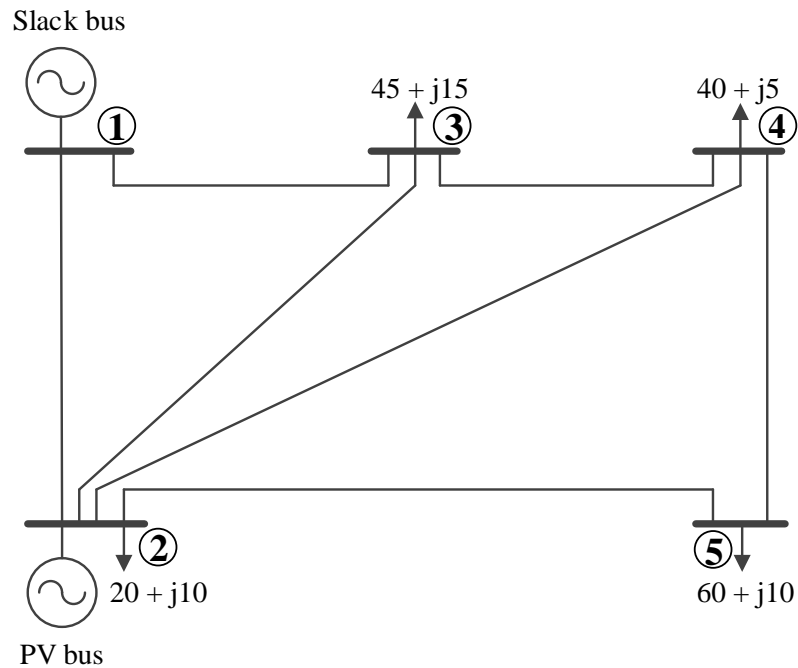


Figure 3.8: A five-bus power system.

The data shows that the voltage of a lower frequency system is more stable than the 60 Hz system. For example, the voltage magnitude at Bus 5 is 0.9717 pu for 60 Hz and 0.9795 pu for 5 Hz. The higher voltage stability in the lower frequency power system is due to smaller impedances, which cause smaller voltage drops on the transmission lines. Since Bus 4 is connected to heavy load, it is expected to be the weakest bus in the system. Indeed, the data shows that Bus 4 has the smallest eigenvalue of the three buses. However, the eigenvalue is increased more than 12 times, i.e. from 7.4813 to 90.8637, if the power system operates at 5 Hz. Additionally, the self-sensitivity value at each bus is another indicator of voltage stability. This value indicates the strength of a bus voltage when it is subjected to reactive power variations [18]. The $V-Q$ self-sensitivity values

are selected from the V - Q sensitivity, which is the inverse of the reduced Jacobian. A small self-sensitivity value indicates a strong bus [11, 18]. Therefore, the power system is more robust if it operates at a low frequency because the self-sensitivity values decrease significantly as the frequency is scaled down.

Table 3.3: Bus Data of Five-Bus System.

	60 Hz	30 Hz	10 Hz	5 Hz
V_3	0.9872	0.9907	0.9935	0.9937
V_4	0.9841	0.9870	0.9897	0.9897
V_5	0.9717	0.9756	0.9789	0.9795
λ_3	72.2566	151.1695	454.8012	907.7094
λ_4	7.4813	15.2164	45.8326	90.8637
λ_5	13.7457	27.7789	83.6118	166.2663
VQ_3	0.0632	0.0311	0.0103	0.0052
VQ_4	0.0653	0.0322	0.0107	0.0054
VQ_5	0.0912	0.0450	0.0149	0.0075

3.4.2 A six-bus system operating at a specific frequency

As shown in Fig. 3.9, a six-bus system representing the power transmission for a wind farm is used to calculate stability conditions. The wind farm is 85 km from Bus 4, and the maximum power the wind farm can produce is 140 MW. The system parameters are detailed in [18].

The entire system is calculated at a fixed operating frequency to validate the results. The wind farm power output is assumed to vary between 0 MW and 100 MW, at which the weakest bus voltage V_5 passes over the lower boundary. Table 3.4 indicates the voltage magnitude at each bus when the wind farm does not generate any output power. The power providing to the loads, therefore, comes from two generators: Gen 1 and Gen

6. Since Bus 1 and Bus 6 are connected directly to the generators, the voltages at these buses are considered to be constant at 1.0 pu for all studied cases. Bus 5 is connected to the wind farm and is assumed to be the most sensitive bus. The V - Q self-sensitivities, presented later on, will explain this assumption. It can be observed from Table 3.4 that the voltage magnitudes at low frequencies are close to 1.0 pu and are much higher than that in a high frequency. Bus 5 voltage V_5 at 60 Hz is 0.9563 pu, which is slightly above the lower boundary value, and it is 0.9717 pu at 30 Hz, 0.9833 pu at 10 Hz, and 0.9864 pu at 5 Hz, correspondingly. The same observations can be seen in voltages at the resting buses V_2 , V_3 , and V_4 .

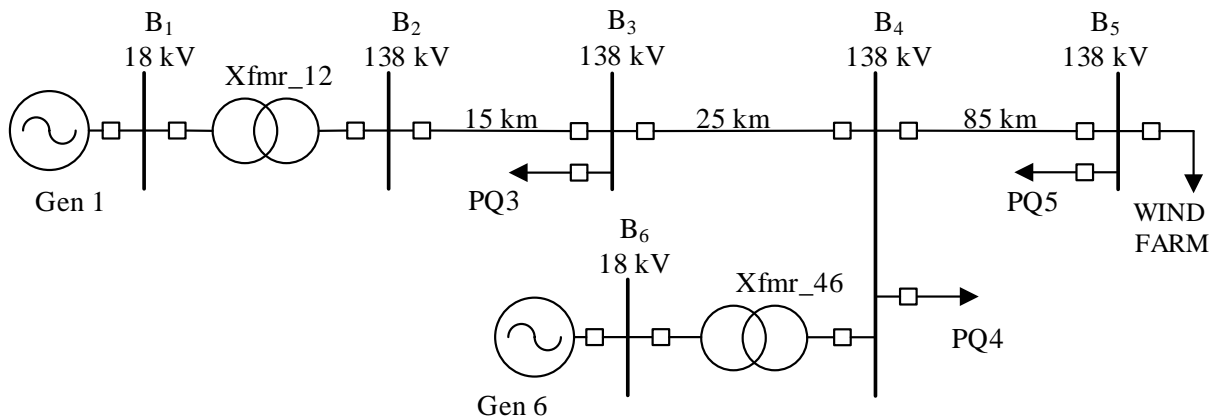


Figure 3.9: A six-bus LFAC system for wind applications.

The eigenvalues, which represent the system voltage stability, are determined via the Jacobian matrix and are shown in Table 3.5 in descending order. Because the voltages at Bus 1 and Bus 6 are fixed, the reduced Jacobian matrix shows the four eigenvalues at other buses. The eigenvalues are improved significantly when the frequency is lowered. For instance, the lowest eigenvalue in 60 Hz ac system 3.0512 is increased to 6.3103 (30

Hz), 19.2789 (10 Hz), and 38.6460 (5 Hz). With higher eigenvalues, the system is more voltage stable [18].

Table 3.4: Bus Voltage Magnitude.

Vmag	60 Hz	30 Hz	10 Hz	5 Hz
V_1	1.0000	1.0000	1.0000	1.0000
V_2	0.9850	0.9926	0.9973	0.9984
V_3	0.9607	0.9782	0.9893	0.9920
V_4	0.9625	0.9788	0.9896	0.9923
V_5	0.9563	0.9717	0.9833	0.9864
V_6	1.0000	1.0000	1.0000	1.0000

Table 3.5: Eigenvalues (top) and self-sensitivities (bottom)at buses.

λ_i	60 Hz	30 Hz	10 Hz	5 Hz
λ_2	104.6664	212.0111	640.7134	1283.066
λ_3	45.5025	92.8477	281.8955	565.4993
λ_4	13.6468	28.2279	86.2896	173.1871
λ_5	3.0512	6.3103	19.2789	38.6460

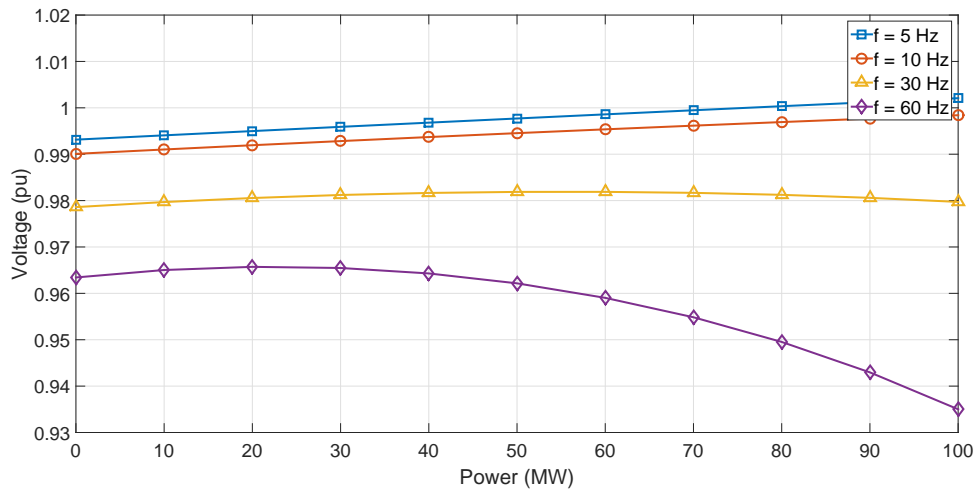
VQ_i	60 Hz	30 Hz	10 Hz	5 Hz
VQ_2	0.019318	0.009473	0.003126	0.001560
VQ_3	0.044492	0.021303	0.006935	0.003451
VQ_4	0.069012	0.033247	0.010856	0.005404
VQ_5	0.299730	0.145362	0.047650	0.023783

The voltage at Bus 2 is the most stable since its self-sensitivity is smallest. This is easy to understand because Bus 2 is connected directly to Bus 1 via a transformer. The voltage at Bus 5, on the other hand, is the most sensitive to the reactive power since it has the smallest value. The self-sensitivity at this bus is 0.30 for 60 Hz ac transmission. This value is reduced to 0.145 in 30 Hz, 0.048 in 10 Hz, and 0.024 in 5 Hz systems. It is true

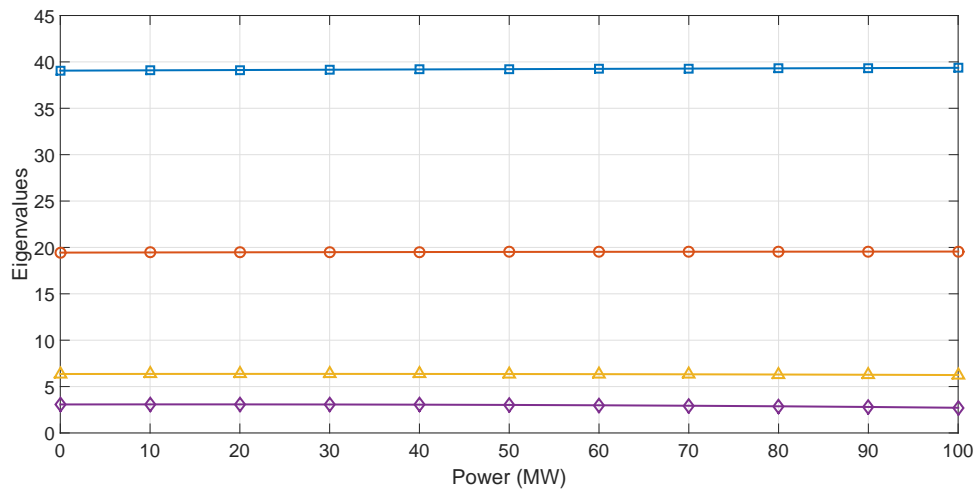
that as the operating frequency is decreased, the self-sensitivity is reduced considerably. In other words, the dependence of voltage on reactive power is less, and the system is more stable at low frequencies.

The calculation results for Bus 5 at different wind farm output power cases are represented in Fig. 3.10. It is worthwhile to summarize some observations here. The bus voltages increase when the power increases. In the conventional 60 Hz transmission system, the voltage begins decreasing when the wind farm produces over 30 MW of power output, and the voltage passes over the lower boundary when the wind farm produces 80 MW of output power. The voltage quickly decreases after it passes over the lower boundary because the capability limit of the system has been reached. Therefore, a high frequency system is less stable when wind power penetration is high. In the low frequency system, the voltage V_5 at Bus 5 builds up slowly but never reaches the upper boundary, i.e. 1.05 pu, when the power output is 100 MW, as shown in Fig. 3.10(a). This means the low frequency system can handle more power without losing its stability. The same conclusions for eigenvalues and self-sensitivity can be drawn from Fig. 3.10(b), 3.10(c).

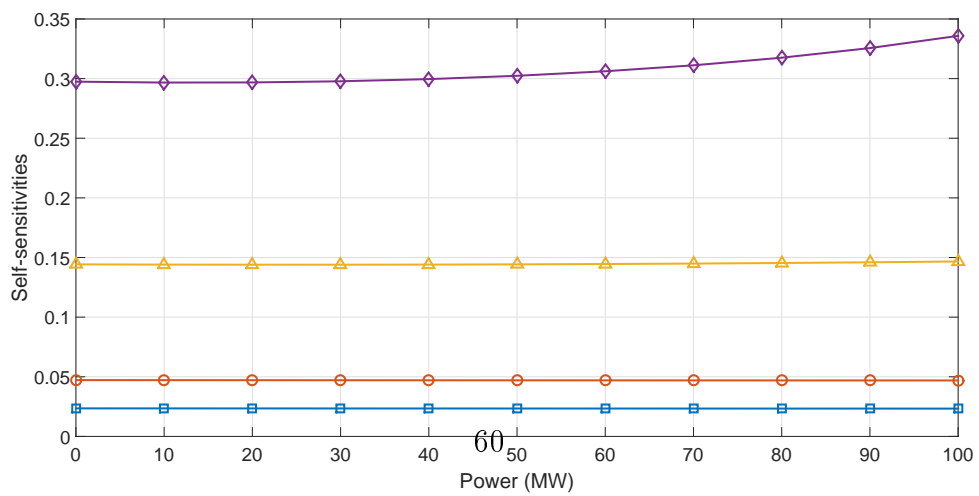
In summary, this section has investigated the voltage stability of low frequency ac (LFAC) transmission. At a low frequency, reactance is reduced and the system is more capable of transferring power. More importantly, because of lower voltage drops along the transmission line, the system exhibits a better voltage profile, and its stability has been extended with less dependence on power variations. The LFAC theory has been applied to two specific case study systems and has demonstrated great benefits to the power system in terms of voltage stability.



(a)



(b)



(c)

Figure 3.10: Bus 5 profiles with different frequencies: (a) voltage magnitudes, (b) eigenvalues, and (c) self-sensitivities (\diamond 60Hz, \triangle 30Hz, \circ 10Hz, \square 5Hz).

Chapter 4

System Modeling for LFAC Transmission

As shown in previous chapters, the low frequency ac transmission offers many advantages in terms of power transfer capability and voltage stability. Given the fact that the power system is already operating at 60 Hz, for a low frequency transmission to cooperate it needs to interface with the existing system. Fig. 4.1 shows the general concepts of how to connect two different frequency power systems using a power converter system. This power converter system converts the voltage and current at a low frequency into a voltage source at 60 Hz by the turn-on and turn-off patterns of the switching devices, i.e IGBTs. The converter output is now at 60 Hz and it can transfer power to the grid naturally. The process is similar if the 60 Hz system wants to transfer power to the low frequency system. To summarize, the power converter system needs to perform the following tasks:

- Grid synchronization: detect the frequencies, voltage magnitudes, and phase angles of both grid sides that the converter connects to in order to synchronize.
- Power conversion: convert power from 60 Hz to a low frequency or vice versa by semi-conductor devices.
- Power flow control: regulate the amount of power exchange between two grids and the power flow direction.

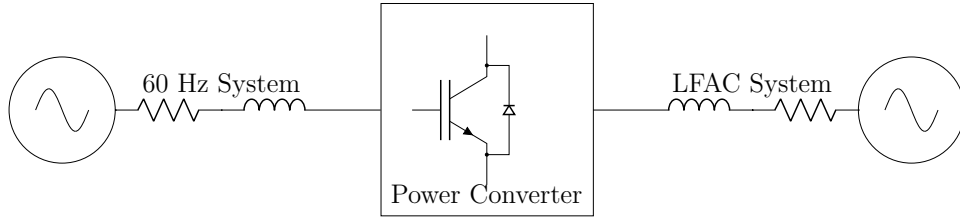


Figure 4.1: Interface between an LFAC and a 60 Hz power system.

This chapter presents our work on modeling an entire power converter system, Fig. 4.2. The grid synchronization is introduced first and followed by the proposed algorithm to improve the grid parameters detection under harmonic conditions. The power converter configurations and controllers are then discussed. Next, our work on the proportional-resonant (PR) controller for converters is described in detail. The entire system mathematical model and simulation results are presented. It is worthwhile to mention that the entire model has been transferred to PSCAD/EMTDC by our Fortran codes under block-set library and is available for graduate students to conduct research.

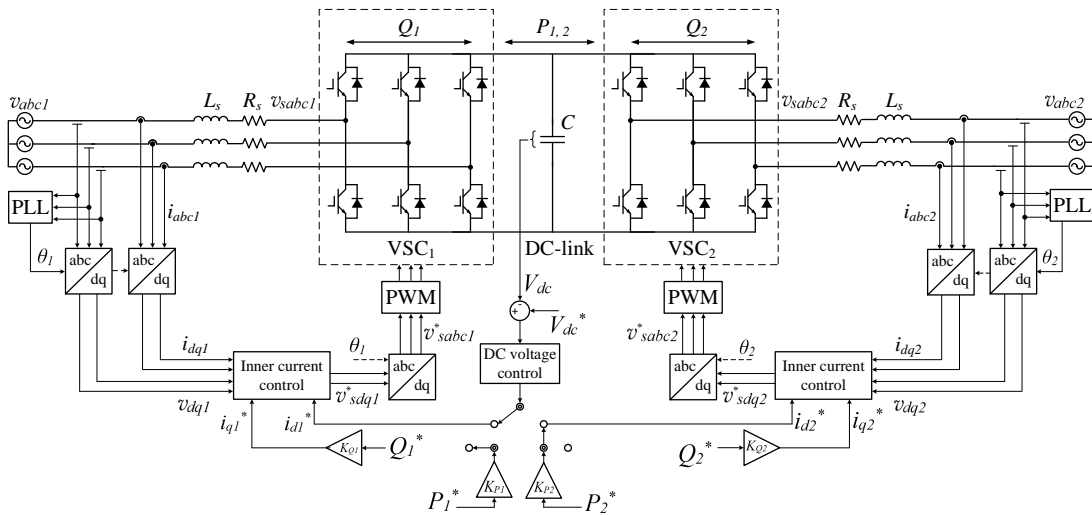


Figure 4.2: The overall power converter system.

4.1 Grid Synchronization for Power Converter Systems

In order to synchronize with the grid, a power converter needs information about voltage magnitude, phase angle, and frequency. There are many methods have been proposed in the literature for grid synchronization. These methods can be based on frequency or time domain [20]. Our focus, however, is on second-order-generalized-integrator frequency-locked loop (SOGI-FLL), a time domain based technique that quickly and accurately detects the grid information. We also propose to use the transfer function approach to derive many grid synchronization configurations that is not only able to identify the grid parameter under normal conditions but high harmonic distortions as well. These configurations are described in detail after the review section of a typical SOGI structure.

4.1.1 Review of SOGI Configuration

The second-order generalized-integrator (SOGI) block diagram, shown in Fig. 4.3, has functions to provide two perfect orthogonal output signals, v' and qv' , from a sinusoidal input voltage v_{in} . By using two integrators, the SOGI behaves as an active filter oscillating at the central frequency ω' [20, 21, 22].

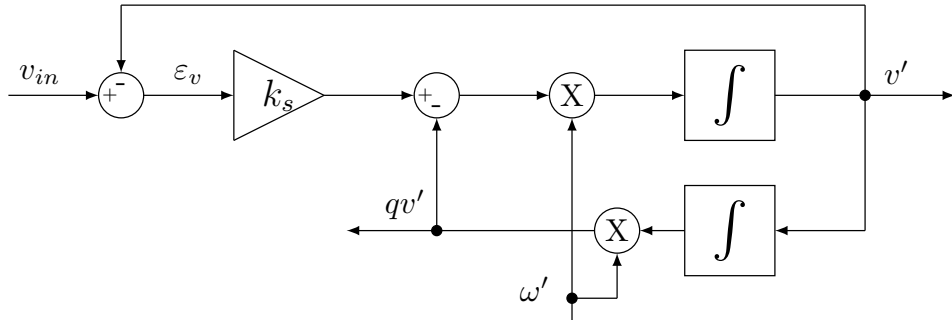


Figure 4.3: A typical SOGI structure.

The SOGI operating principles can be thoroughly explained from analyzing its transfer function and Bode plot [20]. Denoting $G_{V'}(s)$ and $G_{QV'}(s)$ as transfer functions of outputs $V'(s)$ and $QV'(s)$ to input $V_{in}(s)$ respectively, then [23]

$$G_{V'}(s) = \frac{k_s \omega' s}{s^2 + k_s \omega' s + \omega'^2}, \quad G_{QV'}(s) = \frac{k_s \omega'^2}{s^2 + k_s \omega' s + \omega'^2} \quad (4.1)$$

where ω' is the central frequency [24] and k_s is a gain. At the central frequency $s = (j\omega')$, the transfer functions become

$$\begin{aligned} G_{V'}(j\omega') &= \frac{k_s \omega' (j\omega')}{(j\omega')^2 + k_s \omega' (j\omega') + \omega'^2} = 1 \\ G_{QV'}(j\omega') &= \frac{k_s \omega'^2}{(j\omega')^2 + k_s \omega' (j\omega') + \omega'^2} = -j \end{aligned} \quad (4.2)$$

The results from (4.2) explain for the sine and cosine signals in the SOGI if the input is a sinusoidal waveform. If the input signal contains harmonics, the SOGI does not work properly. Fig. 4.4 presents the output signals when the input is given by (4.10) on page 73. The output signals are not sinusoidal and are also different in magnitude. This also results in errors of phase and frequency detections. The SOGI improper operation can be accounted mainly for its filter capability. The SOGI only acts as a second order low-pass filter to block high frequency signals, and thus it cannot remove harmonics completely. The SOGI behaviors become worse when it is used for the three-phase system [25].

An intuitive method to improve filtering performance is increasing the synchronization system to a higher order. Two SOGIs can be cascaded to form a fourth-order system that has better filtering effects to the harmonics. However, the system becomes more complex and requires much computation. After some manipulations the cascaded SOGI system can be reduced to a third-order system with almost the same performances [26]. In the following section, the third-order synchronization system is investigated.

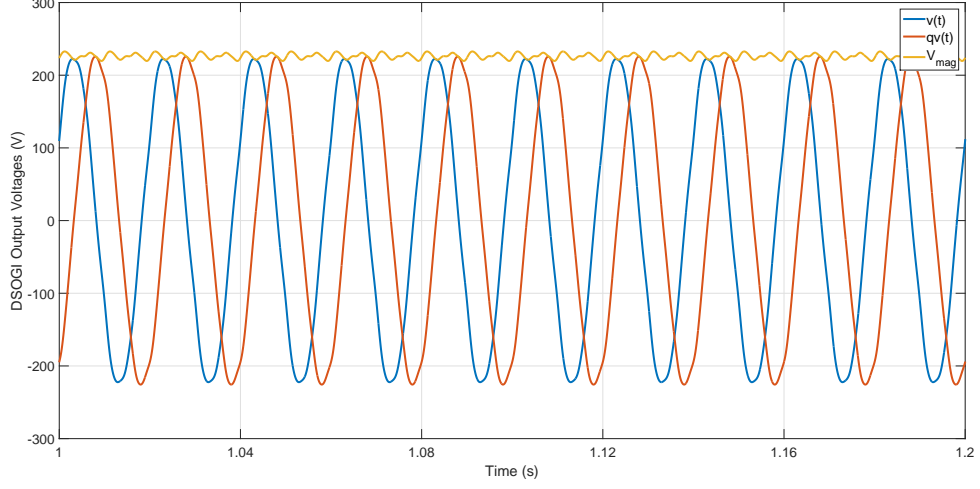


Figure 4.4: Voltage waveforms from a SOGI under distorted conditions.

4.1.2 The Third-Order Grid Synchronization Configurations

The third-order system has two functions: 1) generating two orthogonal output signals and 2) satisfying (4.2) for synchronization. It is worthwhile to note that once the transfer function $G_{V'}(s)$ is formed, $G_{QV'}(s)$ can be found by $G_{QV'}(s) = G_{V'}(s)\omega'/s$. Therefore, the first step is to find $G_{V'}(s)$. Assuming the transfer function starts with a general formulation of a third-order system

$$G_{V'}(s) = \frac{N(s)}{D(s)} = \frac{b_0s^3 + b_1s^2 + b_2s + b_3}{s^3 + a_1s^2 + a_2s + a_3} \quad (4.3)$$

For the sake of simplicity, the denominator of (4.3) is first evaluated at the central frequency, ω' . Denoting $k_i = (a_2 - \omega'^2)$, $k_r = (a_1 - a_3/\omega'^2)$, and $j^2 = -1$, then at $s = j\omega'$

$$\begin{aligned} D(j\omega') &= (j\omega')^3 + a_1(j\omega')^2 + a_2(j\omega') + a_3 = (a_3 - a_1\omega'^2) + j\omega'(a_2 - \omega'^2) \\ &= k_r(-\omega'^2) + k_i(j\omega') = k_r(j\omega')^2 + k_i(j\omega') \\ &= k_r(s)^2 + k_i(s) \quad \text{for } (s = j\omega') \end{aligned} \quad (4.4)$$

From (4.4), the numerator of $G_{V'}(s)$ can be simply selected as: $N(s) = k_r s^2 + k_i s$.

The transfer functions of the third-order synchronization system is thus given by

$$\begin{aligned} G_{V'}(s) &= \frac{k_r s^2 + k_i s}{s^3 + a_1 s^2 + (\omega'^2 + k_i) s + (a_1 - k_r) \omega'^2} \\ G_{QV'}(s) &= \frac{(k_r s + k_i) \omega'}{s^3 + a_1 s^2 + (\omega'^2 + k_i) s + (a_1 - k_r) \omega'^2} \end{aligned} \quad (4.5)$$

Fig. 4.5 shows the Bode plots of two transfer functions in (4.5) with $k_r = 20$, $k_i = 22214.41$, $a_1 = 444.29$. The system is stable at pole locations $s_1 = -402.42$, $s_{2,3} = -20.94 \pm j321.90$ and able to synchronize at the central frequency. The output signals are always orthogonal.

The transfer function in (4.5) can be simplified for some interesting cases: 1) $k_r = 0$ and 2) $k_i = 0$. These two cases can lead to configuration derivations based on SOGI structure in the literature [25, 26].

Case 1: $k_r = 0$ and the output transfer functions $G_{V'}(s)$ and $G_{QV'}(s)$ are simplified as

$$\begin{aligned} G_{V'}(s) &= \frac{k_i s}{s^3 + a_1 s^2 + (\omega'^2 + k_i) s + a_1 \omega'^2} \\ G_{QV'}(s) &= \frac{k_i \omega'}{s^3 + a_1 s^2 + (\omega'^2 + k_i) s + a_1 \omega'^2} \end{aligned} \quad (4.6)$$

Case 2: $k_i = 0$ and the output transfer functions $G_{V'}(s)$ and $G_{QV'}(s)$ become

$$\begin{aligned} G_{V'}(s) &= \frac{k_r s^2}{s^3 + a_1 s^2 + \omega'^2 s + (a_1 - k_r) \omega'^2} \\ G_{QV'}(s) &= \frac{k_r \omega' s}{s^3 + a_1 s^2 + \omega'^2 s + (a_1 - k_r) \omega'^2} \end{aligned} \quad (4.7)$$

It is obvious from Fig. 4.5 that two outputs in (4.6) and (4.7) have the same magnitude and 90° difference in phase, and thus can synchronize with the grid under harmonic conditions. However, the later one requires longer transient time response due to the higher order of the numerator. The following section gives a detailed analysis of the two systems.

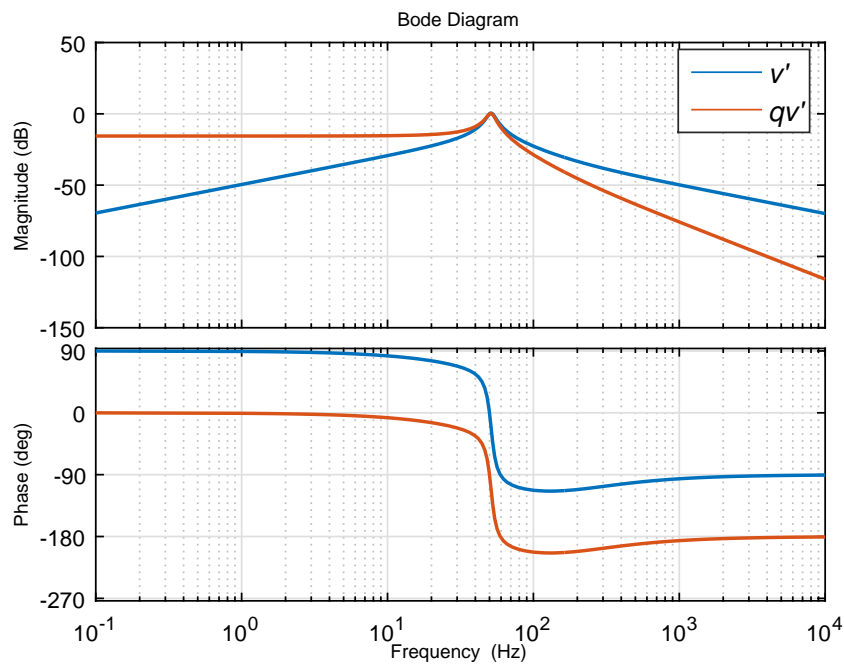


Figure 4.5: Bode plots of third-order synchronization system.

Grid synchronization based on third-order system

From the transfer function expressions in (4.5), (4.6) and (4.7), there are many configurations to construct systems based on state-space model. The most familiar systems are the controllable canonical form (CCF) and the observable canonical form (OCF) [27].

Fig. 4.6 shows an example of synchronization structure for (4.5) under the controllable canonical form.

As mentioned in the previous section, the third-order synchronization system can be constructed based on a typical SOGI configuration. This configuration is convenient and beneficial for the frequency controller. Denoting $a_1 = k_s \omega'$, $k_i = k_a k_s \omega'$, and $k_r = k k_s \omega'$, a state-space model for the system is given by

$$\begin{bmatrix} \dot{x}_1 \\ \dot{x}_2 \\ \dot{x}_3 \end{bmatrix} = - \begin{bmatrix} 0 & -1 & 0 \\ \omega'^2 & k_s \omega' & (k-1)k_s \omega' \\ \omega'^2 & \frac{k_a}{1-k} & 0 \end{bmatrix} \begin{bmatrix} x_1 \\ x_2 \\ x_3 \end{bmatrix} + \begin{bmatrix} 0 \\ k k_s \omega' \\ \frac{k_a}{1-k} \end{bmatrix} V_{in} \quad (4.8)$$

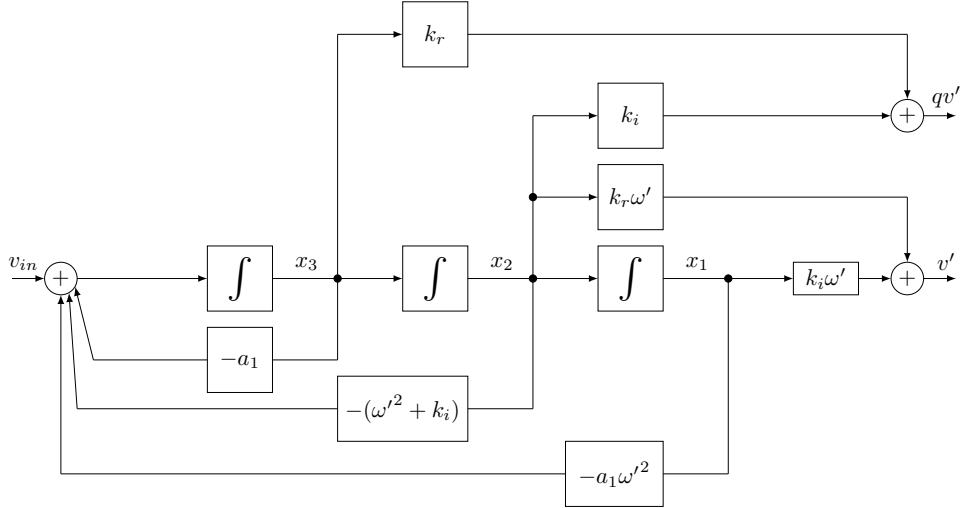
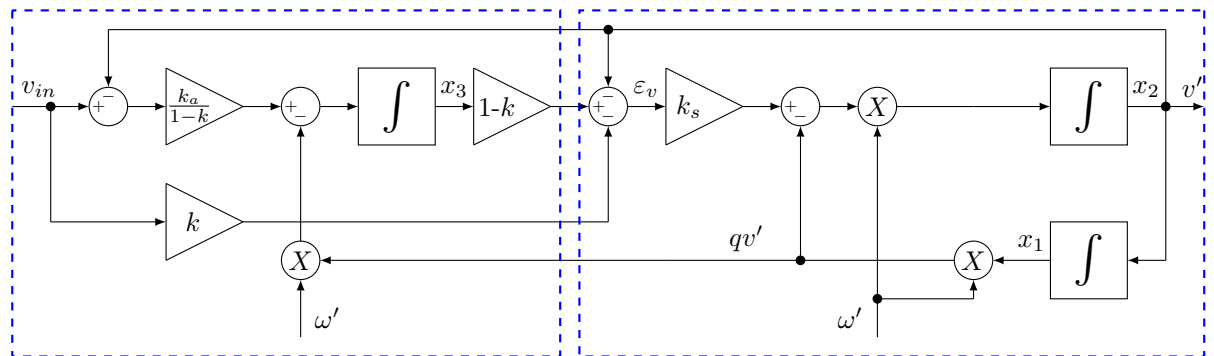
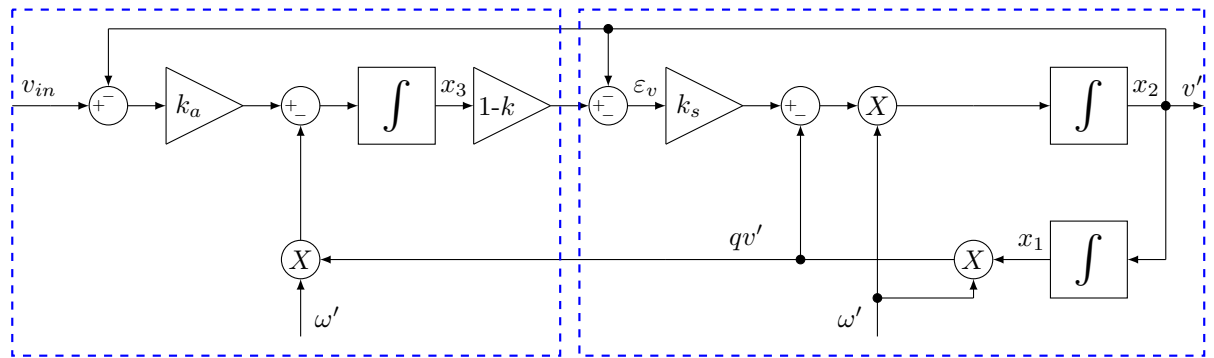


Figure 4.6: A grid synchronization configuration based on CCF.

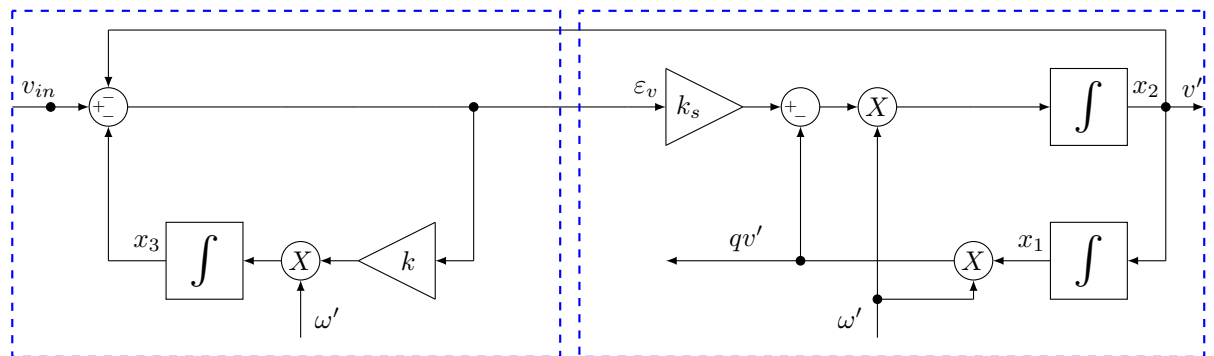
The structure for (4.8) is shown in Fig. 4.7(a). In addition, the configurations for (4.6) and (4.7) are investigated and presented in Fig. 4.7(b) and Fig. 4.7(c), respectively. It is interesting to note that in case where $k_r = 0$ and $k_i = 0$, the configurations match with structures in [25, 26]. The detailed analyses can be found in these references.



(a)



(b)



(c)

Figure 4.7: Configurations based on SOGI: a) general case, b) $k_r = 0$, and c) $k_i = 0$.

The frequency controller and DHOIGI-FLL structure

The grid frequency can be identified by the phase locked-loop (PLL) or frequency locked-loop (FLL) controllers. Since the FLL method has better dynamic performance [20] and the controller is simpler, this section only focuses on the FLL controller. Based on the SOGI configuration, the frequency can be estimated from the error signal ε_v and the output qv' , see Fig. 4.7. The transfer functions of ε_v can be easily derived as

$$G_{\varepsilon_v}(s) = \frac{(ks + k_a)(s^2 + \omega'^2)}{s^3 + k_s\omega's^2 + (\omega'^2 + k_ak_s\omega')s + k_s\omega'^3} \quad (4.9)$$

The phases of ε_v and qv' are the same if $\omega < \omega'$ and are inverted if $\omega > \omega'$, as shown in Fig. 4.8. Therefore, the product of the two signals ε_v and qv' can be used as an input for the frequency locked-loop controller to estimate the frequency [28].

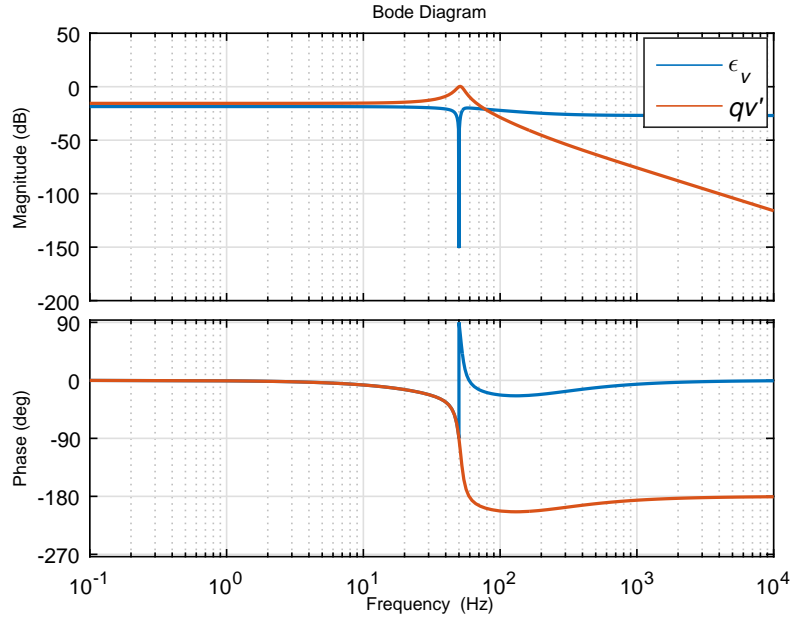


Figure 4.8: Bode plots of ε_v and qv' in a third-order synchronization system.

The overall block diagram for the three-phase grid synchronization is presented in Fig. 4.9. The construction of this configuration is almost the same as in DSOGI-FLL [20, 23, 24] but different in the high-order generalized-integrator (HOGI) blocks, thus performing better. The principles of HOGI configuration is comprehensively discussed in the previous section. The input voltage v_{abc} is converted into stationary frame v_α and v_β , both of which contain harmonics by Clarke's transformation. These signals then pass through two HOGI blocks in order to produce orthogonal outputs at the fundamental frequency. The two orthogonal signal sets are used to determine the positive-sequence component by the PSC block. The errors $\varepsilon_{f\alpha}$ and $\varepsilon_{f\beta}$ coming from the DHOGI are used for the frequency identification in the controller.

The positive-sequence block calculates the positive-sequence component from four output signals of two HOGIs [28]. The instantaneous-sequence voltage on the stationary $\alpha\beta$ frame by Clarke's transformation is given by

$$\begin{aligned} v_{\alpha\beta}^+ &= [T_{\alpha\beta}]v_{abc}^+ \\ &= [T_{\alpha\beta}][T_+]v_{abc} \\ &= [T_{\alpha\beta}][T_+][T_{\alpha\beta}]^{-1}v_{\alpha\beta} \\ &= \frac{1}{2} \begin{bmatrix} 1 & -e^{-j\frac{\pi}{2}} \\ e^{-j\frac{\pi}{2}} & 1 \end{bmatrix} v_{\alpha\beta} \end{aligned}$$

where $[T_+]$ is sequence transformation matrix [29] as $T_+ = \frac{1}{2} \begin{bmatrix} 1 & a & a^2 \\ a^2 & 1 & a \\ a & a^2 & 1 \end{bmatrix}$ and $[T_{\alpha\beta}]$ is Clarke's transformation matrix [28] as $T_{\alpha\beta} = \frac{2}{3} \begin{bmatrix} 1 & -1/2 & -1/2 \\ 0 & \sqrt{3}/2 & -\sqrt{3}/2 \end{bmatrix}$. The PSC block in Fig. 4.9 presents the interpretation of (4.10) to achieve positive-sequence voltage components. The positive component v_α^+ is a subtraction of two outputs (v'_α and qv'_β) while the

signal v_β^+ is a summation of two outputs (qv'_α and v'_β).

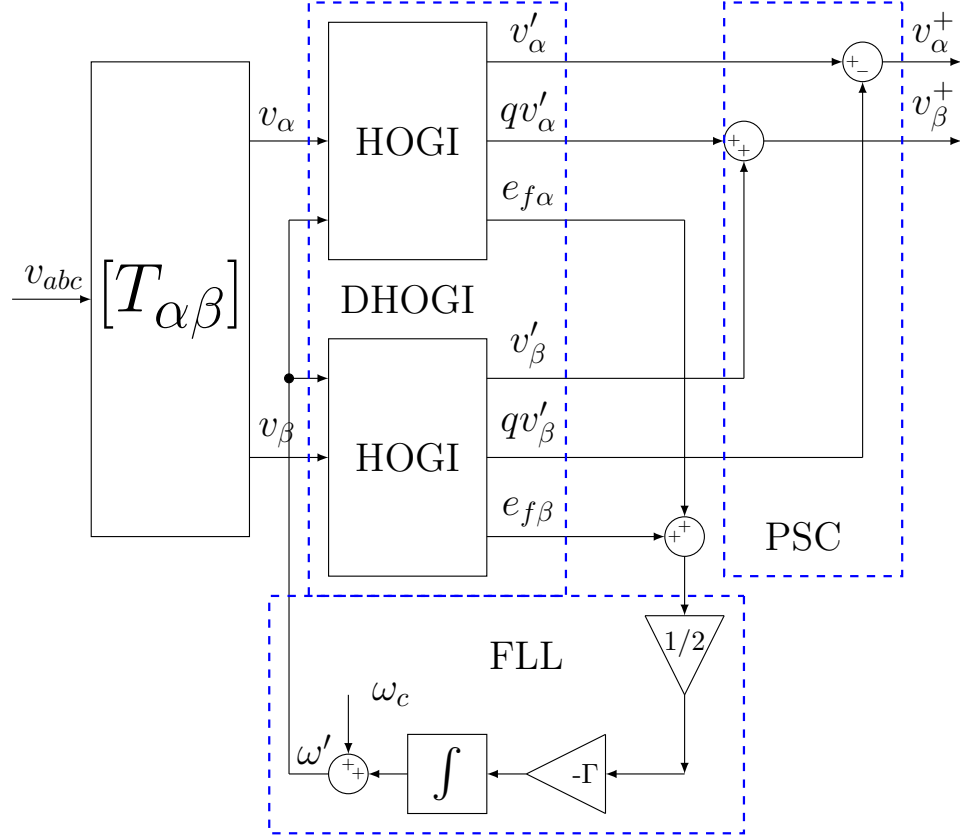


Figure 4.9: The overall block diagram of DHOGI-FLL system.

4.1.3 Simulation Results

The third-order filter performance is tested under several distortion levels of the grid voltage. The gains for the proposed system are set at $k_a = 50$, $k = 0.045$ and $k_s = \sqrt{2}$ for pole locations at $s_1 = -402.42$, $s_{2,3} = -20.94 \pm j321.90$. The third-order system is implemented into two cases: the single-phase power grid with one HOGI configuration and the three-phase power grid using double HOGIs. The power system is assumed to

operate at 50 Hz of frequency. In addition, the grid frequency is assumed to drop to 45 Hz at simulation time $t = 2$ second.

Single-phase grid with a HOGI

In this case study, the grid only experiences unbalanced phenomena. The measured voltage is highly distorted by harmonics as shown in Fig. 4.10(a) and given by

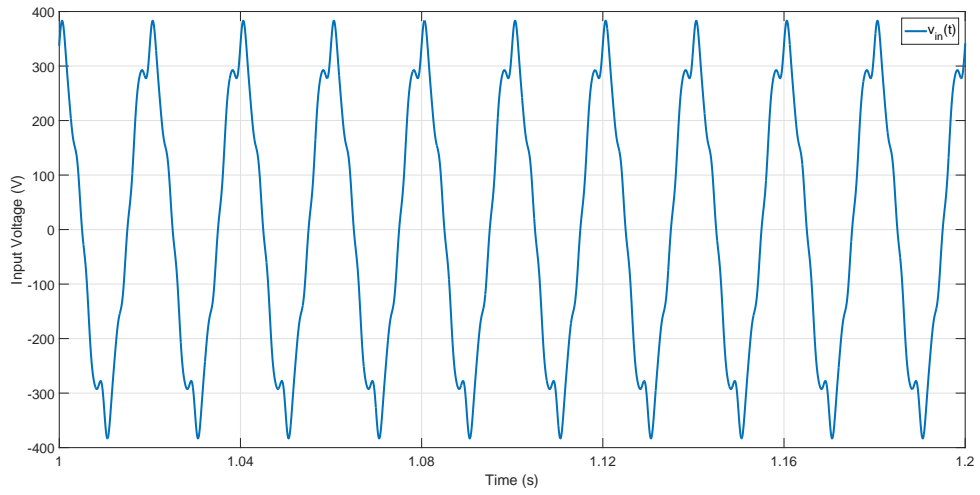
$$v_{in}(t) = 240\sqrt{2}\sin(\omega t + \pi/2) + 40\sin(3\omega t) + 30\sin(5\omega t) + 20\sin(7\omega t) \\ + 10\sin(9\omega t) + 30\sin(11\omega t) \quad (4.10)$$

The fundamental voltage magnitude is $240\sqrt{2} = 339$ V and the third-order system identifies the magnitude correctly with negligible variations. The low frequency harmonic components are removed, and thus two output signals are clean and are sinusoidal as shown in Fig. 4.10(b). Fig. 4.11 presents the frequency waveform of the controller in the new configuration. It can be seen clearly that the system can detect and track the grid frequency accurately when there is a frequency jump from 50 Hz to 45 Hz.

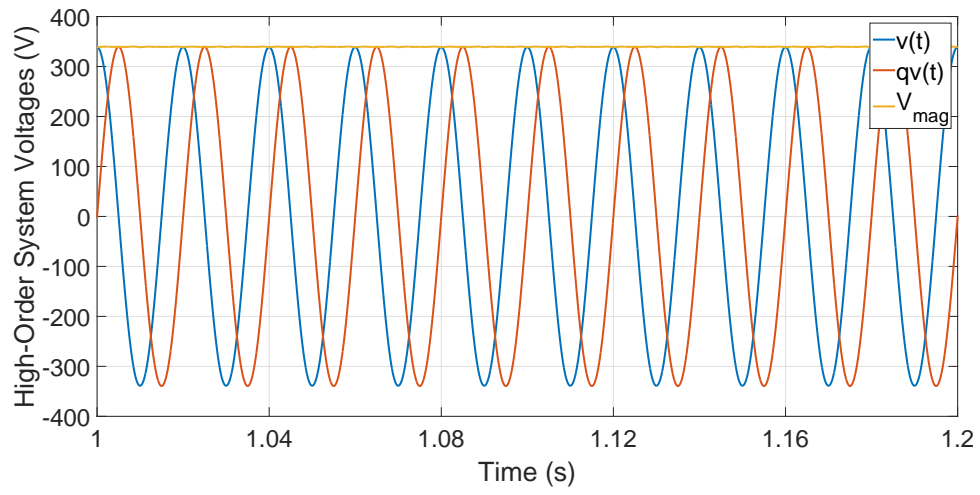
Three-phase grid with HOGIs

In this case, the three-phase voltages contain 5th, 7th, and 11th-order harmonics as shown in Fig. 4.12(a) and given below

$$v_a(t) = 240\sqrt{2}\sin(\omega t + \pi/2) + 30\sin(5\omega t) + 20\sin(7\omega t) + 30\sin(11\omega t) \quad (4.11) \\ v_b(t) = 226\sqrt{2}\sin(\omega t - 5\pi/6) + 35\sin(5\omega t - 2\pi/3) + 9\sin(7\omega t - 2\pi/3) \\ + 10\sin(11\omega t - 2\pi/3) \\ v_c(t) = 247\sqrt{2}\sin(\omega t + 5\pi/6) + 19\sin(5\omega t + 2\pi/3) + 15\sin(7\omega t + 2\pi/3) \\ + 13\sin(11\omega t + 2\pi/3)$$



(a)



(b)

Figure 4.10: a) Single-phase input and b) output waveforms.

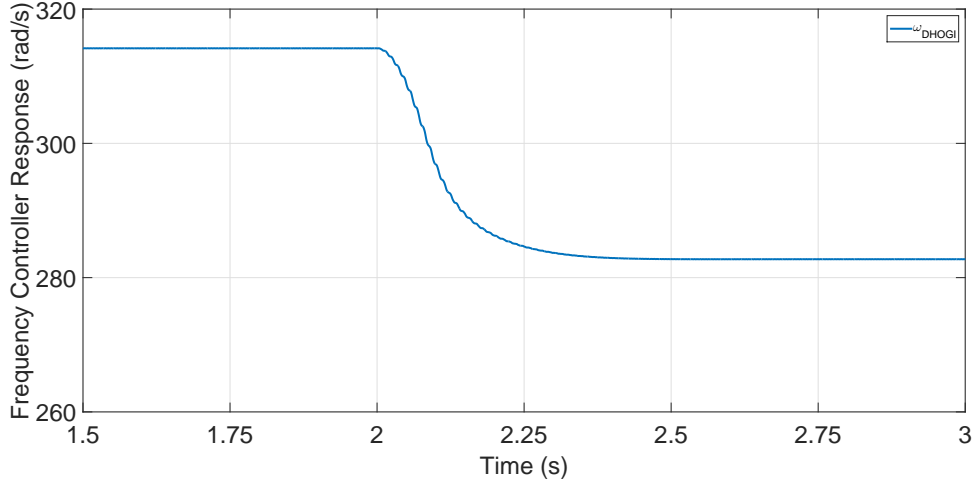
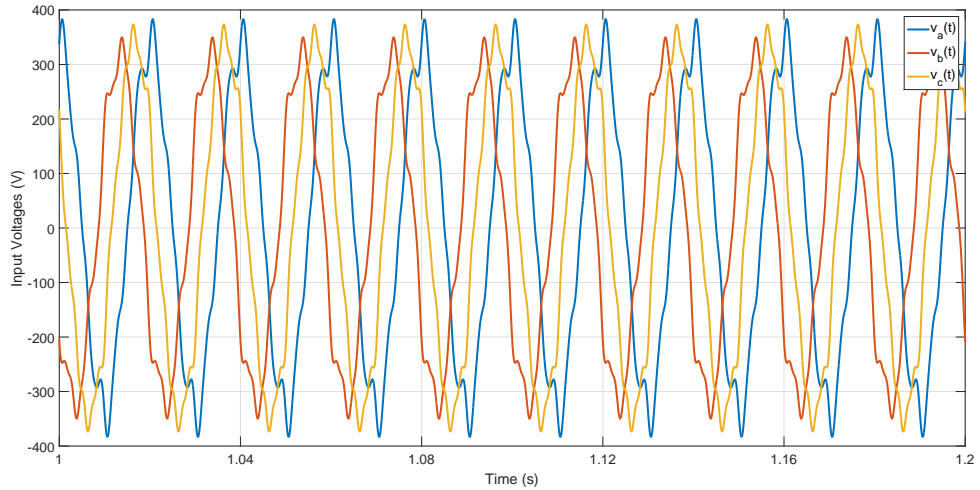


Figure 4.11: The frequency controller response.

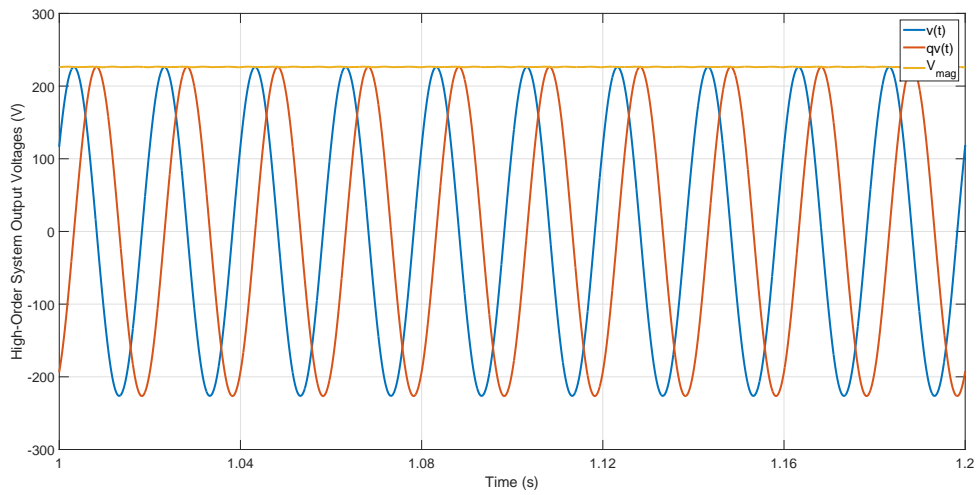
The positive-sequence voltage is simple to find with the Foeste's transformation [20], and it matches with outputs from third-order filter configuration. The output waveforms are orthogonal and purely sinusoidal with a similar output as the previous single-phase but with a smaller magnitude, see Fig. 4.12(b).

The performances of third-order grid synchronization systems are compared with the double SOGI (DSOGI) method and the results are plotted in Fig. 4.13. It is obvious that the proposed configuration has better responses in terms of voltage magnitude and frequency detection. In the conventional method, the voltage magnitude is fluctuated in a range of 220 - 232 V and can result in improper operations of power converter. The third-order system, on the other hand, detects the voltage value constantly as shown in Fig. 4.13(a). It is worthwhile to note that the two output signals are purely sinusoidal and orthogonal. The frequency identification waveforms, Fig. 4.13(b), also conclude that the third-order system has better performances. The two frequencies are close to each

other, however, it can be observed that the result from the DSOGI still has an offset to the exact frequency value.

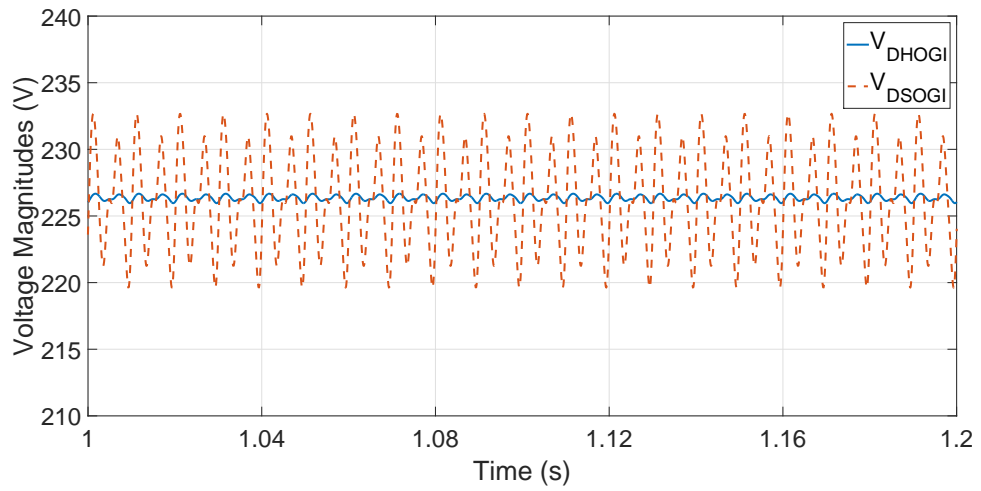


(a)

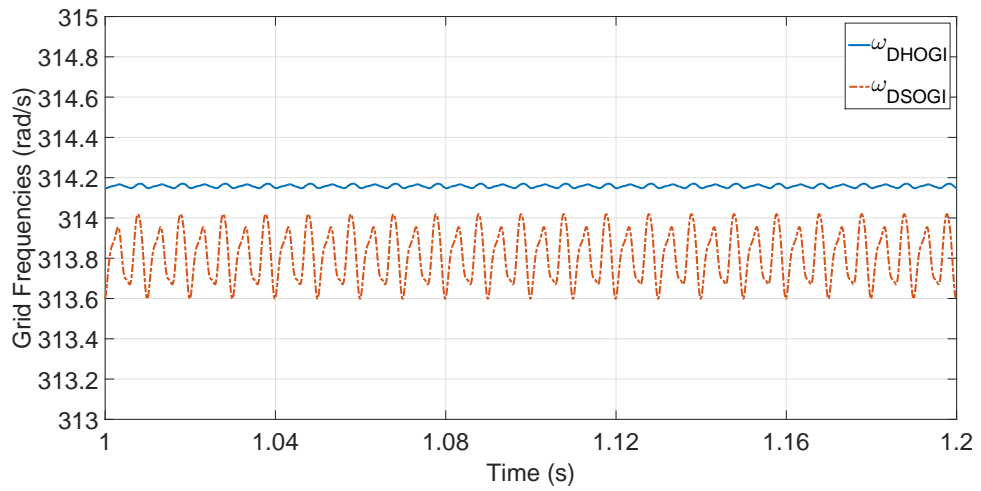


(b)

Figure 4.12: a) Three-phase input voltages and b) output waveforms.



(a)



(b)

Figure 4.13: a) Voltage magnitude and b) frequency detection.

In conclusion, the third-order HOGI has demonstrated its excellent performance in grid synchronization compared to the conventional SOGI method under distorted grid conditions. The outputs are orthogonal and purely sinusoidal waveforms. The voltage

magnitude is thus estimated precisely. The grid frequency is also identified accurately because high-order harmonics are removed from the frequency controller. The third-order HOGI configuration can enhance better performances for a power converter under a distorted and unbalanced grid.

4.1.4 Experimental Results

It is worthwhile to mention that the proposed configuration employs three integrators and that needs to be implemented in discrete-time. The selection process for the digital method is analyzed in depth and discussed in [30], and out of scope in this section. The real-time experimental setup is conducted to verify the theoretical analysis. In the experiments, a three-phase voltage source with high frequency harmonics is programmed to test the proposed method. The experimental system has been run on an RT-LAB real-time platform, allowing the performance to be observed in a real-time environment.

The distorted and unbalanced voltages are generated to simulate the practical grid conditions for the experiments as shown in Fig. 4.14(a). The total harmonic distortions (THD) in each phase of the grid voltage are 10.80 %, 12.79 %, 8.13 %, respectively.

A third-order filter based on the SOGI configuration is constructed, and its performances are the same as in the simulation section. The voltages in stationary frame, Fig. 4.14(b), are distorted and contain harmonics since the Clarke's transformation does not behave as a filter. The two output signals of the third-order synchronization system are shown in Fig. 4.15. Fig. 4.15(a) represents the positive-sequence voltages from the third-order configuration. The voltages are clean and are sinusoidal waveforms with magnitude matching the calculation.

The dynamic response of the frequency controller is tested by a change from 50 Hz to 45 Hz as seen from Fig. 4.15(b). It is clear that the proposed method can track the reference after a transient duration. Since the frequency controller is based on the third-order system, it requires several grid cycles for the frequency to reach the steady-state.

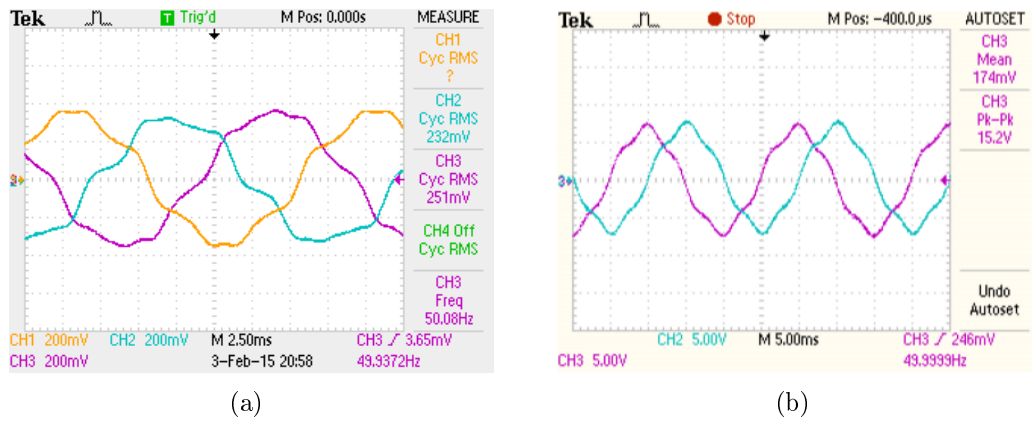


Figure 4.14: a) Distorted grid voltage waveforms (188 V/div), and b) input voltages after Clarke's transformation.

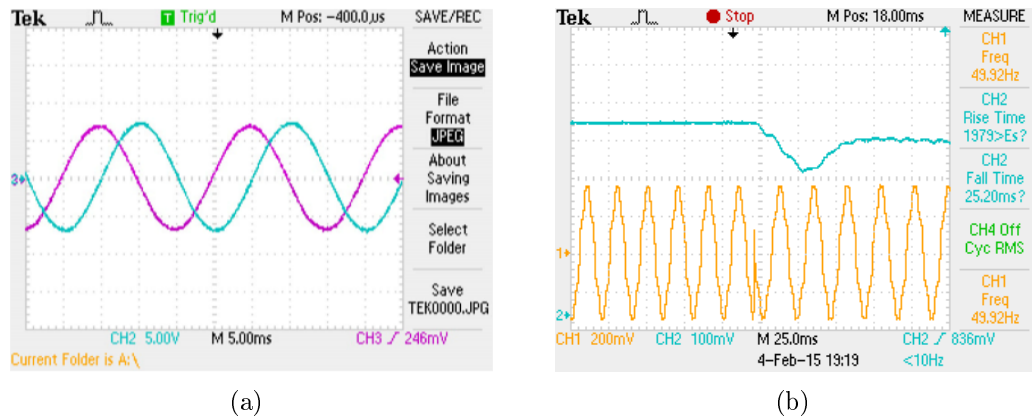


Figure 4.15: a) Positive-sequence outputs, and b) frequency response in the third-order proposed DHOIGI-FLL method.

In summary, in this section a new configuration based on SOGI has been developed for grid synchronization under distorted conditions of distribution system. The approach for deriving a third-order grid synchronization from transfer function can be extended to any system. Several SOGI-based configurations have been constructed, and they are able to eliminate high frequency harmonics. The introduced method still preserves all the advantages of the conventional SOGI-FLL. The grid information is accurately detected and quickly supported to the power converter for grid synchronization. The proposed DHOGI-FLL structure performances have been tested under different unbalanced and low frequency harmonic voltage conditions. The simulation results verify significant improvements in this method compared with the conventional DSOGI-FLL in the accuracy of voltage magnitude and frequency detections. In addition, the experiments have been conducted and validated theoretical analysis.

4.2 Power Converter Configurations

The power converter system interfaces with both 60 Hz grid and a low frequency grid and is able to transform power from one frequency system to another one or vice versa. Depending on the conversion method, the converter system can be classified as either direct frequency conversion system or indirect frequency conversion system.

4.2.1 Direct Frequency Conversion Systems

The direct frequency conversion system converts power from one ac system to another without any dc conversion. The oldest and most familiar system of this type is an asynchronous machine. The input voltages with frequency f_s are connected to the

machine stators, and the rotor circuits are opened to obtain desired output voltages with frequency f_r . The relationship between two frequencies is: $f_r = sf_s$, where s is the slip. By changing the slip, the output voltages have the desired frequency [31, 32]. This method, however, has a limited output frequency and too many losses. Another system that has been developed early is the cyclo-converter. This converter directly converts the input power to the desired output by utilizing the thyristors. However, this converter is limited because its output frequency is only one-third of the input due to line switching, the inductor filter size is large, and the output voltages have high distortions [33, 34].

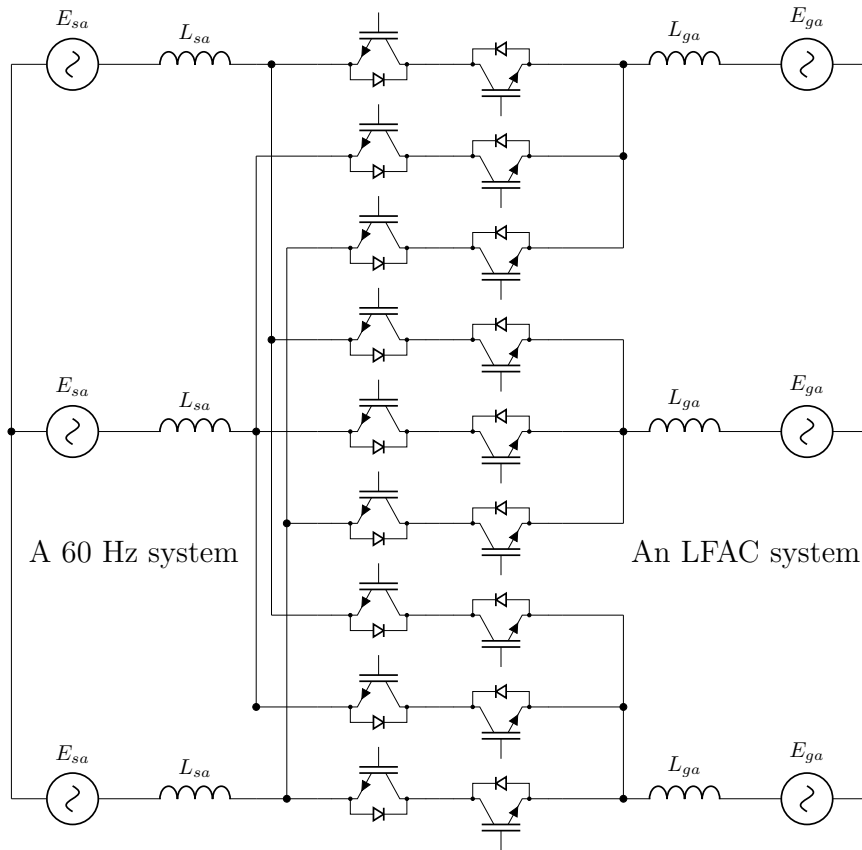


Figure 4.16: A typical matrix converter.

In recent research, the matrix converter, Fig. 4.16, has been focused thoroughly. This converter transforms frequencies directly by using switching semiconductor devices, i.e. IGBTs. It consists of bidirectional switches arranged in a matrix that allows any input frequency to be converted into the desired output frequency. The benefits of this converter is that it requires no bulky storage components such as capacitors [35, 36, 37, 38, 39].

4.2.2 Indirect Frequency Conversion Systems

The indirect conversion method converts frequencies in two stages. First, it rectifies an ac system into a dc system, and then inverts the dc system into the desired ac. Fig. 4.17 presents a typical ac-dc-ac power conversion system. It consists of two identical converters sharing the same dc-link capacitor. These two converters are cooperating to regulate the amount of power transferred back and forth. This conversion system is widely utilized due to its output quality and robustness [33, 38, 40]. This system is chosen for our work of interfacing 60 Hz and low frequency systems, and its mathematical model is presented as follows.

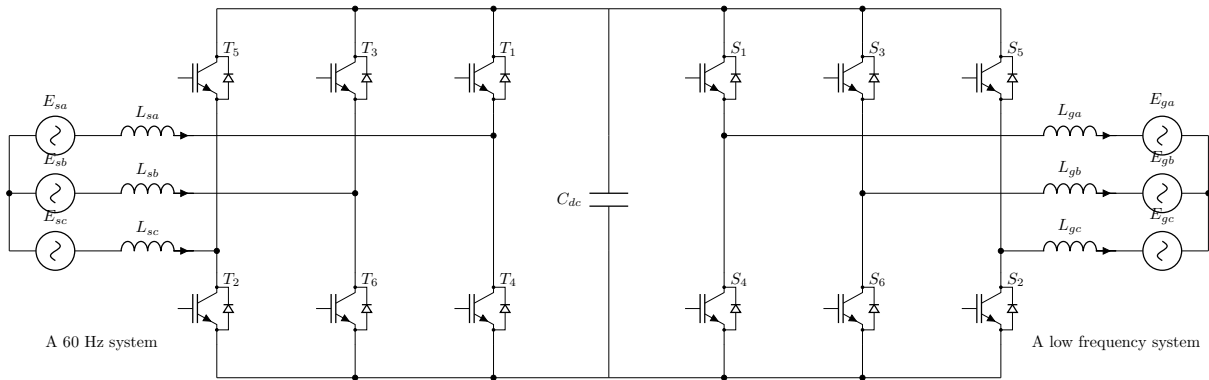


Figure 4.17: A typical back-to-back converter.

Mathematical model of power converter

Due to the identity of two converters, the mathematical model of only one converter is presented. The state variables and denoted symbols are clearly defined in Fig. 4.18.

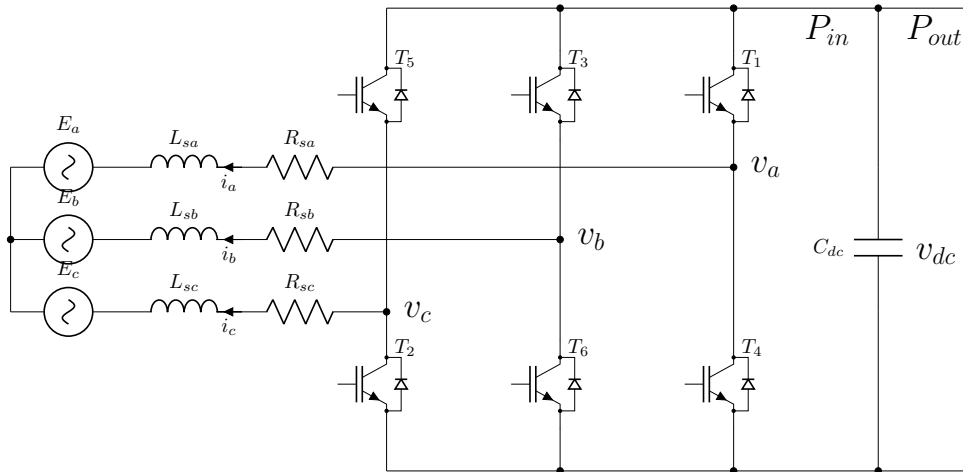


Figure 4.18: A PWM converter configuration.

In the stationary frame, the relationship between converter output voltage and current is given by

$$v_{abc} = R_s i_{abc} + L_s \frac{d}{dt} i_{abc} + e_{abc} \quad (4.12)$$

The capacitor dynamic is described by the amount of output different between P_{in} and P_{out} [41, 42]

$$\frac{d}{dt} \left(\frac{1}{2} C_{dc} V_{dc}^2 \right) = C_{dc} V_{dc} \frac{d}{dt} (V_{dc}) = P_{in} - P_{out} \quad (4.13)$$

In the synchronous frame, rotating with angular speed ω_e , the converter currents

after Park's transformation are

$$\begin{bmatrix} I_{de} \\ I_{qe} \end{bmatrix} = \begin{bmatrix} \cos \theta & \sin \theta \\ -\sin \theta & \cos \theta \end{bmatrix} \frac{2}{3} \begin{bmatrix} 1 & -1/2 & -1/2 \\ 0 & \sqrt{3}/2 & -\sqrt{3}/2 \end{bmatrix} \begin{bmatrix} i_a \\ i_b \\ i_c \end{bmatrix} \quad (4.14)$$

Similarly for the converter output voltages v_{abc} and the grid e_{abc} , (4.12) is then expressed bellow [42, 43, 44, 45]

$$V_{dqe} = R_s I_{dqe} + L_s \frac{d}{dt} I_{dqe} + j\omega_e L_s I_{dqe} + E_{dqe} \quad (4.15)$$

Note that in synchronous frame $E_{de} = 0$ and $E_{qe} = E$. The additional term $j\omega_e L_s I_{dqe}$ in (4.15) appears due to the coordinator change. The real power is then given by

$$P_{in} = e_{abc} \cdot i_{abc} = -(e_a i_a + e_b i_b + e_c i_c) = -\frac{3}{2}(E_{de} I_{de} + E_{qe} I_{qe}) \quad (4.16)$$

And the reactive power

$$Q_{in} = e_{abc} \times i_{abc} = -\frac{3}{2}(E_{qe} I_{de} - E_{de} I_{qe}) \quad (4.17)$$

The capacitor model is then [41, 46]

$$C_{dc} V_{dc} \frac{d}{dt}(V_{dc}) = P_{in} - P_{out} = -\frac{3}{2}(E_{de} I_{de} + E_{qe} I_{qe}) - P_{out} \quad (4.18)$$

In summary, from (4.15) and (4.18) the converter can be modeled by the following two equations

$$V_{dqe} = R_s I_{dqe} + L_s \frac{d}{dt} I_{dqe} + j\omega_e L_s I_{dqe} + E_{dqe} \quad (4.19)$$

$$V_{dc} = \int \left(\frac{(-3/2)(E_{de} I_{de} + E_{qe} I_{qe}) - P_{out}}{C_{dc} V_{dc}} \right) dt \quad (4.20)$$

4.3 Control Methods for a Power Converter

In order to operate stably, the power converter is driven by its controller system. The controller system typically consists of two control-loops: one for current and one for voltage of the dc-link capacitor. Conventionally, the proportional-integrator (PI) is employed in the controllers because of its infinite gain at dc (0 Hz) level. However, all the measurement signals are needed to transform into the rotating frame in order to decouple real and reactive power controlling. In recent research, the proportional-resonant (PR) shows its benefits in tracking sinusoidal waveforms directly and is able to regulate real and reactive power separately. This section reviews both control methods and then presents our work on improving the PR controller under distorted conditions.

4.3.1 PI Controllers

Fig. 4.19 presents the overall control system of a converter. It has the inner (current) loop and the outer (voltage) loop. The current controller directly controls the pulse-width modulation (PWM) signals while the voltage controller stabilizes the dc-link voltage. Both control loops utilize proportional (P) and integral (I) gains to track the references. The construction for each controller is presented in detail below.

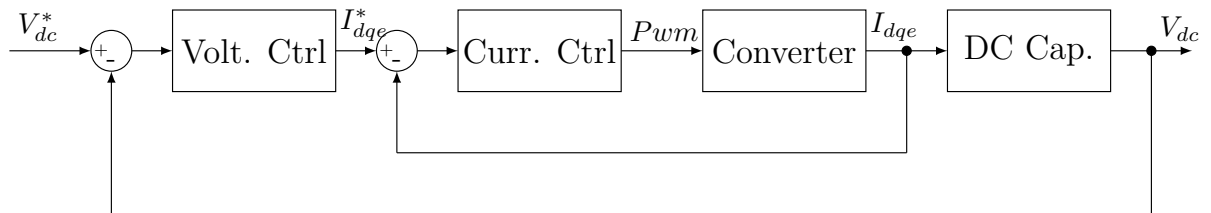


Figure 4.19: The overall control system.

Current controller

The converter output currents (i_a, i_b, i_c) are measured and transformed into i_{dqe} and i_{qe} in the synchronous frame. The reference currents i_{dqe}^* and i_{qe}^* come directly from the outputs of voltage controller, determined by real and reactive power demands. Fig. 4.20 presents the overall concept of the current loop using an PI [41, 46, 47]. The gain selection is based on the pole cancellation method and is described in detail in the following section.

From (4.19), by denoting $s = d/dt$ the converter output voltage and current relation is reconstructed in the dqe -synchronous frame as below

$$V_{dqe} = (R_s + sL_s)I_{dqe} + j\omega_e L_s I_{dqe} + E_{dqe} \quad (4.21)$$

or

$$I_{dqe} = \frac{1}{sL_s + R_s}(V_{dqe} - j\omega_e L_s I_{dqe} - E_{dqe}) \quad (4.22)$$

The current control calculates the reference voltage for the power converter with the feed-forward terms $j\omega_e L_s I_{dqe}$ and \hat{E}_{dqe} in order to have better dynamic performance.

$$V_{dqe}^* = (K_{pi} + \frac{K_{ii}}{s})(I_{dqe}^* - I_{dqe}) + (j\omega_e L_s I_{dqe} + \hat{E}_{dqe}) \quad (4.23)$$

Equate output voltages V_{dqe} and V_{dqe}^* from both (4.21) and (4.23),

$$(R_s + sL_s)I_{dqe} + j\omega_e L_s I_{dqe} + E_{dqe} = (K_{pi} + \frac{K_{ii}}{s})(I_{dqe}^* - I_{dqe}) + (j\omega_e L_s I_{dqe} + \hat{E}_{dqe}) \quad (4.24)$$

Manipulating the above equation with $E_{dqe} = \hat{E}_{dqe}$, the relation between reference and measured currents is given by [41, 46]

$$\frac{I_{dqe}}{I_{dqe}^*} = \frac{K_{pi}s + K_{ii}}{L_s s^2 + (R_s + K_{pi})s + K_{ii}} \quad (4.25)$$

By the pole-zero cancellation method with the current control bandwidth ω_{cc} : $K_{pi} = L_s\omega_{cc}$, $K_{ii} = R_s\omega_{cc}$, the current loop simply becomes a first-order system

$$\frac{I_{dqe}}{I_{dqe}^*} = \frac{\omega_{cc}}{s + \omega_{cc}} \quad (4.26)$$

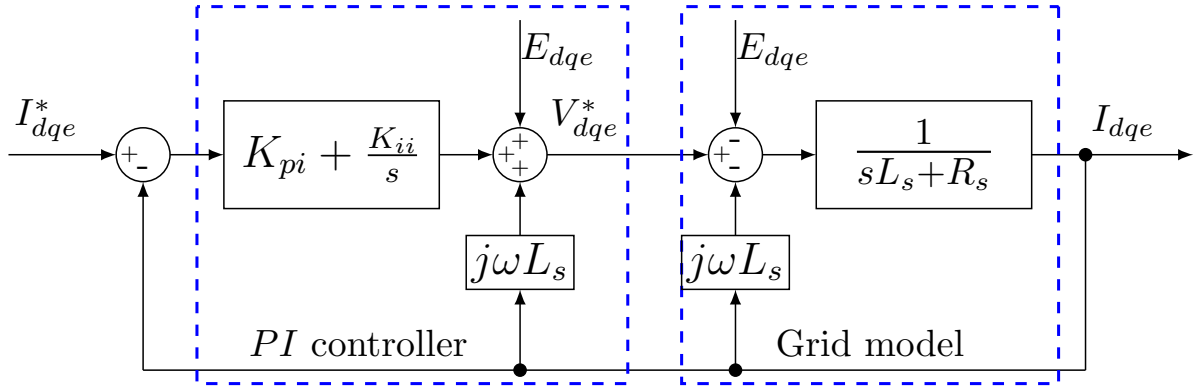


Figure 4.20: The current loop using PI controllers.

Voltage controller

The voltage controller keeps the dc-link voltage at a specific value and generates references for the current loops from real and reactive power demands. Supposing that the real power is regulated by I_{qe} and reactive power controlled by I_{de} , from the physical model in (4.18) the current I_{qe} is given by

$$C_{dc}V_{dc}\frac{d}{dt}(V_{dc}) = P_{in} - P_{out} = -\frac{3}{2}E_{qe}I_{qe} - P_{out} = -\frac{3}{2}EI_{qe} - P_{out} \quad (4.27)$$

or

$$I_{qe} = -\left(\frac{C_{dc}V_{dc}}{(3/2)E}\frac{d}{dt}(V_{dc}) + \frac{P_{out}}{(3/2)E}\right) \quad (4.28)$$

Similar to the current controller the voltage controller, as in Fig. 4.21, with the feed-forward term $\hat{P}_{out}/(3/2E)$ is

$$I_{qe}^* = -\left(\frac{K_{iv}}{s}(V_{dc}^* - V_{dc}) - K_{pv}V_{dc} + \frac{\hat{P}_{out}}{(3/2)E}\right) \quad (4.29)$$

In the steady-state, the measured current tracks the reference one $I_{qe} = I_{qe}^*$ and $\hat{P}_{out} = P_{out}$

$$\frac{V_{dc}}{V_{dc}^*} = \frac{K_{iv}}{s^2 \frac{C_{dc}V_{dc}}{(3/2)E} + K_{pv}s + K_{iv}} = \frac{\omega_n^2}{s^2 + 2\zeta\omega_n s + \omega_n^2} \quad (4.30)$$

The voltage controller gains are then [46]

$$K_{pv} = 4\zeta\omega_n \frac{C_{dc}V_{dc}^*}{3E}, \quad K_{iv} = 2\omega_n^2 \frac{C_{dc}V_{dc}^*}{3E} \quad (4.31)$$

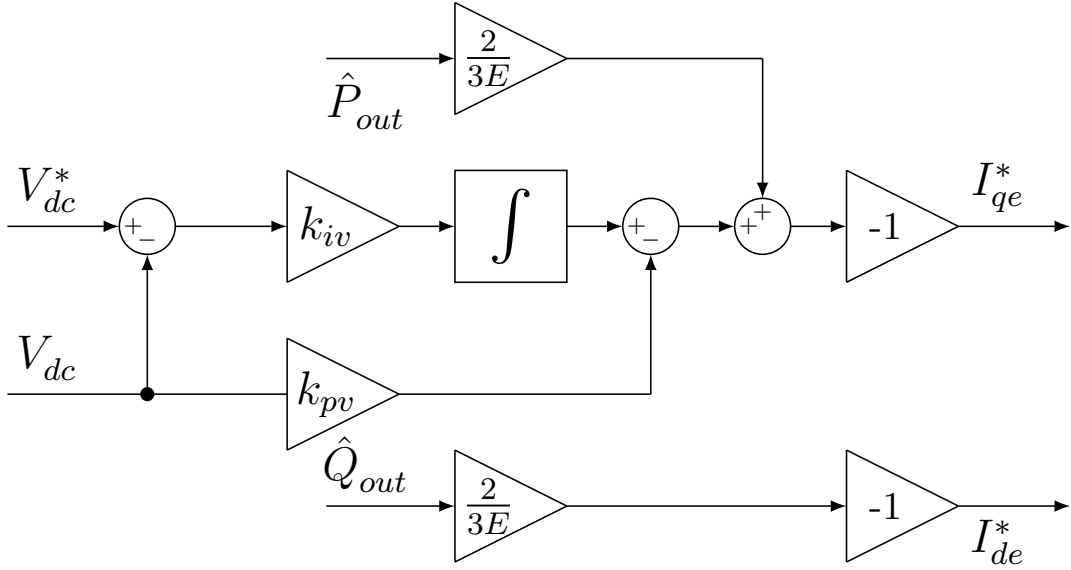


Figure 4.21: The voltage loop using an IP controller.

4.3.2 PR Controllers

The proportional-resonant *PR* controller directly tracks the sinusoidal reference current instead of transforming measured signals into the synchronous frame. The currents (i_a, i_b, i_c) after Clark's transformation are

$$\begin{bmatrix} I_\alpha \\ I_\beta \end{bmatrix} = \frac{2}{3} \begin{bmatrix} 1 & -1/2 & -1/2 \\ 0 & \sqrt{3}/2 & -\sqrt{3}/2 \end{bmatrix} \begin{bmatrix} i_a \\ i_b \\ i_c \end{bmatrix} \quad (4.32)$$

These currents (I_α, I_β) are sinusoidal and fed to the *PR* controllers to track their references. There is an equivalence between a *PI* controller and a *PR* controller which is clarified below.

From (4.25), the opened- and closed-loop transfer functions of current loop are derived

$$G_{sysc}(s) = \frac{G_{syso}(s)}{1 + G_{syso}(s)} = \frac{I_{dqe}}{I_{dqe}^*} = \frac{K_{pi}s + K_{ii}}{L_s s^2 + (R_s + K_{pi})s + K_{ii}} = \frac{\omega_{cc}}{s + \omega_{cc}} \quad (4.33)$$

The transfer function in the stationary frame is a frequency shift of that in the synchronous frame [48, 49, 50]

$$I_{\alpha\beta}(t) = e^{+j\omega_e t} I_{dqe}(t) \longleftrightarrow G_{\alpha\beta}(s) = G_{sysc}(s - j\omega_e) \quad (4.34)$$

If the transfer function of a *PI* controller in the synchronous frame is $G_{dq}(s) = K_{pi} + K_{ii}/s$, the equivalent *PR* for both positive- and negative-sequences is given by [51]

$$\begin{aligned} G_{\alpha\beta PR}(s) &= \frac{1}{2} [G_{\alpha\beta+}(s) + G_{\alpha\beta-}(s)] \\ &= \frac{1}{2} \begin{bmatrix} G_{dq+}(s) + G_{dq-}(s) & -jG_{dq+}(s) + jG_{dq-}(s) \\ jG_{dq+}(s) - jG_{dq-}(s) & G_{dq+}(s) + G_{dq-}(s) \end{bmatrix} \\ &= \begin{bmatrix} K_{pi} + \frac{K_{ii}s}{s^2 + \omega^2} & 0 \\ 0 & K_{pi} + \frac{K_{ii}s}{s^2 + \omega^2} \end{bmatrix} \end{aligned} \quad (4.35)$$

where $G_{dq+}(s) = G_{dq}(s - j\omega)$, $G_{dq-}(s) = G_{dq}(s + j\omega)$. The PR controller has infinite gain at both positive and negative frequencies, $s = \pm j\omega$. This simplifies the PR current loops for the converter as shown in Fig. 4.22. It is also worthwhile to mention that in the PR loop, there is no need to compensate the feed-forward grid voltage, $E_{\alpha\beta}$, in order to improve the controller dynamic performance [51, 52]. The voltage loop in this case is exactly the same as that of the previous PI case.

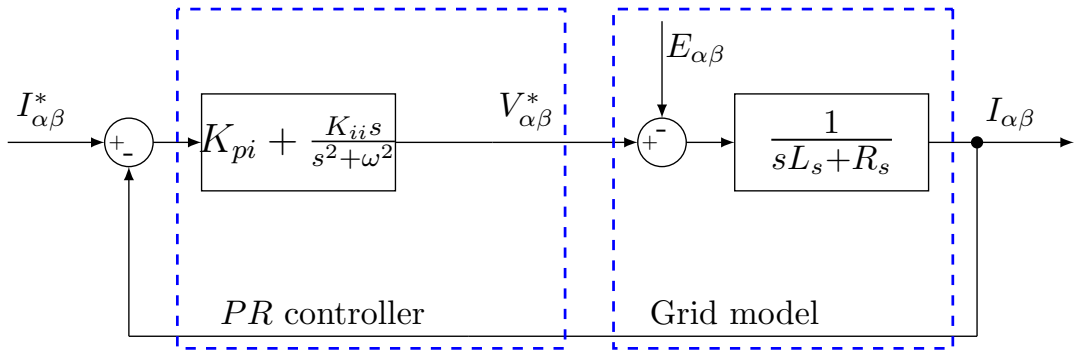


Figure 4.22: The current loop using a PR controller.

4.4 The Proposed PR Controller

As discussed earlier, a PR controller is superior to a PI controller due to its simplicity and capability of operating with positive/negative sequences in power converter applications. The PR behaves as a notch filter and only resonates with the input signal at its own frequency. In other words, the PR controller in the stationary frame has infinite gain at the resonant frequency or it is able to completely track a sinusoidal reference signal without any steady-state errors [48, 53]. However, the major drawback of a PR controller, which can be seen from (4.35), is that its performance relies directly on the

resonant frequency. The integral part uses the frequency information to oscillate with the reference signal. When the power grid has a small frequency variation, the *PR* controller does not perform properly, and the output signal cannot align with its reference signal.

One solution to improve the *PR* controller performance under frequency deviations has been proposed in [54]. Instead of transforming only the *PI* controller in the *dq* synchronous frame into the *PR* controller in the $\alpha\beta$ stationary frame, the entire closed-loop transfer function is rotated to the stationary frame. It is interesting to discover that the two additional cross-coupling terms, called *XControl* and *XFeedback*, appear in the controller of the closed-loop system [54, 55]. Further investigation reveals that the feed-forward branches $j\omega L$ in the synchronous frame have major impacts on the system sensitivity in the frequency domain. Several *PR*-based controllers are then proposed, and they show significant improvements compared with the conventional *PR* method in terms of frequency stabilizing [45, 56, 57, 58, 59, 60]. One challenge, however, to the previous research is that the proposed system is only active within the positive frequency range, and it loses its tracking capability to the negative frequency reference. In addition, the controllers in each loop are dependent and need to communicate to each other for frequency robustness [61, 62, 63, 64, 65, 66].

In this section, the previous *PR*-based controllers are reviewed and then the proposed method is introduced. The new controller is equivalent to the conventional *PR* method and able to operate at both signs of frequency. More importantly, the proposed method is robust and capable of tracking reference signal when the system frequency deviates from its nominal value. Another benefit is dependency reductions between control loops. There should be no current coupling terms between the α -frame and β -frame.

4.4.1 The *PR*-based Controller Review

The previous *PR*-based methods rely on the equivalences of two closed-loop systems in stationary and rotating coordinators. Depending on the coupling terms, (*XControl* and *XFeedback*, named as in [54]), the controller configurations are derived. There are four types of *PR* controllers (*PR*, *PRXF*, *PRXC*, and *PRX2*), Fig. 4.23, and their transfer functions are listed below

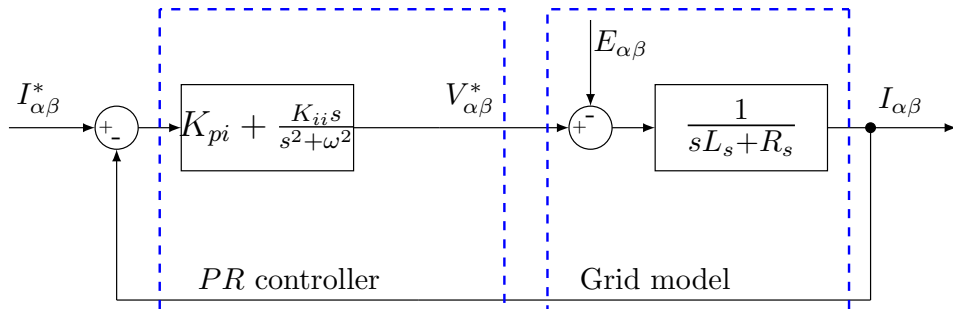
$$G_{PR}(s) = \frac{K_{pi}(s^2 + \omega_e^2) + K_{ii}s}{[sL_s + K_{pi} + R_s](s^2 + \omega_e^2) + K_{ii}s} \quad (4.36)$$

$$G_{PRXF}(s) = \frac{K_{pi}(s^2 + \omega_e^2) + K_{ii}s}{[L_s(s - j\omega_e) + K_{pi} + R_s](s^2 + \omega_e^2) + K_{ii}s} \quad (4.37)$$

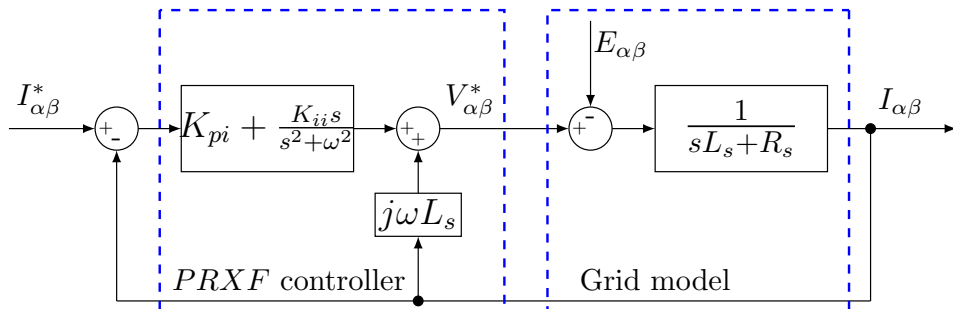
$$G_{PRXC}(s) = \frac{K_{pi}(s - j\omega_e) + K_{ii}}{[sL_s + R_s + K_{pi}](s - j\omega_e) + K_{ii}} \quad (4.38)$$

$$G_{PRX2}(s) = \frac{K_{pi}(s - j\omega_e) + K_{ii}}{[L_s(s - j\omega_e) + R_s + K_{pi}](s - j\omega_e) + K_{ii}} \quad (4.39)$$

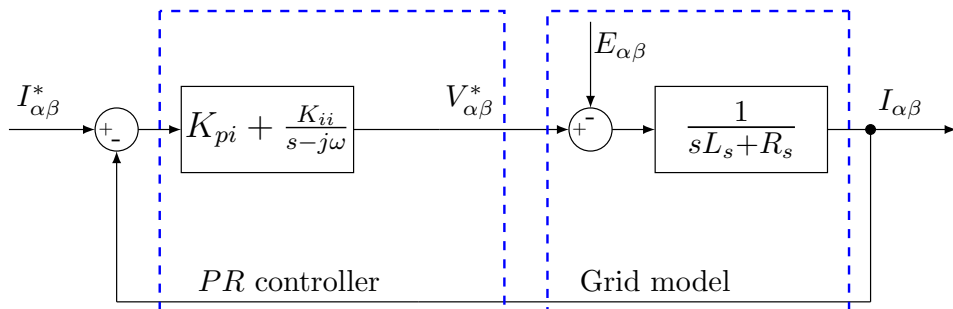
It is worthwhile to mention that the two *PRXC* and *PRX2* controllers are only able to work with positive-sequence since they particularly have infinitive gain at $s = j\omega$. The *PR* and *PRXF* controllers, on the other hand, have infinitive gains at both signs of frequency. The Bode plots of four configurations are shown in Fig. 4.24 in order to understand these controllers under frequency deviations. As can be observed from these figures, the open-loop systems (top-blue) all have infinite gains at the resonant frequency, ω_e . The magnitudes of closed-loop systems (bottom-red) are all zero at ω_e . However, there are stiff changes at $\omega_e = 60\text{Hz}$ in the conventional *PR* and *PRXC* controllers. These changes are smaller around the resonant frequency neighborhood in the *PRXF* and *PRX2* controllers due to the *XFeedback* terms. However, note again that two of these configurations are only active with the positive frequency or positive-sequence.



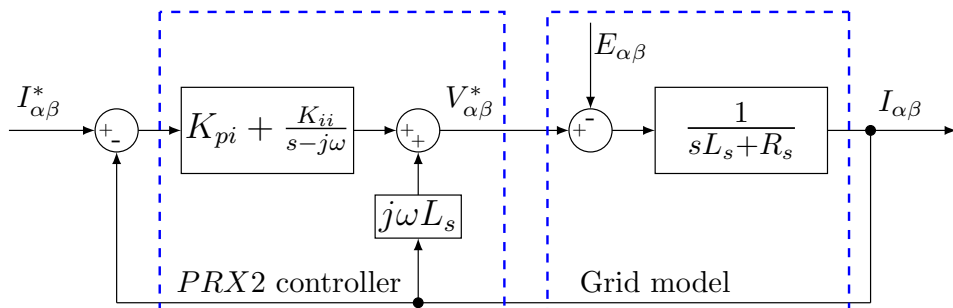
(a)



(b)

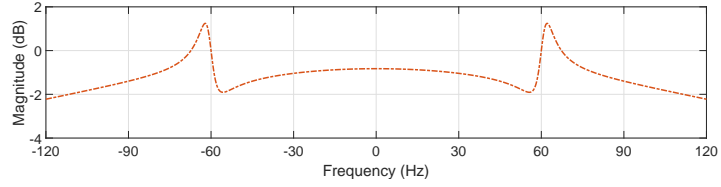
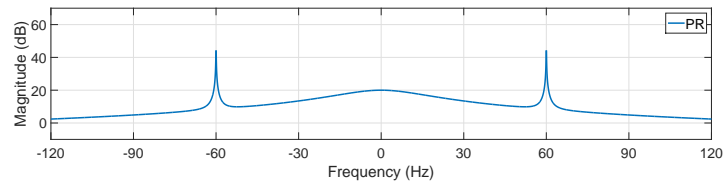


(c)

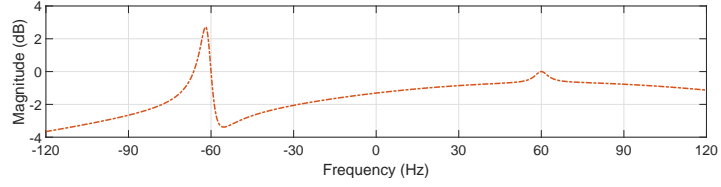
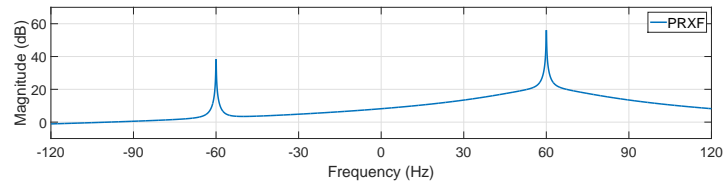


(d)

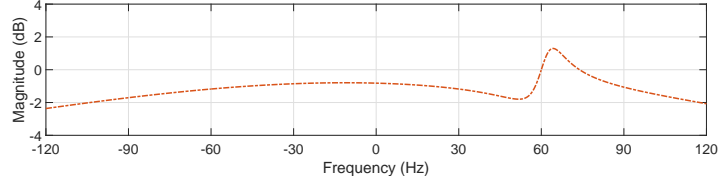
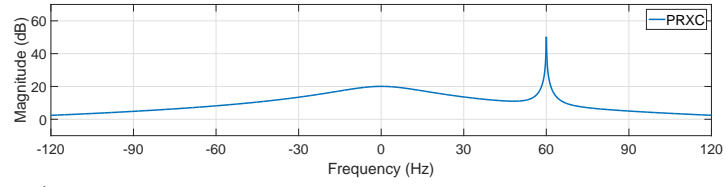
Figure 4.23: The PR-based controllers: a) *PR*, b) *PRXF*, c) *PRXC*, and d) *PRX2* configurations.



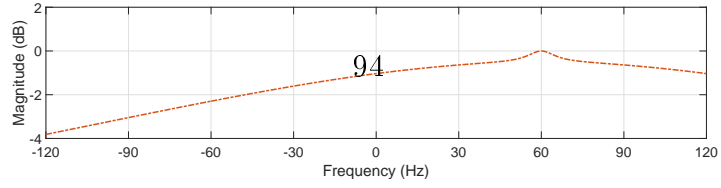
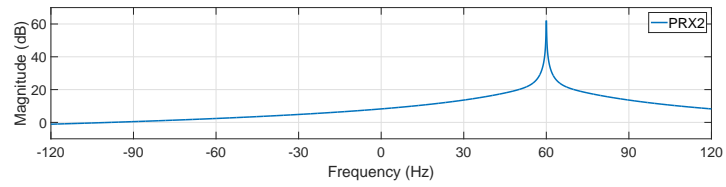
(a)



(b)



(c)



(d)

Figure 4.24: Bode plots of opened-loop (top-blue) and closed-loop (bottom-red): a) PR , b) $PRXF$, c) $PRXC$, and d) $PRX2$.

In order to more deeply understand the robustness of these configurations, the sensitivity of each function with respect to frequency is derived. For example, the sensitivity functions of (4.38) and (4.39) are below

$$\frac{\partial G_{PRXC}}{\partial s} = \frac{-L_s K_{pi}(s - j\omega_e)^2 - 2L_s K_{ii}(s - j\omega_e) - K_{ii}(j\omega_e L_s + R_s)}{([sL_s + R_s + K_{pi}](s - j\omega_e) + K_{ii})^2} \quad (4.40)$$

$$\frac{\partial G_{PRX2}}{\partial s} = \frac{-L_s K_{pi}(s - j\omega_e)^2 - 2L_s K_{ii}(s - j\omega_e) - K_{ii}R_s}{([L_s(s - j\omega_e) + R_s + K_{pi}](s - j\omega_e) + K_{ii})^2} \quad (4.41)$$

The sensitivities of four configurations with respect to frequency are presented in Fig. 4.25 in detail. At the resonant frequency $\omega_e = 60\text{Hz}$, the magnitudes of sensitivity functions are smaller in *XFeedback* controllers (dashed-line) compared to *PR* and *PRXC* ones. The G_{PRX2} has the least variation. This means the *PRX2* controller is less sensitive to frequency variations, and thus is preferred for the resonant control.

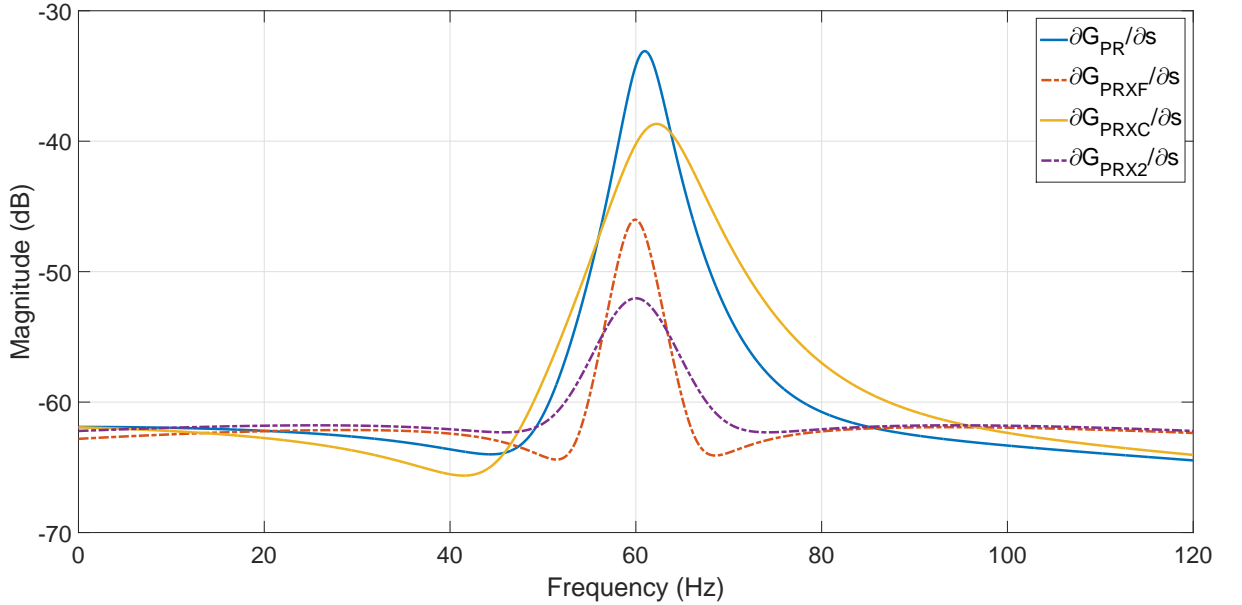


Figure 4.25: Sensitivities versus frequency in the four controller configurations.

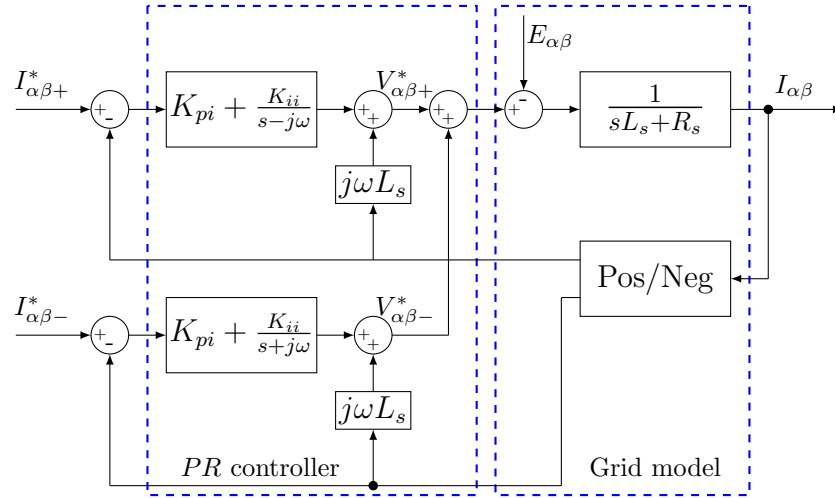
4.4.2 The proposed controller for frequency stability

The proposed controller is not only robust to frequency variations but also is able to operate with positive-/negative-sequence components. Assume that a configuration, which is able to operate with positive and negative frequencies at the same time as the conventional *PR*, is obtained. This means the controller has infinite gains at both signs of resonant frequency with opened-loop, and has small gain variations around zero in closed-loop form. Our first approach is to find this transfer function $G_o(s) = N_o(s)/D_o(s)$, which satisfies two necessary conditions: 1) having infinite gains at $s = \pm j\omega$, and 2) achieving maximum/minimum at $s = \pm j\omega$: $\partial G_c(s = \pm j\omega)/\partial s = 0$. The transfer function is given

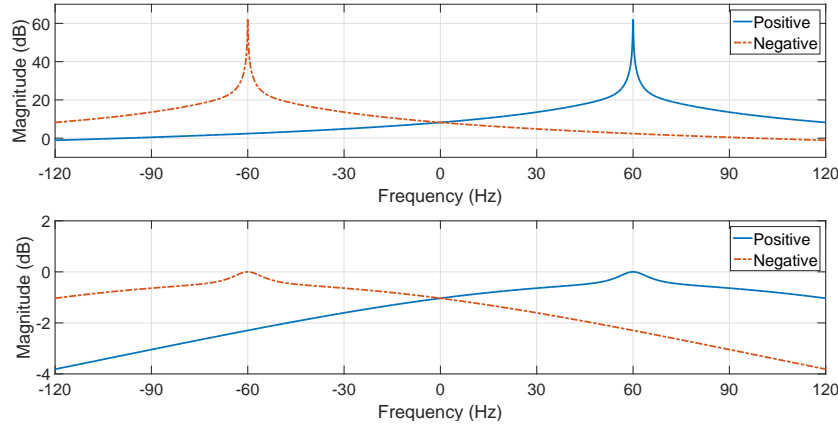
$$G_o(s) = \frac{N_o(s)}{D_o(s)} \implies G_c(s) = \frac{N_o(s)}{N_o(s) + D_o(s)(sL_s + R_s)} \quad (4.42)$$

The first condition means that at the resonant frequencies $D_o(\pm j\omega)$ equals 0, and the second criteria implies that the derivative of $D_o(s)$ is zero at $s = \pm j\omega$: $D'_o(\pm j\omega) = 0$. The control denominator thus has the form $D_o(s) = (s^2 + \omega^2)^k$ with $k \geq 2$. This results in a complex and high-order controller system, and is not applicable in practice.

It is worthwhile to recall the fact that the coupling term $j\omega L_s$ in the *PRX2* controller has a major contribution to frequency stabilizing. If the controller is constructed based on *PRX2*, it needs separate loops for positive- and negative-sequences as shown in Fig. 4.26(a). The controller has an infinite gain at both signs of frequency. More importantly, the system is robust to frequency variations as in the Bode plot Fig. 4.26(b). However, this control system is complicated to implement in converters. In each stage, there are two different controllers for I_α and I_β , and this configuration requires four stationary controllers.



(a)



(b)

Figure 4.26: a) The concept controller with two *PRX2*, and b) its Bode plot.

Given the fact that currents in the stationary frame are sine/cosine functions, and at the steady-state they are equal in magnitude. The coupling terms for a current controller in Fig. 4.26(a) thus can be replaced by their derivatives. The modified controllers in $\alpha\beta$ frame are presented in Fig. 4.27. The measured current is fed back directly to its

own control loop, and there is no need to split the current into positive- and negative-sequence components. The Bode plot, Fig. 4.27(b), shows that the controller is able to operate with both signs of frequency and is also stable to frequency variations. This configuration is much simpler in comparison to that in Fig. 4.26(a) because it only requires two controllers to regulate $I_{\alpha\beta}$.

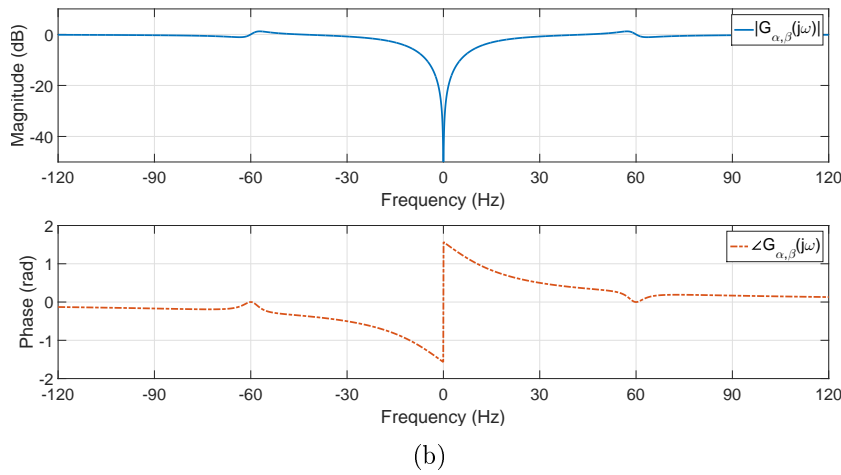
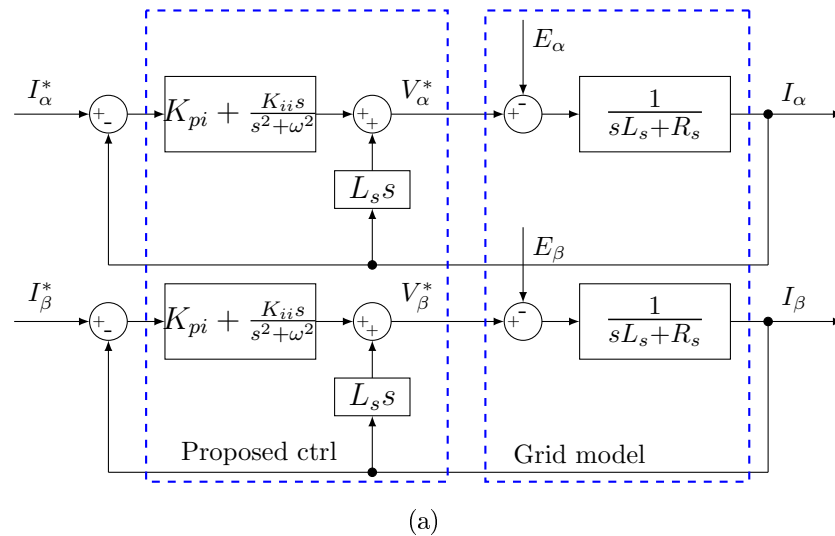


Figure 4.27: a) The proposed controller configuration, and b) its closed-loop Bode plot.

4.4.3 Simulation Results

The proposed controller configuration is first verified by simulation results. A power converter is modeled, and the proposed configuration is implemented in the control system. The power converter is assumed first operating at the steady-state and injecting a 50 A peak current into the grid. At simulation time $t = 1(sec)$, the converter also needs to add a negative sequence current with the peak value of 10 A. Moreover, the frequency is increased from 60 Hz to 61 Hz or the frequency deviation is 1 Hz. The controller gains are $K_{pi} = 1$, $K_{ii} = 80$, and the grid side parameters are $L_s = 2$ mH, $R_s = 0.1 \Omega$. The reference current waveforms in the time-domain and $\alpha\beta$ stationary frame are shown in Fig. 4.28. Before changes, the current waveforms are balanced, and the references I_α^* and I_β^* are sinusoidal with 50 A in magnitude. After $t = 1$ second, due to the negative-sequence, the reference signals are unbalanced. The stationary current references becomes different in magnitude with 60 A in I_α^* and 40 A in I_β^* .

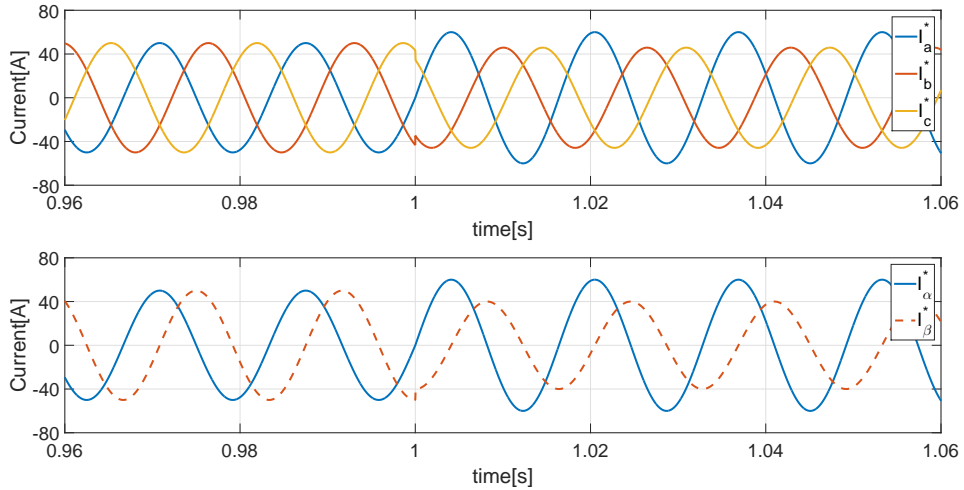
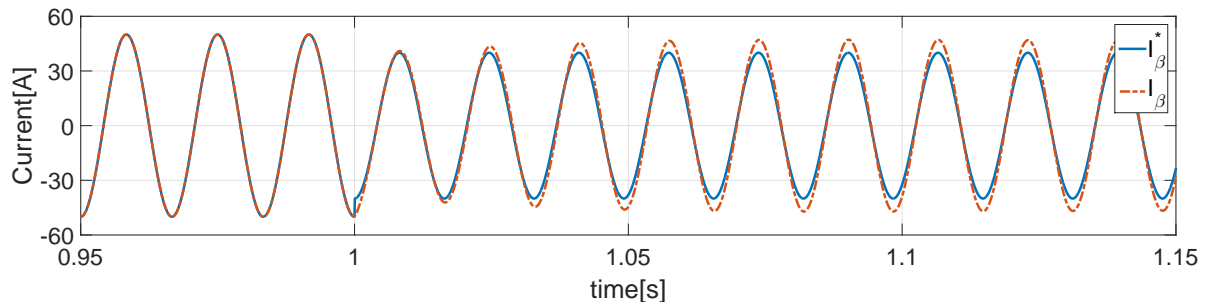
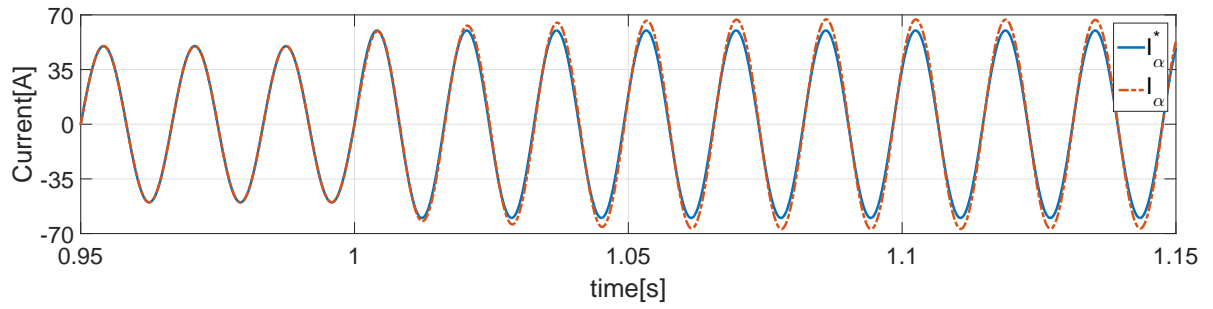


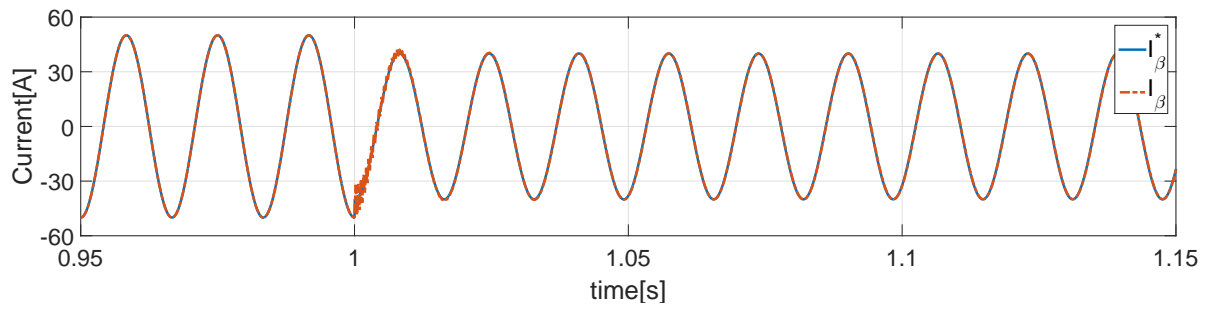
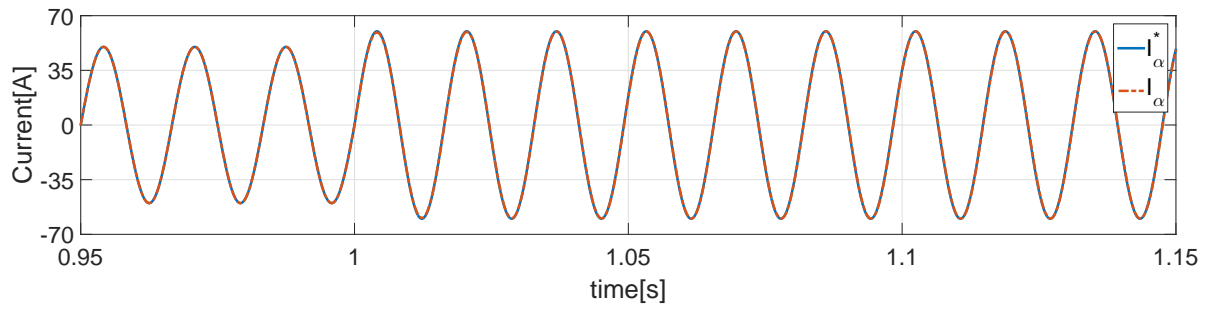
Figure 4.28: The control reference currents in time-domain (top) and $\alpha\beta$ frame (bottom).

The responses of the conventional PR and proposed methods are presented in Fig. 4.29. The performances in the two controllers are the same if the grid frequency is not varied. Two controllers are able to track sinusoidal reference signals without any steady-state errors. However, with 1 Hz variation at simulation time $t = 1$ second, the conventional PR method cannot completely track the reference signals I_α^* and I_β^* as shown in Fig. 4.29(a). There are steady-state errors in this case or, in other word, the conventional PR configuration is sensitive to frequency variations. The proposed method, on the other hand, is able to follow the control signals without any noticeable errors as shown in Fig. 4.29(b). It is also worthwhile to notice that the proposed controller responds quickly to track the references. In other words, the introduced control configuration performs better under frequency variations.

In summary, the proposed controller based on the PR configuration has improved the control system capability of a power converter under frequency variation conditions. The new controller has not only extended the frequency range of the previous work to the negative value but also significantly reduced the dependences between controllers in the two stationary frames (α -frame and β -frame). The introduced controller is equivalent to and preserves all advantages from the conventional PR method. The simulation results have verified significant improvements from the proposed controller compared with the conventional PR controller in terms of frequency variations. The new method shows no noticeable steady-state error when tracking a reference under frequency deviations. The constructions of the proposed controller are also much simpler. The simulation results of a power system that includes a 60 Hz and a low frequency systems are presented in the next section with all implementations of grid synchronization, converters, and its control.



(a)



(b)

Figure 4.29: Current waveforms on the stationary frame in the: a) conventional *PR* controller, and b) proposed *PR* controller.

4.5 Simulation Results of a Multi-frequency Power Systems

This section presents the simulation results of a 60 Hz system interfacing with a low frequency system. In order to save simulation time and for better presentation, the low frequency is fixed at 30 Hz. The two systems, as in Fig. 4.1, exchange 100 MW at a voltage level of 345 kV through a power converter. The grid synchronization and control systems are implemented in the converter, and the results are presented as below.

Grid synchronization waveforms

The grid synchronization system detects the phase angle of voltage at sides that the converter interfaces with. Fig. 4.30 accurately presents the angles of a 60 Hz system (top) and a 30 Hz system (bottom). Note that the angle waveform has the same frequency as the voltage waveform.

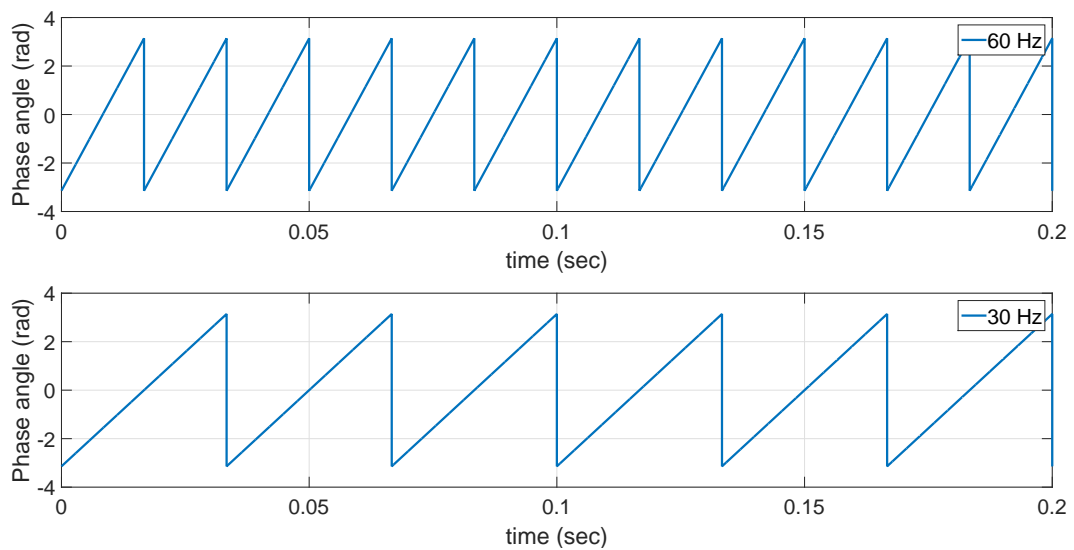


Figure 4.30: Phase angles from the synchronization system: 60 Hz (top) and 30 Hz (bottom).

Power converter waveforms

The power converter output waveforms include the voltage on the DC-link capacitor and the currents in both sides. Fig. 4.31 shows the DC-link voltage waveform with its transient. It can see that the capacitor voltage is stable at the reference voltage, 20 kV, after an overshoot and a short transient duration less than 0.05 seconds because the voltage control loop is a second-order system as in (4.30). The current waveforms of phase *A* in 60 Hz side and 30 Hz side are presented in Fig. 4.32 with their references. As can be seen, the converter output currents track their reference ones by utilizing the proportional-resonant controllers. The currents are sinusoidal waveforms with small ripples caused by the switching of semi-conductor devices.

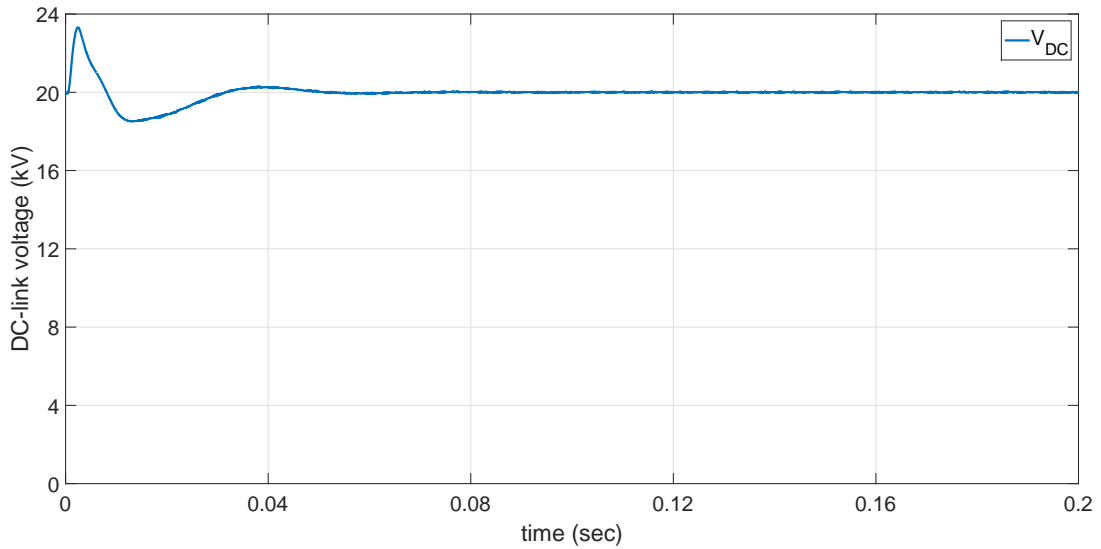
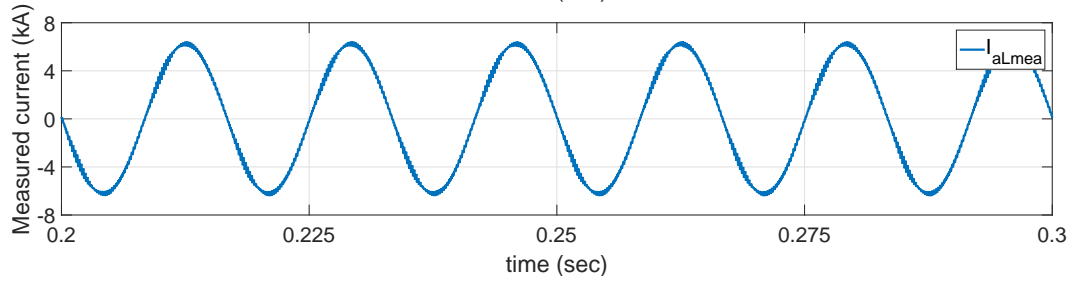
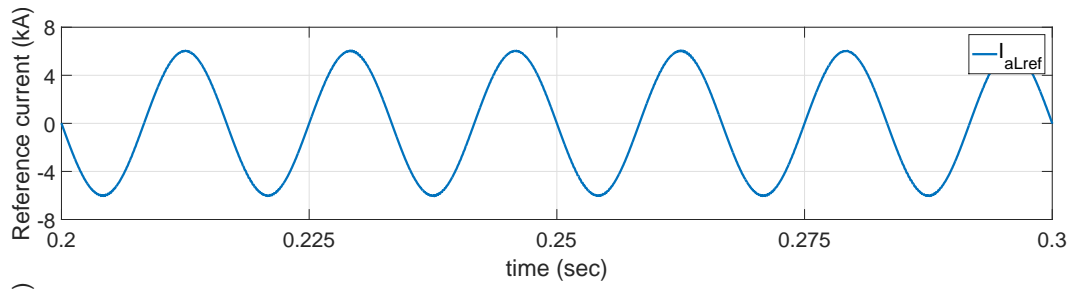
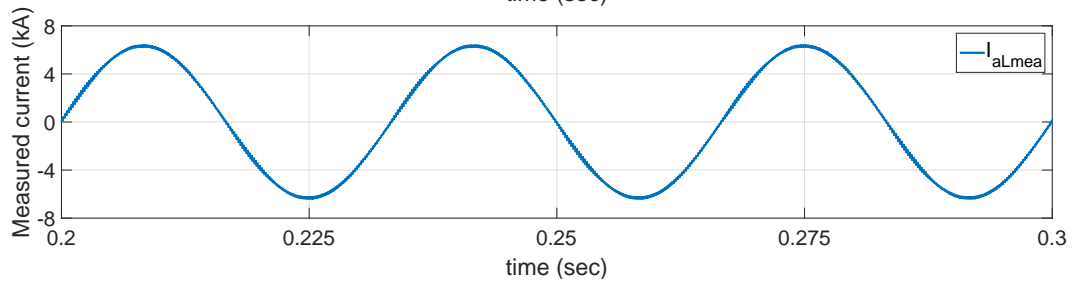
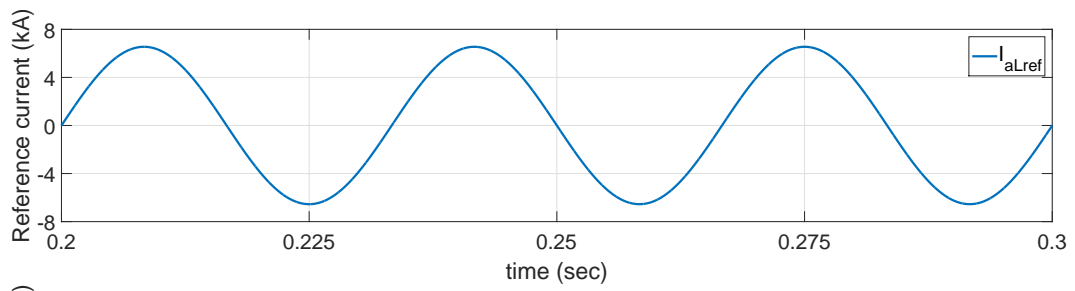


Figure 4.31: The DC-link voltage waveform.



(a)



(b)

Figure 4.32: Converter output currents in: a) 60 Hz side, and b) 30 Hz side.

The transmission waveforms

Fig. 4.33 presents the voltage and current waveforms on both systems of transmission level, 345 kV. The currents are clean and sinusoidal at desired frequencies.

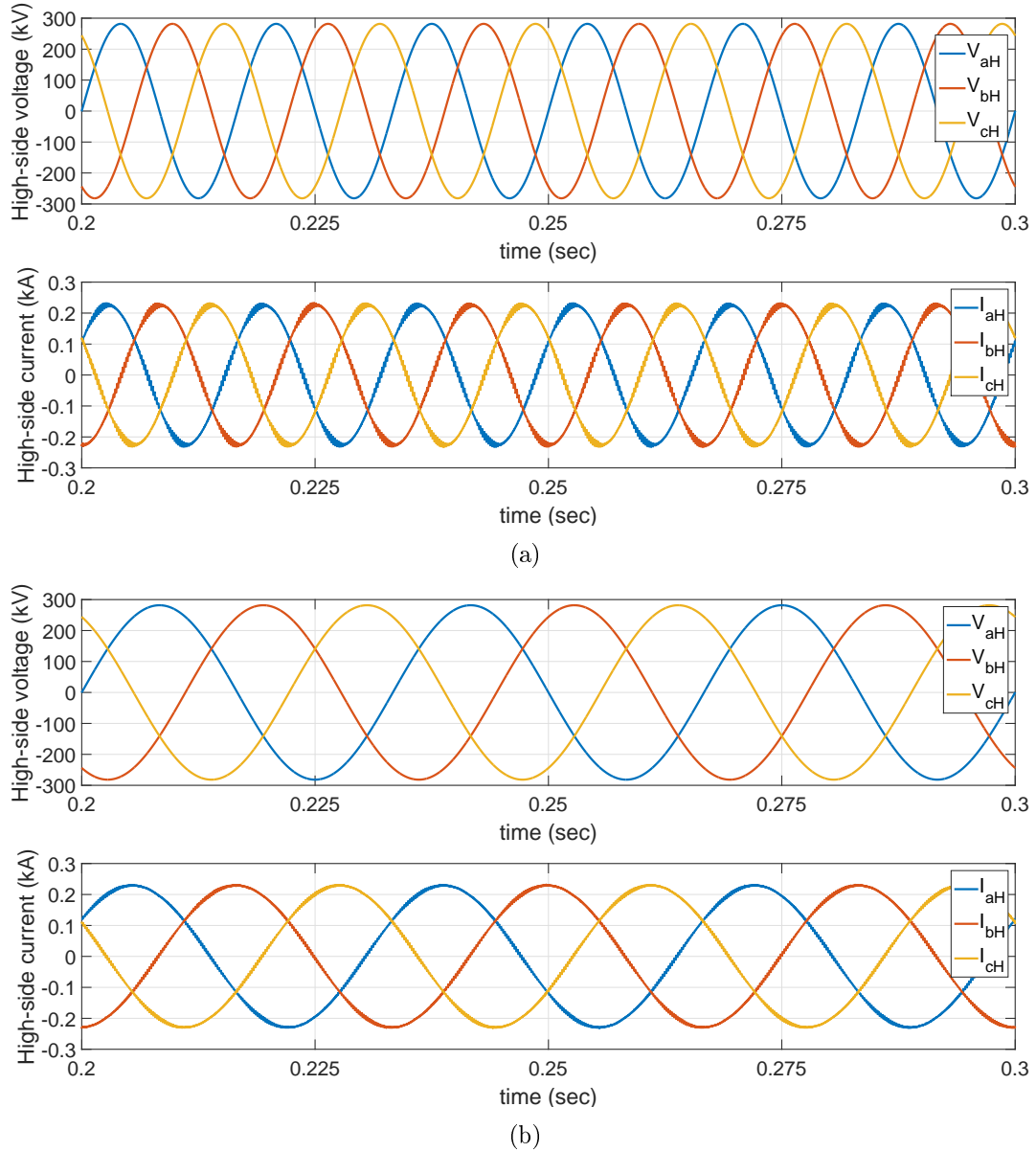


Figure 4.33: Voltages and currents on transmission level: a) 60 Hz system, and b) 30 Hz system.

Chapter 5

System Protection for LFAC Transmission

This chapter presents our investigations on a low frequency ac transmission system in terms of protection perspectives. One obvious challenge that a low frequency power transmission line faces is the high fault currents caused by the reduction of system impedance at low frequency operations. It is also obvious that a low frequency system has a longer wavelength compared to the conventional 60 Hz system, and it will take a longer time for an LFAC transmission system to clear faults. Assuming that both a 60 Hz system and an LFAC at 10 Hz system are able to clear fault at the zero-crossing of current, in a 60 Hz system the fault can stay up to 3 cycles before the mechanical circuit breakers are opened. This means the power system can withstand a fault in a duration $t = 3/60 = 0.05$ seconds. However, if a fault is allowed to stay up to 3 cycles in a 10 Hz system as same as in the 60 Hz one, the duration that the power system experiences a fault is $t = 3/10 = 0.3$ seconds. This amount of time is quite long and the equipment on the power system is damaged by the dissipated heat, $E = I^2Rt$. This challenge thus requires for a fast and robust method to detect a fault once it happens to the transmission system. This chapter first investigates the protection in a low frequency system to see the benefits in terms of critical clearing time, distance protection, and relay loadability. Next, a fault clearing mechanism for a power transmission line that operates at a low frequency is developed based on the second-order generalized-integrator grid synchronization tech-

nique. The protection system is designed in such a manner that it is capable of detecting faults quickly and accurately.

5.1 System Protection Analysis for LFAC Transmission

This section investigates the critical clearing time and distance protection in a power system under different frequencies. Due to operation at a low frequency, the transmission line reactance is reduced and thus creates a drawback in LFAC systems when faults occur. The fault currents are expected to be much higher than in a 60 Hz system. In addition, an LFAC system has a longer current wavelength and requires the protection system perform quickly to clear faults. The analysis, however, shows that the critical clearing time (in seconds) is longer for an LFAC system compared to conventional 60 Hz systems. This means the fault can stay longer in an LFAC before the system loses its stability. Moreover, this section also examines distance protection in LFAC systems and discovers that an LFAC system has a larger separation between distance protection zone characteristic impedance and load impedance in comparison to a 60 Hz system. This result would allow for more certainty in setting the load encroachment blocking function in modern relays.

5.1.1 Critical Fault Clearing Time

The critical clearing time is understood as the maximum time during which a disturbance can be applied without the system losing its stability [11]. This section provides an analysis of the critical clearing time for a power system at different frequencies when a fault occurs. The equal-area technique is utilized to find the critical clearing angle.

The analysis assumes $P_{max} = 1.0$ pu maximum power and that a fault occurs when the power is P_m , as shown in Fig. 5.1. From this figure, the area A_1 is given by [10, 67]

$$A_1 = \int_{\delta_0}^{\delta_{cr}} P_m d\delta = P_m(\delta_{cr} - \delta_0) \quad (5.1)$$

Similarly, the area A_2 is found from $x = \delta_{cr}$, $y_1 = P_m$ and $y_2 = \sin(x)$ curves in Fig. 5.1

$$A_2 = P_{max}(\cos \delta_{cr} - \cos \delta_{max}) - P_m(\delta_{max} - \delta_{cr}) \quad (5.2)$$

From (5.1) and (5.2), the critical clearing angle δ_{cr} is given by

$$\delta_{cr} = \cos^{-1}[(\pi - 2\delta_0) \sin \delta_0 - \cos \delta_0] \quad (5.3)$$

The critical clearing time is calculated as [10, 67]

$$t_{cr} = \sqrt{\frac{4H(\delta_{cr} - \delta_0)}{\omega_s P_m}} \quad (5.4)$$

where ω_s is angular frequency and H is inertia.

A fault in the system with $P_m = 0.8$ pu and $H = 5$ (MJ/MVA) is used to illustrate the critical clearing angle and time at different frequencies. The results are summarized in Table 5.1. As the frequency is reduced, the power capability is improved, and thus the critical clearing angle is significantly increased for a fixed value of P_m . For example, the clearing angle at 60 Hz is $\delta_{cr} = 64.56^\circ$ and is almost double at 10 Hz, $\delta_{cr} = 127.43^\circ$. At 5 Hz, this clearing angle is equal to $\delta_{cr} = 142.87^\circ$. Because the critical clearing angle is increased, the critical clearing time is also increased. At 60 Hz, the relay needs to perform quickly to clear the fault in 115 ms. The critical clearing time is increased in low frequency operations since it is 912 ms for 10 Hz and 1390 ms for 5 Hz. This means

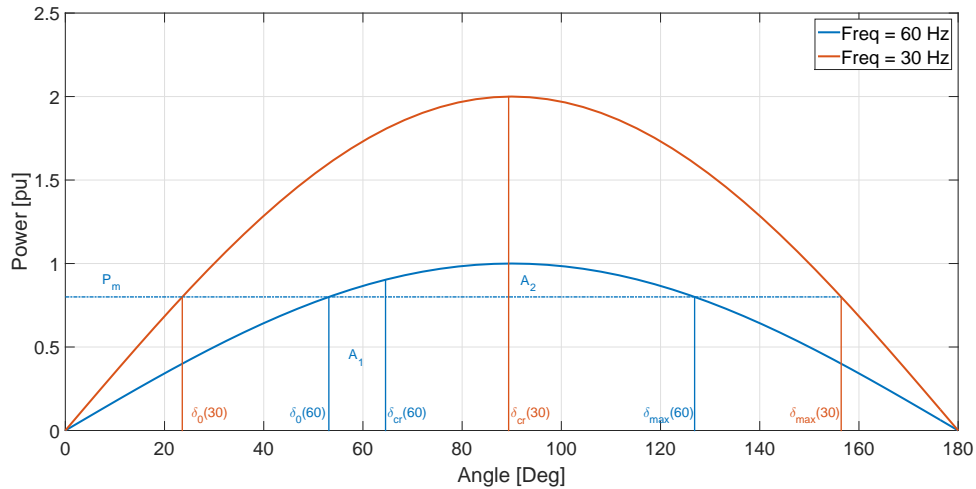


Figure 5.1: Critical clearing time calculation.

the LFAC system has more time to clear the fault before it loses its stability. However, it is observed that the critical clearing time in cycles does not increase monotonically with reduced frequency. This suggests a frequency between 5 Hz and 30 Hz would provide the best trade-off between clearing time in seconds and zero crossings.

Table 5.1: Critical clearing angle and clearing time.

Freq.	60 Hz	30 Hz	10 Hz	5 Hz
$\delta_0(deg)$	53.13°	23.58°	7.66°	3.82°
$\delta_{cr}(deg)$	64.56°	89.38°	127.43°	142.87°
$t_{cr}(s)$	0.1150	0.3903	0.9120	1.3896
Cycle(s)	6.90	11.71	9.12	6.95

5.1.2 Distance Protection

In order to examine the impact of low frequency transmission and reduced line impedance on stepped-distance protection using three protection zones, a three-bus system, as shown in Fig. 5.2, is used for the theoretical analysis. The transmission line

length is 100 miles with parameters per mile at 60 Hz: $r = 0.0103 \Omega$, $x_L = 0.2481 \Omega$, and $x_C = 2.3574 \times 10^{-6} \Omega$. The relay at A considered in this analysis protects transmission line 1 from the sending-end S to the receiving-end R . In order to see the impact of frequency on distance protection, the two short transmission lines are simplified as: $Z_1 = Z_2 = 2R + j2X$.

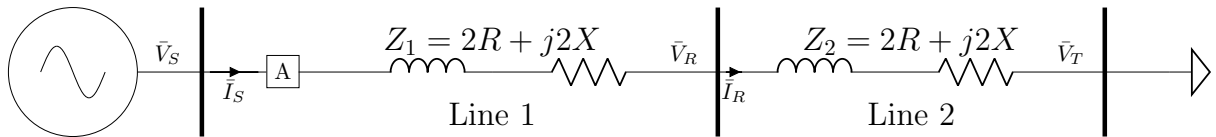


Figure 5.2: Single-line diagram of three-bus system used in protection studies.

Impact on load encroachment

Load encroachment can cause unintended operations in distance relays when heavy loading causes the apparent impedance to enter a protection zone. This section therefore investigates how the separation between apparent load impedance and line impedance in the complex impedance plane changes at different frequencies. Results show that this separation is increased at lower frequencies, suggesting that load encroachment failures are less likely to occur. In order to have a common quantity for comparison, the shortest distance is first defined. The shortest distance is the line from the load to the closest point in each zone circle. In distance relaying protection, there are three protective zones. Zone 1 is the underreaching zone where the relays cover 85% of the impedance of the protected line. Zone 2 is the overreaching zone where the relays cover 120% of the impedance of the protected line. And zone 3 is the remote backup protection zone where the relays cover 210% of the impedance of the protected line [11]. Fig. 5.3 shows the shortest distance to

each zone from the load. This distance is the segment in the line from the load point to the circle center. The shortest distances at different frequencies are then compared to see the benefits of low frequency operations in terms of distance protection.

Assuming the receiving-end terminal voltage is $V_R = 1.0$ pu and supplies to load a power $S = P + jQ$. The current is then given by $I_S = (S/V_R)^* = P - jQ$. The sending-end voltage is

$$V_s = V_R + I_S Z = 1 + (P - jQ)(2\lambda R + j2\lambda X) \quad (5.5)$$

The impedance seen from the distance protection for relays is calculated as

$$\begin{aligned} Z_s &= \frac{V_s}{I_S} = \frac{1 + (P - jQ)(2\lambda R + j2\lambda X)}{(P - jQ)} \\ &= (2\lambda R + \frac{P}{P^2 + Q^2}) + j(2\lambda X + \frac{Q}{P^2 + Q^2}) \end{aligned} \quad (5.6)$$

where $\lambda = 0.85, 1.20, 2.10$ is the percentage of the protected line impedance corresponding to zone 1, zone 2, and zone 3.

Denoting $u = P/(P^2 + Q^2)$ and $v = Q/(P^2 + Q^2)$, the shortest distance from the load to a zone can be calculated as a function of reactance or frequency

$$D_{Z_k}(X) = \sqrt{(\lambda R + u)^2 + (\lambda X + v)^2} - \sqrt{(\lambda R)^2 + (\lambda X)^2} \quad (5.7)$$

To see the evolution of $D_{Z_k}(X)$ with reactance or frequency, let us examine its derivative:

$$\frac{\partial D_{Z_k}(X)}{\partial X} = \frac{\lambda(\lambda X + v)}{\sqrt{(\lambda R + u)^2 + (\lambda X + v)^2}} - \frac{\lambda^2 X}{\sqrt{(\lambda R)^2 + (\lambda X)^2}} \quad (5.8)$$

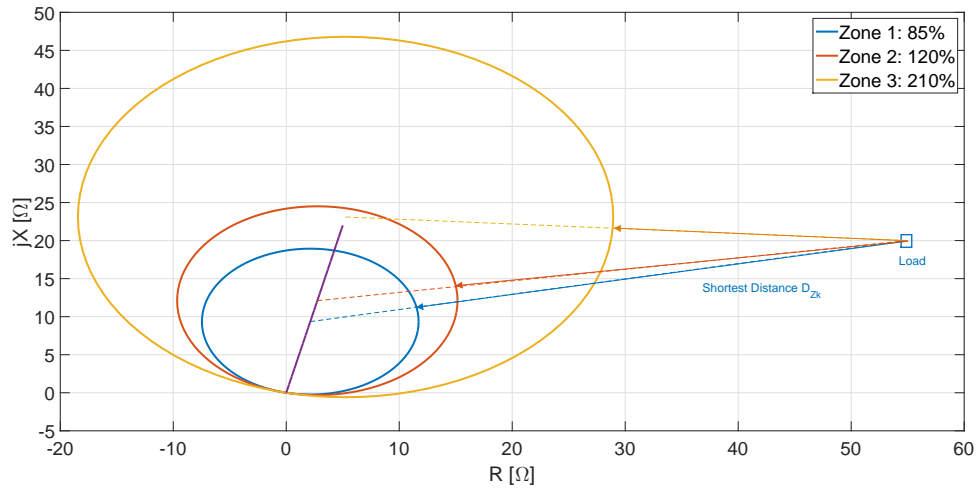


Figure 5.3: Shortest distance definition for protection at 60 Hz.

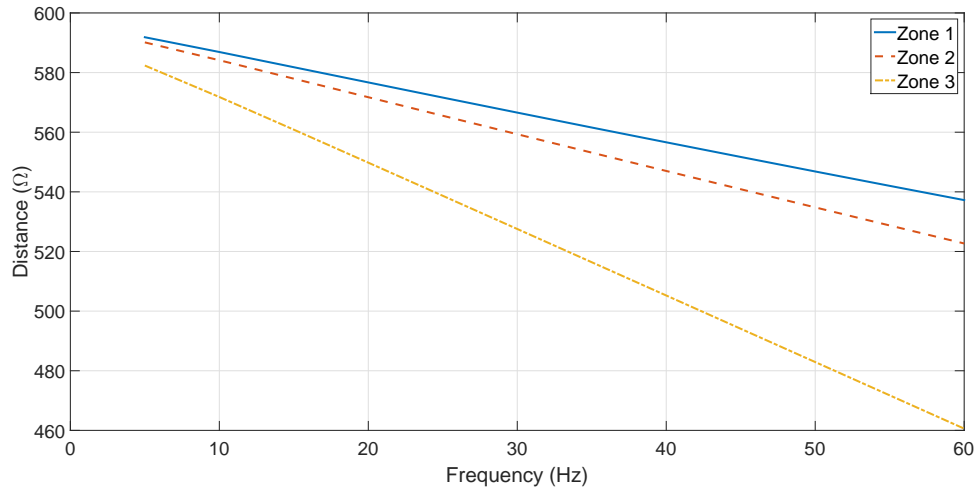


Figure 5.4: Shortest protection distance with different frequencies.

Note that in the transmission system, $u > v$ and $R < X$ then $D'_{Z_k}(X)$ is always negative. This means D_{Z_k} increases as the reactance or frequency is decreased. Fig. 5.4 shows the change in D_{Z_k} as frequency decreases from 60 Hz to 5 Hz for three different protection zones. The zones are calculated as a fixed percentage for the line impedance as 85%, 120%, and 210% for zone 1, zone 2, and zone 3, respectively. Only the *mho* characteristic is considered in this analysis. It can be observed that the relationship between D_{Z_k} and frequency is almost linear, with zone 3 having the steepest slope. This means that as frequency is reduced, the separation increases between the zone reach characteristic and load impedance. The change in separation is observed to be largest for the remote backup protection zone, i.e., zone 3. This result indicates that the setting of the remote backup zones, i.e. zone 3, can be simplified in LFAC systems when considering load encroachment due to the increased margin in the complex impedance plane.

Impact on relay loadability

In stepped-distance protection, the maximum loadability is the maximum power that a line can transfer until the load impedance encroaches upon the outermost circle, i.e zone 3 circle. Fig. 5.5 represents the concept of maximum loadability for a specific load. The maximum loadability of the relay is then calculated as

$$S_{Relay} = \frac{kV_{LL}^2}{Z_{L,Relay}^*} \quad (5.9)$$

where kV_{LL} is line-to-line voltage in kV and $Z_{L,Relay}$ is the load impedance measured by the relay and given by [68]

$$Z_{L,Relay} = Z_3 \cos \beta \quad (5.10)$$

where β is interior angle between load and line impedance curves and Z_3 is the line impedance value as shown in Fig. 5.5.

The maximum loadability (in per unit) for different power factor angles in each frequency is presented in Table 5.2. At lower frequencies, the loadability is improved significantly. The maximum power at $\theta = 30^\circ$ in a 10 Hz system is 74.33 pu, which is more than 8 times that in a 60 Hz system. Furthermore, as power factor angle is increased, the necessary power to trip the line is reduced. For example, at 60 Hz the maximum power is 16.55 pu for $\theta = 30^\circ$ of power factor and reduced to 9.08 pu for $\theta = 75^\circ$.

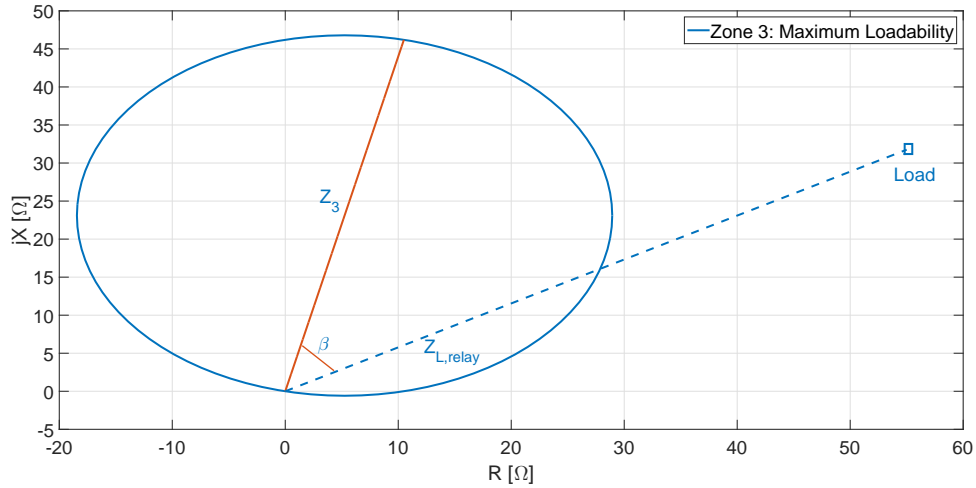


Figure 5.5: Maximum relay loadability with *mho* characteristics.

In summary, this section investigates the impact of the reduced transmission line impedance in an LFAC system in terms of protection prospective. Three notable benefits are observed for LFAC operation, along with one drawback. First, the critical clearing time in an LFAC system is larger, allowing relays more time to detect and clear faults. Another benefit is, for conventional stepped-distance protection schemes, an LFAC system has a

Table 5.2: Relay Loadability Limits at Different Frequencies (pu).

Power factor	60 Hz	30 Hz	10 Hz	5 Hz
0°	213.36	213.36	213.36	213.36
15°	29.67	52.31	106.48	143.70
30°	16.55	31.01	74.33	114.20
45°	12.04	23.16	60.24	100.43
60°	10.00	19.55	53.72	95.42
75°	9.08	17.97	51.64	97.20
90°	8.87	17.74	53.22	106.44

larger separation in the complex impedance plane between line and load impedance. This allows for simplified setting of features such as load encroachment blocking as the margin is increased. Relay loadability is also increased. However, compared with to the conventional 60 Hz systems, an LFAC system has higher fault currents due to the significant reduction in transmission line reactance. One possible solution, to be investigated in a subsequent analysis, is to utilize a superconducting fault current limiter (SCFCL). In the next section, a fault detection method based on SOGI technique is presented in detail.

5.2 A Fast Fault Detection for LFAC Systems based on SOGI Technique

This section presents a new method to detect short-circuit faults in an ac power system based on the positive-/negative-sequence and phase angle of the currents. The new method is based on the second-order generalized-integrator frequency-lock loop (SOGI-FLL) technique and performs in the time domain. The proposed method is able to detect the fault quickly and accurately. In addition, throughout the analysis it is observed that the current phase angle waveforms are changed corresponding to different events. The

current phase angle waveform is thus recommended as a reference for post-event classifications. Various scenarios of faults, capacitor switching, and transformer energization are simulated for the proposed method in strong and weak power systems. The results verify that the new method is able to detect faults quickly and guarantees that the protection system recovers properly after fault events occur. But before describing the new method in detail, the literature review for power system protection methods, which are performed in frequency domain, are presented first.

Strong power systems are characterized by low impedance and benefit from better power quality from reduced voltage variations and impact from harmonics. However, due to the low impedance, the systems suffer from high fault currents. Subsequently, there is a need to detect and clear faults quickly before the equipment is damaged. It has been shown that there is an increasing trend toward decreasing system impedance, resulting in increased short-circuit currents [69, 70, 71]. Another motivating factor is the growing trend for distribution systems to interconnect more distributed generators (DGs), resulting in higher short-circuit current [72]. Therefore, in systems with high short-circuit current, it is beneficial to detect and clear a fault before the first peak to allow for circuit breaker operation at the first zero crossing. Furthermore, fast detection limits damage to equipment and provides better coordination with current limiting devices that require mechanical operation. However, detection is complicated by the fact that switching transients such as capacitor switching and transformer energization will also produce high currents due to the low impedance. In such cases, it is then important to be able to quickly discriminate between faults and switching transients.

There are several existing methods allowing for fast detection in strong systems.

The most common methods rely on rms, FFT, and least-squares estimation of fault current. In general, more accurate algorithms require more time [73]. Other methods that have been proposed that involve travelling wave, wavelets, pattern recognition, and PLL [74, 75, 76, 77, 78, 79, 80, 81, 82, 83]. The authors in [74, 75] propose a fast detection algorithm based on the phase-locked-loop (PLL) technique for coordination with FCL. The method uses empirically determined thresholds on instantaneous current and error output from the PLL to discriminate faults from switching transients. However, the method may not be robust due to the use of instantaneous signals and difficulty in determining threshold settings in practical systems. The magnitude of error is significantly changed with gain settings, and thus it is not accurate to use the limits on this instantaneous signal for fault detections. The PLL is used in [75] for fault detection in direct-drive wind turbines but is designed for a specific scenario. In [84], a second-order generalized-integrator frequency-lock loop (SOGI-FLL) is demonstrated for fault detection in inverters, but it does not consider aspects of security and discrimination from other transient events.

Our target is to propose an alternative for fast and robust fault detection based on the second-order generalized-integrator frequency-lock loop (SOGI-FLL) technique that is able to detect faults within $1/5$ of a 60-Hz cycle. Furthermore, the output of the SOGI-FLL further provides signals allowing for simple discrimination between faults and switching transients. The objective of the proposed method is to provide a dependable and secure detection as well as a classification of short-circuit faults in strong power systems. The proposed method is intended to provide an alternative to Fourier based methods.

5.2.1 Fault Characteristics and Frequency-Lock Loop Method

This section starts by analyzing the fault current characteristics in terms of magnitude and phase. A single-line to ground fault is used to demonstrate the theory. After that, the operating principles of a frequency-locked loop is introduced to see how this method can help to detect change in magnitude and phase once a fault occurs.

The Fault Analysis

A single line-to-ground fault at phase A is analyzed in this study to see how the current magnitude and phase angle changes with frequency. Assuming the fault impedance is purely resistive and represented by R_f . Before the fault occurs, the power system is balanced and the currents are given by

$$\begin{bmatrix} I_a \\ I_b \\ I_c \end{bmatrix} = \begin{bmatrix} \frac{1}{Z_s+Z_L} & 0 & 0 \\ 0 & \frac{1}{Z_s+Z_L} & 0 \\ 0 & 0 & \frac{1}{Z_s+Z_L} \end{bmatrix} \begin{bmatrix} V\angle 0^\circ \\ V\angle -120^\circ \\ V\angle 120^\circ \end{bmatrix} \quad (5.11)$$

When the fault occurs, the current at phase A is high due to significant reduction of impedance

$$\begin{bmatrix} I_a^f \\ I_b^f \\ I_c^f \end{bmatrix} = \begin{bmatrix} \frac{3V}{Z_1^{eq}+Z_2^{eq}+Z_0^{eq}+3R_f} \\ 0 \\ 0 \end{bmatrix} \quad (5.12)$$

where R_f is the equivalent fault impedance and $(Z_1^{eq}, Z_2^{eq}, Z_0^{eq})$ are the equivalent circuit impedances looking at the fault point as explained in detail in [29].

During the fault, the three-phase currents are typically unbalanced. The currents then need to be decomposed into the positive-, negative-, and zero-sequence components in order to analyze power system status. The positive-sequence currents, for example, are

given from the phasor transformation.

$$\begin{bmatrix} I_{a1}^f \\ I_{b1}^f \\ I_{c1}^f \end{bmatrix} = \frac{1}{3} I_a^f \begin{bmatrix} 1 & 0 & 0 \\ 0 & 1 & 0 \\ 0 & 0 & 1 \end{bmatrix} \begin{bmatrix} 1 \angle 0^\circ \\ 1 \angle -120^\circ \\ 1 \angle 120^\circ \end{bmatrix} \quad (5.13)$$

The current magnitude and phase angle versus operating frequencies for our studied system are plotted in Fig. 5.6. Due to the impedance drop, the current magnitude is significantly increased. The same observation can be seen in the negative-sequence component. It is worthwhile to notice that the phase angle has a jump when the fault occurs. This motivates us to use the phase angle as an additional indicator to detect faults.

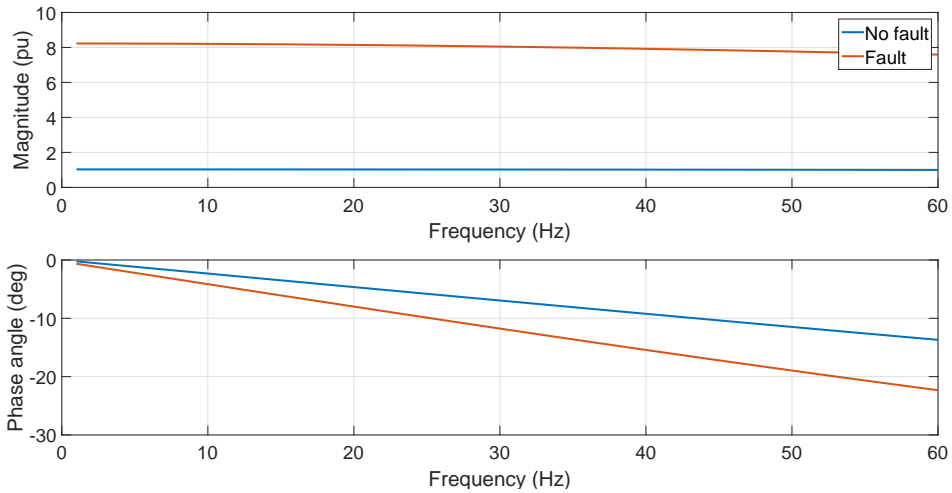


Figure 5.6: The current magnitude and phase angle at different operating frequencies.

Frequency-Lock Loop Operating Principles and its Utilizations for Fault Detection

As mentioned in the previous section, when a fault occurs, the protection system needs to response quickly in order to trip the circuit breaker. The fault events can be

detected immediately by the frequency-lock loop technique in the time domain. The second-order generalized-integrator frequency-lock loop (SOGI-FLL) technique was first introduced in [23] to identify the grid voltage parameters to synchronize an inverter with the power system. The introduction of this technique is presented in great detail in Section 4.1. In comparison to the phase-lock loop (PLL), this technique has no steady-state error in the output signal and only utilizes one controller for frequency instead of two feedback loops in the PLL, i.e, one for frequency and one for phase-angle detection [20]. However, the benefits of this method have strayed from its initial application and this method is proposed to be used for fault detection. The frequency-lock loop basically consists of a second-order generalized-integrator (SOGI) and a frequency controller. The SOGI is able to generate sine/cosine signals (v' and qv'), which can be used to calculate the rms value, from a single sinusoidal input v_{in} , Fig. 5.7.

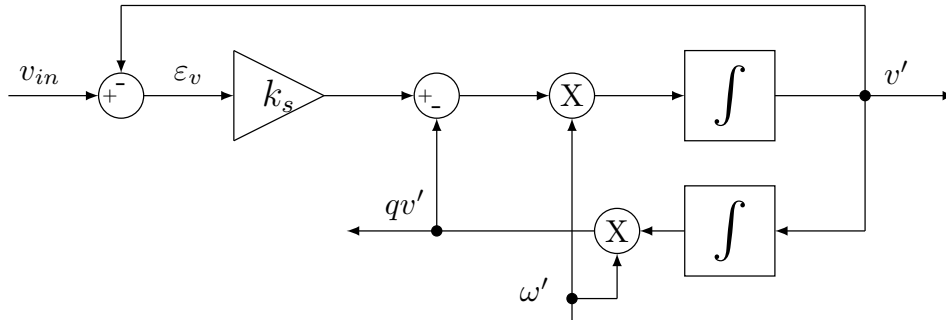


Figure 5.7: A typical SOGI structure.

In a three-phase power system application, two SOGI or double SOGI (DSOGI) blocks need to be employed in order to detect the voltage/current information. The general block diagram is shown in Fig. 5.8. Each block provides the error signals, i.e $\varepsilon_{f\alpha}$ and $\varepsilon_{f\beta}$, to the frequency controller. These signals are similar to the output error in

[74] and have magnitudes characterized for each events. The frequency-lock loop needs only one controller, which is a first-order system, and its bandwidth can be adjusted directly by setting gain F . Therefore this method has faster performance in terms of time response compared to the phase-lock loop method implemented in [74]. One significant and important benefit from the SOGI-FLL method is the ease with which the positive- and negative-sequence components (PNSC) can be computed from outputs of each SOGI block [20]. The mathematical foundation of this technique is described in detail in Section 4.1. The instantaneous positive-/negative-sequence components are

$$\begin{aligned} v_{\alpha\beta}^+ &= [T_{\alpha\beta}]v_{abc}^+ = [T_{\alpha\beta}][T_+]v_{abc} \\ &= [T_{\alpha\beta}][T_+][T_{\alpha\beta}]^{-1}v_{\alpha\beta} = \frac{1}{2} \begin{bmatrix} 1 & -e^{-j\frac{\pi}{2}} \\ e^{-j\frac{\pi}{2}} & 1 \end{bmatrix} v_{\alpha\beta} \end{aligned} \quad (5.14)$$

$$\begin{aligned} v_{\alpha\beta}^- &= [T_{\alpha\beta}]v_{abc}^- = [T_{\alpha\beta}][T_-]v_{abc} \\ &= [T_{\alpha\beta}][T_-][T_{\alpha\beta}]^{-1}v_{\alpha\beta} = \frac{1}{2} \begin{bmatrix} 1 & e^{-j\frac{\pi}{2}} \\ -e^{-j\frac{\pi}{2}} & 1 \end{bmatrix} v_{\alpha\beta} \end{aligned} \quad (5.15)$$

It can be seen from (5.14) and (5.15) that in order to calculate the sequence components, a (90° - lagging) phase-shift is needed for α and β components. The benefits of SOGI can solve these requirements directly because a SOGI is able to generate two orthogonal waveforms, as seen in Fig. 4.5. The positive-/negative-sequence calculation, therefore, is straightforward from the output signals of two SOGIs as presented in Fig. 5.8. The calculation of zero-sequence is simple because it is the summation of three measured signals. Since the SOGI behaves as an adaptive filter to harmonics, the SOGI-FLL is thus able to attenuate noises and detect the positive-sequence and negative-sequence components quickly and accurately. Moreover, the phase jump during a fault can be used as an additional indicator for fault detection. This means the protection system is a

combination of current limiters and the phase angle to identify faults.

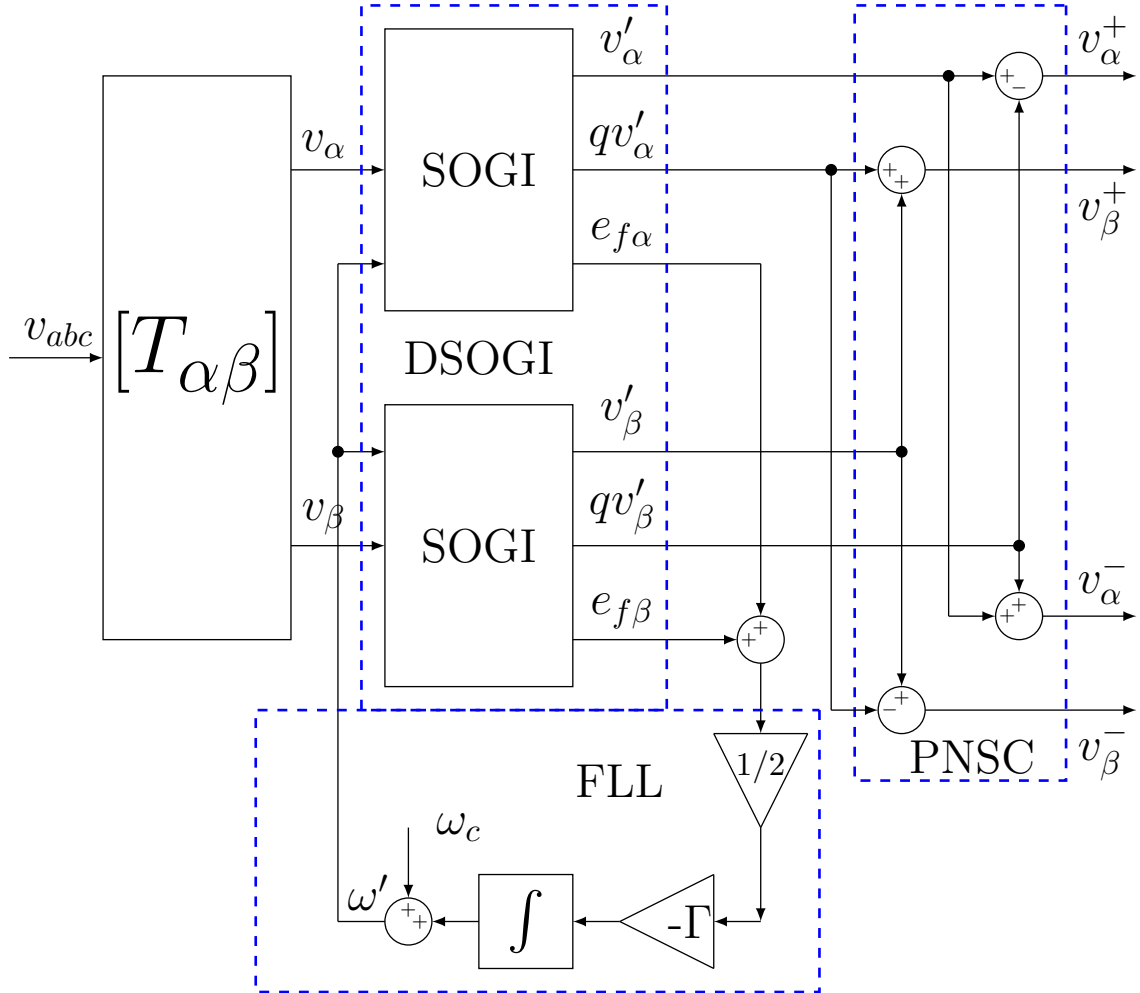


Figure 5.8: The block diagram of SOGI-FLL for positive-/negative-sequence calculation.

Fig. 5.9 presents the overall block diagram of the proposed fast fault detection method. The three-phase currents are measured and passed through the SOGI-FLL to detect the fault event. The current signals are decomposed into positive-sequence and negative-sequence components in order to compute magnitudes and phases. These quan-

tities are then compared with the threshold in the limiters block to decide whether or not the fault occurred. If there is a fault on the system, the current magnitudes exceed the thresholds and the limiters block will send a tripping signal to the circuit breakers to shut down the system.

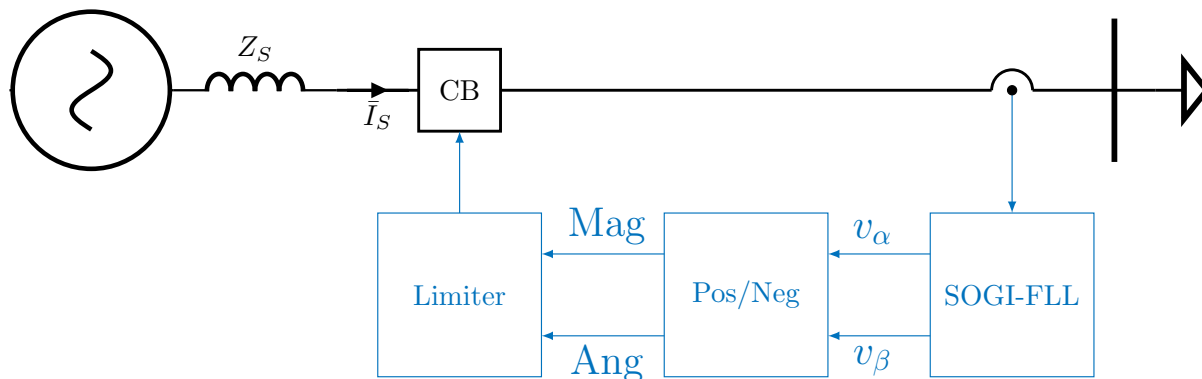


Figure 5.9: The overall block diagram of fast fault detection using SOGI-FLL.

5.2.2 Simulation Results

This section presents the simulation results to verify the effectiveness of the proposed fault detection method. The testing system setup and parameters are similar to the system in [74]. In addition, two different cases of strong and weak power systems are simulated to observe the performances of the proposed method. The single-line-to-ground (SLG) fault is simulated since this is the most likely fault in the system. In each case, three different events are considered: SLG fault, capacitor switching, and transformer energizing. These events are assumed to happen at simulation time $t = 0.3$ seconds. First, the results in a strong power system are presented as follows.

Simulation Results in a Strong Power System

The three different events occur in the power system are summarized in Fig. 5.10. The system parameters and load conditions are exactly the same as in paper [74]. The supply voltage is $V_{LL} = 12$ kV, $Z_S = (12.2 + j207.24)$ m Ω , $Z_L = (10.77 + j2.42)$ Ω and is able to deliver approximately 630 A of load currents.

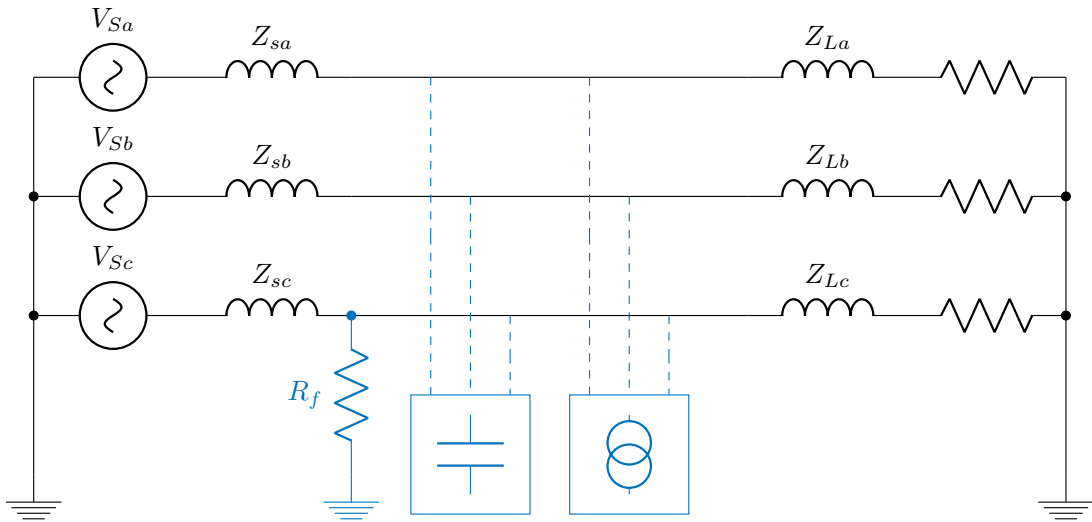


Figure 5.10: The power system with three different events.

Single Line-to-Ground Faults

The fault happens in phase A at simulation time $t = 0.3$ seconds with the fault resistance $R_f = 0.5$ Ω . As expected, the current in phase A increases significantly due to impedance drop. This results in large the magnitudes of positive- and negative-sequence components as shown in Fig. 5.11(a). The current magnitudes are higher than six times rated and above the threshold, i.e typically two or three times of the load current. It is worthwhile to mention here that all the calculations are in the time domain.

It is interesting to see from Fig. 5.11(b) how the current phase angle changes when the fault event occurs. The phase angle starts experiencing distortions after 0.3 second. The angle error fluctuates six times in three cycles of the grid. In other words, the angle error oscillates with a frequency that is twice that of the power system frequency. This information about the frequency of phase angle error can be used to differentiate events.

Capacitor Switching

The shunt capacitor is switched to the power system with capacitance $C = 90.19 \mu\text{F}$ at the simulation time $t = 0.3$ seconds. The current waveforms are shown in Fig. 5.12(a) with high frequency oscillations when the capacitors are on. These current oscillations are caused by the resonance between capacitor and inductor in the system. The instantaneous current magnitudes can be very high, i.e 5.0 pu in this system, and then they die out quickly after less than two cycles. The positive-sequence current magnitude also oscillates up to 1.45 pu. However, this magnitude is not higher than 2.0 pu because the SOGI behaves as a low-pass filter that attenuates mostly high frequency current components generated by capacitor switchings. A more detailed analysis of the capacitor switching phenomenon can be found in [29]. Again, the phase angle waveform looks interesting in case of capacitor switchings. Fig. 5.12(b) shows a close up the signal, which has a very high resonant frequency in approximately two grid cycles.

Transformer Energizing

A three-phase 12/0.24-kV, 10.2 MVA, $\Delta - Y$ connection transformer is connected to the system. The transformer model also includes the saturation properties and it

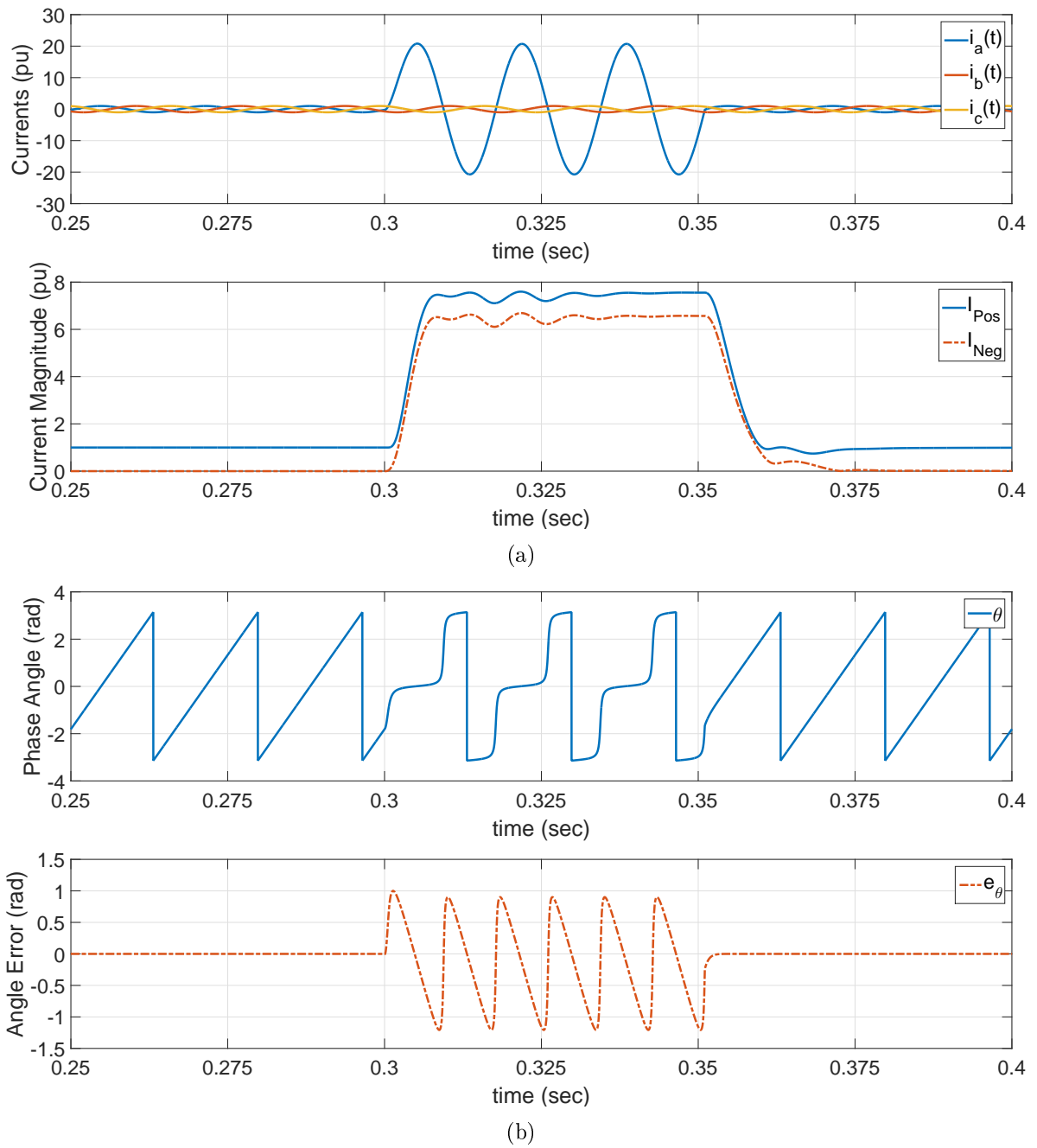


Figure 5.11: A single-phase to ground in a strong power system: (a) current magnitudes and (b) phase angle waveforms.

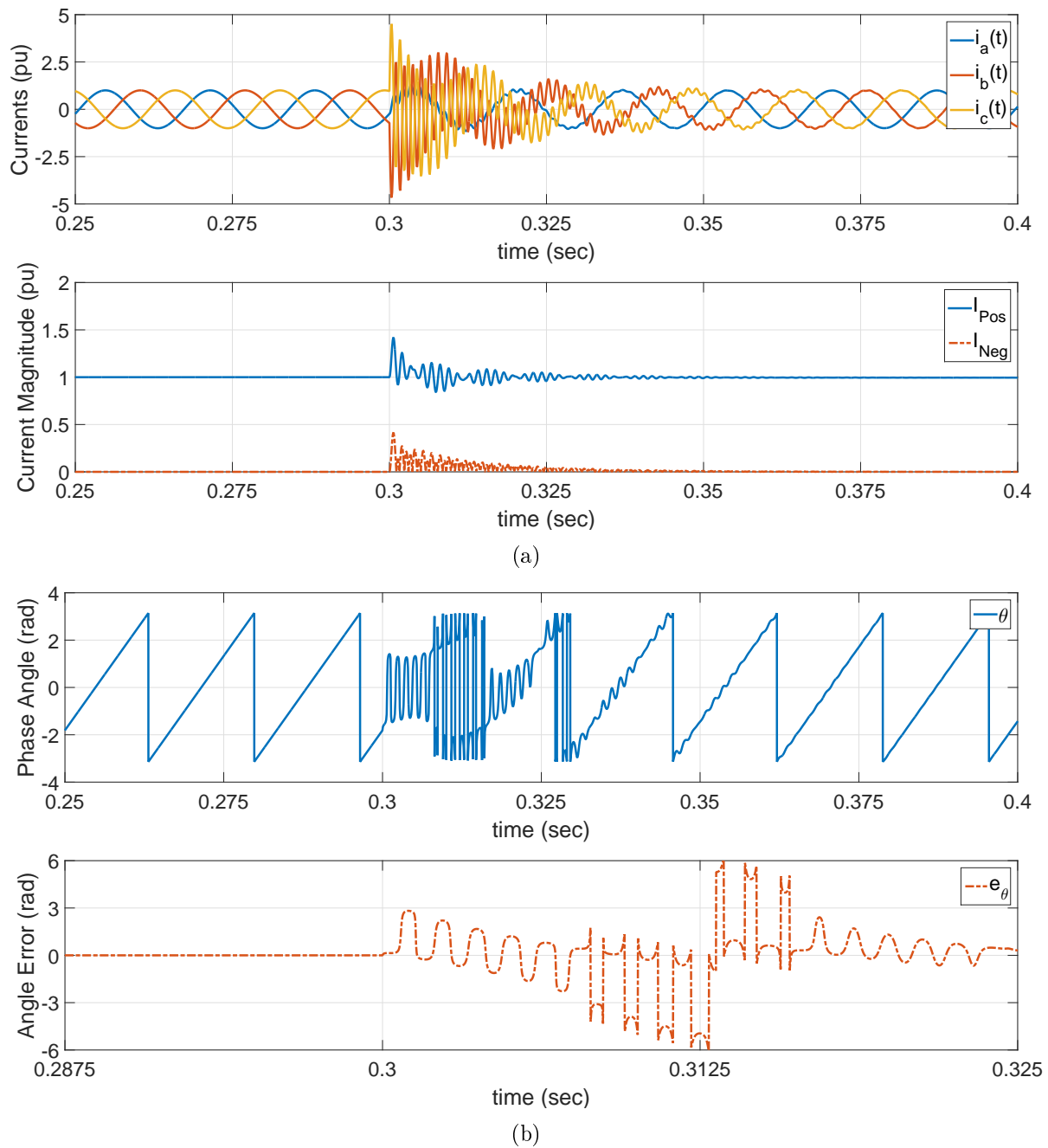


Figure 5.12: Capacitor switching in a strong power system: (a) current magnitudes and (b) phase angle waveforms (zoomed in).

starts energizing at simulation time $t = 0.3$ seconds. The transformer energizing can be treated as large inductors connected to the system at the Point of common coupling (PCC). Because the magnetizing impedances are extremely large, the system impedance is not changed much and therefore the currents in this case are not expected to be as high. As shown in Fig. 5.13(a), the current magnitude fluctuates but never reaches 1.5 pu in this case. This means the current does not pass over the current threshold for the fault events. The current phase angle is also expected to have small oscillations as shown in Fig. 5.13(b). It is worthwhile to note that the phase angle error in the transformer energizing has the same frequency as the power system.

In summary, three different events have been simulated and display different properties. The fault event has the highest current magnitude while the capacitor switching event has high frequency oscillation in the phase angle. Each event property is listed in detail in Table. 5.3.

Table 5.3: Event properties under SOGI-FLL analysis.

Events	Fault	Cap. switching	Xfmr energizing
Pos. mag.(pu)	> 3 times	< 2	< 2
Neg. mag.(pu)	> 3 times	< 0.5	< 0.5
Phase angle freq.	= 2 times	> 2 times	= 1 time

Timing Diagram

The responses of the protection system when faults occur are shown in Fig. 5.14. The current limits are set at three times that of the rated load currents. The fault occurs at simulation time $t = 0.3$ seconds. The system is simulated for two different fault detection

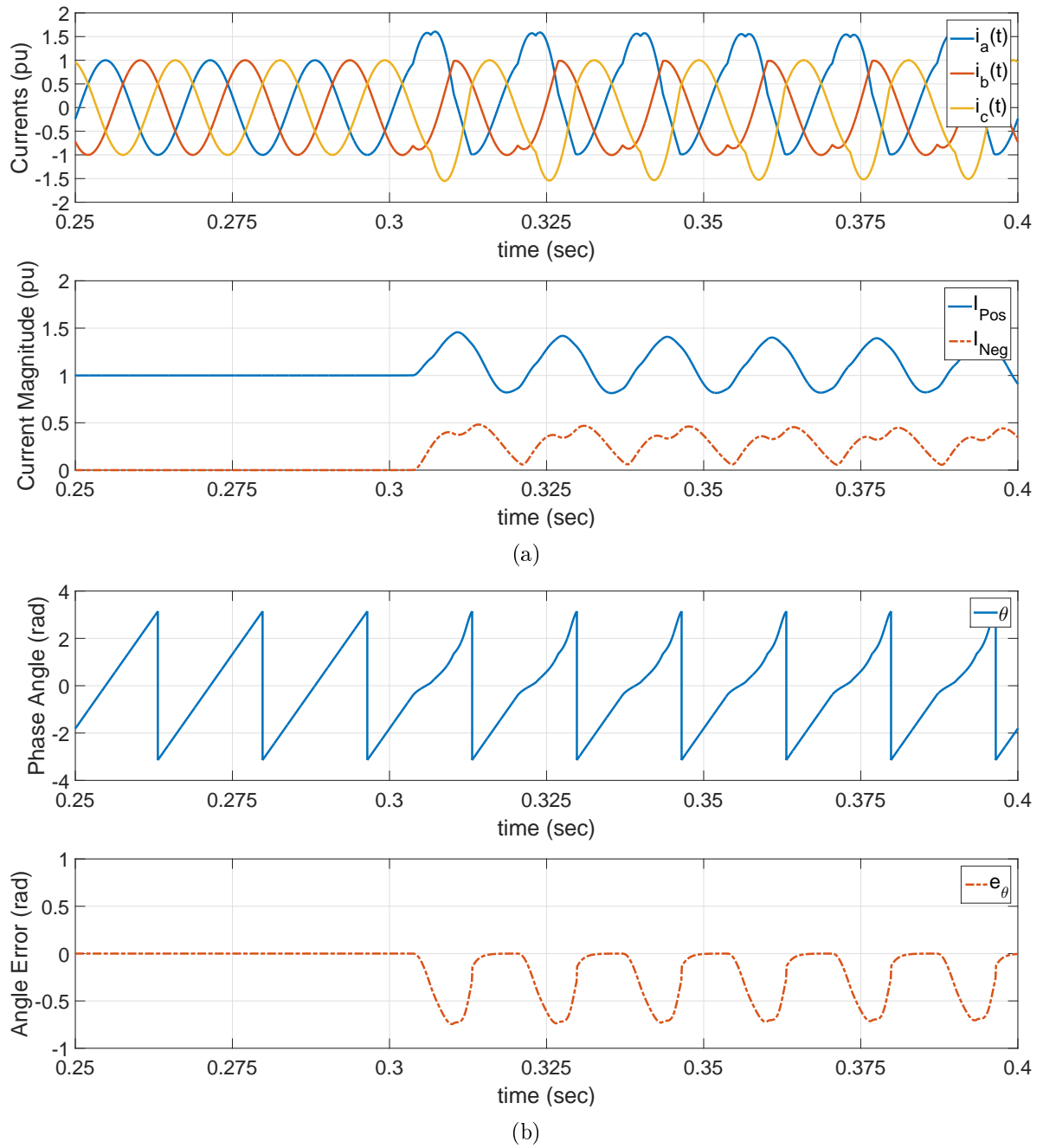


Figure 5.13: Transformer energizing in a strong power system: (a) current magnitudes and (b) phase angle waveforms.

methods: the proposed method and the cosine filter one. When the fault happens, the proposed protection system detects a fault quickly and sends the tripping/clearing signals to the circuit breaker. In the case of 60 Hz, the clearing time is sent at $t = 0.30317$ seconds or it takes 3.17 ms, i.e approximately 0.19 cycles of the 60 Hz system, for the protection system to respond. The cosine filter method triggers the clearing signal slower at $t = 0.3052$ seconds, or this method takes 5.2 ms to detect the fault.

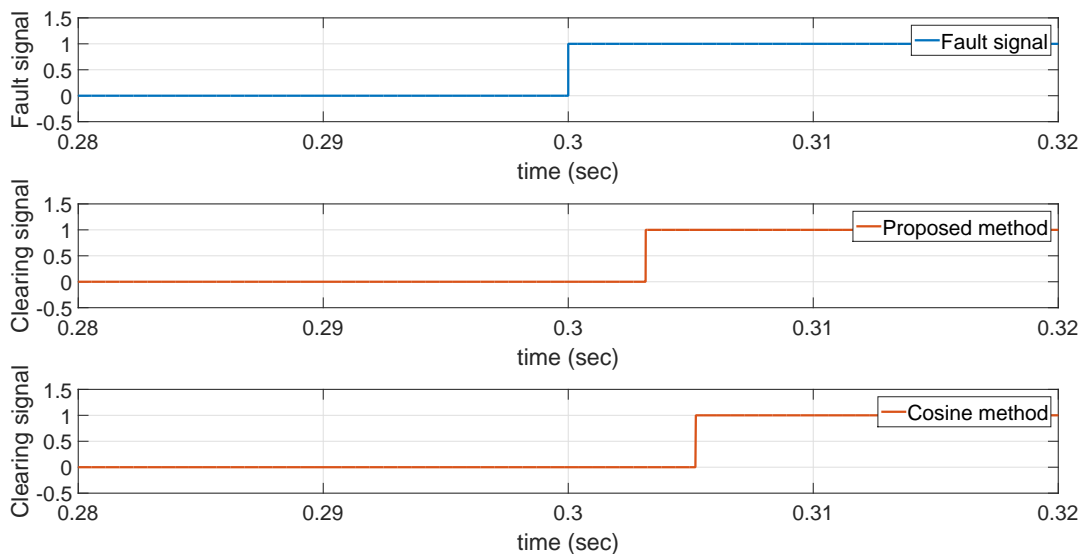


Figure 5.14: The proposed and cosine filter methods responses in a strong 60-Hz system.

Simulation Results in a Weak Power System

The new fast fault detection algorithm is also simulated in a weak system in order to verify its effectiveness. The simulation setups are similar to that of the strong system case except for the grid impedance Z_S . As recalling from the previous section, the system short-circuit capacity is nearly 700 MVA when $Z_S = (12.2 + j207.24)$ m Ω and increasing Z_S makes the system weaker. In the simulations, the impedance Z_S is gradually increased

from one time to ten times, in which the system short-circuit capacity is approximately 70 MVA. The results are shown in Fig. 5.15, Fig. 5.16, and Fig. 5.17 for faults, capacitor switchings, and transformer energizings, respectively.

As in a weak grid, the impedances become larger and thus the fault current magnitudes are reduced. However, the positive-sequence current is still higher than the threshold, and interestingly the phase angle error continues to oscillate at the double grid frequency as shown in Fig. 5.15(a) and Fig. 5.15(b). In the case of capacitor switching, since the grid reactances are increased, the resonance between capacitor banks and inductors are less intensive as in Fig. 5.16(a). The current magnitude is no higher than 1.5 pu, and the phase angle still contains a high frequency resonance as shown in Fig. 5.16(b). When a transformer is energized, the current magnitude fluctuates less than in a strong system as plot in Fig. 5.17(a). The phase angle, shown in Fig. 5.17(b), has its typical waveform of transformer energizing events with the frequency is the same as the system frequency.

The time responses of the proposed method and the cosine filter method with the same current limit in a strong system case are shown in Fig. 5.18. Because it requires more time for a smaller current to reach the threshold, the proposed method response is predicted to be slower compared to that of a strong power system. In the case of 60 Hz, the fault is detected in 5.625 ms, which approximately 0.34 grid cycles. The cosine filter method detects the fault slower at $t = 0.3135$ seconds. In other words, this method takes 13.5 ms to trigger the clearing signal. Fig. 5.19 shows the linear relation between the algorithm time response in cycle versus the 60 Hz power system short-circuit capacity. As the short-circuit capacity increases or the grid is more stiff, the protection system response is faster. For example, the fault is detected in approximately 0.5 cycles and 0.19

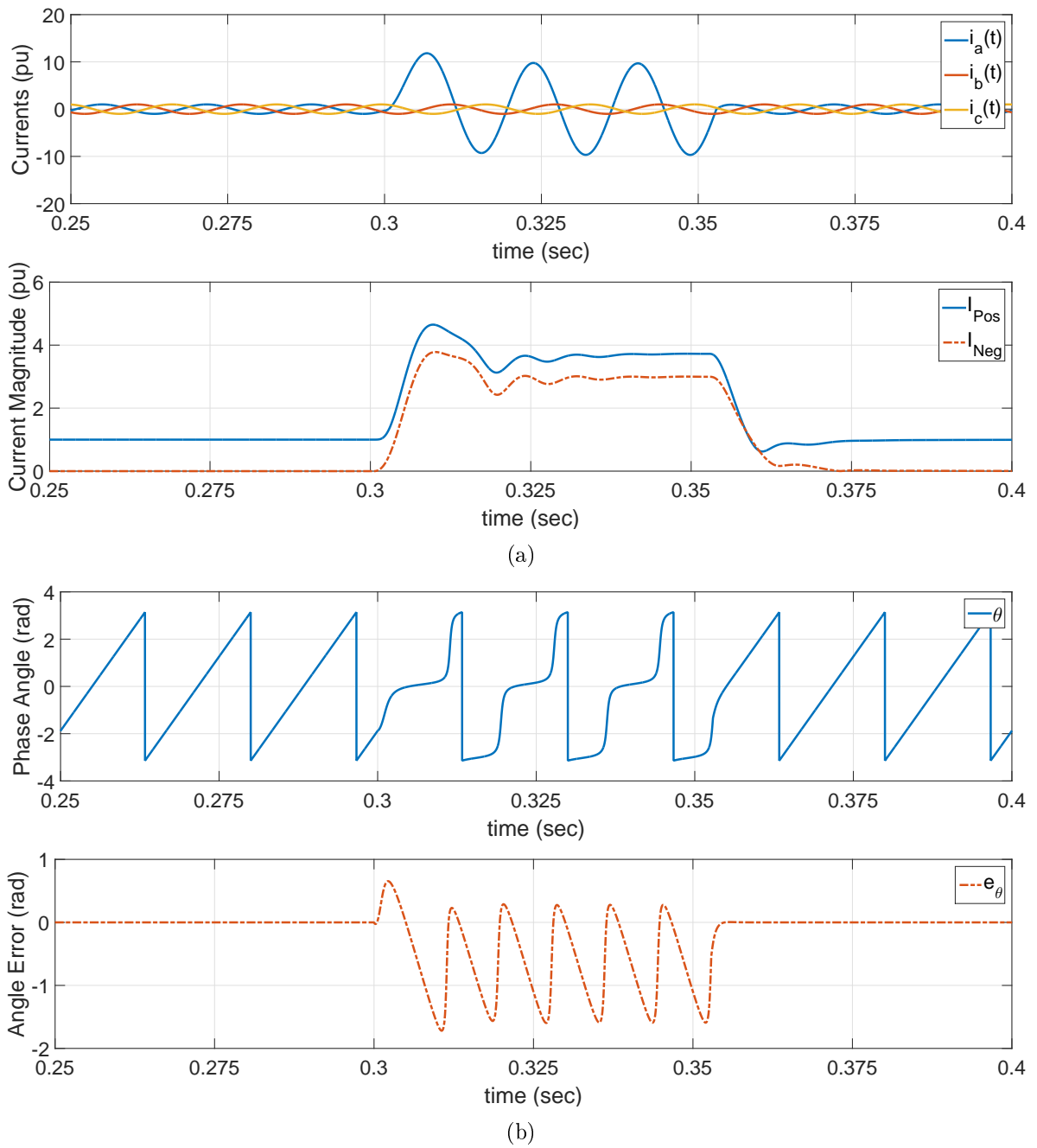


Figure 5.15: A single-phase to ground in a weak power system: (a) current magnitudes and (b) phase angle waveforms.

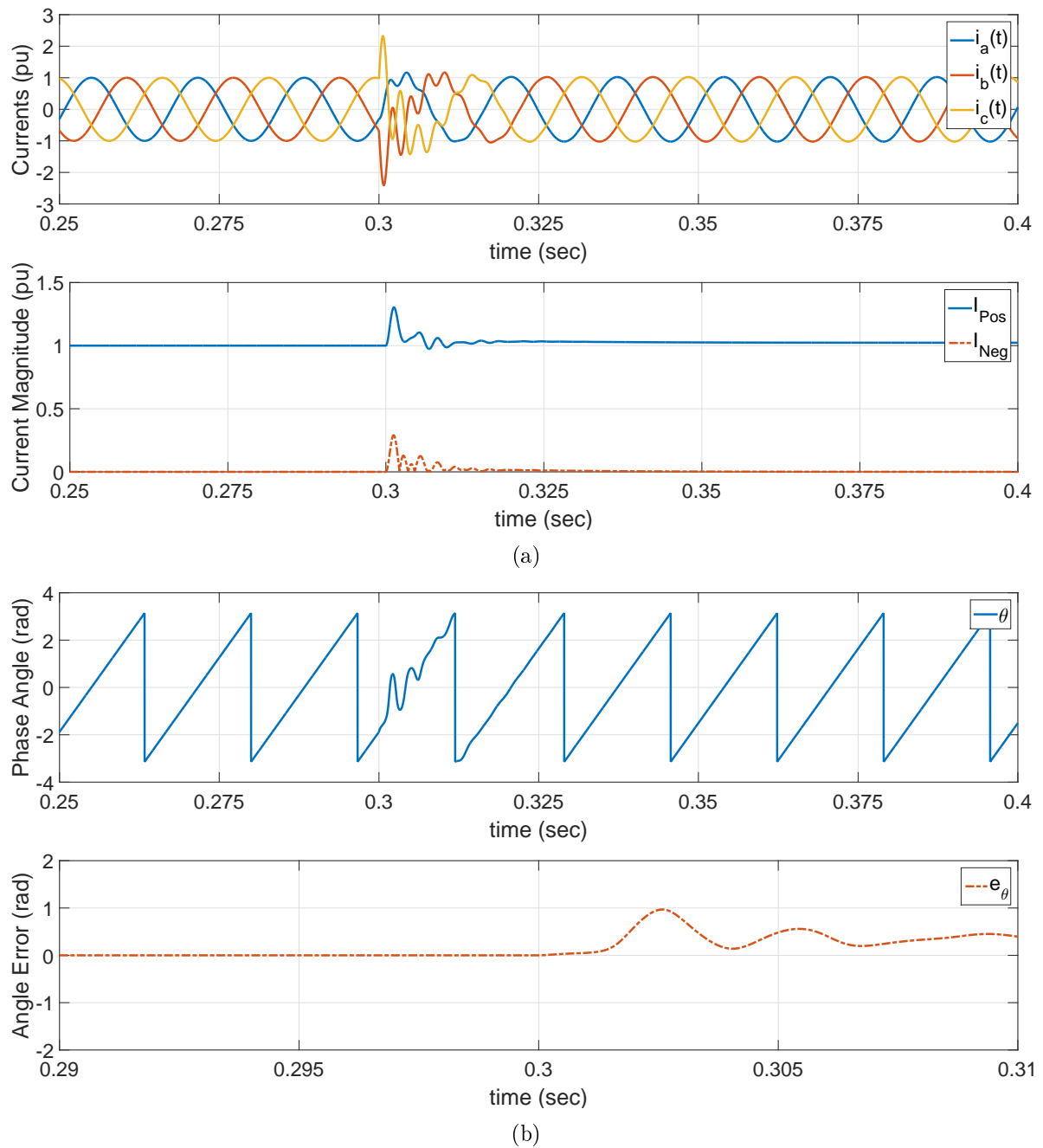


Figure 5.16: Capacitor switching in a weak power system: (a) current magnitudes and (b) phase angle waveforms (zoomed in).

cycles in 70-MVA and 700-MVA systems, respectively. In other words, the performance of the proposed method in a strong system is better than that in a weak system.

The Proposed Method in LFAC Power Systems

The new protection method based on SOGI-FLL technique is implemented in an LFAC system to verify its superior performance. For example, Fig. 5.20 presents the performance of the proposed and cosine filter methods in a low frequency system, i.e. the operating frequency is lowered to 10 Hz. The clearing signal in the proposed method is enabled at $t = 0.31255$ seconds. In other words, it takes 12.55 ms, i.e. nearly 0.13 cycles of the 10 Hz system, to clear the faults. The response time of the 10 Hz system is still less than one cycle of 60 Hz grid (16.67 ms) and can be considered to be a fast performance. The cosine filter method, on the other hand, detects the fault after 26.6 ms at $t = 0.3266$ seconds. In the case of a weak 10-Hz LFAC system, the fault is detected and the tripping signal is sent after 17 ms or nearly one 60 Hz-cycle for the proposed method. This response time is acceptable since the circuit breaker can typically be opened within three 60 Hz-cycles [85]. The cosine filter method takes 31.3 ms to detect the fault. The excellent performance of the proposed method can be accounted for the quick adaption of the SOGI-FLL method in the time domain.

Our next step is to test the protection method on practical data that comes from both transmission and distribution levels. The results are positive with all fast and accurate fault detections. The results of one transmission case and one distribution case are presented below in more detail. Fig. 5.21 shows the currents in a single-phase fault, and the results are similar to the previous analysis. It is interesting to see the performance

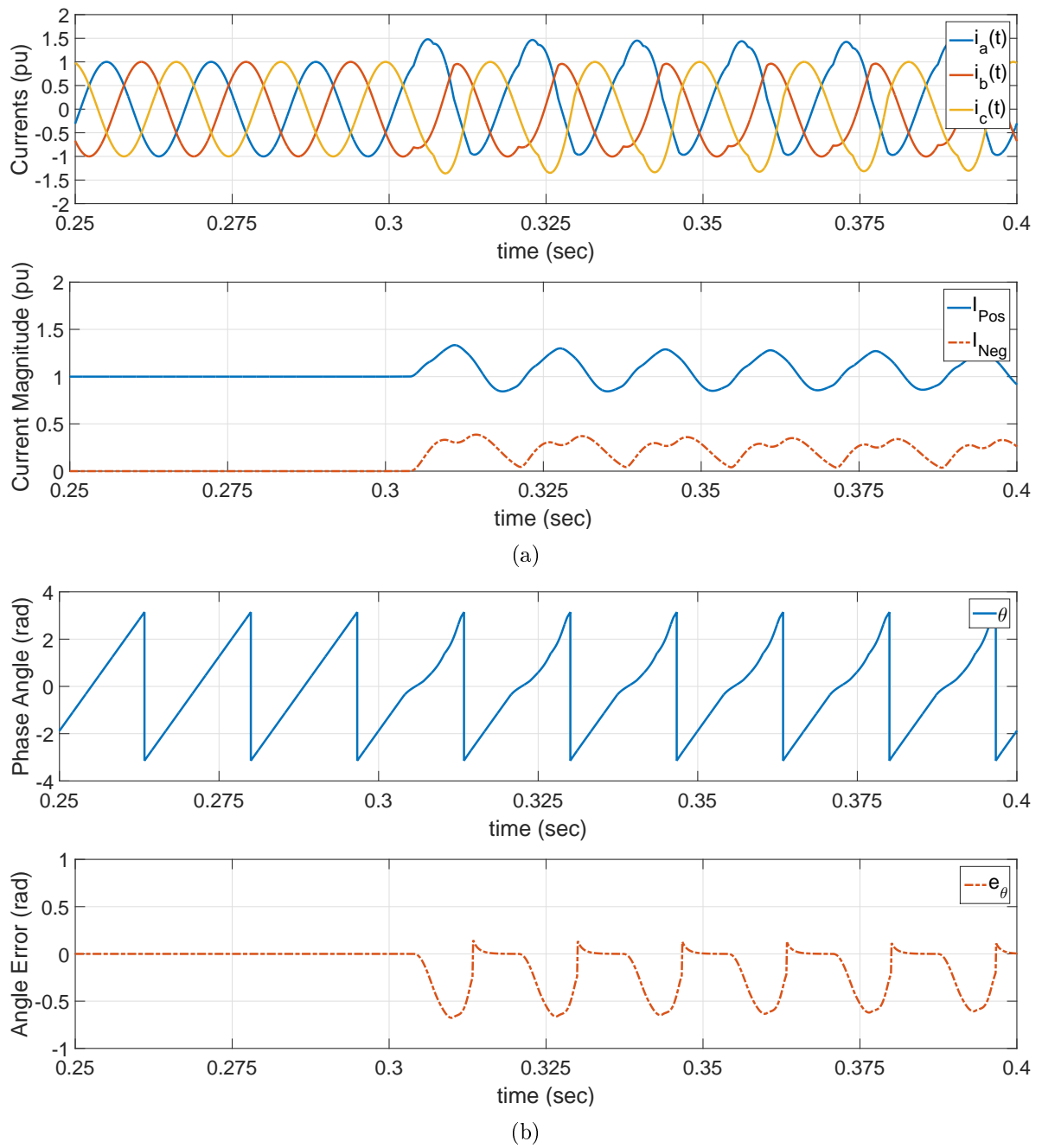


Figure 5.17: Transformer energizing in a weak power system: (a) current magnitudes and (b) phase angle waveforms.

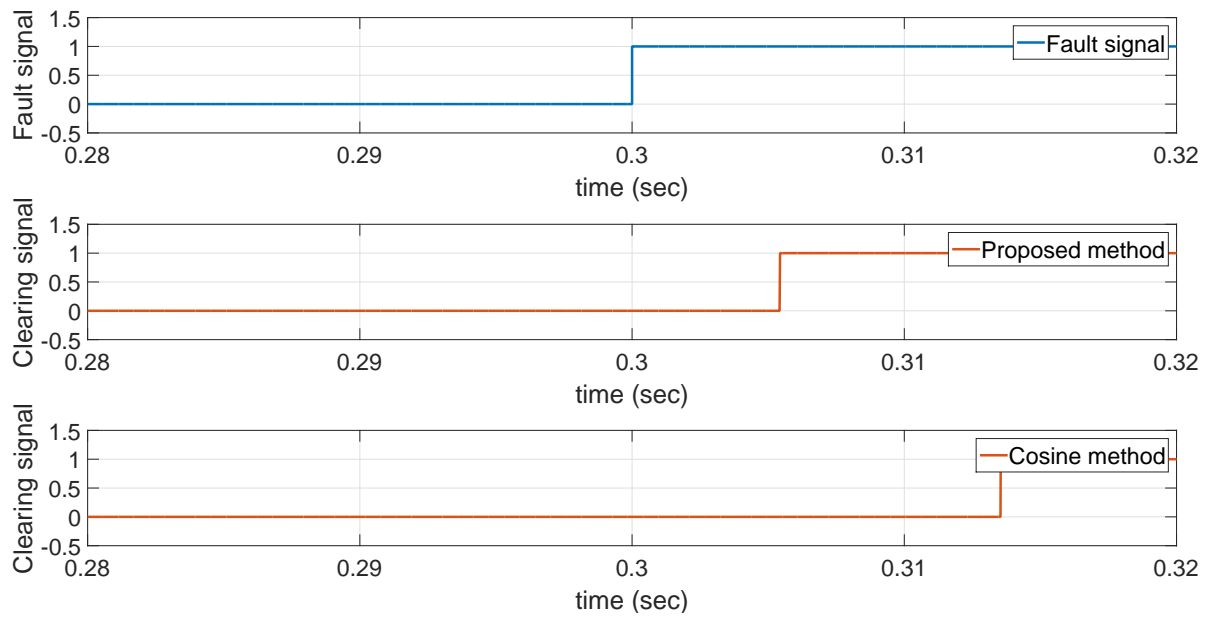


Figure 5.18: The proposed and cosine filter methods responses in a weak 60-Hz system.

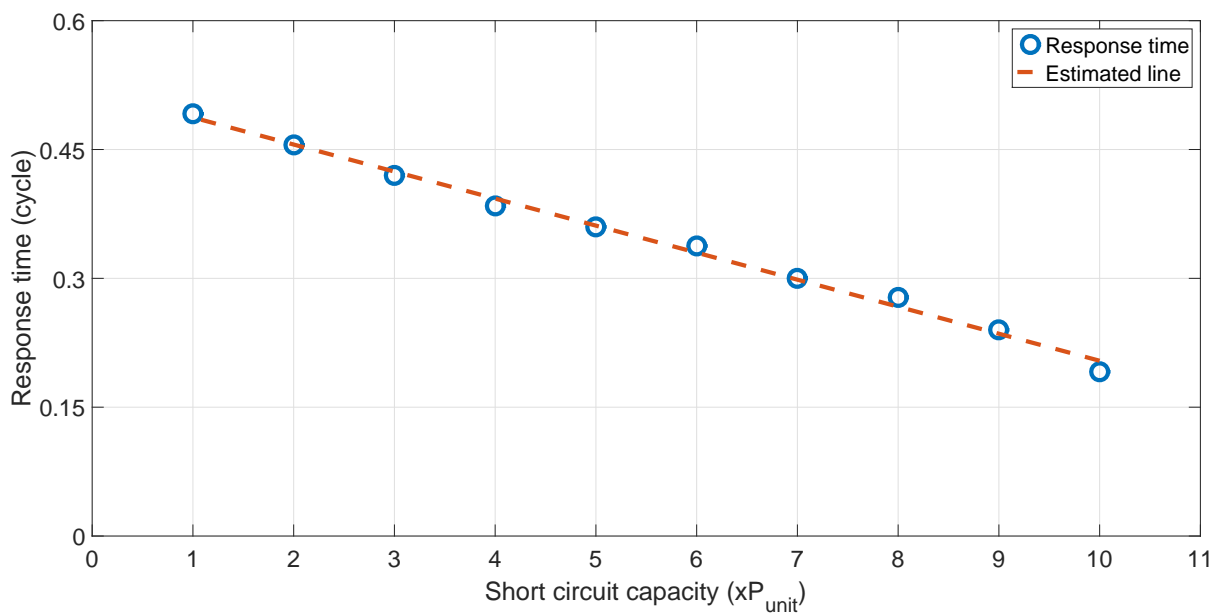


Figure 5.19: Relationship between the new method time response and the power system short-circuit capacity.

of this method in a distribution system, where the currents are unbalanced and contain harmonics. Fig. 5.22 presents distribution current data for the duration of 30 seconds. It is worthwhile to mention that the two events (in red boxes) are not faults but energizing events. The proposed method is able to detect faults accurately as shown in Fig. 5.22(b).

The proposed method and the cosine filter method, which is implemented in Schweitzer Engineering Laboratories (SEL) protection relays, are then compared and analyzed in detail. The rms current of each phase is calculated and then compared with a threshold to detect faults. Without a loss of generality, the current at each phase is assumed to change from 100 A to 200 A, as seen in Fig. 5.23(a), and these changes are detectable by both methods with a threshold of 150 A. It is interesting to see the proposed method can detect faster than the cosine filter as shown in Fig. 5.23(b), 5.24(a), 5.24(b). For example, the proposed SOGI method can trigger the protection signal in 3.5 ms, which is approximately one-fifth of grid cycle, and faster than the cosine filter method in phase a . This can be explained by the quick output update in the proposed method. Assuming that the input signal is $u(t)$ and the output is $y(t)$ in both methods, then the SOGI is considered as a second-order system in the digital implementation [86]

$$y_n(SOGI) = a_0u_n + a_1u_{n-1} + a_2u_{n-2} + b_1y_{n-1} + b_2y_{n-2} \quad (5.16)$$

$$y_n(Cosine) = a_0u_n + a_1u_{n-1} + a_2u_{n-2} + \dots + a_Nu_{n-N} \quad (5.17)$$

where a_i, b_i are coefficients and N is the number of samples in cosine filter, $N = 8, 16, \dots, 128$. The proposed SOGI method only requires two previous values to update its output while the cosine filter method relies more on the previous $(N - 1)$ values. This explains the faster response of the SOGI method in tracking the rms current value changes during

fault events. The ability of the SOGI method to calculate positive-, negative-, and zero-sequence components is proved in Fig. 5.25(a). The three-phase currents are balanced at the magnitude of 20 A and suddenly change with 100 A of positive-sequence, 50 A of negative-sequence, and 25 A of zero-sequence. These magnitudes are identified correctly as seen in Fig. 5.25(b). Since the proposed method can provide information about sequence components, it can be utilized for fault location applications as well.

In summary, a new method for fault detection is proposed and verified in this chapter. The introduced method is based on the time domain analysis of the positive-sequence, negative-sequence, and zero-sequence current components to detect the faults. Whenever the magnitude of positive-/negative-sequence current reaches the preset threshold, the circuit breaker tripping signal is activated. The protection system employing the proposed algorithm thus performs quickly to clear the fault. In addition, throughout the analysis, the phase angle waveforms can be used as a reference for post-event classifications. For example, in a fault condition, the phase angle oscillates with the frequency of double power system frequency whereas, in a transformer energized case, the phase angle oscillates at the same frequency as the grid. In a capacitor switching event, this frequency is high due to the resonance between inductor and capacitor bank. The proposed method is verified under the various events of the strong and weak grid systems, and is verified with practical data. It is worth reiterating that the faults are detected quickly, i.e. in less than half of a 60 Hz-cycle. Particularly in a strong power system, the introduced method performance is superior to that of a weak system. In conclusion, the new method based on the SOGI-FLL technique has demonstrated its excellent fault detection performance and can be thus easily implemented in any ac protection system.

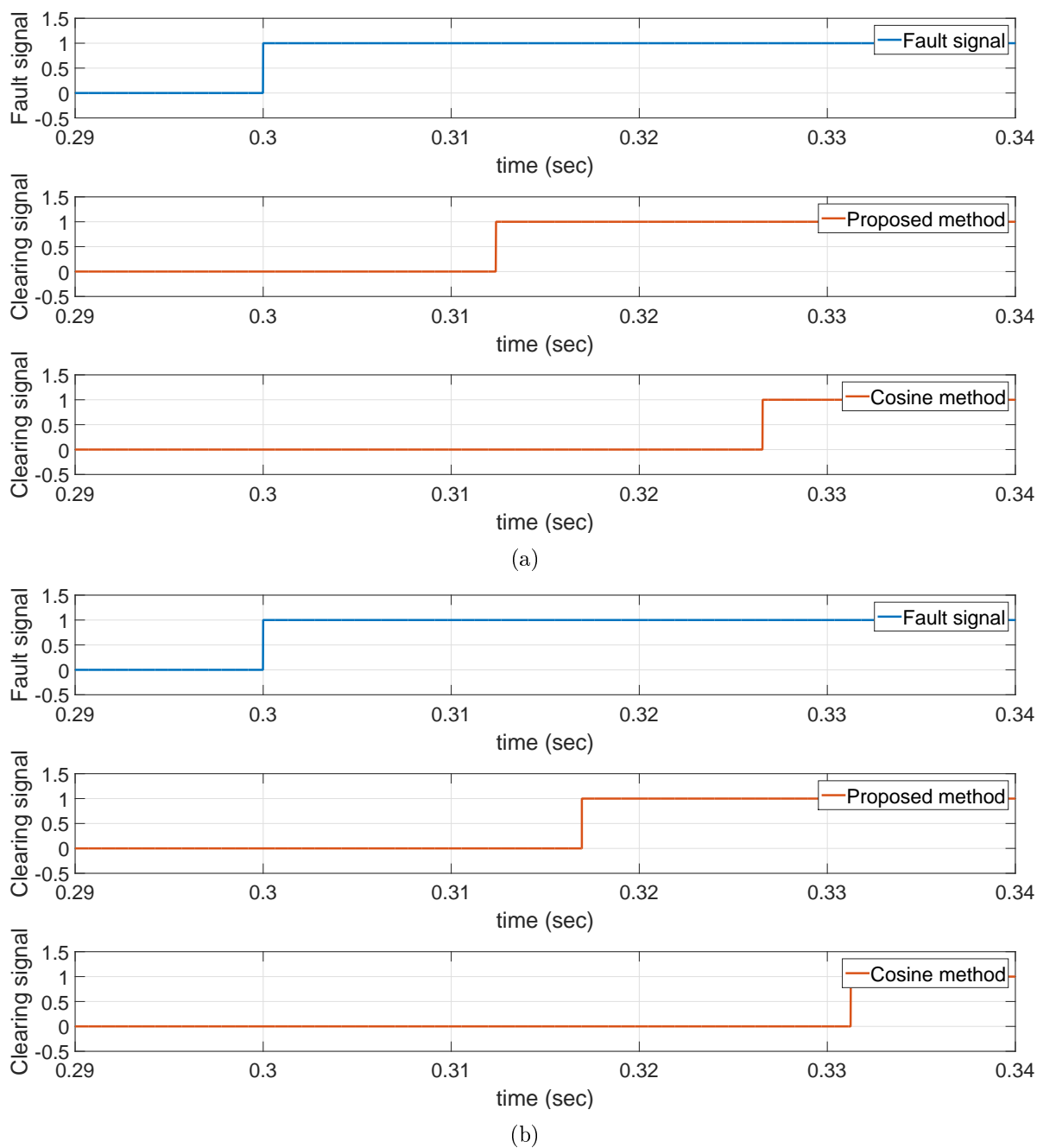


Figure 5.20: Timing diagrams in: (a) a strong and (b) a weak 10-Hz LFAC power systems.

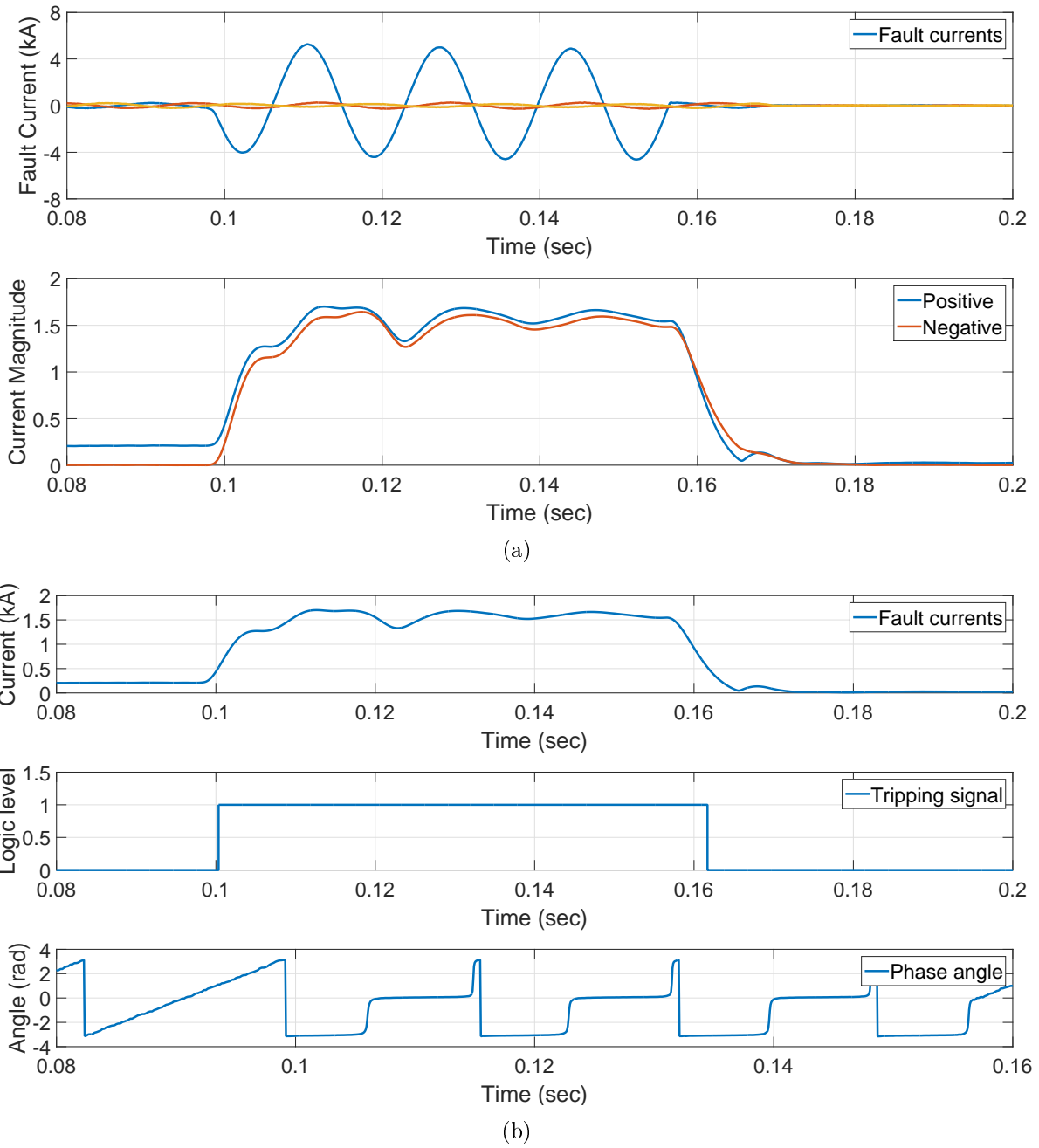


Figure 5.21: Simulation results with transmission data: (a) currents and its sequences, and (b) tripping signal and angle.

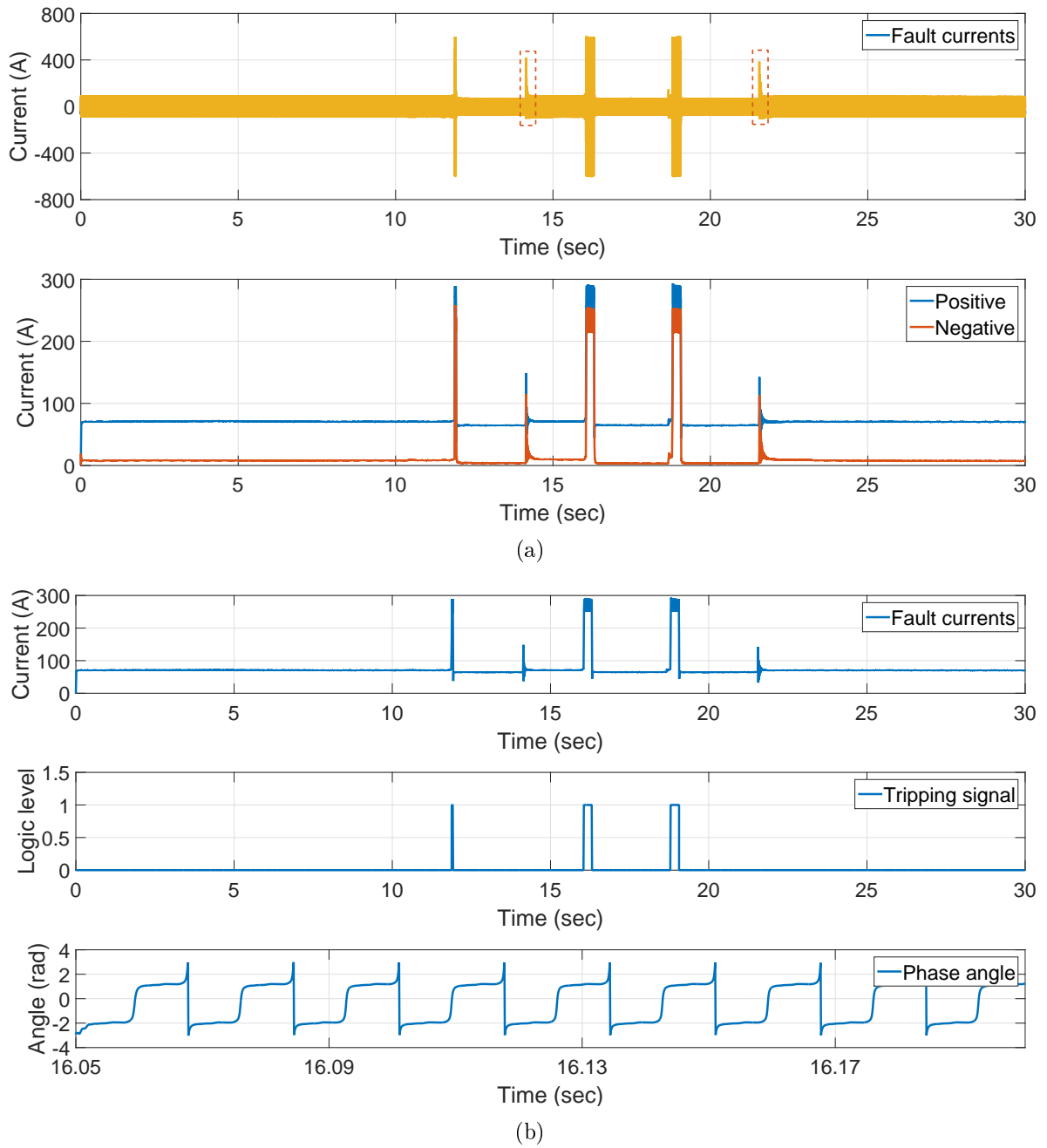
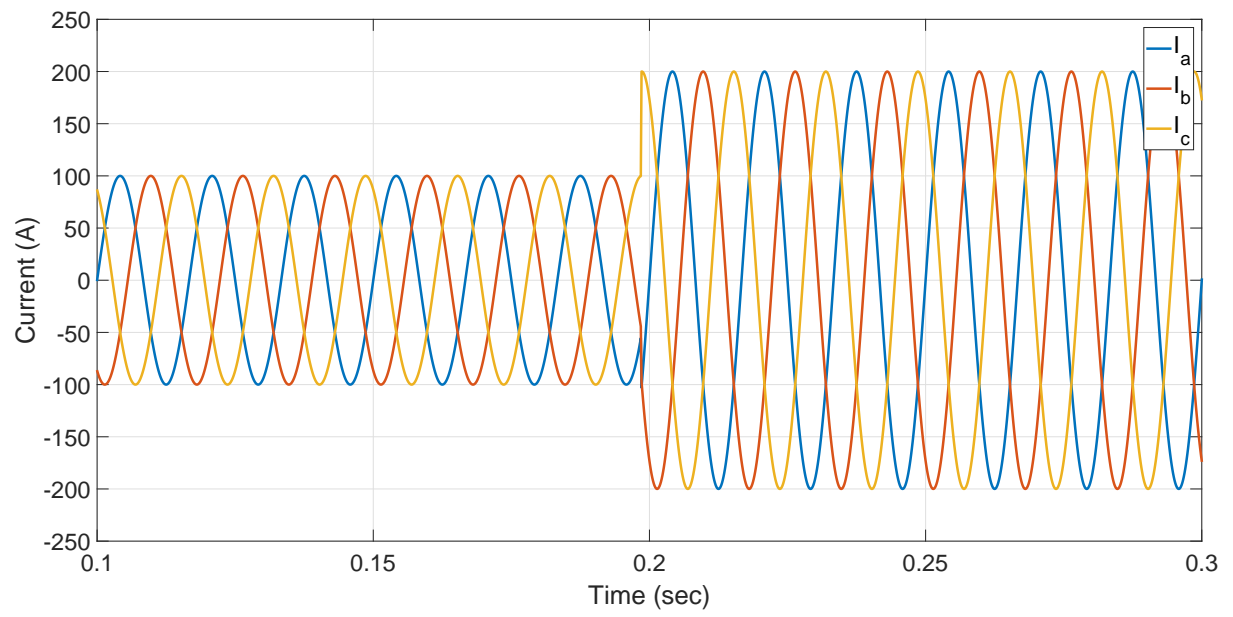
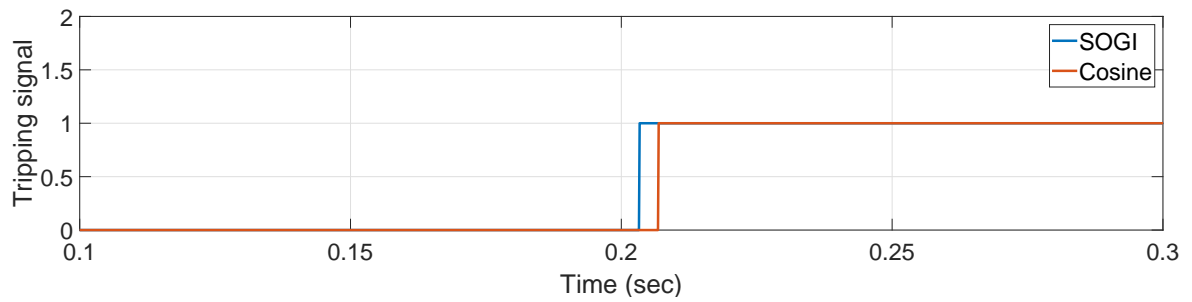
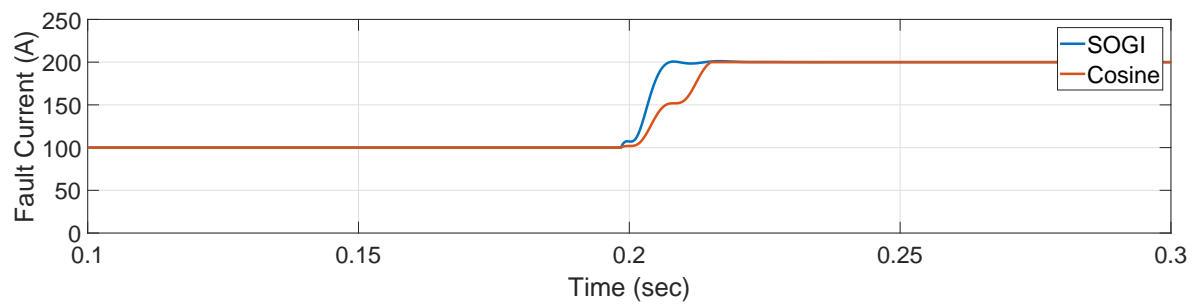


Figure 5.22: Simulation results with distribution data: (a) currents and its sequences, and (b) tripping signal and angle.



(a)



(b)

Figure 5.23: (a) Fault current waveforms, and (b) fault detections in phase a .

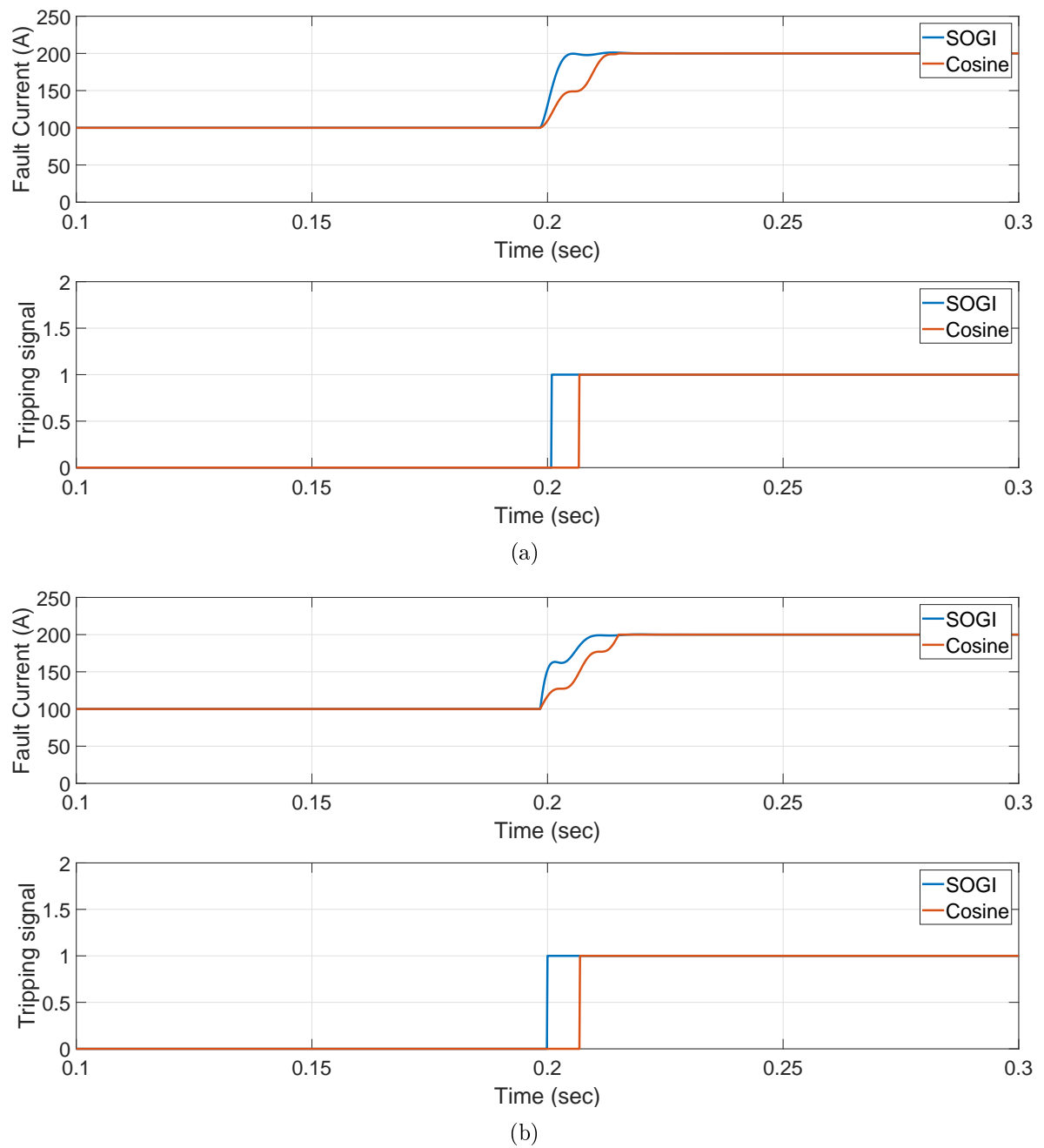
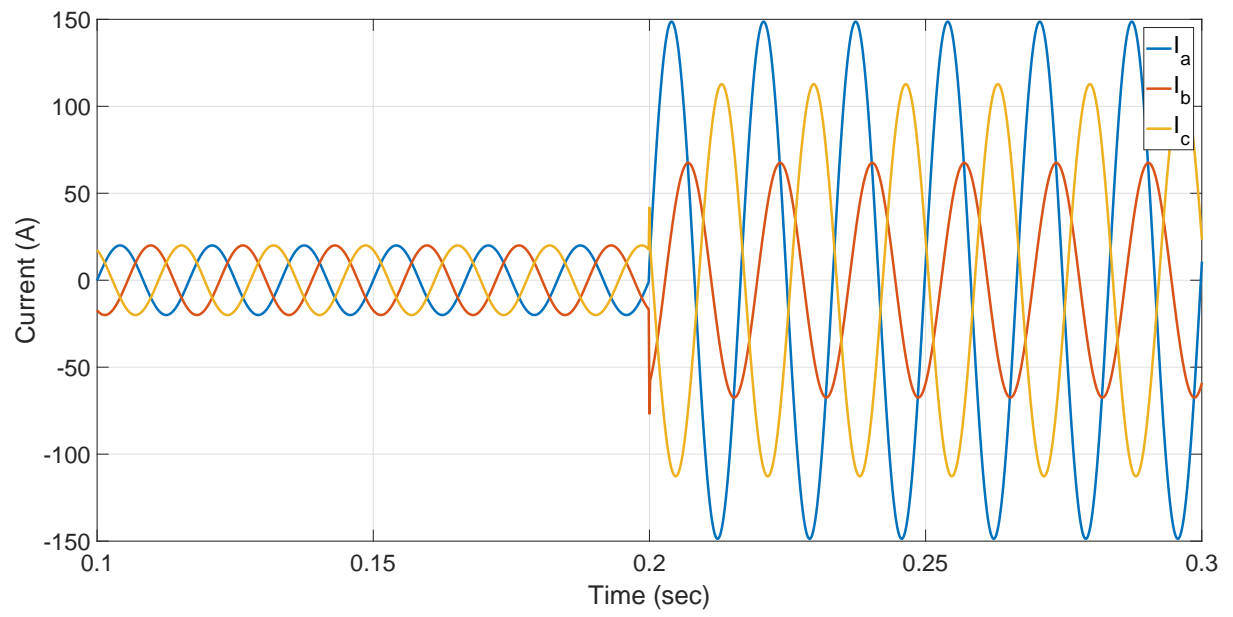
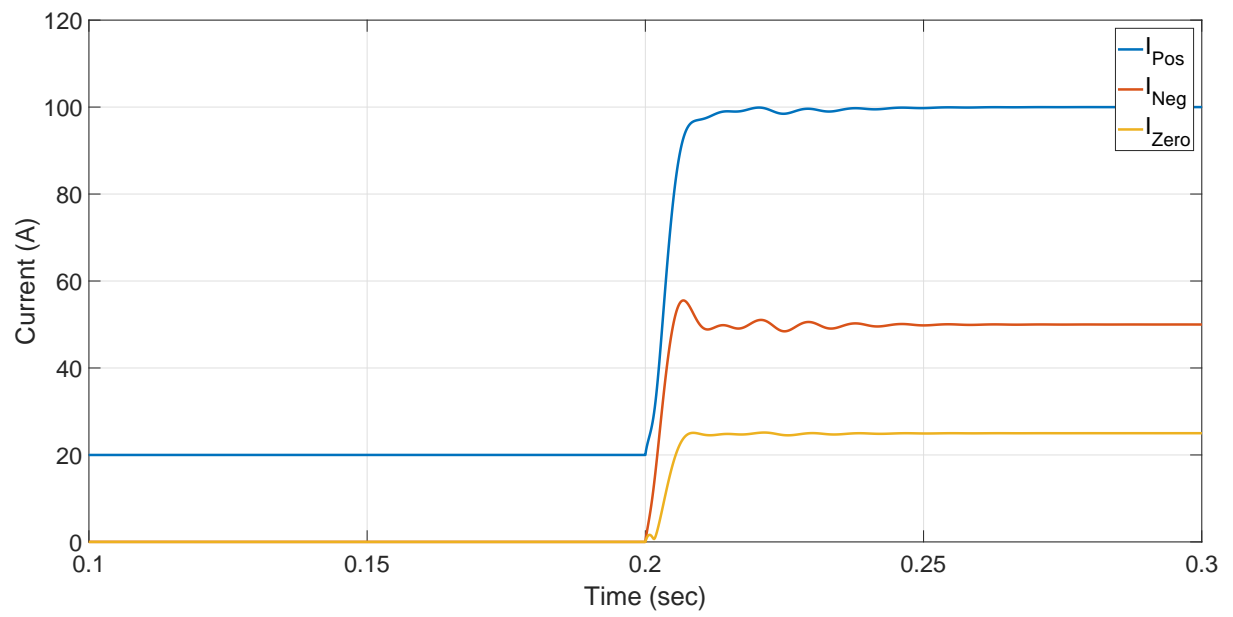


Figure 5.24: (a) Fault detections in phase *b*, and (b) fault detections in phase *c*.



(a)



(b)

Figure 5.25: Sequence estimation: (a) the current waveforms, and (b) current magnitudes.

Chapter 6

Hardware Testing for LFAC Transmission

This chapter presents our preliminary testing results for our hardware experiments for low frequency transmission systems. We want to verify the benefits of low frequency operation over the conventional 60 Hz by the voltage profile along the line. Our final target is testing a multi-frequency power system operation, which consists of a 60 Hz and a low frequency system, on our test-bed facility. The test-bed is a complete model of a real world power system with the transmission level scaled at 208 V, and distribution level with loads scaled at 41.6V. A power converter system is also developing to integrate a low frequency system into the test-bed for further study and testing. The following sections update our current work on this project.

6.1 Hardware Testing for Low Frequency AC Transmissions

The entire test-bed power system to verify theoretical analysis and simulation results for low frequency operations is shown in Fig. 6.1. This test-bed is a reflection of a transmission system and a distribution system that are scaled down to 208 V and 41.6 V, respectively. This system has two types of transmission lines: one for a normal 60 Hz and one for a low frequency. Since we only do the experiments on the low frequency transmission line, the detailed description of the setup system is presented as follows.

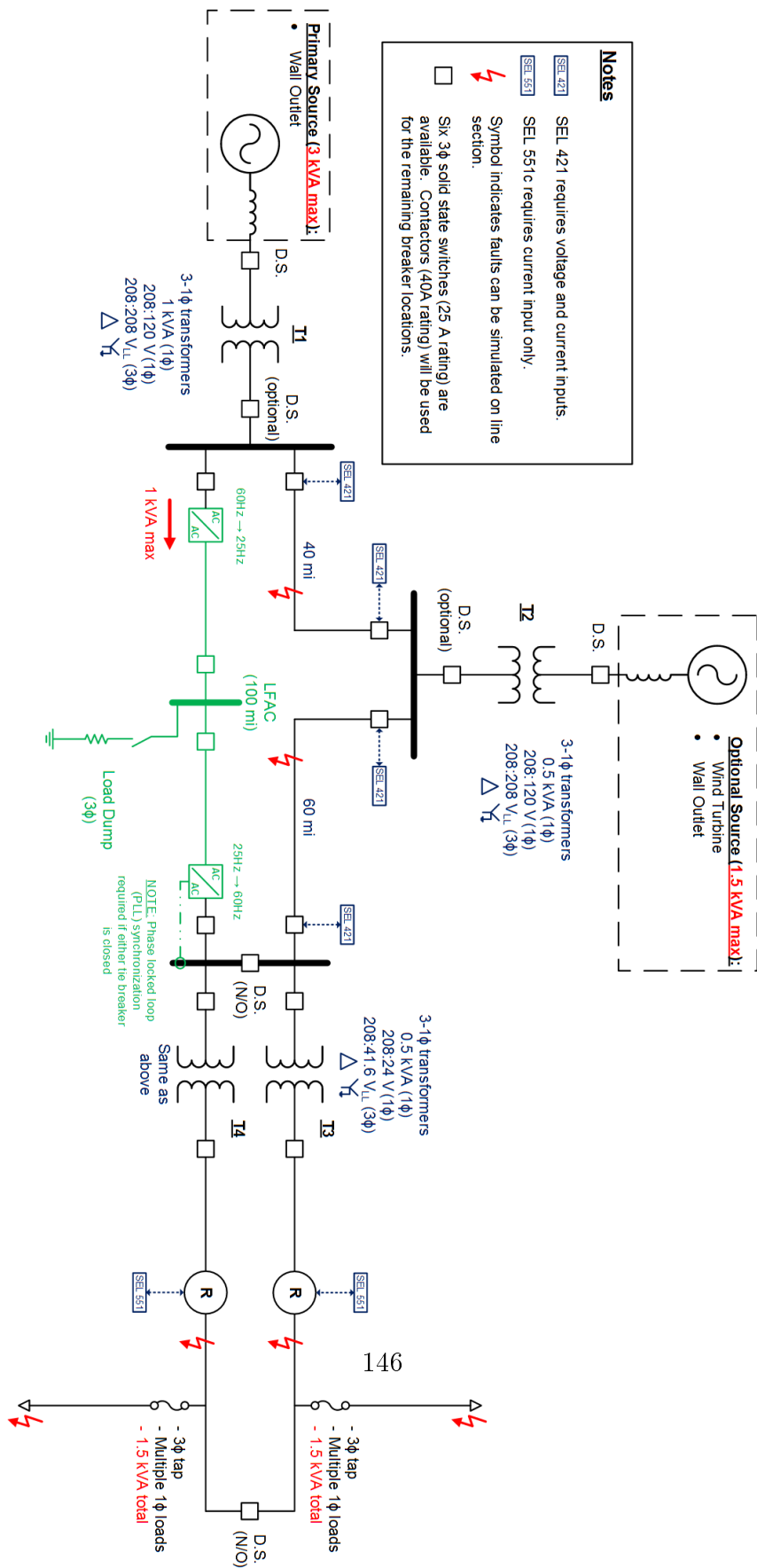


Figure 6.1: One-line diagram of the small-scaled testbed power system.

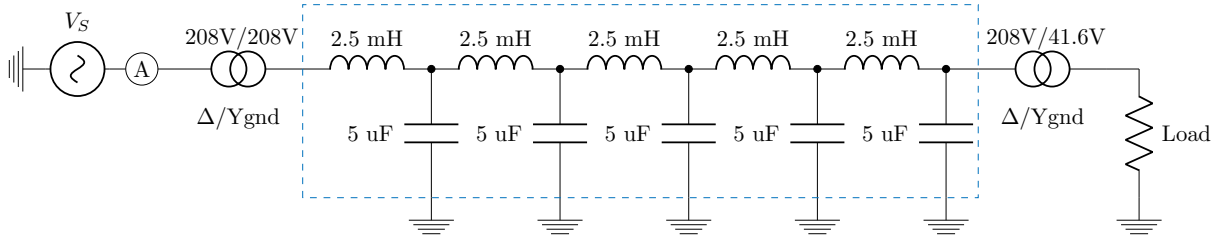


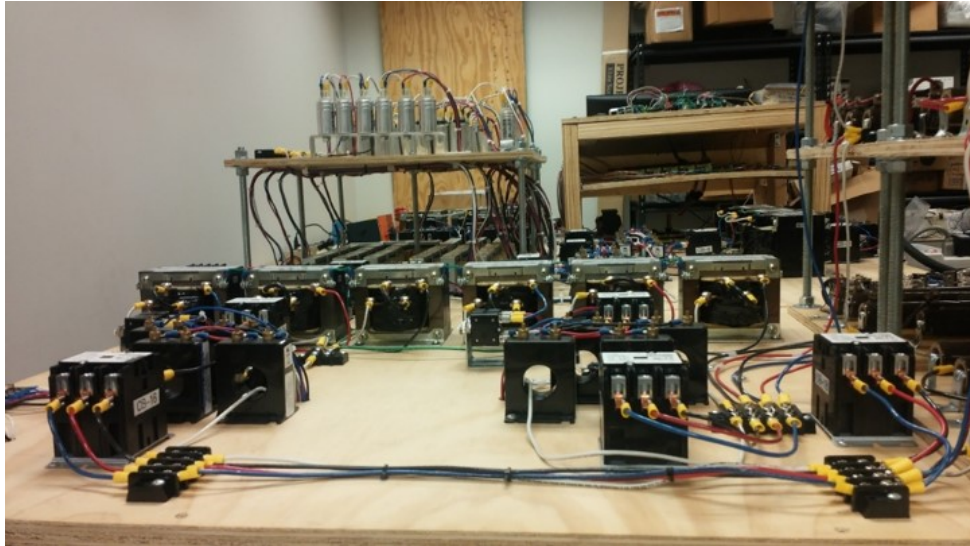
Figure 6.2: One-line diagram of the power system for LFAC operation testing.

The Hardware System for LFAC Operation Testing

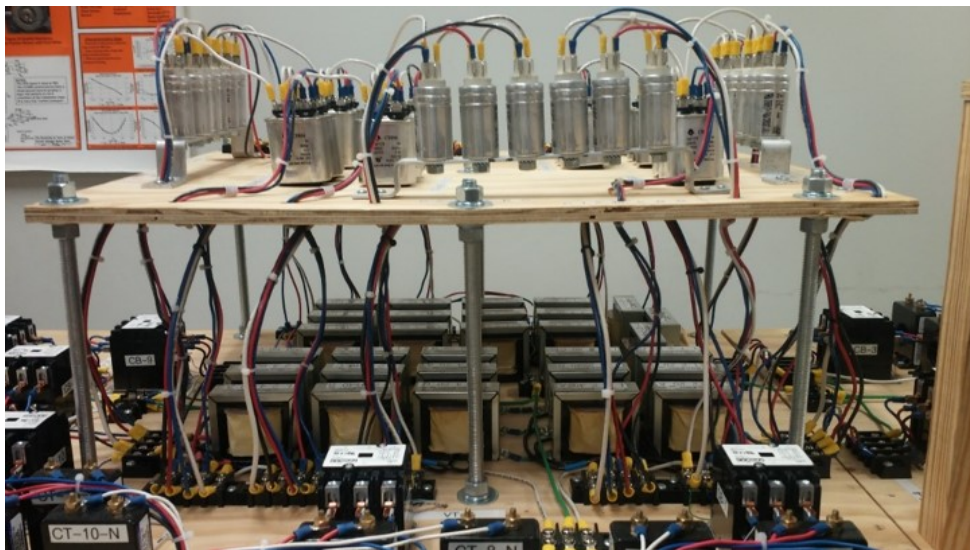
Fig. 6.2 presents the one-line diagram of our hardware system. This system is powered by a variable frequency voltage source V_S . This source is isolated from the remaining circuit by a 3-kVA, 208V/208V transformer connected in Δ -Y_{gnd}. The other terminal of this transformer is then connected to an LC circuit, which is a model of a 100-mile transmission line. The transmission line is subdivided into five 20-mile segments, making it is easier to access voltage data along the line. Each line segment consists of a 2.5-mH inductor with 0.1Ω internal resistance and a $5\text{-}\mu\text{F}$ capacitor, as shown in Fig. 6.3(b). The transmission line is then connected to a step-down 1.5-kVA, 208V/41.6V transformer. This transformer supplies power to a resistive load. The total load is $R_{load} = 0.7143\Omega$ which consists of two $2.5\text{-}\Omega$ and three $5\text{-}\Omega$ resistors connected in parallel.

In order to generate variable frequency, a Yaskawa G7 inverter is used as a power source. Since this inverter is primary utilized for motor drive, the frequency range is 40 - 400 Hz. Thus, our experiments are conducted with a frequency range from 40 Hz to 80 Hz to verify the theories. The inverter output voltage is set at 170 V line-to-line to avoid the over current issues. It is also important to mention that the inverter output contains

harmonic components and that these harmonics are expected to have some effect on the measurement, especially at light load conditions.



(a)



(b)

Figure 6.3: (a) The test-bed power grid, and (b) transmission line model.

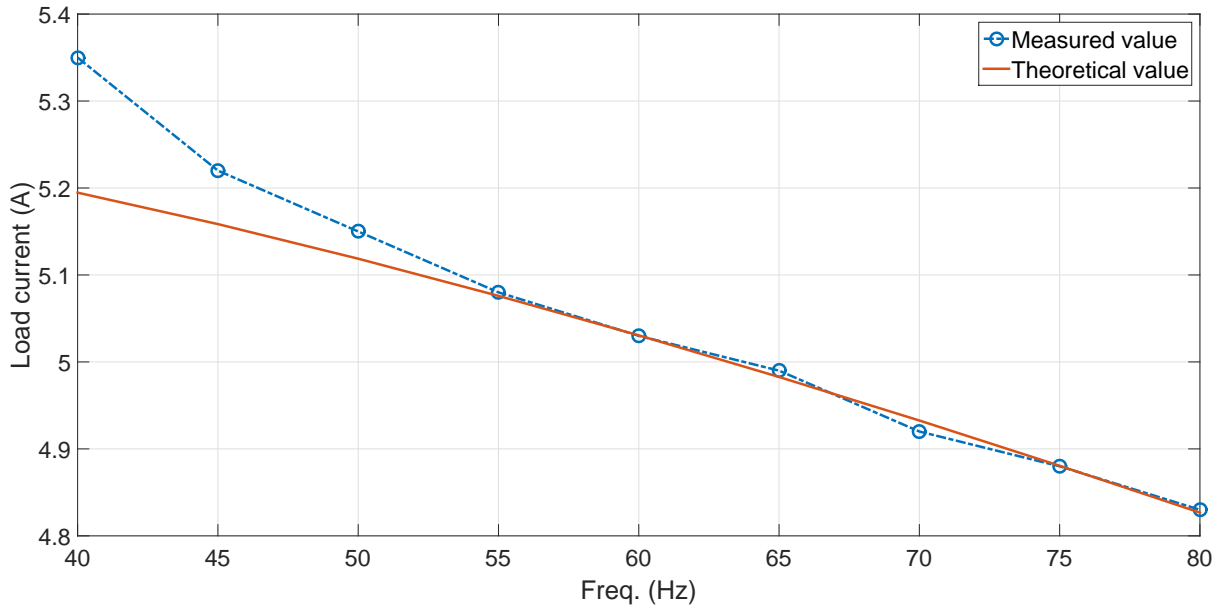
The test-bed system is powered and tested with two scenarios: at no-load ($R_{load} = \infty$) condition and at loaded ($R_{load} = 0.7143\Omega$) condition. It is also worthwhile to mention that because the loads are resistors, the effects of frequency changes are observed by current waveforms. The currents are measured at the inverter output terminals, denoted as (A) in Fig. 6.2. The current values at different frequencies are collected in detail in Table. 6.1, and visualized in Fig. 6.4. At loaded condition, the measured current values are close to the theoretical values because the inductors can filter harmonic currents. Fig. 6.5 presents the current waveforms that the source supplies to the power system for three different frequencies, i.e. 40 Hz, 60 Hz, and 80 Hz, respectively. The loaded currents are given by

$$I_{Load} = \frac{V_S}{\sqrt{(R_{eq}^2 + X_{eq}^2)}} = \frac{V_S}{\sqrt{(R_{eq}^2 + (2\pi L_{eq}f)^2)}} \quad (6.1)$$

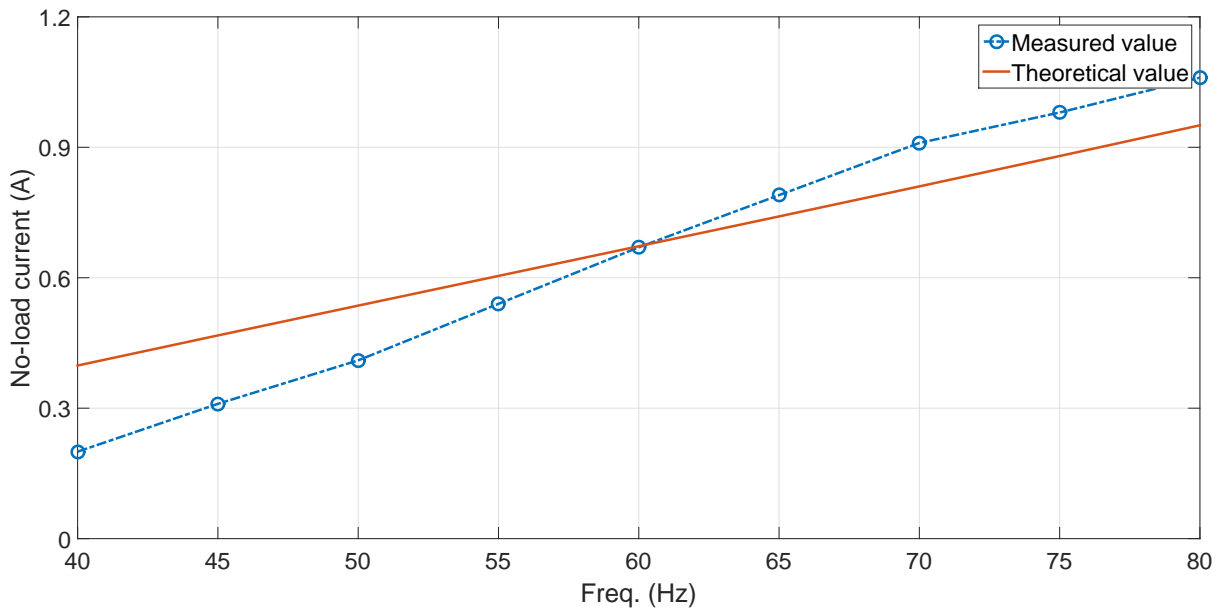
where R_{eq} and L_{eq} are denoted as the equivalent resistance and inductance of the circuit. As the operating frequency is lowered, the current magnitude is increased due to the system impedance as shown in Fig. 6.4(a). At no-load condition, the inverter supplies power to charge the capacitors. The charging current in a low frequency system is predictably less than that in a 60 Hz system. This result agrees with the analysis in Fig. 2.9(b). Note that at the no-load condition, there is a large difference in current between the measured value and the theoretical value due to the harmonics as seen in Fig. 6.6.

Table 6.1: Current magnitude (A) at different load conditions.

Freq.	40 Hz	50 Hz	60 Hz	70 Hz	80 Hz
$I@R_{load} = 0.7143\Omega$	5.35	5.15	5.03	4.92	4.83
$I@R_{load} = \infty$	0.21	0.41	0.67	0.91	1.06

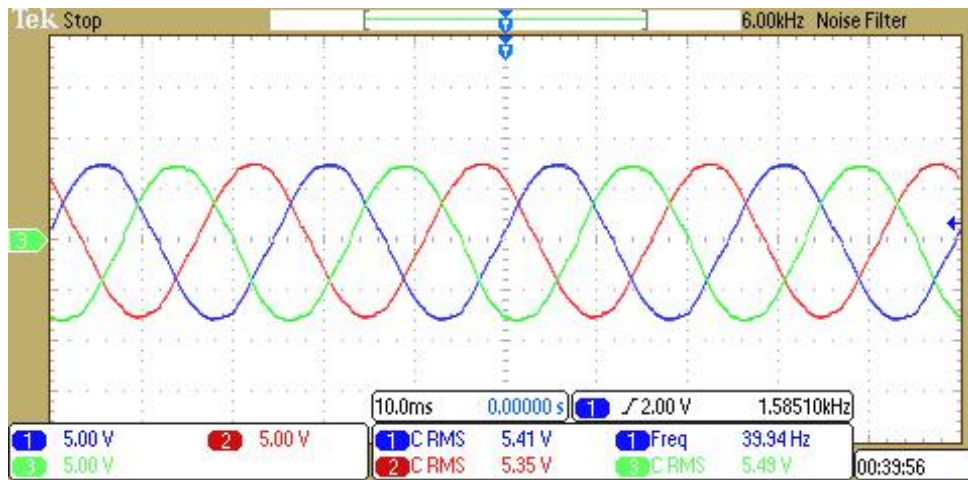


(a)

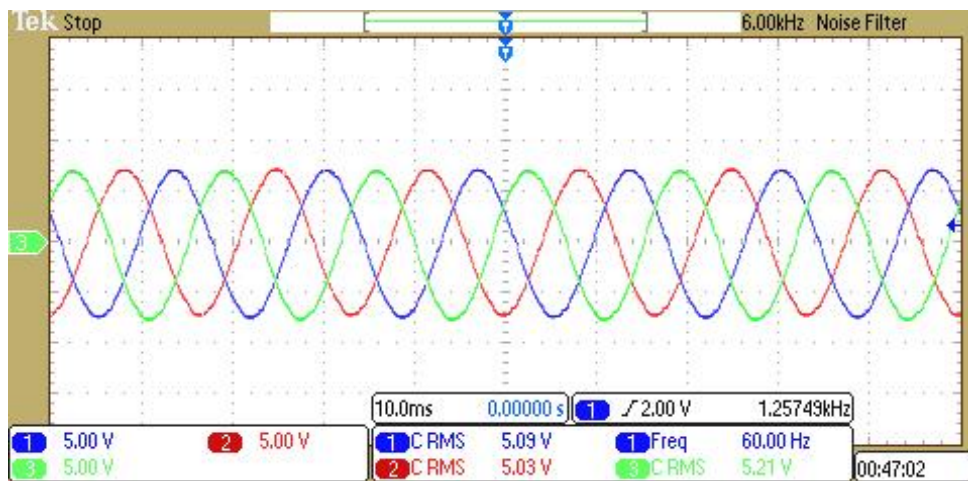


(b)

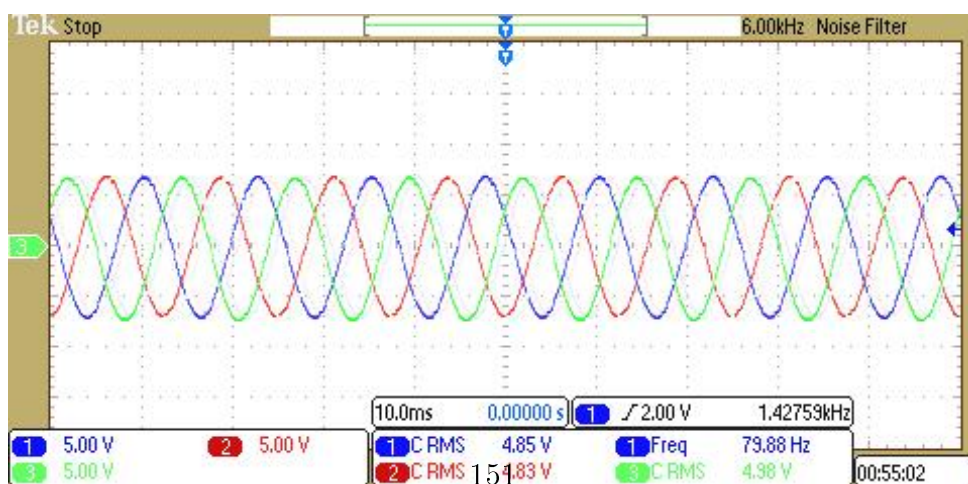
Figure 6.4: Current magnitude at different frequency at: (a) loaded condition, and (b) no-load condition.



(a)

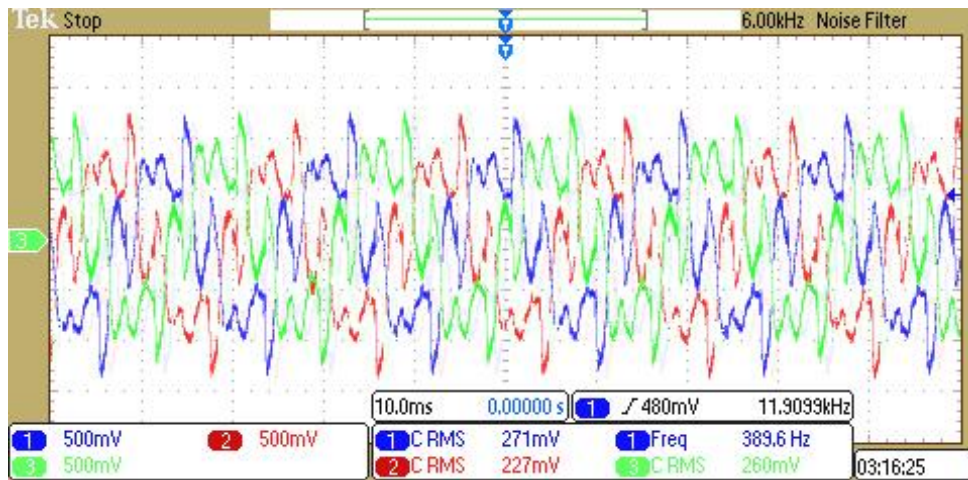


(b)

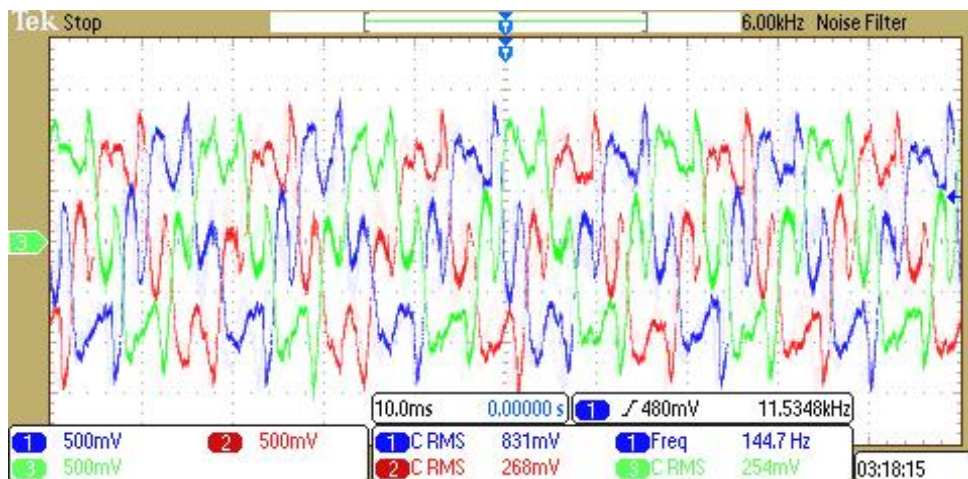


(c)

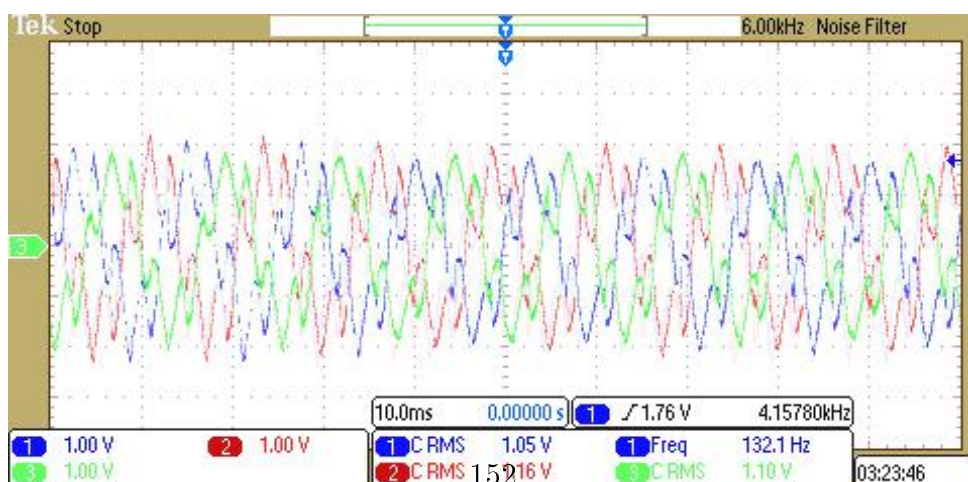
Figure 6.5: The load current waveforms flowing into the system: a) 40 Hz, b) 60 Hz, and c) 80 Hz.



(a)



(b)



(c)

Figure 6.6: The no-load current waveforms flowing into the system: a) 40 Hz, b) 60 Hz, and c) 80 Hz.

The next step is to verify the voltage profile along the transmission line. The voltage of each line segment is measured on the capacitor. The circuit in Fig. 6.2 is also simulated in PSCAD/EMTDC to compare. The data is presented in Table. 6.2 and in Fig. 6.7(a). The measured voltage values are close to the simulated ones. The voltage along the line in a low frequency system is larger compared to that in a 60 Hz system, which is matching with the analysis in Fig. 2.10. This is because less voltage drop on the transmission line at low frequency. The sending-end and the receiving-end voltage waveforms at different frequencies are also presented in Fig. 6.8 and Fig. 6.9, respectively.

Table 6.2: RMS Voltage (V) along the line at different frequencies.

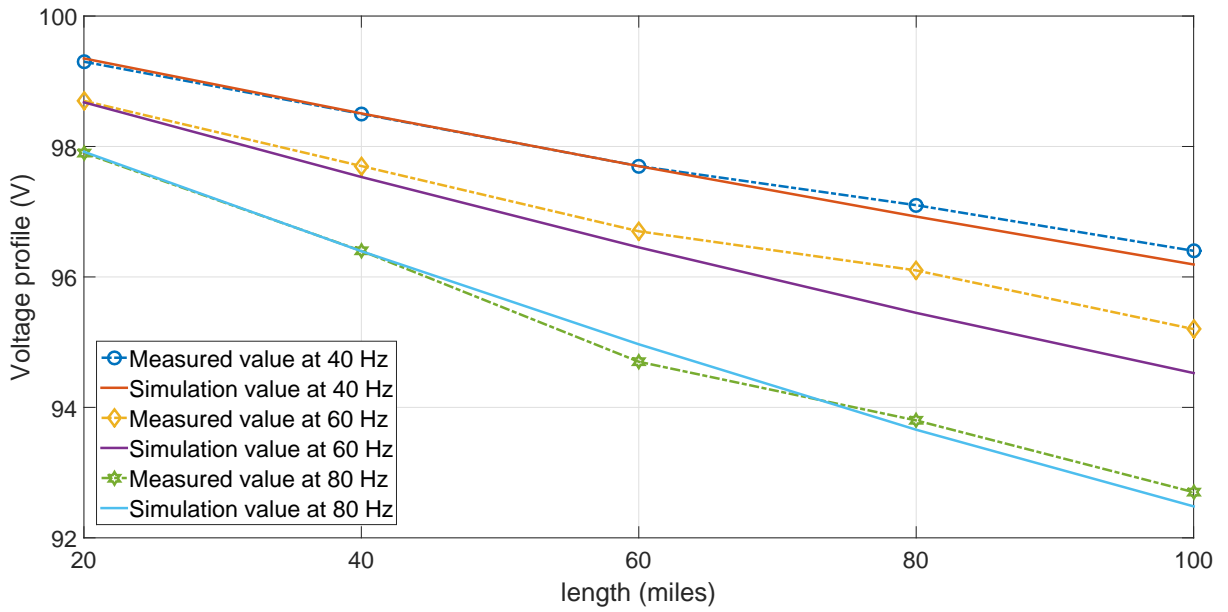
Freq.	V20	V40	V60	V80	V100
40 Hz	99.3	98.5	97.7	97.1	96.4
50 Hz	98.9	98.2	97.3	96.7	95.8
60 Hz	98.7	97.7	96.7	96.1	95.2
70 Hz	98.3	96.9	96.0	95.0	94.0
80 Hz	97.9	96.4	94.7	93.8	92.7

The experimental voltage data is also compared with the voltage from the distributed line model which is calculated from (2.4) as follows:

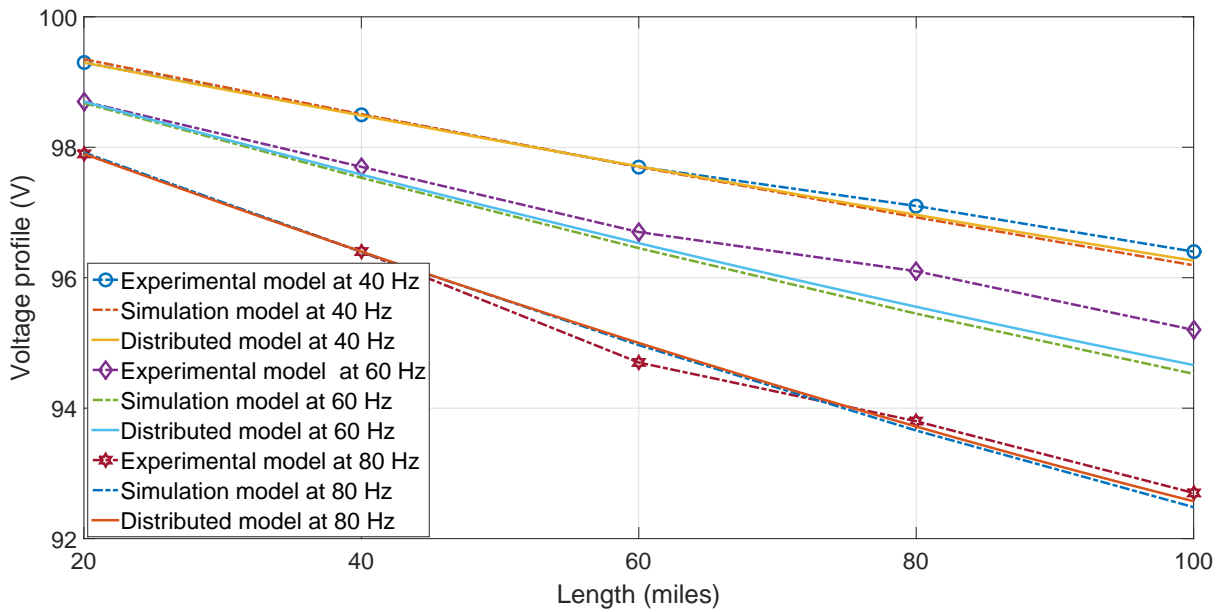
$$V(x) = \cosh(\gamma x)V_R + Z_c \sinh(\gamma x)I_R$$

$$I(x) = (1/Z_c)\sinh(\gamma x)V_R + \cosh(\gamma x)I_R$$

The voltage data is calculated from the above equations. For example, with $Z_C = 22.42\angle-3^\circ \Omega$ and $\gamma = 0.0021\angle 87^\circ$ at 60 Hz, the voltage and current at the receiving-end are: $V_R = 94.66\angle-11.58^\circ \text{ V}$ and $I_R = 5.29\angle-15.28^\circ \text{ A}$. The voltage data at different frequencies are shown in Fig. 6.7(b) for detail. The results are similar to those in Fig. 6.7(a). The voltages from simulation and theoretical calculation are almost the same. The results again are matched with the studies for low frequency operation in Chapter 2.

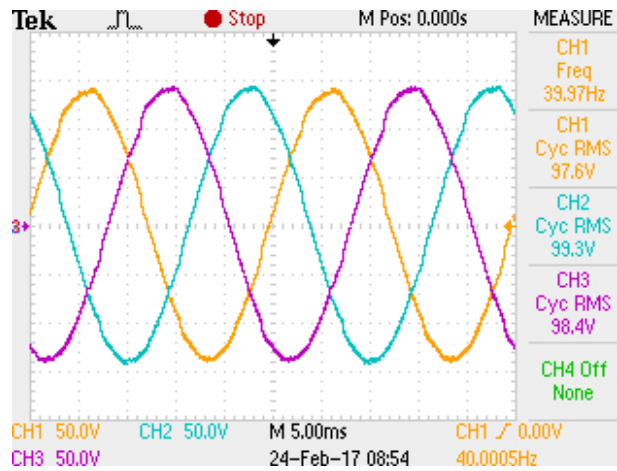


(a)

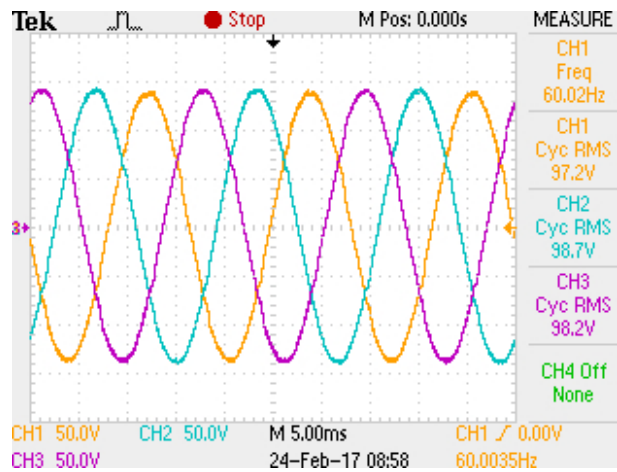


(b)

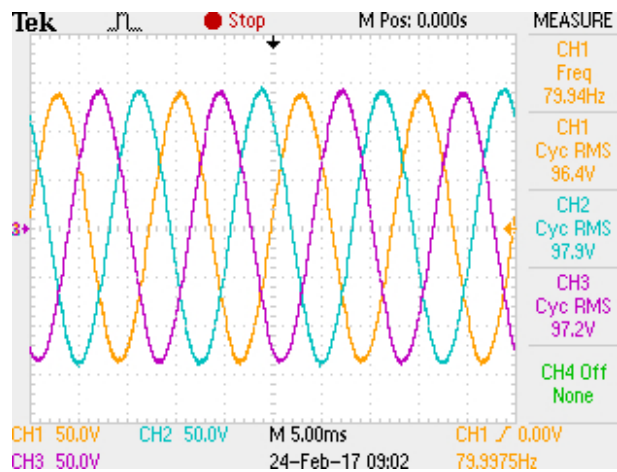
Figure 6.7: Voltage magnitude along the transmission line: (a) Experiment and simulation data, and (b) experimental, simulation, and theoretical data.



(a)

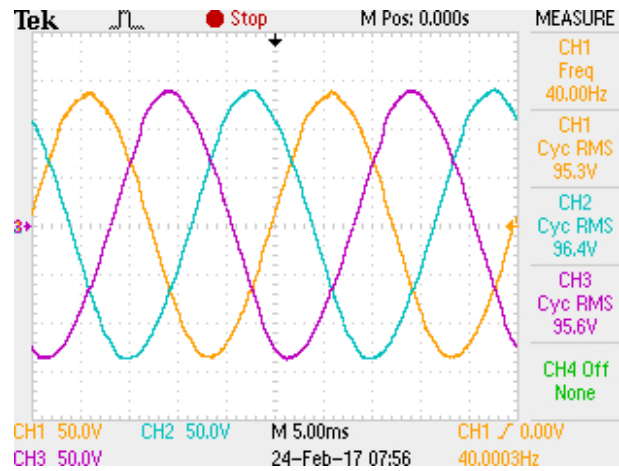


(b)

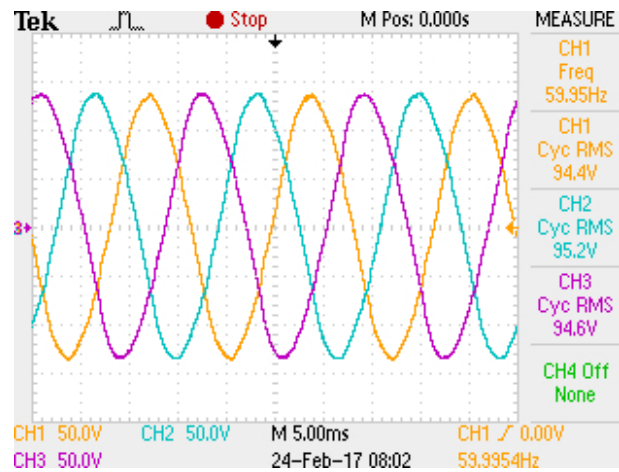


(c)

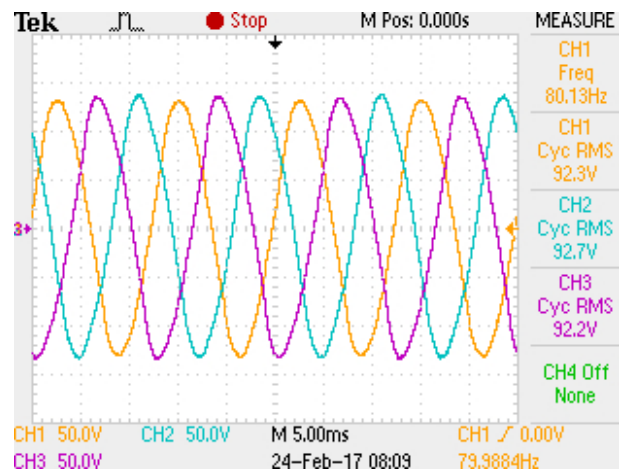
Figure 6.8: Voltages at the sending-end terminal: a) 40 Hz, b) 60 Hz, and c) 80 Hz.



(a)



(b)



(c)

Figure 6.9: Voltages at the receiving-end terminal: a) 40 Hz, b) 60 Hz, and c) 80 Hz.

Chapter 7

Conclusion

7.1 Conclusion

The objective of the work outlined in this dissertation is to explore the benefits of a low frequency ac transmission system at steady-state, study the voltage stability, and improve the system protection for low frequency operation. Chapter 2 investigates the steady-state performances of the transmission line at a low frequency operation. First, the skin effect on transmission line parameters is modeled. It is concluded that the transmission line model developed in 60 Hz system is applicable to a low frequency system. Next, the power transfer capability is examined carefully and compared between different frequencies. As the operating frequency is reduced, the transmission line is more capable of transmitting power. For example, a transmission line can increase its capability six times if the operating frequency is 10 Hz instead of 60 Hz. In this chapter, the voltage profile along the transmission line is also studied. The results show that at the full-load condition, the voltages at low frequencies are higher compared to those of 60 Hz. At the no-load condition, the voltage at the receiving-end terminal in a 60 Hz system is above the upper limit, i.e. 1.05 pu, and thus it is required to have compensation devices at the terminals to reduce the voltage. In a low frequency system, for example a 5 Hz system, the voltage is close to 1.0 pu and ideally this system does not need the compensation devices. The detail of low frequency steady-state performance can be found in [87].

Chapter 3 presents work on the system voltage stability under low frequency operation. First, the conventional $V - P$ and $Q - V$ characteristic curves are investigated. The results show that the Q-reserve margin in a 5 Hz system is more than 8 times that of the 60 Hz system. This means the low frequency system is more stable compared to the conventional 50/60 Hz system. Next, the eigenvalue at each bus, a critical index for system stability, is calculated based on the modal analysis method. This eigenvalue decreases significantly as the operating frequency increases. For example, the eigenvalue in a two-bus system is 100.2511 at 5 Hz and reduces to 8.6873 at 60 Hz. This means the low frequency operation helps improve power system stability by driving each bus further away from the instable operating point. In this chapter, we also propose to use the modified eigenvalue index for a low frequency system. This index considers both impacts of real and reactive power variations on the voltage, and thus better represents the low frequency stability. This work on low frequency stability is published in [14, 15, 88].

Chapter 4 demonstrates the work on interfacing two power systems operating at different frequencies. The SOGI-FLL method - a synchronization method which is utilized in the power converters to identify the grid information such as voltage phase and magnitude, and frequency - is first explored. Under harmonic conditions, however, the SOGI-FLL cannot determine accurately the grid information. The third-order SOGI-based is thus proposed to improve the grid synchronization system performance. Simulation results show that the proposed method can identify accurately the voltage magnitude, phase angle, and frequency. Next, the proportional-resonant (PR) controller for power converters is studied. This control approach reduces the complexity of the converter control system. However, this PR controller is sensitive to frequency variations, and thus

we propose a new *PR* controller. The proposed controller is less sensitive and is able to completely track reference signals under frequency variation conditions. This chapter also presents the time domain simulation of voltage and current waveforms at low frequency operation. The voltage and current are sinusoidal and contains less harmonics compared to those from the cyclo-converter. The work from this chapter is published in [89, 90, 91].

Chapter 5 first presents a study on low frequency transmission in terms of protection perspectives. The critical clearing time, the maximum time that a fault can stay in the system without losing its stability, is calculated for different operating frequencies. The results show that a low frequency system is more robust and allows faults to stay longer compared to a 60 Hz system. For example, with the same fault the critical clearing time in a 5 Hz is 1.3896 seconds while it is 0.115 seconds in a 60 Hz system. Next, we propose to use the SOGI-FLL technique to quickly detect the faults. The proposed method shows it is superior compared to the cosine filter method, which is used in protection relays. For example, the proposed method detects a single line-to-ground fault in a 60 Hz system in 3.17 milliseconds while the cosine filter method requires 5.2 milliseconds. The fast performance of the proposed method is clearer in a low frequency system. For example, in a 10 Hz system, the proposed method detects the fault after 12.55 milliseconds while the cosine filter method identifies this fault after 26.6 milliseconds. Part of this work on low frequency protection is published in [92]. Chapter 6 shows the experiments to verify the theoretical analysis of low frequency operation. A test-bed power system in our laboratory is used for demonstrations. The experiments verify that low frequency operation has benefits in terms of power transfer and voltage profile along the transmission line.

In summary, this dissertation presents our key contributions to the low frequency transmission research as follows:

- Provided a comprehensive study of steady-state performance of a power system under low frequency operation.
- Studied the power system voltage stability under low frequency operation and proposed a modified eigenvalue index that better represents low frequency system stability.
- Developed a new grid synchronization configuration and a new proportional-resonant controller that improve power converter performance under harmonic and frequency variation conditions, modeled in the time domain the interfacing of a 60 Hz system and a low frequency system.
- Studied the protection and proposed a new method to quickly detect faults in a low frequency system.
- Demonstrated the low frequency transmission benefits in terms of power transfer and voltage profile in a test-bed platform.

Bibliography

- [1] T. Funaki and K. Matsuura, “Feasibility of the low frequency ac transmission,” in *Power Engineering Society Winter Meeting, 2000. IEEE*, vol. 4, 2000, pp. 2693–2698 vol.4.
- [2] PSERC, *Low Frequency Transmission*. PSERC Publication, 2012, http://www.pserc.wisc.edu/documents/publications/reports/2012_reports/Meliopoulos_PSERC_Report_S-42_Oct_2012_ExSum.pdf.
- [3] W. Fischer, R. Braun, and I. Erlich, “Low frequency high voltage offshore grid for transmission of renewable power,” in *Innovative Smart Grid Technologies (ISGT Europe), 2012 3rd IEEE PES International Conference and Exhibition on*, Oct 2012, pp. 1–6.
- [4] H. Chen, M. Johnson, and D. Aliprantis, “Low-frequency ac transmission for offshore wind power,” *Power Delivery, IEEE Transactions on*, vol. 28, no. 4, pp. 2236–2244, Oct 2013.
- [5] N. Qin, S. You, Z. Xu, and V. Akhmatov, “Offshore wind farm connection with low frequency ac transmission technology,” in *Power Energy Society General Meeting, 2009. PES '09. IEEE*, July 2009, pp. 1–8.
- [6] Y. Cho, “Transient modeling of converters for hvdc system and lfacs systems,” Ph.D. dissertation, Georgia Institute of Technology, 2013.

- [7] J. Zaborszky and J. W. Rittenhouse, *Electric Power Transmission: The Power System in the Steady State*. The Rensselaer Bookstore, 1977.
- [8] J. Traphoner, “Evaluation of Impedance Parameters in Transmission Lines,” Master’s thesis, The University of Texas at Austin, Texas, 2014.
- [9] R. E. Collin, *Foundations for Microwave Engineering*. Wiley-IEEE Press, 2001.
- [10] J. Glover, M. Sarma, and T. Overbye, *Power System Analysis and Design*. Cengage Learning, 2011.
- [11] P. Kundur, *Power System Stability and Control*. McGraw-Hill, Inc, 1994.
- [12] A. Bergen and V. Vittal, *Power System Analysis*. Prentice Hall, 2000.
- [13] A. Canelhas, S. Karamitsos, U. Axelsson, and E. Olsen, “A low frequency power collector alternative system for long cable offshore wind generation,” in *AC and DC Power Transmission, 11th IET International Conference on*, Feb 2015, pp. 1–6.
- [14] T. Ngo and S. Santoso, “Modal-based voltage stability analysis of low frequency ac transmission systems,” in *2016 IEEE/PES General Meeting (IEEE PES16)*, July 2016, pp. 1–5.
- [15] Q. Nguyen, T. Ngo, and S. Santoso, “Power flow solution for multi-frequency ac and multi-terminal hvdc power systems,” in *2016 IEEE Power and Energy Society General Meeting (PESGM)*, July 2016, pp. 1–5.

- [16] ———, “Power flow solution for multi-frequency ac power systems,” in *2016 IEEE/PES Transmission and Distribution Conference and Exposition (T D)*, May 2016, pp. 1–5.
- [17] S. G. W and A. H. El-Abaid, *Computer Methods in Power System Analysis*. McGraw-Hill, Inc, 1968.
- [18] H. Le and S. Santoso, “Analysis of voltage stability and optimal wind power penetration limits for a non-radial network with an energy storage system,” in *Power Engineering Society General Meeting, 2007. IEEE*, June 2007, pp. 1–8.
- [19] B. Gao, G. Morison, and P. Kundur, “Voltage stability evaluation using modal analysis,” *Power Systems, IEEE Transactions on*, vol. 7, no. 4, pp. 1529–1542, Nov 1992.
- [20] R. Teodorescu, M. Liserre, and P. Rodriguez, *Grid Converter for Photovoltaic and Wind Power Systems*. John Willey and Son, Ltd, 2011.
- [21] M. Ciobotaru, R. Teodorescu, and F. Blaabjerg, “A new single-phase pll structure based on second order generalized integrator,” in *37th IEEE PESC '06.*, 2006, pp. 1–6.
- [22] P. Rodriguez, A. Luna, I. Candela, R. Teodorescu, and F. Blaabjerg, “Grid synchronization of power converters using multiple second order generalized integrators,” in *34th IEEE IECON 2008.*, 2008, pp. 755–760.

- [23] P. Rodriguez, R. Teodorescu, I. Candela, A. Timbus, M. Liserre, and F. Blaabjerg, “New positive-sequence voltage detector for grid synchronization of power converters under faulty grid conditions,” in *37th IEEE PESC '06.*, 2006, pp. 1–7.
- [24] P. Rodriguez, J. Pou, J. Bergas, J. Candela, R. Burgos, and D. Boroyevich, “Decoupled double synchronous reference frame pll for power converters control,” *Power Electronics, IEEE Trans. on*, vol. 22, no. 2, pp. 584–592, 2007.
- [25] W. Li, X. Ruan, C. Bao, D. Pan, and X. Wang, “Grid synchronization systems of three-phase grid-connected power converters: A complex-vector-filter perspective,” *Industrial Electronics, IEEE Transactions on*, vol. 61, no. 4, pp. 1855–1870, April 2014.
- [26] J. Li, J. Zhao, J. Wu, and P. ping Xu, “Improved dual second-order generalized integrator pll for grid synchronization under non-ideal grid voltages including dc offset,” in *Energy Conversion Congress and Exposition (ECCE), 2014 IEEE*, Sept 2014, pp. 136–141.
- [27] F. Golnaraghi and B. Kuo, *Automatic Control Systems*. Wiley, 2009.
- [28] P. Rodriguez, A. Luna, M. Ciobotaru, R. Teodorescu, and F. Blaabjerg, “Advanced grid synchronization system for power converters under unbalanced and distorted operating conditions,” in *32nd IEEE Industrial Electronics Conference, 2006. IECON 2006*, 2006, pp. 5173–5178.
- [29] S. Santoso, *Fundamentals of Electric Power Quality*. CreateSpace Independent Publishing Platform, 2010.

- [30] F. Rodriguez, E. Bueno, M. Aredes, L. Rolim, F. Neves, and M. Cavalcanti, "Discrete-time implementation of second order generalized integrators for grid converters," in *Industrial Electronics, 2008. IECON 2008. 34th Annual Conference of IEEE*, Nov 2008, pp. 176–181.
- [31] F. I. Bakhsh and D. K. Khatod, "Variable frequency transformer - state of the art review," in *2013 International Conference on Energy Efficient Technologies for Sustainability*, April 2013, pp. 1012–1017.
- [32] R. J. Piwko, E. V. Larsen, and C. A. Wegner, "Variable frequency transformer - a new alternative for asynchronous power transfer," in *2005 IEEE Power Engineering Society Inaugural Conference and Exposition in Africa*, July 2005, pp. 393–398.
- [33] N. Mohan, M. Undelan, and P. Robbins, *Power Electronics: Converters, Applications, and Design*. Wiley, 2002.
- [34] M. D. Singh. and K. B. Khanchandani., *Power Electronicsn*. McGraw-Hill, 2006.
- [35] L. Empringham, J. W. Kolar, J. Rodriguez, P. W. Wheeler, and J. C. Clare, "Technological issues and industrial application of matrix converters: A review," *IEEE Transactions on Industrial Electronics*, vol. 60, no. 10, pp. 4260–4271, Oct 2013.
- [36] J. Rodriguez, M. Rivera, J. W. Kolar, and P. W. Wheeler, "A review of control and modulation methods for matrix converters," *IEEE Transactions on Industrial Electronics*, vol. 59, no. 1, pp. 58–70, Jan 2012.

- [37] P. W. Wheeler, J. Rodriguez, J. C. Clare, L. Empringham, and A. Weinstein, "Matrix converters: a technology review," *IEEE Transactions on Industrial Electronics*, vol. 49, no. 2, pp. 276–288, Apr 2002.
- [38] J. W. Kolar, T. Friedli, J. Rodriguez, and P. W. Wheeler, "Review of three-phase pwm ac - ac converter topologies," *IEEE Transactions on Industrial Electronics*, vol. 58, no. 11, pp. 4988–5006, Nov 2011.
- [39] L. Empringham, J. W. Kolar, J. Rodriguez, P. W. Wheeler, and J. C. Clare, "Technological issues and industrial application of matrix converters: A review," *IEEE Transactions on Industrial Electronics*, vol. 60, no. 10, pp. 4260–4271, Oct 2013.
- [40] M. D. Bellar, T. S. Wu, A. Tchamdjou, J. Mahdavi, and M. Ehsani, "A review of soft-switched dc-ac converters," *IEEE Transactions on Industry Applications*, vol. 34, no. 4, pp. 847–860, July 1998.
- [41] S.-K. Sul, *Control of Electric Machine Drive Systems*. Willey-IEEE Press, 2011.
- [42] K. H. Nam, *AC Motor Control and Electrical Vehicle Applications*. CRC Press, 2010.
- [43] D. G. Holmes and T. A. Lipo, *Pulse Width Modulation for Power Converters Principles and Practice*. IEEE Press Series on Power Engineering, 2003.
- [44] T. A. Lipo, *Introduction to AC Machine Design*. University of Wisconsin, 2007.
- [45] H.-S. Song and K. Nam, "Dual current control scheme for pwm converter under unbalanced input voltage conditions," *IEEE Transactions on Industrial Electronics*, vol. 46, no. 5, pp. 953–959, Oct 1999.

- [46] A. Yoo, "Design and practice of motor drive system," Seoul National University, Tech. Rep., 2011.
- [47] M. P. Kazmierkowski and L. Malesani, "Current control techniques for three-phase voltage-source pwm converters: a survey," *IEEE Transactions on Industrial Electronics*, vol. 45, no. 5, pp. 691–703, Oct 1998.
- [48] R. Teodorescu, F. Blaabjerg, M. Liserre, and P. Loh, "Proportional-resonant controllers and filters for grid-connected voltage-source converters," *Electric Power Applications, IEE Proceedings*, vol. 153, no. 5, pp. 750–762, September 2006.
- [49] M. Ciobotaru, R. Teodorescu, and F. Blaabjerg, "Control of single-stage single-phase pv inverter," in *Power Electronics and Applications, 2005 European Conference on*, 2005, pp. 10 pp.–P.10.
- [50] D. Zmood, D. Holmes, and G. Bode, "Frequency domain analysis of three phase linear current regulators," in *Industry Applications Conference, 1999. Thirty-Fourth IAS Annual Meeting. Conference Record of the 1999 IEEE*, vol. 2, 1999, pp. 818–825 vol.2.
- [51] R. Teodorescu and F. Blaabjerg, "Proportional-resonant controllers. a new breed of controllers suitable for grid-connected voltage-source converters," in *International Conference on Optimization of Electrical and Electronic Equipments, Optim 2004*, vol. 3, 2004, pp. 9–14 vol.3.
- [52] A. Kuperman, "Proportional-resonant current controllers design based on desired transient performance," *IEEE Transactions on Power Electronics*, vol. 30, no. 10,

pp. 5341–5345, Oct 2015.

- [53] D. Zmood and D. Holmes, “Stationary frame current regulation of pwm inverters with zero steady-state error,” *Power Electronics, IEEE Transactions on*, vol. 18, no. 3, pp. 814–822, May 2003.
- [54] J. Hwang, P. Lehn, and M. Winkelnkemper, “A generalized class of stationary frame-current controllers for grid-connected ac-dc converters,” *Power Delivery, IEEE Transactions on*, vol. 25, no. 4, pp. 2742–2751, Oct 2010.
- [55] ———, “Control of grid connected ac-dc converters with minimized dc link capacitance under unbalanced grid voltage condition,” in *Power Electronics and Applications, 2007 European Conference on*, Sept 2007, pp. 1–10.
- [56] F. Blaabjerg, R. Teodorescu, M. Liserre, and A. V. Timbus, “Overview of control and grid synchronization for distributed power generation systems,” *IEEE Transactions on Industrial Electronics*, vol. 53, no. 5, pp. 1398–1409, Oct 2006.
- [57] J. W. G. Hwang, M. Winkelnkemper, and P. W. Lehn, “Design of an optimal stationary frame controller for grid connected ac-dc converters,” in *IEEE Industrial Electronics, IECON 2006 - 32nd Annual Conference on*, Nov 2006, pp. 167–172.
- [58] X. Yuan, J. Allmeling, W. Merk, and H. Stemmler, “Stationary frame generalized integrators for current control of active power filters with zero steady state error for current harmonics of concern under unbalanced and distorted operation conditions,” in *Industry Applications Conference, 2000. Conference Record of the 2000 IEEE*, vol. 4, Oct 2000, pp. 2143–2150 vol.4.

- [59] N. R. Zargari and G. Joos, "Performance investigation of a current-controlled voltage-regulated pwm rectifier in rotating and stationary frames," *IEEE Transactions on Industrial Electronics*, vol. 42, no. 4, Aug 1995.
- [60] S. A. Richter and R. W. D. Doncker, "Digital proportional-resonant (pr) control with anti-windup applied to a voltage-source inverter," in *Power Electronics and Applications (EPE 2011), Proceedings of the 2011-14th European Conference on*, Aug 2011, pp. 1–10.
- [61] S. Zhou, J. Liu, L. Zhou, and H. She, "Cross-coupling and decoupling techniques in the current control of grid-connected voltage source converter," in *Applied Power Electronics Conference and Exposition (APEC), 2015 IEEE*, March 2015, pp. 2821–2827.
- [62] H. Cha, T. K. Vu, and J. E. Kim, "Design and control of proportional-resonant controller based photovoltaic power conditioning system," in *Energy Conversion Congress and Exposition, 2009. ECCE 2009. IEEE*, Sept 2009, pp. 2198–2205.
- [63] S. Fukuda and T. Yoda, "A novel current-tracking method for active filters based on a sinusoidal internal model [for pwm invertors]," *IEEE Transactions on Industry Applications*, vol. 37, no. 3, pp. 888–895, May 2001.
- [64] R. I. Bojoi, G. Griva, V. Bostan, M. Guerriero, F. Farina, and F. Profumo, "Current control strategy for power conditioners using sinusoidal signal integrators in synchronous reference frame," *IEEE Transactions on Power Electronics*, vol. 20, no. 6, pp. 1402–1412, Nov 2005.

- [65] D. G. Holmes, T. A. Lipo, B. P. McGrath, and W. Y. Kong, "Optimized design of stationary frame three phase ac current regulators," *IEEE Transactions on Power Electronics*, vol. 24, no. 11, pp. 2417–2426, Nov 2009.
- [66] P. Rodriguez, A. Luna, R. S. Munoz-Aguilar, I. Etxeberria-Otadui, R. Teodorescu, and F. Blaabjerg, "A stationary reference frame grid synchronization system for three-phase grid-connected power converters under adverse grid conditions," *IEEE Transactions on Power Electronics*, vol. 27, no. 1, pp. 99–112, Jan 2012.
- [67] J. Grainger and W. Stevenson, *Power System Analysis*, 1st ed. McGraw-Hill, Inc, 1994.
- [68] C. Rincon and J. Perez, "Calculating loadability limits of distance relays," in *Protective Relay Engineers, 2012 65th Annual Conference for*, April 2012, pp. 467–480.
- [69] H. I. Du, Y. J. Kim, D. H. Lee, B. S. Han, S. S. Song, S. C. Han, and J. P. Lee, "Effect of the resistance of two different coated conductor on the current-limiting performance of flux-lock type superconducting fault current limiters," *IEEE Transactions on Applied Superconductivity*, vol. 21, no. 3, pp. 1254–1257, June 2011.
- [70] B. W. Lee, J. Sim, K. B. Park, and I. S. Oh, "Practical application issues of superconducting fault current limiters for electric power systems," *IEEE Transactions on Applied Superconductivity*, vol. 18, no. 2, pp. 620–623, June 2008.
- [71] K. H. Hartung and V. Schmidt, "Limitation of short circuit current by an is-limiter," in *2009 10th International Conference on Electrical Power Quality and Utilisation*, Sept 2009, pp. 1–4.

- [72] C. Gandioli, M. C. Alvarez-Herault, P. Tixador, N. Hadjsaid, and D. M. R. Medina, “Innovative distribution networks planning integrating superconducting fault current limiters,” *IEEE Transactions on Applied Superconductivity*, vol. 23, no. 3, pp. 5 603 904–5 603 904, June 2013.
- [73] A. G. Phadke and J. S. Thorpe, *Computer Relaying for Power Systems*, 2nd ed. Wiley, 2009.
- [74] M. Öhrström and L. Söder, “Fast protection of strong power systems with fault current limiters and pll-aided fault detection,” *Power Delivery, IEEE Transactions on*, vol. 26, no. 3, pp. 1538–1544, July 2011.
- [75] X. Gong and W. Qiao, “Imbalance fault detection of direct-drive wind turbines using generator current signals,” *IEEE Transactions on Energy Conversion*, vol. 27, no. 2, pp. 468–476, June 2012.
- [76] M. El-Hami, L. L. Lai, D. J. Daruvala, and A. T. Johns, “A new travelling-wave based scheme for fault detection on overhead power distribution feeders,” *IEEE Transactions on Power Delivery*, vol. 7, no. 4, pp. 1825–1833, Oct 1992.
- [77] P. Jafarian and M. Sanaye-Pasand, “A traveling-wave-based protection technique using wavelet/pca analysis,” *IEEE Transactions on Power Delivery*, vol. 25, no. 2, pp. 588–599, April 2010.
- [78] X. Li, A. Dysko, and G. M. Burt, “Traveling wave-based protection scheme for inverter-dominated microgrid using mathematical morphology,” *IEEE Transactions on Smart Grid*, vol. 5, no. 5, pp. 2211–2218, Sept 2014.

- [79] C. Pang and M. Kezunovic, "Fast distance relay scheme for detecting symmetrical fault during power swing," *IEEE Transactions on Power Delivery*, vol. 25, no. 4, pp. 2205–2212, Oct 2010.
- [80] Z. He, L. Fu, S. Lin, and Z. Bo, "Fault detection and classification in ehv transmission line based on wavelet singular entropy," *IEEE Transactions on Power Delivery*, vol. 25, no. 4, pp. 2156–2163, Oct 2010.
- [81] A. R. Sedighi, M. R. Haghifam, O. P. Malik, and M. H. Ghassemian, "High impedance fault detection based on wavelet transform and statistical pattern recognition," *IEEE Transactions on Power Delivery*, vol. 20, no. 4, pp. 2414–2421, Oct 2005.
- [82] U. B. Parikh, B. Das, and R. P. Maheshwari, "Combined wavelet-svm technique for fault zone detection in a series compensated transmission line," *IEEE Transactions on Power Delivery*, vol. 23, no. 4, pp. 1789–1794, Oct 2008.
- [83] K. M. Silva, B. A. Souza, and N. S. D. Brito, "Fault detection and classification in transmission lines based on wavelet transform and ann," *IEEE Transactions on Power Delivery*, vol. 21, no. 4, pp. 2058–2063, Oct 2006.
- [84] D. G. Patino, E. G. G. Erira, E. E. Rosero, and J. R. FuelagÃn, "Sogi-fl for synchronization and fault detection in an inverter connected to the grid," in *Innovative Smart Grid Technologies Latin America (ISGT LATAM), 2015 IEEE PES*, Oct 2015, pp. 833–838.
- [85] "IEEE standard for ac high-voltage circuit breakers rated on a symmetrical current basis - preferred ratings and related required capabilities for voltages above 1000

- v,” *IEEE Std C37.06-2009*, pp. 1–46, Nov 2009.
- [86] F. J. Rodriguez, E. Bueno, M. Aredes, L. G. B. Rolim, F. A. S. Neves, and M. C. Cavalcanti, “Discrete-time implementation of second order generalized integrators for grid converters,” in *2008 34th Annual Conference of IEEE Industrial Electronics*, Nov 2008, pp. 176–181.
- [87] T. Ngo, M. Lwin, and S. Santoso, “Steady-state analysis and performance of low frequency ac transmission lines,” *IEEE Transactions on Power Systems*, vol. 31, no. 5, pp. 3873–3880, Sept 2016.
- [88] T. Ngo, Q. Nguyen, and S. Santoso, “Voltage stability of low frequency ac transmission systems,” in *2016 IEEE/PES Transmission and Distribution Conference and Exposition (T D)*, May 2016, pp. 1–5.
- [89] —, “Detecting positive-sequence component in active power filter under distorted grid voltage,” in *2015 IEEE Power Energy Society General Meeting*, July 2015, pp. 1–5.
- [90] T. Ngo and S. Santoso, “Improving proportional-resonant controller for unbalanced voltage and frequency variation grid,” in *2016 IEEE/PES Transmission and Distribution Conference and Exposition (T D)*, May 2016, pp. 1–5.
- [91] T. Ngo, Q. Nguyen, and S. Santoso, “Improving performance of single-phase sogi-fll under dc-offset voltage condition,” in *Industrial Electronics Society, IECON 2014 - 40th Annual Conference of the IEEE*, Oct 2014, pp. 1537–1541.

- [92] T. Ngo, M. Lwin, and S. Santoso, "Analysis of distance protection in low frequency ac transmission systems," in *2016 IEEE Power and Energy Society General Meeting (PESGM)*, July 2016, pp. 1–5.
- [93] —, "Analysis of distance protection in low frequency ac transmission systems," in *2016 IEEE/PES General Meeting (IEEE PES16)*, July 2016, pp. 1–5.
- [94] H. T. Le, "Increasing wind power penetration and voltage stability limits using energy storage systems," Ph.D. dissertation, The University of Texas at Austin, Texas, USA, May 2010.
- [95] S. Zhou, J. Liu, L. Zhou, and H. She, "Cross-coupling and decoupling techniques in the current control of grid-connected voltage source converter," in *Applied Power Electronics Conference and Exposition (APEC), 2015 IEEE*, March 2015, pp. 2821–2827.
- [96] A. Morandi, "Fault current limiter: An enabler for increasing safety and power quality of distribution networks," *IEEE Transactions on Applied Superconductivity*, vol. 23, no. 6, pp. 5 604 608–5 604 608, Dec 2013.
- [97] F. B. Costa, B. A. Souza, N. S. D. Brito, J. A. C. B. Silva, and W. C. Santos, "Real-time detection of transients induced by high-impedance faults based on the boundary wavelet transform," *IEEE Transactions on Industry Applications*, vol. 51, no. 6, pp. 5312–5323, Nov 2015.
- [98] P. Dutta, A. Esmailian, and M. Kezunovic, "Transmission-line fault analysis using synchronized sampling," *IEEE Transactions on Power Delivery*, vol. 29, no. 2, pp.

942–950, April 2014.

- [99] P. Nayak, A. Pradhan, and P. Bajpai, “Secured zone 3 protection during stressed condition,” *IEEE Trans. on Power Delivery*, vol. 30, no. 1, pp. 89–96, Feb 2015.
- [100] S. Das, S. Santoso, and A. Maitra, “Effects of distributed generators on impedance-based fault location algorithms,” in *2014 IEEE PES General Meeting*, July 2014, pp. 1–5.
- [101] B. Chattopadhyay, M. Sachdev, and T. Sidhu, “An on-line relay coordination algorithm for adaptive protection using linear programming technique,” *Power Delivery, IEEE Trans. on*, vol. 11, no. 1, pp. 165–173, Jan 1996.
- [102] A. Urdaneta, R. Nadira, and L. Perez Jimenez, “Optimal coordination of directional overcurrent relays in interconnected power systems,” *IEEE Trans. on Power Delivery*, vol. 3, no. 3, pp. 903–911, Jul 1988.
- [103] A. Noghabi, J. Sadeh, and H. Mashhadi, “Considering different network topologies in optimal overcurrent relay coordination using a hybrid ga,” *IEEE Trans. on Power Delivery*, vol. 24, no. 4, pp. 1857–1863, Oct 2009.
- [104] A. Noghabi, H. Mashhadi, and J. Sadeh, “Optimal coordination of directional overcurrent relays considering different network topologies using interval linear programming,” *IEEE Trans. on Power Delivery*, vol. 25, no. 3, pp. 1348–1354, July 2010.
- [105] J. Sykes, V. Madani, J. Burger, M. Adamiak, and W. Premerlani, “Reliability of protection systems (what are the real concerns),” in *2010 63rd Annual Conference for Protective Relay Engineers*, March 2010, pp. 1–16.

- [106] D. Tziouvaras, "Relay performance during major system disturbances," in *60th Annual Conference for Protective Relay Engineers, 2007.*, March 2007, pp. 251–270.
- [107] E. Bernabeu, J. Thorp, and V. Centeno, "Methodology for a security/dependability adaptive protection scheme based on data mining," *Power Delivery, IEEE Transactions on*, vol. 27, no. 1, pp. 104–111, Jan 2012.
- [108] S. Brahma, "Distance relay with out-of-step blocking function using wavelet transform," *Power Delivery, IEEE Transactions on*, vol. 22, no. 3, pp. 1360–1366, July 2007.
- [109] D. Novosel, G. Bartok, G. Henneberg, P. Mysore, D. Tziouvaras, and S. Ward, "IEEE PSRC report on performance of relaying during wide-area stressed conditions," *Power Delivery, IEEE Transactions on*, vol. 25, no. 1, pp. 3–16, Jan 2010.
- [110] H.-S. Choi, S.-H. Lim, and D.-C. Chung, "Discharge and current limiting characteristics of a superconducting fuse," *IEEE Transactions on Applied Superconductivity*, vol. 15, no. 2, pp. 2360–2363, June 2005.
- [111] G. b. Zou and H. l. Gao, "The current differential and travelling wave based algorithm for ultra high speed hybrid protection," in *Electric Utility Deregulation and Restructuring and Power Technologies, 2008. DRPT 2008. Third International Conference on*, April 2008, pp. 1693–1697.
- [112] A. K. Sinha and A. K. Yadav, "Design of hv transmission line protection and control system using wavelet transform for microcontroller application," in *2006 IEEE Power India Conference*, 2006, pp. 5 pp.–.

- [113] M. Ciobotaru, R. Teodorescu, and V. Agelidis, "Offset rejection for pll based synchronization in grid-connected converters," in *23rd IEEE Applied Power Electronics Conference and Exposition, 2008. APEC 2008.*, 2008, pp. 1611–1617.
- [114] F. Freijedo, A. Yepes, O. Lopez, A. Vidal, and J. Doval-Gandoy, "Three-phase plls with fast postfault retracking and steady-state rejection of voltage unbalance and harmonics by means of lead compensation," *Power Electronics, IEEE Transactions on*, vol. 26, no. 1, pp. 85–97, Jan 2011.
- [115] F. Freijedo, J. Doval-Gandoy, O. Lopez, and E. Acha, "Tuning of phase-locked loops for power converters under distorted utility conditions," *Industry Applications, IEEE Transactions on*, vol. 45, no. 6, pp. 2039–2047, Nov 2009.
- [116] X. Guo, W. Wu, and Z. Chen, "Multiple-complex coefficient-filter-based phase-locked loop and synchronization technique for three-phase grid-interfaced converters in distributed utility networks," *Industrial Electronics, IEEE Transactions on*, vol. 58, no. 4, pp. 1194–1204, April 2011.
- [117] Y. Cho, G. Cokkinides, and A. Meliopoulos, "LFAC-transmission systems for remote wind farms using a three-phase, six-pulse cycloconverter," in *Power Electronics and Machines in Wind Applications (PEMWA), 2012 IEEE*, July 2012, pp. 1–7.
- [118] C. Mau, K. Rudion, A. Orths, P. B. Eriksen, H. Abildgaard, and Z. Styczynski, "Grid connection of offshore wind farm based dfig with low frequency ac transmission system," in *Power and Energy Society General Meeting, 2012 IEEE*, July 2012, pp. 1–7.

- [119] W. Xifan, C. Chengjun, and Z. Zhichao, “Experiment on fractional frequency transmission system,” *Power Systems, IEEE Transactions on*, vol. 21, no. 1, pp. 372–377, Feb 2006.
- [120] R. Nakagawa, T. Funaki, and K. Matsuura, “Installation and control of cycloconverter to low frequency ac power cable transmission,” in *Power Conversion Conference, 2002. PCC-Osaka 2002. Proceedings of the*, vol. 3, 2002, pp. 1417–1422 vol.3.
- [121] A. Merkhouf, P. Doyon, and S. Upadhyay, “Variable frequency transformer x2014;concept and electromagnetic design evaluation,” *Energy Conversion, IEEE Transactions on*, vol. 23, no. 4, pp. 989–996, Dec 2008.
- [122] W. Fischer, R. Braun, and I. Erlich, “Low frequency high voltage offshore grid for transmission of renewable power,” in *Innovative Smart Grid Technologies (ISGT Europe), 2012 3rd IEEE PES International Conference and Exhibition on*, Oct 2012, pp. 1–6.
- [123] C. Taylor, *Power System Voltage Stability*. McGraw-Hill, Inc, 1994.
- [124] GWEC, *Global Wind Statistics 2013*. Global Wind Energy Council, 2014, http://www.gwec.net/wp-content/uploads/2014/02/GWEC-PRstats-2013_EN.pdf.
- [125] R. Wiser and B. Mark, *2012 Wind Technologies Market Report*. US Department of Energy, 2013, <http://emp.lbl.gov/sites/all/files/lbnl-6356e.pdf>.
- [126] T. Cutsem and C. Vournas, *Voltage Stability of Electric Power Systems*. Springer, 1998.

- [127] EPRI, *Transmission line reference book 115 - 138 kV compact line design*. Electric Power Research Institute, 1978.
- [128] ———, *Transmission line reference book 345 kV and above*. Electric Power Research Institute, 1982.
- [129] A. Merkhouf, S. Upadhyay, and P. Doyon, “Variable frequency transformer - an overview,” in *Power Engineering Society General Meeting, 2006. IEEE*, 2006, pp. 4 pp.–.
- [130] J. Kang, N. Takada, E. Yamamoto, and E. Watanabe, “High power matrix converter for wind power generation applications,” in *Power Electronics and ECCE Asia (ICPE ECCE), 2011 IEEE 8th International Conference on*, 2011, pp. 1331–1336.
- [131] PUCT, *CREZ Transmission Projects*, 2014, <http://www.texascrezprojects.com/>.
- [132] B. Wu, Y. Lang, N. Zargari, and S. Kouro, *Power Conversion and Control of Wind Energy Systems*. Wiley-IEEE Press, 2011.
- [133] S. Barakati, M. Kazerani, and X. Chen, “A new wind turbine generation system based on matrix converter,” in *Power Engineering Society General Meeting, 2005. IEEE*, June 2005, pp. 2083–2089 Vol. 3.

Vita

Tuan Anh Ngo was born in Yen Thanh, Nghe An, Vietnam on 21 April 1985. He received the Bachelor of Engineering degree in Electrical Engineering from Hanoi University of Technology in 2008 and Master's degree from Pohang University of Science and Technology (POSTECH) in 2011. He then worked as research engineer for R&D center in LS/LG company before came to the United States of America for Ph.D. degree in 2013. He is currently enrolled in the Ph.D. program in electrical and computer engineering department at the University of Texas at Austin. His research interests include power transmission, power quality, power system studies, renewable energy, applied control, and power electronics.

Permanent address: 1102 CT1A, KDT Xala Hadong
Hanoi, Vietnam 100000

This dissertation was typeset with L^AT_EX[†] by the author.

[†]L^AT_EX is a document preparation system developed by Leslie Lamport as a special version of Donald Knuth's T_EX Program.